Japan Concrete Institute

Proceedings of 2012 JCI-KCI-TCI Symposium on

Recent Advancement of Technologies in Concrete Engineering

Hiroshima, Japan, July 2-3, 2012

Organizing Committee

Hirozo Mihashi	Chairman, Contact Person of JCI, Tohoku University, Japan
Kenro Mitsui	Secretary, Takenaka Corporation, Japan
Takafumi Noguchi	Secretary, The University of Tokyo, Japan
Koji Sakai	Secretary, Kagawa University, Japan
Ryoichi Sato	Secretary, Hiroshima University, Japan
Tsutomu Kanazu	Central Research Institute of Electric Power Industry, Japan
Tetsushi Kanda	Kajima Corporation, Japan
Toshiharu Kishi	The University of Tokyo, Japan
Yasuhiro Kuroda	Shimizu Corporation, Japan
Yuko Ogawa	Hiroshima University, Japan
Etsuo Sakai	Tokyo Institute of Technology, Japan
Takumi Shimomura	Nagaoka University of Technology, Japan
Yu-Chen OU	Contact Person of TCI, National Taiwan University of Science and Technology, Taiwan
Soobong Shin	Contact Person of KCI, Inha University, Korea

Sponsor:
Japan Concrete Institute (JCI)

Co-sponsors:
Korea Concrete Institute (KCI) & Taiwan Concrete Institute (TCI)

Auspices:
Chugoku Electric Power Co., Inc.

Table of Contents

Applications of Synchrotron X-ray Radiation on Structural Materials Research in Nano/Micro-scale
Jae-Eun OH and Paulo J. M. MONTEIRO /KCI

Carbon Dioxide Uptake during Concrete Life Cycle
Yasuhiro KURODA and Toshifumi KIKUCHI /JCI

“

Long-term Behavior and Durability of Concrete Structures

Cyclic Behavior of Reinforced Concrete Beams with Corroded Transverse Reinforcement
Yu-Chen OU and Hou-Heng CHEN /TCI

Simulation of Shrinkage Related Behavior of Concrete Structures Based on Durability Mechanics
Takumi SHIMOMURA /JCI

An Analytical Study of Long-term Deformation in SRC Columns Considering Differential Moisture Distribution
Jin-Keun KIM and Gyeong-Hee AN /KCI

Relative Humidity and Drying Shrinkage of Hardening Concrete Containing Normal- and Light-Weight Coarse Aggregates: a Comparative Experimental Study
Seongcheol CHOI and Young Soo CHUNG /KCI

Reliability-based Design for Concrete-cover Thickness Considering the Corrosion Hazard of Reinforcing Steel Bars: Coastal Regions in Taiwan
Chien-Kuo CHIU and Fung-Chung TU /TCI

The Abrasion of Concrete Made of Industry By-products
Wen-Chen JAU /TCI

Preface

Since new technologies for increasing the strength and lifespan of concrete structures and for reducing project's environmental impacts are being constantly developed, exchanging ideas and better understanding of recent advancement of technologies in concrete engineering could be useful for shaping the future of Asia we live in.

In 2007, President of Korea Concrete Institute (KCI) Young-Soo Chung proposed Japan Concrete Institute (JCI) and Taiwan Concrete Institute (TCI) to organize Joint Symposium of these three institutes for this purpose.

The first KCI-JCI-TCI symposium was held during November 6-8, 2008 in Ilsan, Korea. The symposium consisted of a one-day seminar and a technical visit. Eighteen papers on Assessment of Existing Concrete Structures & Recent Advancements in Concrete Technology were presented at the symposium. The first symposium gave a form to the framework of the symposium of three institutes very appropriately.

Then the second TCI-JCI-KCI symposium was held during November 26-28, 2010 in Taipei, Taiwan. The second symposium consisted of a one-day seminar and a technical visit, too. The symposium themes were Sustainable Concrete Technology & New RC Structures and totally seventeen papers were presented.

The third JCI-KCI-TCI symposium on Recent Advancement of Technologies in Concrete Engineering is held during July 1-3, 2012 in Hiroshima, Japan. As the same as the previous two symposiums, a one-day seminar and a technical visit are organized. Seventeen papers are presented on Control of Cracking, New Materials and Technology & Long-term Behavior and Durability of Concrete Structures.

As usual, the organizers of symposiums were responsible for pointing out the main themes and concrete related problems on which we should work and debate. These themes and research directions usually change in time. Accordingly I am sure that future research cooperation of the three institutes will have helpful and useful effects on further development of concrete technology. Furthermore it is expected that outcomes of the joint symposiums could contribute to stimulate the activities of Asian Concrete Federation (ACF).

Finally, I would like to express my sincere thanks to the great support of the Japan Concrete Institute, the Korea Concrete Institute, and the Taiwan Concrete Institute, which made this joint symposium possible. In addition, I also wish to acknowledge the auspices of the Chugoku Electric Power Co., Inc. as well as all of members of the Organizing Committee and, in particular, the authors for their excellent contributions.

July 1st, 2012

Hirozo Mihashi
Chairman of the Organizing Committee

Proceedings of the 3rd JCI-KCI-TCI Symposium on Recent Advancement of Technologies in Concrete Engineering
Japan Concrete Institute, July 2012

Shrinkage cracking control technology for R/C structures by combining SRA and expansive agents in concrete

Tetsushi. Kanda, Haruki. Momose and Fumitoshi. Sakuramoto
Kajima Technical Research Institute, Chofu-shi, Japan

ABSTRACT

Mix proportions and building application of Crack Reducing Concrete, CRC, using expansive agent and shrinkage reducing agent, were studied for a crack restriction measure of floor slab construction. Basic properties such as compressive strength and fresh behavior of CRC were clarified and mix proportions applicable to real constructions were determined. Stability of fresh concrete based on the mix design was confirmed through constructions and strain behavior of the hardened structure was monitored. It was shown that the CRC has excellent construction executability, and higher crack reducing capability thanks to the introduction of chemical prestressing and subsequent development of shrinkage reducing effects.

Keywords:

1 INTRODUCTION

Growing interest in durability of building structures has marked the crack controlling technology that plays significant role on the durability of concrete structures. Cracking mechanisms have been quantitatively studied on the basis of the largely accumulated research results and some countermeasures have been proposed from the viewpoints of material science, construction technology and structural engineering (AIJ 2003). However, very few technologies were proven to be effective in a quantitative manner and used as a crack control design method.

For the establishment of crack controlling design method in the future, a notable technology with considerable impact and quantitative measure is the Crack Reducing Concrete (CRC) characterized by a combined use of expansive agent and shrinkage reducing agent (SRA) (Tomita 1994, Kanda et al. 2004). It has been reported that the synergetic effect of combining expansive agent and SRA is notable and it is possible to produce a concrete with very low shrinkage, which is effective in reducing shrinkage at real structures (Tomita et al. 1986).

However, CRC application in construction sites involves several unknown factors such as mix design procedure, manufacture and placement know-how and influences on the cracking mechanism of structures. This paper deals with these problems quantitatively executing experiments on mix design, construction and strain behavior of real structures and reports the practicability and shrinkage reducing effects of CRC.

2 SELECTION OF SRA MATERIALS

2.1 Overview of SRA Material Selection Experiment

(1) Experimental parameters

The targeted structure was a 4-story car parking tower with steel frames and R/C slabs. CRC was applied to its floor to examine crack controllability. Mix design experiment was formulated to determine the type of SRA with parameters shown in Table 1. This study is necessary because the effect of SRA on fresh properties such as air content is significant (Tomita 1988) while the range of air content at discharge in this construction was specified within 4.5% plus or minus 1.5% pursuant to Japanese Architectural Standard Specification 5 of Architectural Institute of Japan. The fresh concrete temperature included 30°C in addition to 20°C taking into account temperatures of the season of the construction.

(2) Materials used and mix proportions

Four types of SRA, all of them were alcohol type and major in the market, were tested as shown in Table 1. Products B and C were the modified versions of product A for a better air entraining capability, while product D was by another manufacturer. The other materials were common to

all the experiments: ordinary portland cement, a low-dosage lime-CSA type expansive agent, AE agent pursuant to JIS A 6204 and a superplasticizer of type I polycarbonic acid type were used. Mix proportions are listed in Table 2 where a part of unit water content was substituted with SRA. Water-binder ratio of 0.45 and unit water content of 170 kg/m^3 were common to all the mixes and the expansive agent of 20 kg/m^3 was admixed as a part of binder. The AE agent and the superplasticizer were prepared to have an air content of 4.5% and slump of 18 cm respectively.

Table 1 Items for material selection

Factor	Level	Parameter
SRA type	5	SRA 4 types and control
Fresh concrete temperature	2	20°C, 30°C

Table 2 Mix proportions for material selection

Mix	Water-binder ratio (%)	Unit water (kg/m^3)	Fine aggr. content (%)	Expansive agent (kg/m^3) *1	SRA (%) *2	SRA type
Mix-N	45	170	45	20	0	-
Mix-A	45	170	45	20	5	A
Mix-B	45	170	45	20	5	B
Mix-C	45	170	45	20	5	C
Mix-D	45	170	45	20	5	D

*1 Inclusive mix, *2 Included in the unit water content

Table 3 Test items

Test name	Method	Purpose
Fresh property	JIS A 1128, 1101	Changes in air content and slump
Compressive strength	JIS A 1108	Possible reduction by the type of SRA
Restrained strain	JIS A 6202 *1	Initial expansion and drying shrinkage
Spacing factor	ASTM C 457	Confirm frost resistance

*1 A 7-day sealed curing after mixing before drying

(3) Test items

Test items for SRA selection may be chosen are shown in Table 3. Changes in air content and slump in the fresh state and compressive strength decreasing due to SRA addition were particularly focused on. Volume changes of hardened specimens were compared using the standard restrain test (method B in JIS A 6202). Air void spacing factor was measured with the linear traverse method for fear of coarsening of entrained air voids due to SRA addition.

2.2 Results of the SRA material selection experiment

Fresh properties of all the mixes are shown in Table 4. Dosage of superplasticizer was not significantly different according to the type of SRA and fresh concrete temperatures while that of AE agent differs considerably to assure the targeted air contents. A larger amount of AE agent was required for Mix-A compared to other cases using different types of SRA and air entraining was impossible at 30°C.

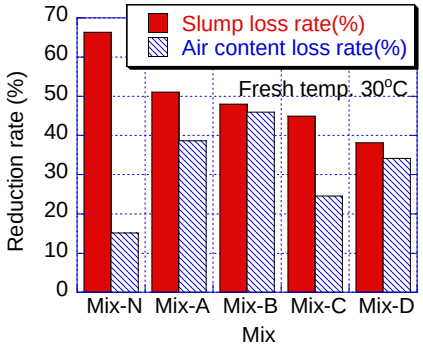

Figure 1 Changes in fresh properties with time

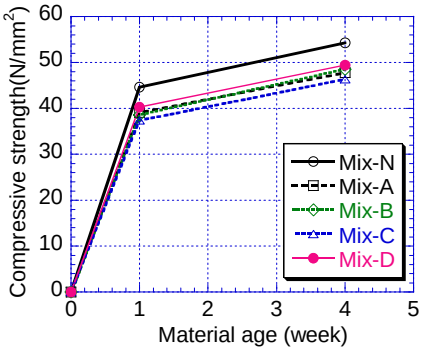

Figure 2 Compressive strength by the type of SRA

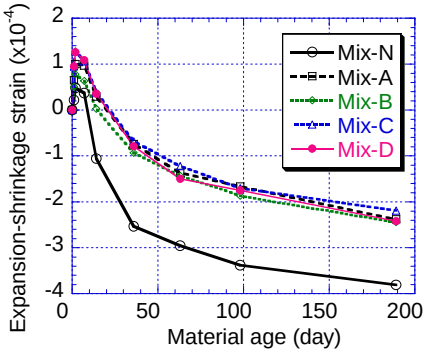

Figure 3 Volume change behavior by the type of SRA

Slump losses and changes in air content from mixing to an age of 60 min. are shown as a decreasing rate in Figure 1. The fresh property tests at the age of 60 min. were performed with remixing of the concrete that was left without external effects after the first test at mixing. This generally led to a large slump loss but effect of SRA addition was small compared with the control specimen (Mix-N).

Table 4 Fresh properties in material selection

Mix	Fresh concrete temperature 20°C						Fresh concret temperature 30°C					
	*1)Super-plasticizer (%)	*2)AE agent (A)	Age (min)	Slump (cm)	Air content (%)	Fresh concrete temp. (°C)	*1)Super-plasticizer (%)	*2)AE agent (A)	Age (min)	Slump (cm)	Air content (%)	Fresh concrete temp. (°C)
Mix-N	0.75	0	0	18.5	3.3	22.1	0.60	0	0	15.5	4.6	27.1
			30	10.5	3.1	22.0			30	6.0	3.9	25.9
			60	6.5	2.8	21.7			60	3.0	3.2	26.9
Mix-A	0.70	6	0	19.5	4.4	22.0	0.65	40	0	18	2.2	31.7
			30	14	3.3	22.1			30	4	1.8	31.9
			60	9.5	2.7	22.2			60	12	1.6	31.4
Mix-B	0.70	1	0	20.0	5.0	21.6	0.65	1	0	18.5	4.6	31.6
			30	13.5	2.8	21.5			30	6.5	3.3	31.6
			60	10.5	2.7	21.7			60	4.5	2.5	31.1
Mix-C	0.65	1	0	18	5.7	21.9	0.65	1	0	17	3.8	31.6
			30	12.5	4.6	21.4			30	3.5	2.0	31.8
			60	10	4.3	21.4			60	2	2.0	31.8
Mix-D	0.65	1	0	19.5	4.1	21.7	0.65	1	0	17.5	3.0	31.6
			30	15	2.8	21.7			30	6	2.2	31.8
			60	12	2.7	21.6			60	3	1.9	31.5

*1 weight ratio to binder *2 unit: 1A = 0.003% of binder weight

In spite of this tendency, decreasing rate of air content was small in the control specimen and significant in SRA added specimens depending on the type of SRA. Among SRA added mixes, air content was most stable in Mix-C. Changes in compressive strength with age, at a fresh concrete temperature of 20°C, are shown in Figure 2 where the addition of SRA leads to the compressive strength reduction at most 10% without regard to the type of SRA.

Restrained strain test results are shown in Figure 3, where the initial expansion of SRA added specimen was twice as large as that of the control specimen and the drying shrinkage of SRA added specimen was 40% as small as that of the control specimen. The reduction of drying shrinkage at an SRA dosage of 5 kg/m^3 was approximately 30% according to a literature (Tomita 1988) whereby synergetic effect with expansive agent is significant.

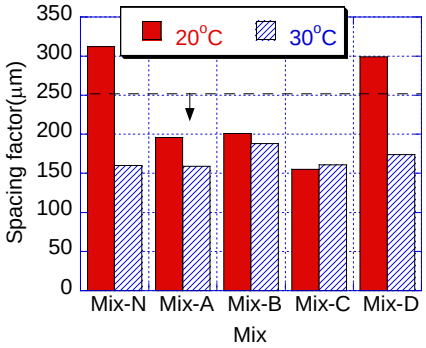

Figure 4 Spacing factor by the type of SRA

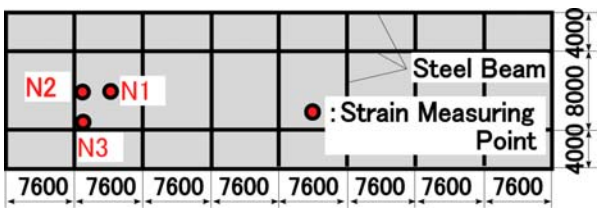

Figure 5 Floor plan of the test building and strain measurement points

Results of spacing factor measurement are shown in Figure 4. At a fresh concrete temperature of 20°C, each case except for Mix-N and Mix-D satisfies a spacing factor of 250 μm or less that is preferable for a better frost resistance (Kasai 1995), while Mix-D still shows a spacing factor of approximately 300 μm that is slightly greater than 250 μm and almost equal to that of the control specimen (Mix-N). The effect of SRA addition on the coarsening of entrained air void may be small as a whole.

The above results imply that the product A with in appropriate air entrainment may cause problems during construction at high temperatures in the summer. No particular difference in properties was found between other SRA added specimens but overall estimation resulted in the use of product C in the construction experiment.

3 CONSTRUCTION EXPERIMENTS

3.1 Execution plan

(1) Concrete construction plan

The plan view of the applied car-parking tower is shown in Figure 5. CRC was used for floor slabs from the second to fourth floor for 960 m^2 per floor. Placement for each floor was performed every three days using concrete pump for a necessary amount of 140 m^3 per floor. Floor surface was finished directly with a trowel for three times and was subsequently wet-cured with water spraying intensively. Slab thickness was 140 mm with a doubled reinforcing bar of D10@200 and designed as a one-way slab for the span direction using flat deck plate.

(2) Mix proportion of concrete and production plan

The CRC used for the construction was designed to have a slump of 18cm and specified compressive

strength of 27N/mm^2 and the mix proportion was determined after a trial mixing as shown in Table 5. The original mix proportion of the manufacturing plant capable of satisfying the specification is also shown but the water-binder ratio was reduced from 0.58 to 0.54 taking into account possible decrease in compressive strength and scatter of air content. In addition to AE agent, anti-foaming agent was used to restrict entrapped air during transportation. The anti-foaming agent was a polyoxialkylene type and dosed 0.0025% of the binder mass.

During manufacturing of CRC, the expansive agent was introduced from the storage tank on the ground by a dedicated pump and SRA was introduced to the water-measuring tank by hand. Mixing time was extended from standard 30 seconds to 45.

(3) Measurement plan

Strain behavior of structural concrete was measured at a unit area of the 3rd floor slab. A control steel bar with a strain gauge was embedded three points of the floor slab and strains of three directions were traced continuously and subjected to a rosette analysis. In this study, all-in-one behavior of the control steel bars and concrete was assumed, hence the thermal strain can be separated by measuring the concrete temperatures (Momose *et al.* 2003).

As shown in Figure 6, slab specimens were prepared as an internally restrained model where concrete was placed at the same time as that of the floor concrete and strain behavior responsible solely by the internal restraint was monitored. In addition, slightly restrained specimen with a reinforcement ratio of 0.1%, capable of stabilizing expansion and of representing free volume changes, was subjected to strain measurement. Stability of properties was confirmed through the execution of fresh property tests and specimen sampling for compressive strength test.

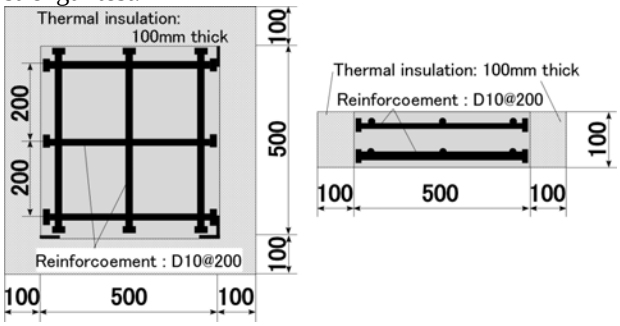

Fig.6 Model specimen (internally restrained)

Table 5 Mix proportion of concrete for construction

Mix	Water-binder ratio (%)	Unit water (kg/m^3)	Fine aggr. Content (%)	Expansive agent (kg/m^3)	SRA (kg/m^3)	Superplasticizer (l/m^3)
Original	58	180	47	-	-	0.78
CRC	54	180	46	20	5	1.08

3.2 Results of the construction test

Concrete placement was performed in a three days at the beginning of September when 28 agitating trucks per day successfully completed the placement for the floor of one story. Compaction and troweling of slab surface were executed in the same way as in the normal concrete though the CRC temperatures at discharge exceeded 30°C.

Results of the fresh property test, variations of slump and air content, for every 4 trucks are shown in Figures 7 and 8. Variations at discharge are distributed within the control limit of 18±2.5cm and 4.5±1.5%. Both slump and air content values after mixing were set higher taking into account subsequent transportation time of 30 minutes. It appears that variation of air content, which was the primary concern, was fully controlled thanks to the frequent fresh property tests and resulting fine dosage control of AE agent and anti-foaming agent.

Compressive strength of specimen, cured in water on site and performed at an independent organization, was greater than approximately 35 N/mm^2 and easily satisfied the spcified value of 27 N/mm^2.

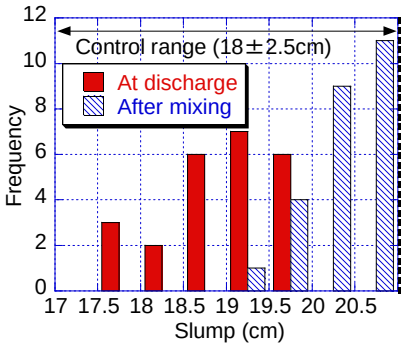

Figure 7 Variation of slump

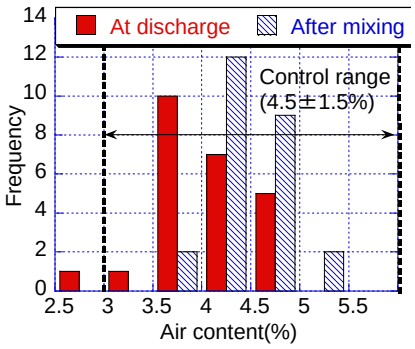

Figure 8 Variation of air content

3.3 Results of strain measurement

No cracking was found in the concrete slabs of 960 m^2 at each floor until the age of four months though concrete of each floor slab was placed at one time without any crack-inducing grooves.

Strain behavior was examined with total strain and net strain: the total strain is considered to represent the real concrete behavior after compensating the

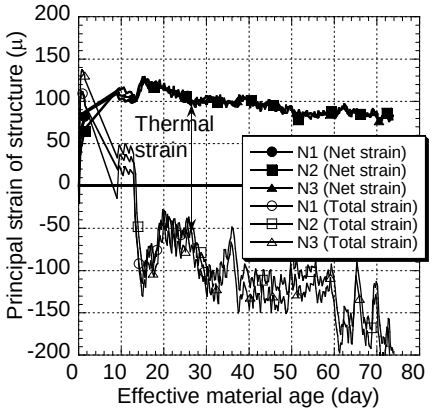

Figure 9 Changes in strain of the structure

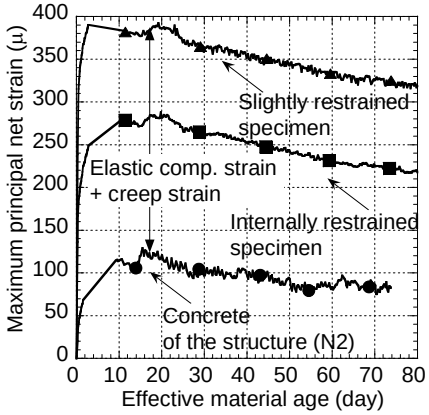

Figure 10 Effect of restraint on strain

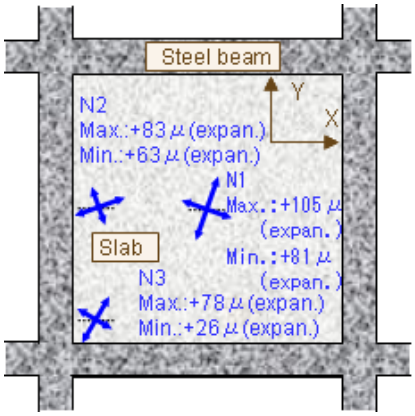

Figure 11 Strain distribution

temperature dependency of strain gauge and the net strain is a result of eliminating thermal strain from the total strain.

Thermal strain was calculated on the basis of a linear expansion coefficient of 10.3×10^{-6}/deg which was obtained as a least-square linear regression of incremental strains associated with temperature changes of every 6 hours in the slightly restrained specimens. The linear expansion coefficient involves some effects of material age and water content because data acquisition was performed at an age form 11 to 91days when hydration reactions of cement and expansive agent were supposed to become stable.

Strain behavior of floor concrete is shown in Figure 9. Effective material age according to CEB-FIP90 and maximum principal strain are represented in the horizontal and vertical axes. Both in the total and the net strain, the maximum principal strain behaved similarly at points N1, N2 and N3 and difference by measuring point was small, though the measurement at the point N1 became impossible after 32 days by some errors. Approximately 100μ of the initial expansion strain remained until the age of 75 days in the net strain while the total strain showed an expansion of 100 to 150μ at early ages and subsequent shrinkage of 200μ at the age of 75 days. The difference can be attributed to a fluctuation in the concrete floor temperature of approximately 20 degree between that at the placement and that at the age of 75 days.

Difference in strain behavior with the difference in degree of restraint is shown in Figure 10 where the strains of the internally restrained specimen and the floor concrete were 100μ and 300μ smaller than that of the slightly restrained specimens. The strain shown in this figure are the net strain and showing that drying proceeds slower than that in Figure 3 because surface area is relatively small compared to its volume.

The principal strains of the concrete floor and their directions are shown in Figure 11. Maximum strain ranged from 80 to 150μ and minimum strain ranged from 25 to 80μ showing the small difference in strain between the maximum and the minimum.

4 DISCUSSION

The restrained stress σ_c predominant to concrete cracking is briefly discussed in this section while the estimation method involves considerable assumptions and the result should not be decisive. However, taking into account the lack in such a study dealing with the restrained stress of full-scale floor elements, this discussion could be of some contributions to this field.

In this discussion, strain of the restrained body is estimated from the net strain of the floor slab and using the balance of forces σ_c is calculated. Unlike building walls that is restrained by the footing beams, the floor slabs of the targeted building could exhibit a thermal behavior in conjunction with the restraints such as internal reinforcing steel and steel beams under the same ambient temperatures. In addition, the difference in linear expansion coefficient of the floor slab and the restraints is so small that the thermal stress in the restrained concrete floor is of minor concern. Hence the net strain can be used for the estimation of σ_c.

For simplicity, the floor slab is treated as a uniaxial member. The balance of forces between concrete and the restraints is given by equation (1)

$$\sigma_c A_c + \varepsilon_d E_d A_d + \varepsilon_s E_s A_s + \varepsilon_r E_r A_r = 0 \quad (1)$$

where σ: restrained stress, ε: elastic strain, E: Young's modulus, A: sectional area and subscripts c, d, s and r denote concrete, deck plate, steel beam and reinforcing bar respectively. Strains ε_d, ε_s and ε_r should be known to obtain σ_c using equation (1). These strains were not measured in this study but can be substituted with a strain of concrete floor at the longitudinal direction of N1 and N3 points that are close to a steel beam, and strains ε_d, ε_s and ε_r are assumed to be equal. It was reported that strain distribution of the two dimensional member can be simplified as a one dimensional member without significant errors (Imamoto 2003). The input values

and the result of this estimation are shown in Tables 6 and 7. When strains at N2 and N3 are averaged, it was estimated that a compressive stress of σ_c=0.84N/mm^2 was created at the maximum expansion as a chemical prestressing and it remained for 0.49N/mm^2 at the age of 75 days. This shows a stress relaxation of approximately -0.3N/mm^2 was taken place due to drying shrinkage.

Table 6 Numerical data for stress estimation

Item	Dimensions	Cross sectional area (mm^2)
Concrete	7600x140mm	1058034
Deck plate	7600x1mm	7600
Reinforcement	D10@200mm double	5966
Steel structure	400x200x12x22mm	26144
Elastic modulus of steel	210kN/mm^2	-

Table 7 Estimation of restrained stress of concrete

Time /Point	Input value		Estimated value
	Point	Strain ε_s and ε_r (μ)	Stress σ_c (N/mm^2)
At maximum expansion	N2	110	0.87
	N3	104	0.82
	Mean	107	0.84
At 75-day	N2	65	0.51
	N3	58	0.46
	Mean	62	0.49

This compressive stress, even under subsequent drying shrinkage strain development, can be expected to contribute to a long-term cracking control. When applying JSCE formula to this building condition, the shrinkage strain is estimated to have developed 70% of the ultimate drying shrinkage strain. If we assume that the drying shrinkage of floor concrete develops more than half of the ultimate value, the compressive stress due to chemical prestressing will be nearly cancelled in a long term. If otherwise assumed that the cracking strength is a 70% of the splitting strength (AIJ 2003), at least a tensile stress of 1.5N/mm^2 remains at the tension side as a margin and the risk of cracking in the floor slab is supposed to be small. Floor slabs restrained both steel beams and deck plate are normally inescapable from cracking while use of CRC resulted in a successful cracking control.

5 CONCLUSIONS

Practical solutions necessary for the construction of Crack Reducing Concrete have been studied through the experiments of mix design, trial construction and strain behavior of a real structure. Major findings are as follows.

(1) Stable air entraining was performed during construction thanks to the selection of lower alcohol type shrinkage reducing agent leading to a satisfactory construction results.
(2) No cracking was found in the concrete slabs of 960 m^2 at each floor until the age of four months though the concrete of each floor slab was placed without any crack-inducing grooves.
(3) Risk of long-term cracking of the structure is supposed to be low thanks to an introduced chemical prestressing of 0.8N/mm^2 estimated with an approximate calculation.

ACKNOWLEDGEMENT

Authors express their sincere thanks to those involved in this study at Denki Kagaku Kogyo ltd. and Asahi Denka Kogyo ltd. for their generous cooperation.

REFERENCES

[1] AIJ. 2003. *Shrinkage cracking of concrete structures – Mechanisms and state-of-the-Art of technical measures.* Tokyo: Architectural Institute of Japan.
[2] Imamoto, K. 2003. Shrinkage behavior of various types of concrete walls. *Journal of Structural and Construction Engineering* (Japan). 568: 15-20.
[3] JSCE. 2002. *Standard specifications for design and construction of concrete structures – Verification for structural performance*. Chapter 3, Japan Society of Civil Engineers: 30-34.
[4] Kanda, T., et al. 2004. Experimental investigation of anti-cracking effects in concrete slab applying Expansive agent and shrinkage reducing agent, *JCI annual proceedings* (Japan). 26(1): 501-506.
[5] Kasai, Y. 1995. *The Concrete.* Tokyo: Gijyutsu Shoin.
[6] Momose, H. et al. Shrinkage behavior of real RC structure using low-heat portland cement and expansive agent. *JCI Symposium on High Performance Structures using Expansive Concrete, 2003. Tokyo*: Japan Concrete Institute: 21-26.
[7] Tomita, R. 1986. Shrinkage reducing effect of some chemical admixtures on RC building structures. *Concrete Engineering* (Japan). 24(5): 14-21.
[8] Tomita, R. 1988. Shrinkage reducing agent. *Concrete Engineering* (Japan). 26(3): 55-60.
[9] Tomita, R. 1994. Super low shrinkage concrete. *Concrete Engineering* (Japan). 32(7): 105-109.

Proceedings of the 3rd JCI-KCI-TCI Symposium on Recent Advancement of Technologies in Concrete Engineering
Japan Concrete Institute, July 2012

EVALUATION OF FIBER REINFORCED CONCRETE ON THE IMPACT AND BLAST RESISTANCE PERFORMANCE

Gyuyong Kim, Jeongsoo Nam, Hongseop Kim and Moohan Kim
Department of Architectural Engineering, Chungnam National University, Korea

ABSTRACT

Recently, projectiles or fragments generate localized effect characterized by penetration or perforation, spall scabbing, as well as more widespread crack propagation. The military and related research institutes began work on the project to reduce the blast damage. Therefore, in this study, we present results from an experimental study on the impact and blast resistance of fiber reinforced concrete with fiber types by high velocity steel projectile test and emulsion explosive explosion test. In the present work, the effectiveness of fiber reinforcement on the impact and blast resistance performance of concrete specimen has been investigated. Tensile and bending strengths of fiber reinforced concrete specimens were higher than of plain specimens, and the fiber reinforced concrete decrease in rear side spall was also higher. Fiber reinforced concrete has higher impact and blast resistance than plain specimen.

Keywords: *impact resistance, blast resistance, fiber reinforcement, shock damage, fracture mode*

1 INTRODUCTION

In recent years, the terror activity has happened due to the ideological conflicts around the world and involves the mechanical blast at times. It was reported that the damage of these mechanical forces is more enormous than the natural disasters, such as gale and earthquake. The concrete structures suffer damage by the blast wave when the explosion occurs. In addition, the destruction of structures by such explosion produces the fragments such as concrete and metal and then, the fragments impact the surrounding facilities at the speed of hundreds m/s, thereby damaging the loss of life and property. [1].

Recently, the military and related research institute began work on the project to reduce the blast damage. In particular, the research on the impact resistance performance of concrete with fibers was carried out[2]. The concrete with fibers have high strength, high-energy absorption and lightweight, which means that a small quantity of FRP can significantly increase the resistance of a structural member to resist tensile loads and bending moments, without significantly increasing its mass and stiffness[3]. To establish a design method which protects structures from explosive load, the mechanism of structural failure should be investigated[4].

According to previous studies[4-8], reported that relation on the concrete performance of compressive strength, tensile strength and strain, thickness for impact resistance performance.

Therefore, in this study, presents results from an experimental study on the Impact resistance of fiber reinforced concrete with fiber types by high velocity projectile test and emulsion explosive explosion test. The effects of the compressive and tensile strength of the concrete and fiber reinforced concrete, and the performance of reinforcement types of the concrete are discussed.

2 EXPERIMENTAL PLAN AND METHODS

2.1 Materials and mixture program

The mix proportions of the normal and fiber reinforced concrete are shown in Table 1. The water/binder ratio (W/B) was 0.3(Case of PC specimen) or 0.4 and unit weight of the binder was 533kg/m^3 (Case of PC specimen) or 1,129kg/m^3. Details pertaining the type and properties of the materials are shown in Table 2.

2.2 Experimental setup

All specimens subjected to impact tests had a common size of 100×100mm and a thickness of 10mm. The specimens for a compressive, tensile and

Table 1 Mix proportions of concrete

Mix ID[1)]	W/B	Cement (kg/m^3)	Fly-ash (kg/m^3)	Water (kg/m^3)	Coarse aggregate (kg/m^3)	Desalting sand (kg/m^3)	Silica sand (kg/m^3)	Fibers[2)] (kg/m^3)	Admixture[3)] (kg/m^3)
PC	0.3	533	-	160	948	750	-	-	4.3
PM	0.4	960	169	452	-	-	395	-	0.0
PVA	0.4	960	169	452	-	-	395	25.5	16.9
PE	0.4	960	169	452	-	-	395	18.6	22.6
S	0.4	960	169	452	-	-	395	153.9	5.6
PVA-S	0.4	960	169	452	-	-	395	12.9+77.7	11.3
PE-S	0.4	960	169	452	-	-	395	9.4+77.7	16.9

Note 1) PC : plain concrete, PM : plain mortar, PVA : polyvinyl alcohol, PE : polyethylene, S : steel fiber, PVA-S : PVA+S, PE-S: PE+S

2) Fiber ratio : 2, Case of PVA-S and PE-S was PVA 1:S 1 and PE 1:S 1

3) High range water reducer, Setting flow of BC : 550±50(mm), Setting flow of the rest : 170±20(mm)

bending strength test at 28days, after removal from the molds at 1 day, were cured in water at 20±3℃ until an age of 27days.

The experimental arrangement for projectile impact tests is shown in Fig. 1. This system can launch projectile with the velocity of ~370m/s. And steel projectile with a diameter of 4mm were used.

The schematic diagram of the blast test experimental setup is shown in Fig. 2. Specimens are put on wooden supports and emulsion explosive is placed on the center of a specimen. Concrete specimens are square plates of 1,000mm×1,000mm and 100mm in thickness, and the shape of emulsion explosive shown in Fig. 3.

A detonator is inserted on the side of emulsion explosive. The mass of emulsion explosive is set at 100 g to examine the effect of mass of explosive on the damage of specimen.

Table 2 Materials

Materials		Physical and chemical properties
Cement		▪Ordinary Portland cement ▪Density : 3.15(g/cm^3) ▪Fineness : 3,770(cm^2/g)
Fly-ash		▪Density : 2.30(g/cm^3) ▪Fineness : 3,228(cm^2/g)
Fine aggregate	▪Desalting sand	▪Density : 2.54(g/cm^3), ▪Absorption ratio : 1.01
	▪Silica sand	▪Density : 2.64(g/cm^3), ▪Absorption ratio : 1.01
Coarse aggregate		▪Crushed aggregate ▪Max size : 25(mm) ▪Density : 2.65(g/cm^3), ▪Absorption ratio : 1.39
Fiber	▪ PVA	▪Density : 1.30(g/cm^3) ▪Tensile strength : 1,300(N/mm^2) ▪Length : 12(mm) ▪Diameter : 40(㎛)
	▪ PE	▪Density : 0.95(g/cm^3) ▪Tensile strength : 2,700(N/mm^2) ▪Length : 15(mm) ▪Diameter : 12(㎛)
	▪ Steel	▪Density : 7.85(g/cm^3) ▪Tensile strength : 1,140(N/mm^2) ▪Length : 50.9(mm) ▪Diameter : 700(㎛)
High range water reducer		▪Polycarboxylic acid type

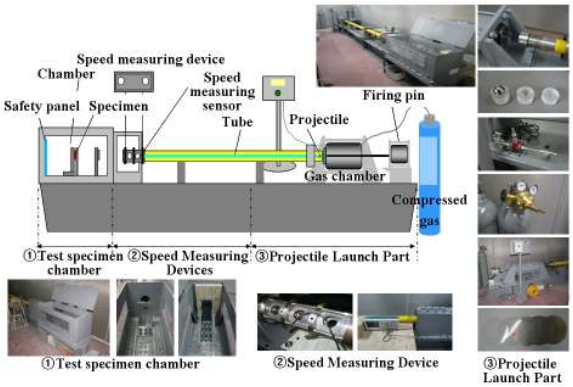

Fig.1 Schematic graph of the impact test setup

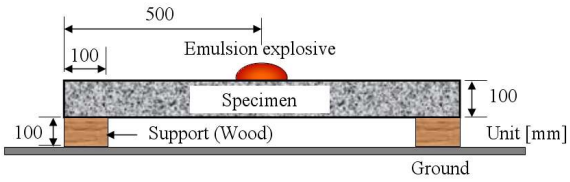

Fig.2 Schematic graph of the blast test setup

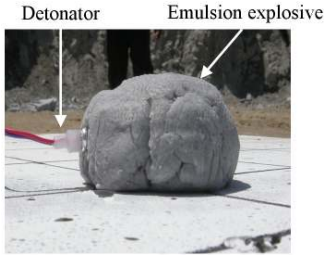

Fig.3 Emulsion explosive and detonator

Emulsion explosives have been used widely in explosion tests for structural members. In this study, Emulsion explosive is used in explosion tests because it is very safe chemically and easier to cast. Since the thermal energy obtained from detonation tests of emulsion explosive is 4605 kJ/kg.

2.3 Evaluation method

Failure modes of specimens subjected to impact and blast load have been commonly classified into "crater", "crater and spall" and "perforation" as shown in Fig. 4. A setup of impact and blast testing is shown in Fig. 5 and Fig. 6.

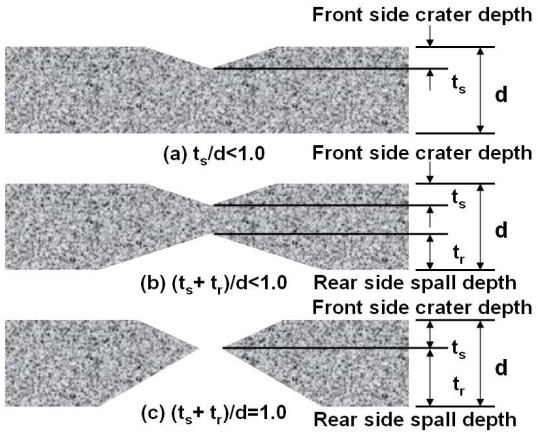

Fig.4 Damage evaluation of crate and spall

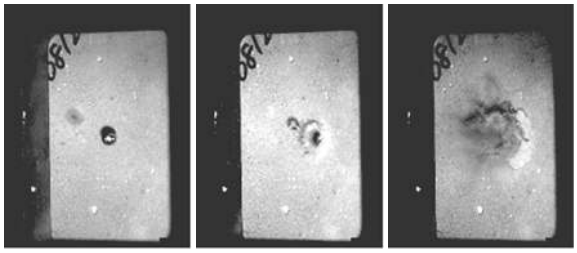

Fig.5 Setup of impact testing

Fig.6 Setup of blast testing

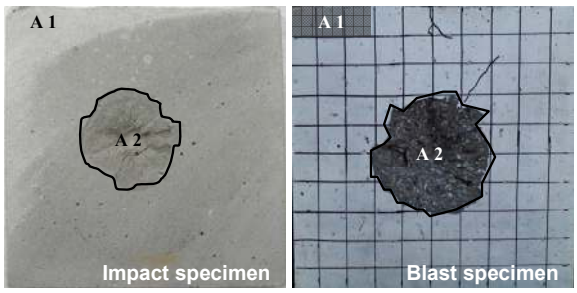

Fig.7 Example of damage mapping on specimen

The extent of the damage to each specimen was quantified graphically by mapping the craters on the front and rear sides and comparing the crater area, A1, to the total area, A1 + A2. This is demonstrated in Fig. 7. The percent of surside damage was calculated by 100% × A2/(A1 + A2).

3 RESULTS AND DISCISSION

3.1 Test results of engineering properties

Fig. 8, Table 3 summarizes the test results of engineering properties for 7 concrete mixtures with reinforcement type at age 28days. Compressive strength of fiber reinforced concrete specimen was lower than it of PC and PM specimen. However tensile and bending strength of fiber reinforced concrete specimen was higher than it of PC and PM specimen.

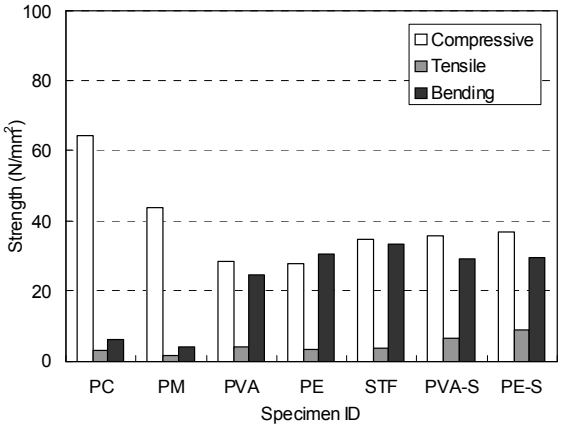

Fig.8 Test results of specimen strength

Table 3. Test results of engineering properties

Specimen ID	Ave. compressive strength (N/mm^2)	Ave. tensile strength (N/mm^2)	Ave. tensile strain (%)	Ave. bending strength (N/mm^2)	Ave. bending length (mm)
PC	64.3	2.78	0.01	5.87	0.31
PM	43.7	1.71	0.05	4.13	0.14
PVA	28.5	3.96	6.33	24.66	2.35
PE	27.9	3.61	4.01	30.74	4.24
STF	34.7	3.92	2.27	33.15	2.78
PVA-S	35.8	6.34	2.12	29.08	1.68
PE-S	36.7	8.88	2.87	29.37	3.16

3.2 Test results of impact resistance

The local damage of Plain specimen and fiber reinforced concrete specimen are shown in Fig. 9, respectively. The cross-sections images in these figures show perpendicular sections to support direction.

The projectile impact velocity ranged from 350 to 363m/s. PE, PVA-S and PE-S specimen was shown crater condition, and reduced the spall of concrete by fiber reinforcement.

The results of surside damage of front and rear sides are shown in Fig. 10. In case of PM specimen,

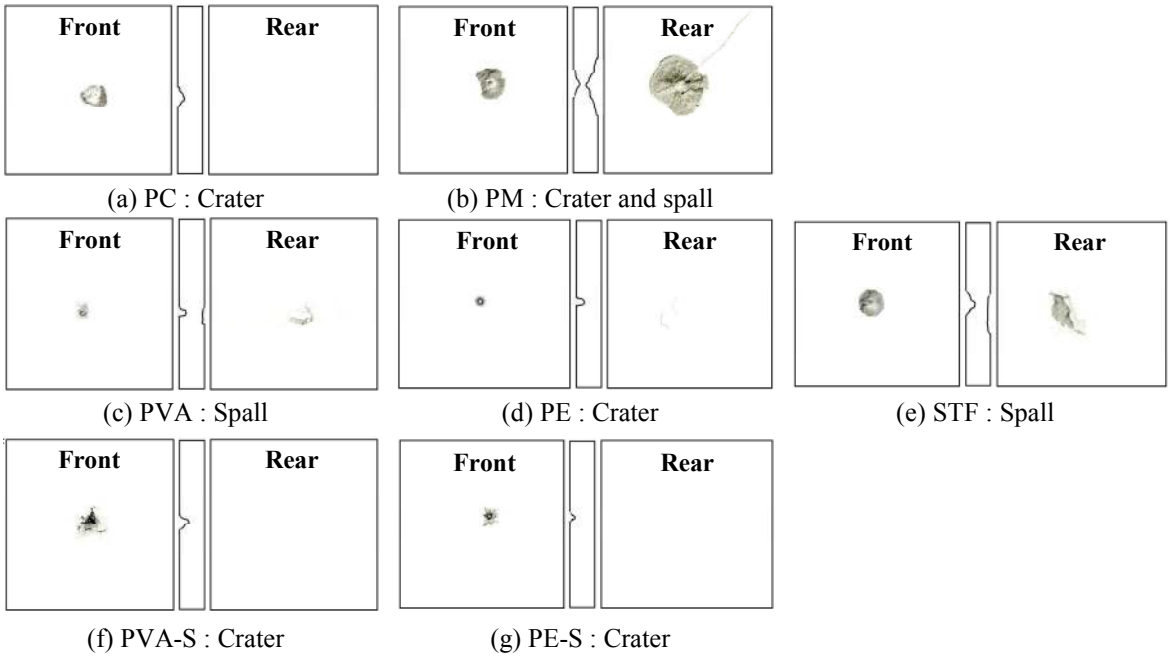

Fig. 9 Damage of specimens after impact test

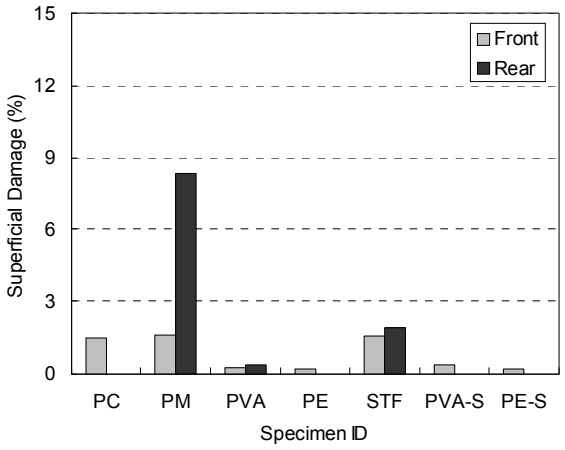

Fig. 10 Surside damage of front and rear sides by impact test

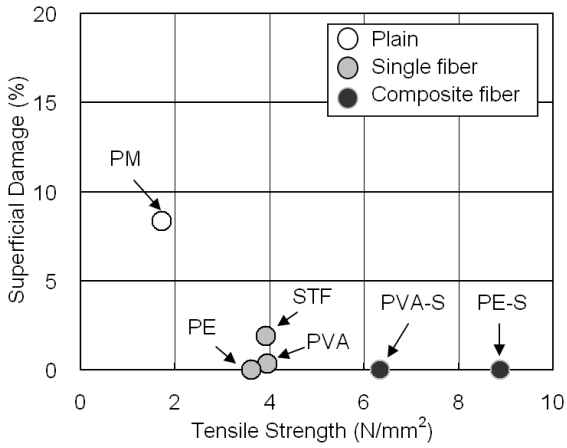

Fig. 12 Correlation of rear side damage and tensile strength by impact test

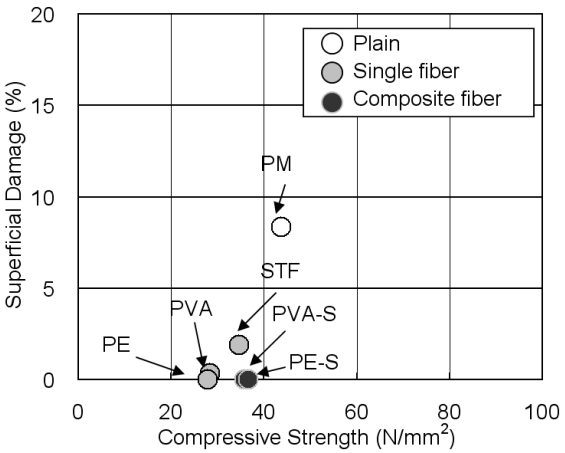

Fig. 11 Correlation of rear side damage and compressive strength by impact test

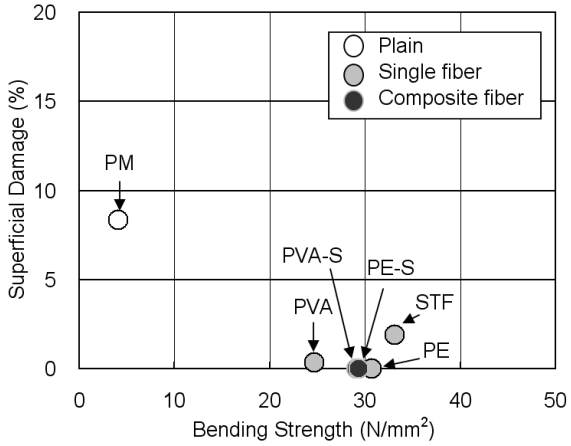

Fig. 13 Correlation of rear side damage and bending strength by impact test

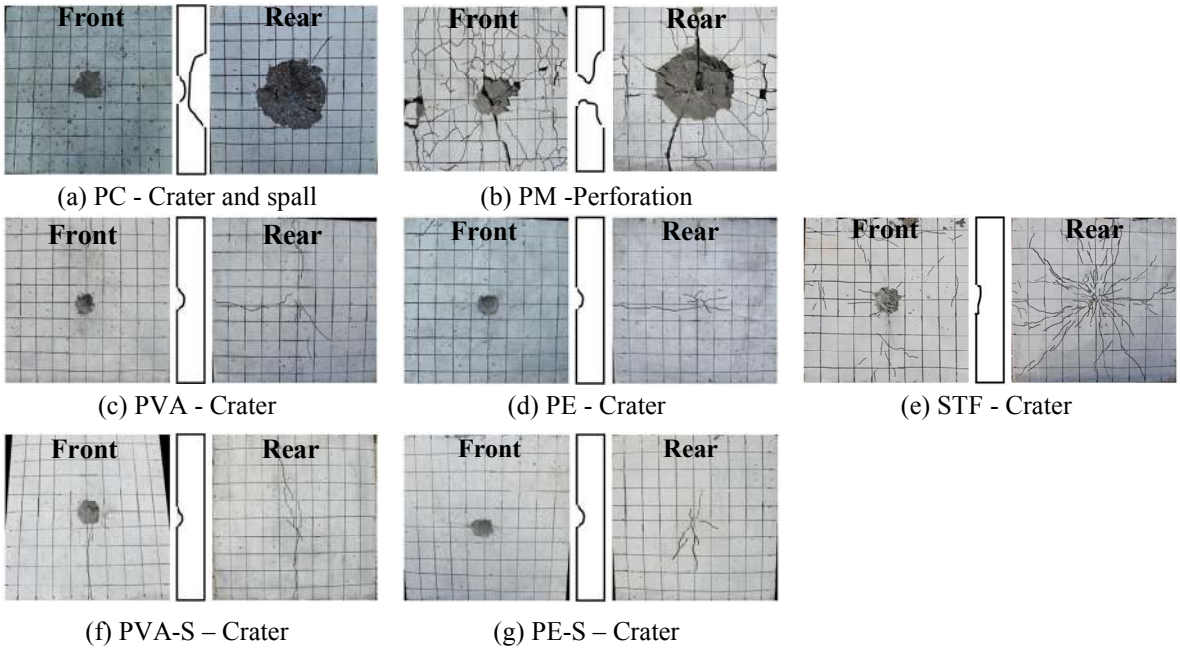

(a) PC - Crater and spall (b) PM -Perforation

(c) PVA - Crater (d) PE - Crater (e) STF - Crater

(f) PVA-S – Crater (g) PE-S – Crater

Fig. 14 Damage of specimens after blast test

superficial damage was occurred more 6.7% in rear side than front side. Thus, In case of PE, PVA-S and PE-S specimen, superficial damage was reduced and the destruction of front side was bigger than rear side in contrast with PM specimen. Case by PC specimen was not occurred spall in rear side, because projectile shocked coarse aggregate of specimen.

The correlation of superficial damage and compressive, tensile and bending strength of specimen by impact are shown in Fig. 11, 12, 13.

The more tensile and bending strength higher, the less superficial damage of rear side. And compressive strength have no direct effect on impact resistance performance.

3.3 Test results of blast resistance

The local damage of PC, PM specimen and fiber reinforced concrete specimen is shown in Figs. 14, respectively. The cross-sections images in these figures show perpendicular sections to support direction.

It can be seen in Fig. 14. that in the case with “no fiber reinforcement (PC and PM), the failure modes were “crater and spall” and “perforation”. In the case with “fiber reinforced concrete” (PVA, PE, STF, PVA-S and PE-S), the failure modes were “crater” , where the degree of damage was less than that of “no fiber reinforcement”.

The results of surside damage of front and rear sides are shown in Fig. 15. In case of PC and PM specimen, superficial damage was occurred more 10.1 to 12.7% in rear side than front side. However, In case of fiber reinforced concrete specimen, superficial damage was reduced and the destruction of front side was bigger than rear side in contrast with PC and PM specimen.

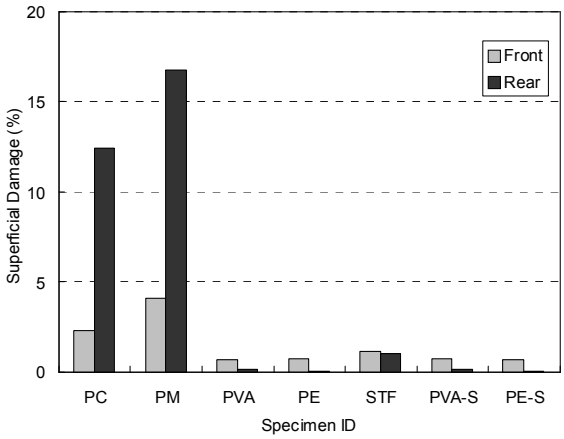

Fig. 15 Surside damage of front and rear sides by impact test

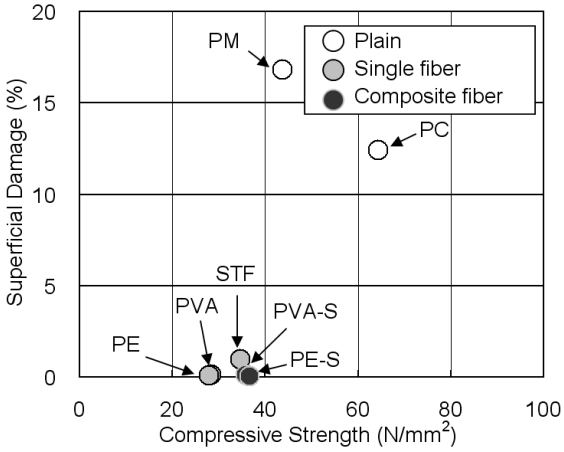

Fig. 16 Correlation of rear side damage and compressive strength by blast test

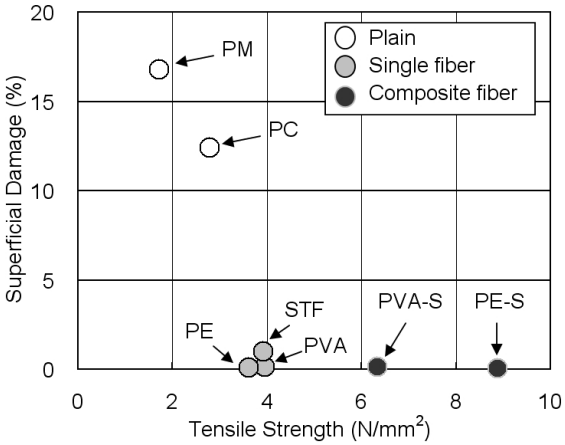

Fig. 17 Correlation of rear side damage and tensile strength by blast test

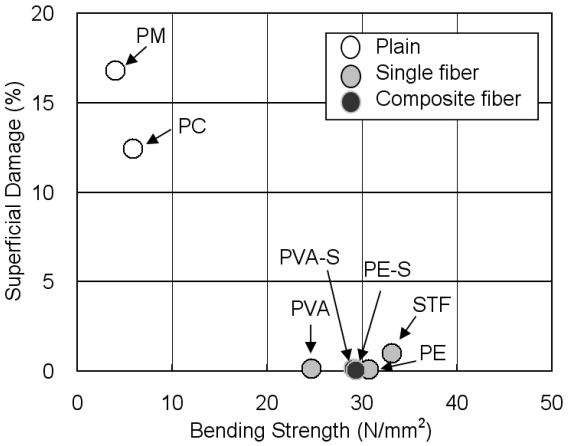

Fig. 18 Correlation of rear side damage and bending strength by blast test

The correlation of superficial damage and compressive, tensile and bending strength of specimen by impact are shown in Fig. 16, 17, 18.

The more tensile and bending strength higher, the less superficial damage of rear side. And compressive strength have no direct effect on impact resistance performance.

3.4 The correlation between impact and blast

The correlation between impact and blast resistance performance from depth and area of destruction are shown in Fig. 19, 20. Result of compared impact and blast test, area of destruction by blast test are larger than result of impact test. However, the destruction depth ratio showed similar results. Small specimens and real specimens could be attributed to the size of the same ratio.

The correlation between area of destruction by impact and blast test is shown in Fig. 21. Area of destruction of fiber reinforced concrete has been reduced comparison with PC and PM specimen.

In this study, the area of the destruction caused by the explosion is greater than that of the impact.

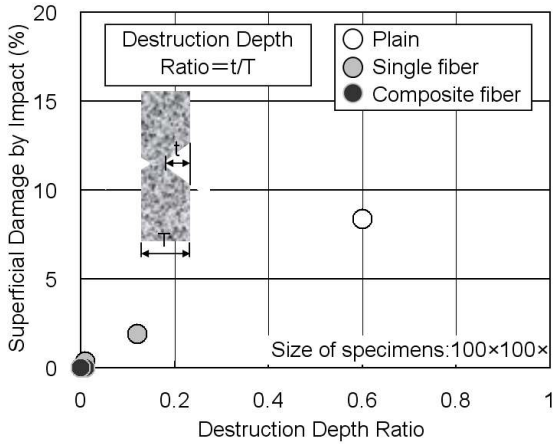

Fig. 19 Correlation of rear side destruction depth and area by impact test

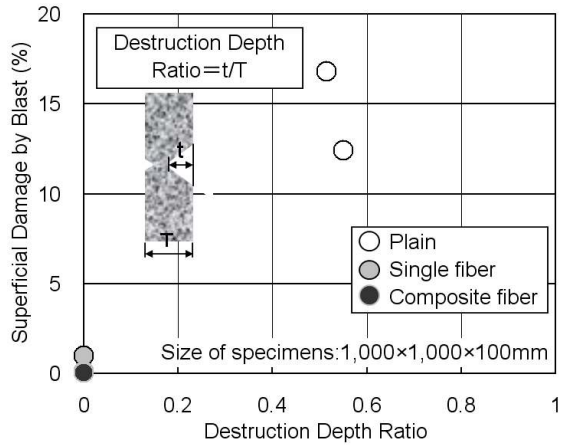

Fig. 20 Correlation of rear side destruction depth and area by blast test

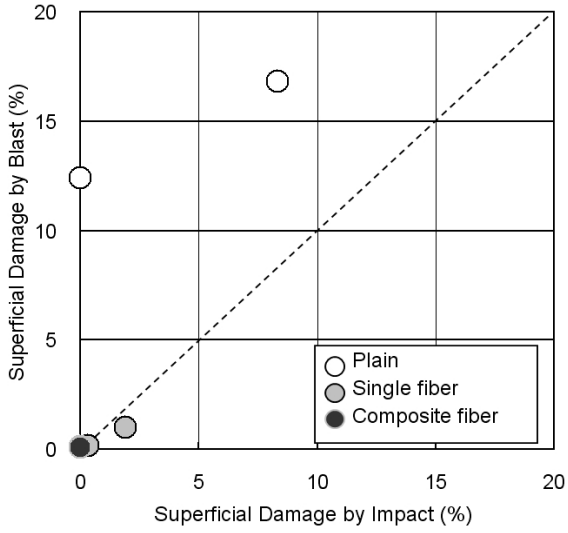

Fig. 21 Correlation between area of destruction by impact and blast test

On the other hand, the impact and blast resistance performance of specimen by non fiber reinforced and various types of reinforcement is shown in Fig. 22. Destruction of rear side does not proceed from

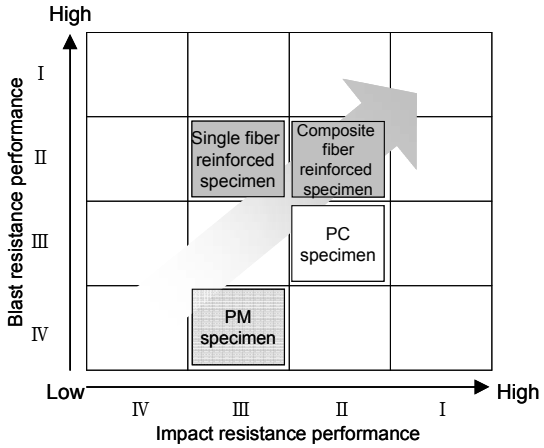

Fig. 22 Impact and blast resistance performance of specimen by non fiber reinforced and various types of reinforcement

composite fiber reinforced specimen. And that has been recognized high safety performance.

4 CONCLUSIONS

In the light of the findings obtained from this experimental study, the following conclusions can be drawn :

(1) The compressive strength of PC specimen and PM specimen is 10~40N/mm^2 higher than fiber reinforced specimens. However, the area of rear side of the PC and PM specimen compared to fiber reinforced specimens resistance decreased, due to the compressive strength of impact and blast resistance performance could not be confirmed.
(2) The effectiveness of fiber reinforcement on the impact and blast resistance performance of concrete specimen has been investigated.
(3) Tensile and bending strength of fiber reinforced concrete specimen was higher than it of PC and PM specimen and such as the fiber reinforced concrete was more decrease rear side damage.
(4) Fiber reinforced concrete has higher impact and blast resistance than PC and PM specimen.
(5) In this study, destruction of rear side does not proceed from composite fiber reinforced specimen. And that has been recognized high safety performance.

ACKNOWLEDGEMENT

This work was supported by the National Research Foundation of Korea(NRF-No.2010-0014723) grant funded and Brain Korea 2th (BK21) by the Korea government(MEST).

REFERENCES

[1] A. Ghani Razaqpur, Ahmed Tolba, Ettore Contestabile : Blast loading response of reinforced concrete panels reinforced with externally bonded GFRP laminates, Composites: Part B 38, pp. 535-546, 2007
[2] K. Ohkubo, M. Beppu, T. Ohno, K. Satoh : Experimental study on the effectiveness of fiber sheet reinforcement on the explosive-resistant performance of concrete plates, International Journal of Impact Engineering, Vol.35, pp.1702-1708, 2008
[3] A.M. Coughlin, E.S. Musselman, A.J. Schokker, D.G. Linzell : Behavior of portable fiber reinforced concrete vehicle barriers subject to blasts from contact charges, International Journal of Impact Engineering, Vol.37, pp.521-529, 2010
[4] M.H. Zhang, V.P.W. Shim, G. Lu and C.W. Chew : Resistance of high-strength concrete to projectile impact, International Journal of Impact Engineering, Vol. 31, pp.825-841, 2005
[5] F. Vossoughi, C.P. Ostertag, P.J.M. Monterio and G.C. Johnson : Resistance of concrete protected by fabric to projectile impact, Cement and Concrete Research, Vol. 37, pp.96-106, 2007
[6] Q.M. Li and D.J. Tong : Perforation thickness and ballistic limit of concrete target subjected to rigid projectile impact, J.Eng.Mech., ASCE, Vol. 129, pp.1083-1091, 2003
[7] D.Z. Yankelevsky : Local response of concrete slabs to low velocity missile impact, Journal of Impact Engineering, Vol. 19, pp.331-343, 1997
[8] M. Beppu, K. Miwa, M. Itoh, M. Katayama and T. Ohno : Damage evaluation of concrete plates by high-velocity impact, International Journal of Impact Engineering, pp.1419-1426, Dec. 2008
[9] L. Joosef : Concrete subjected to projectile and fragment impacts:Modelling of crack softening and strain rate dependency in tension, International Journal of Impact Engineering, 2006
[10] R.N. Swamy, A.H. Jojagha, "Impact resistance of steel fibre reinforced lightweight concrete", International Journal of Cement Composites and Lightweight Concrete, Vol. 4, No.4, pp. 209-220, Nov. 1982
[11] P. Soroushian, A. Tlili, A. Alhozaimy, and A. Khan, "Development and Characterization of Hybrid Polyethylene Fiber Reinforced Cement Composites," ACI Material Journal, Vol.90, No.2, pp.182-190, 1993
[12] Maalej, M. and Li, V. C., "Introduction of Strain Hardening Engineered Cementitious Composites in the Design of Reinforced Concrete Flexural Members for Improved

Durability", American Concrete Institute Structural J., Vol.92, No.2, pp.167-176, Mar. 1995
[13] Lim, Y. M. and Li, V. C., "Durable Repair of Aged Infrastructures Using Trapping Mechanism of Engineered Cementitious Composites, J. Cement and Concrete Composites, Vol.19, No.4, pp.373-385, 1997
[14] Banthia N, Sappakittipakorn M : Toughness enhancement in steel fiber reinforced concrete through fiber hybridization, Cement and Concrete Research, Vol.37, pp.1366-1372, 2007
[15] Wang ZL, Liu YS, Shen RF : Stressestrain relationship of steel fiber-reinforced concrete under dynamic compression, Construction and Building Materials, Vol.22, pp.811-819, 2008
[16] P. Soroushian, M. Elzafraney : Damage effects on concrete performance and microstructure, Cement and Concrete Composite, 26, pp.853-859, 2004
[17] A.N. Dancygier, D.Z. Yankelevsky : High strength concrete response to hard projectile impact, International Journal of Impact Engineering, 18, pp.583-599, 1996
[18] A.N. Dancygier, Rear face damage of normal and high-strength concrete elements caused by hard projectile impact, ACI Structure Journal, 95, pp.291-304, 1998

Proceedings of the 3rd JCI-KCI-TCI Symposium on Recent Advancement of Technologies in Concrete Engineering
Japan Concrete Institute, July 2012

RESISTANCE OF CRACK OPENING OF HIGHLY FLOWABLE STRAIN HARDENING FIBER REINFORCED CONCRETE (HF-SHFRC) UNDER TENSILE AND SHEAR FORCES

Wen-Cheng Liao
Department of Civil Engineering, National Taiwan University, Taiwan

ABSTRACT

Highly flowable strain hardening fiber reinforced concrete (HF-SHFRC) has good workability in the fresh state and exhibits the strain-hardening and multiple cracking characteristics of high performance fiber reinforced cementitious composites (HPFRCC) in the hardened state. HF-SHFRC can be easily manufactured and delivered by ready-mix trucks for cast on the job site. Structural large scale test results from several research programs also showed that HF-SHFRC is effective in increasing shear strength, displacement capacity and damage tolerance in members subjected to large inelastic deformations. The results of two tests, long prismatic tensile test with continuous reinforcement and in-plane pure shear panel test, are carried out in this paper. Compared to conventional concrete, not only much better mechanical performances, HF-SHFRC also presents the lower crack potential and excellent crack width control. These characteristics of HF-SHFRC can further diminish work of repair, rehabilitation, and maintenance after extreme loading events and give infrastructure longer service life, and eventually lower the life-cycle cost.

Keywords: *SCC, FRC, HPFRCC, Strain hardening, Control of cracking, Crack opening*

1 INTRODUCTION

Highly-flowable strain hardening fiber reinforced concrete (HF-SHFRC) combine the self-consolidating property of self-consolidating concrete (SCC) in their fresh state, with the strain-hardening and multiple cracking characteristics of high performance fiber reinforced cement composites (HPFRCC) in their hardened state. SCC has a high flowability and a moderate viscosity, and has no blocking by the reinforcement during flow. With proper use of superplasticizer (SP) and viscosity modifying agents (VMA), SCC can achieve higher flowability and higher slump without segregation, and also maintain better slump retention, thus making concrete more durable due to its lower water/cementitious ratio, and reducing sulfate attack and salt penetration. Not only the fresh state characteristics of SCC, HF-SHFRC also has excellent mechanical properties as HPFRCC. HPRCC has the tensile strain-hardening response with multiple cracking exhibits instead of the tensile strain-softening response observed in conventional fiber reinforced concrete (FRC) as shown in Figure 1.

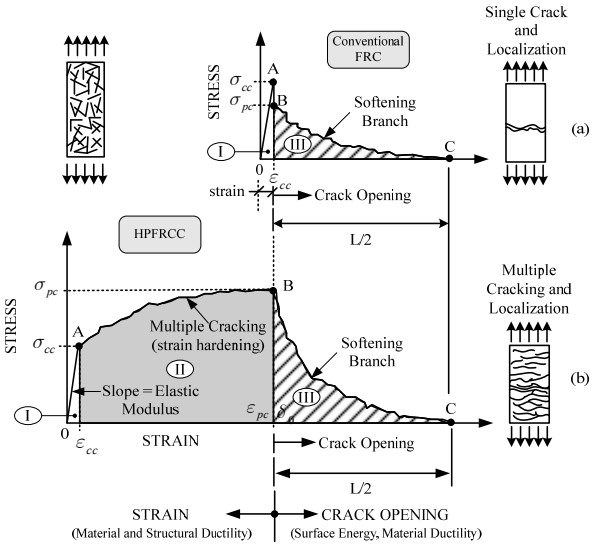

Fig.1 Stress-strain response of conventional FRC and HPFRCC[1]

Series of HF-SHFRC for different compressive strength demands (30, 40, 50 and 60 MPa) have been successfully developed by modifying SCC mixtures

recommended in previous studies and using the available local materials, including 30 mm long high strength steel hooked fibers in volume fractions of 1.5% [2]. It is also worth mentioning substantial content of cement were substituted for fly ash in the mix design considering cost, durability and sustainability.

Two tests, long prismatic tensile test with continuous reinforcement and in-plane pure shear panel test, are also carried out to verify the resistance of crack opening of HF-SHFRC. all the mixtures. The results shows that compared to conventional concrete, not only much better mechanical performances, HF-SHFRC also presents the lower crack potential and excellent crack width control.

2 MIX DESIGN CONCEPTS

It is generally agreed that adding fibers can expand the applications of SCC; however, a reduction in workability due to fiber addition may become a barrier for its application in practice. By modifying SCC mixtures recommended in previous studies and using locally available materials, HF-SHFRC mixtures for different strength demands can be easily manufactured and delivered by ready-mix trucks for cast-in-place applications.

While adding fibers can significantly enhance mechanical properties, particularly tensile behavior, of SCC, a reduction in workability due to fiber addition may become a handicap in practice. Thus, the mix design of SCC should be further adjusted if fibers are added. Numerous commercial laboratories have been involved in the development of SCC with fibers and continuously improving their performance. Following is a summary of key findings based on their studies[3]:

(1) The coarse-to-fine aggregate ratio in the mix needs to be reduced so that individual coarse aggregate particles are fully surrounded by a layer of mortar. Furthermore, it is recommended by Johnston (1996) to reduce the volume of coarse aggregates at least 10 % compared with plain concrete to facilitate pumping.
(2) Before addition of fibers, slump flow of SCC must be relatively high. The slump flow criterion of qualified SCC is 600 mm for a 300 mm high cone.
(3) Everything else being equal, addition of fibers reduces slump flow of SCC; higher fiber volume and higher aspect ratio of fibers reduce slump flow of SCC as well, thereby leading to higher possibility of blocking and segregation.

3 EXPREIMENTAL PROGRAM

3.1 Materials and Mix Proportions

The cementitious materials used in this study were ASTM Type I Portland cement and class C fly ash. The coarse aggregate (CA) had a maximum size of 12.7 mm and consisted of solid crushed limestone from a local source, with a density of about 2.70 g/cm^3. The fine aggregate was #16 flint silica sand. Polycarboxylate-based superplasticizer (SP) was used to achieve desired workability. In addition to the SP, a viscosity modifying admixture (VMA) was also used to enhance the viscosity and avoid fiber segregation. This mixture has 1.5% volume fraction of hooked steel fiber with circular cross-section was used with tensile strength of 2300MPa and aspect ratio of 79 (diameter= 0.38mm and length= 30mm). Average 28-day compressive strength based on 100×200 mm cylinders is approximately 40 MPa. Details of matrix composition are given in Tables 1.

Table 1 Relative composition of HF-SHFRC mixture by weight

Cement	Fly ash	Sand	CA	SP	Water	VMA	Steel Fiber
1.00	0.88	2.20	1.2	0.005	0.8	0.038	0.32

3.2 Direct Tensile Test

The direct tensile test was needed to ascertain that the developed HF-SHFRC give a strain-hardening response in tension after first cracking. Dog-bone shaped tensile specimens were prepared and tested for the HF-SHFRC mixture. The specimen has a cross-sectional dimension of 25.4 × 50.8 mm as shown in Figure 2.

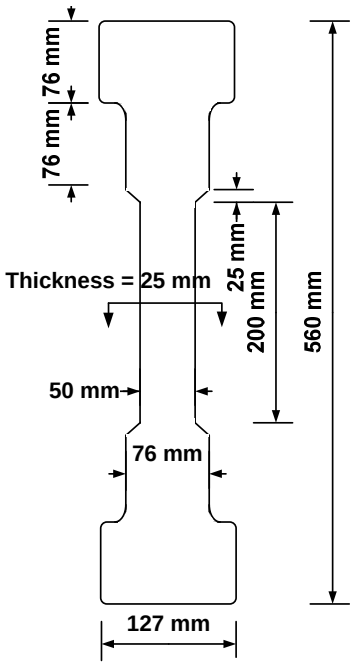

Fig.2 Geometry and dimensions of direct tensile test specimen

The applied load was monitored by the load cell of the testing machine and the elongation was recorded by a pair of linear variable differential

transformers (LVDT) attached to the specimen (Figure 3), with a gauge length of about 178 mm. It is noted that compared to the fiber length, the relatively smaller cross section may lead to a somewhat two-dimensional distribution of fibers.

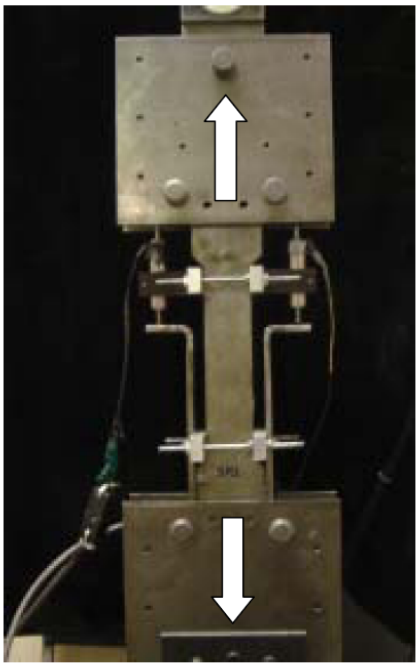

Fig.3 Direct tensile test setup

3.3 Long Prismatic Reinforced Tensile Test

It has been established that the presence of continuous reinforcement helps concrete to carry tension between cracks through transfer of bond forces. This in turn results in better control on member stiffness, deformation, and crack widths in RC members as compared to plain concrete members. In this study, an unstressed prestressing steel strand was placed at the centroid of the specimen to simulate the presence of reinforcing steel in HF-SHFRC. The advantage of using a prestressing steel tendon is that a strain as high as 0.9% can be applied while the tendon remains linear elastic, thus allowing a stable environment for loading-unloading and for measurements of crack width and spacing at every loading step. Moreover, tests conducted by Chao et al.[4] have shown that HPFRC composites lead to a much higher bond strength between a seven-wire strand and surrounding matrix than plain concrete (as high as three times), thus ensuring the tension stiffening effect in the test specimens.

Details of the specimen geometry, test setup, and instrumentation are shown in Figure 4. The long prismatic specimen has a cross-sectional dimension of 64×76mm. The specimen was placed in a prestressing bed and supported by a few steel strips which allowed the specimen to move easily on its bed support during tension. The strand going through the specimen was attached at each end by a prestressing chuck. The tensile load was applied monotonically to the strand through a hydraulic jack and recorded by a pair of load cells at both ends of the prestressing bed as shown in Figure 4(a). Five zones in the middle of the specimen were selected to record the strains in the concrete through the use of LVDTs, as shown in Figure 4(b) (Zones 1 thru 5). The gauge length of each zone was 250 mm. Elongation of the entire specimen was also monitored by two LVDTs attached to the ends of the specimen. Strains in the strand (inside the matrix) were measured by strain gauges attached at pre-designated locations corresponding to the middle points of the five zones (Zones 1 thru 5) mentioned above. Strain gauges were also mounted on the strand outside the matrix (Figure 4b) in order to obtain the stress-strain curve of the bare strand.

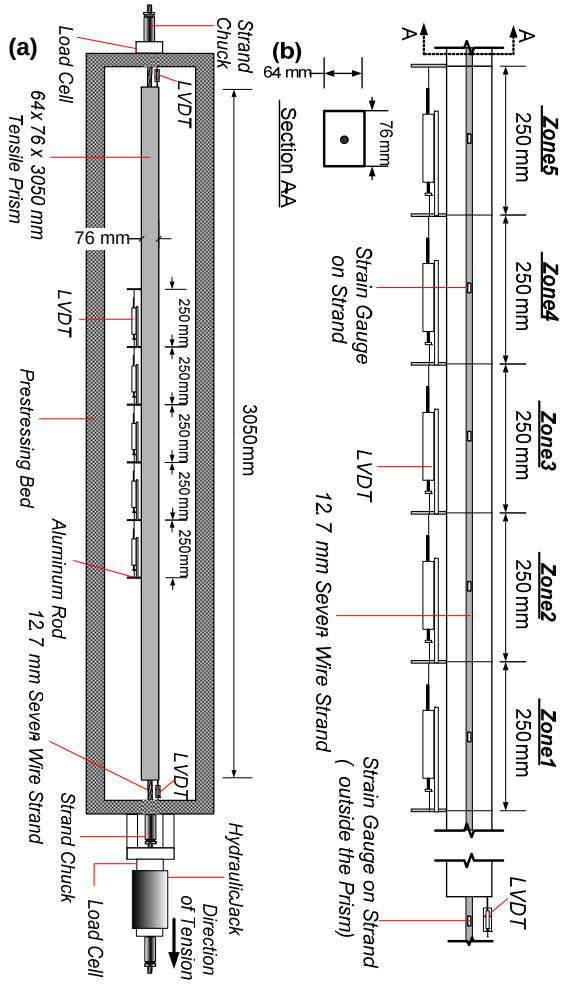

Fig.4 (a) Geometry and dimensions of tensile test specimen; (b) Tensile test set-up; (c)

The stress in the fiber concrete for the long

prismatic reinforced tensile test was calculated by:

$$\sigma_c = (F - E_s\varepsilon_s)/(A_t - A_s)$$

where σ_c is the tensile stress in fiber concrete (MPa); F is the total force measured by load cell (kN); E_s is the elastic modulus of strand (MPa) ; ε_s is the strain in strand measured by strain gauge (mm/mm); A_t is the gross cross-sectional area of the specimen (= 4860 mm^2) ; A_s is the nominal cross-sectional area of a 12.7 mm seven-wire strand (= 100 mm^2). It was mentioned previously that a prestressing steel strand remains linear elastic when the strain reaches as high as 0.9%. This was indeed the case in the strand used in this study, as indicated by the stress-strain relation obtained based on strain gauges mounted outside the matrix; the curve was linear with an elastic modulus of 206 GPa. Since the specimen was able to move freely during testing with minor frictional force, the force measured by the load cell (F) can be taken as constant along the specimen and used for Zones 1 thru 5. The force sustained by the fiber concrete was calculated by the difference between F and force in the strand, $E_s \cdot \varepsilon_s$. The average tensile stress was then calculated by dividing the force difference using the net concrete area A_t - A_s. The tensile strains in the fiber concrete were obtained by dividing the elongation (measured through LVDTs) by the gauge length of each zone (= 250 mm).

3.4 In-plane Pure Shear Panel Test

A 890×890×70 mm concrete panel was fabricated for the shear panel test. Figure 5 illustrates the geometry and reinforcement layout of the panel. In order to provide an adequate post-cracking resistance of the panel, forty D6 deformed wires were provided for the x-direction reinforcement, giving a total reinforcement area of 1543 mm², which equated to a reinforcement ratio of 2.47%.

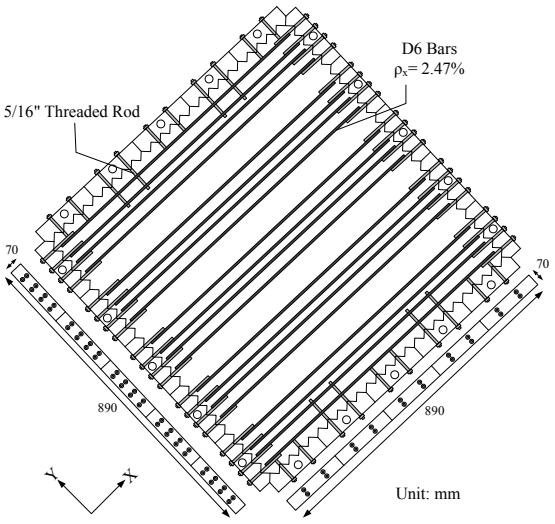

Fig.5 Dimension, reinforcement layout of panel

This in-plane pure shear panel test was conducted by using the Panel Tester Machine developed by Vecchio [5] at the University of Toronto. This machine and experimental setup were designed to apply various in-plane loading conditions to a concrete panel. The in-plane shear forces are generated by the horizontal and vertical jacks on each opposing side of the panel. There are adjustable links on the frame to prevent out-of-plane displacement and keep the panel aligned. Deformations (strains) of the panel were obtained continuously from the LVDTs and strain gauges throughout the duration of each test. Figure 6 shows the arrangement of LVDTs setup. Additional data were also obtained from Zurich gauge readings that were taken at each load stage to verify the accuracy of LVDT. These data were subsequently analyzed to investigate the response characteristics of the concrete panels under in-plane pure shear loading.

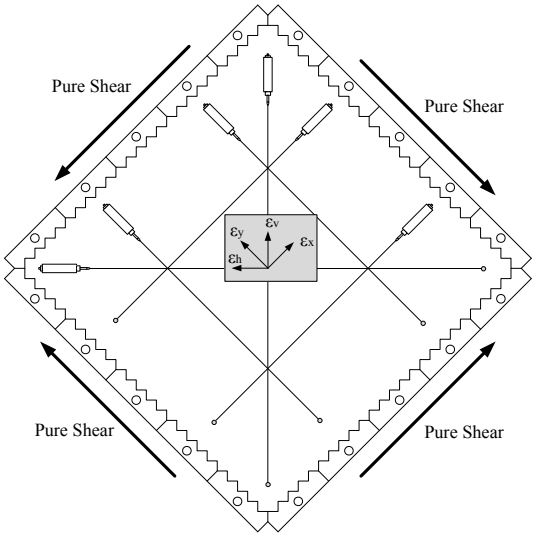

Fig.6 LVDT setup of panel test

4 TEST RESULTS

4.1 Direct Tensile Test

The stress-strain curves were recorded from the dog-bone specimens tested. Multiple cracks developed up to peak stress (post-cracking strength) at which crack localization occurred. Typical stress-strain curves are shown in Figure 7. It can be observed that the tensile stress increases with an increase in strain after the first crack. Thus these mixtures all satisfy the requirement of strain-hardening behavior of HPFRCC. Beyond the peak stress, the tensile stress dropped gradually due to fiber kinematic pullout from the matrix. Some key results are summarized in Table 2.

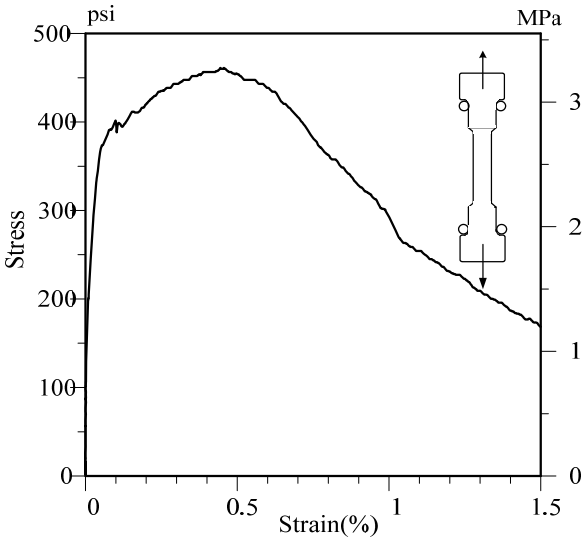

Fig.7 Typical tensile stress-strain curve of HF-SHFRC

Table 2 Key results of direct tensile test of HF-SHFRC

Tensile properties of HF-SHFRC	
Average Post-Cracking Strength (MPa)	3.61
Average Strain at Peak Stress (%)	0.45
Stress at apparent strain = 0.5% (% of peak stress)	3.54 (98)
Average Number of Cracks	6
Average Crack Spacing (mm)	25.7

4.2 Long Prismatic Reinforced Tensile Test

Typical tensile load-elongation responses of the composite and bare strand in Zone 3 are shown in Figure 8.

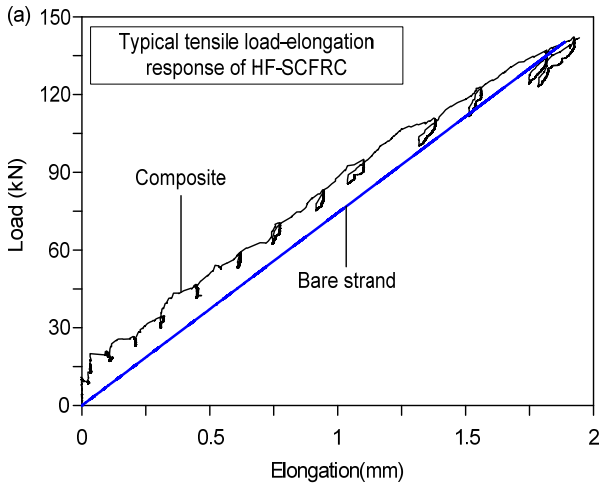

Fig.8 Typical tensile load-elongation of reinforced HF-SHFRC prism

Stress-strain response of the HF-SHFRC was also obtained based on the equation mentioned in section 3.3 and plotted in Figure 9, along with an envelope curve. The unloading loops were the result of softening of the hydraulic jack during crack measurement and photographing.

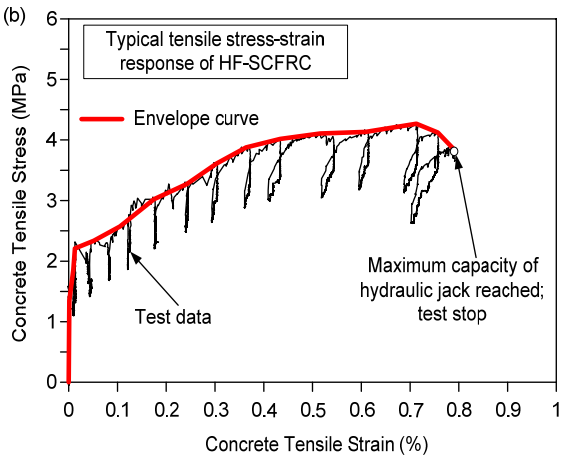

Fig.9 Typical tensile stress-strain responses of HF-SHFRC

Figure 9 shows that the HF-SHFRC used in this study exhibited tensile strain-hardening behavior up to 0.7% composite strain, along with extensive multiple cracking. The stress-strain curve is generally very stable without any sudden degradation in strength. This can be attributed to the presence of the longitudinal reinforcement, which was able to redistribute tensile stress through bond when cracks occurred.

Figure 10 compares the tensile stress-strain responses of the direct tensile test and long prismatic reinforced tensile test specimens made of the same HF-SHFRC mixture. It is observed that the peak tensile strength of the former one is higher than that of the long prismatic reinforced specimen. This can be attributed to scale effects and to the possible two-dimensional versus three-dimensional fiber orientations in each specimen, respectively. In addition, the onset of damage localization as a result of fiber pullout at peak stress is significantly delayed in the presence of continuous reinforcement. Indeed, the tensile strain up to the peak strength in the long prismatic reinforced specimen is more than two times that of the dog-bone shaped specimen. The smaller strain in the dog-bone shaped specimen possibly resulted from the fact that smaller specimens are more sensitive to defects such as non-uniformly distributed fibers and coarse aggregates. Furthermore, without continuous reinforcement, crack extension is more likely to become unstable during stressing.

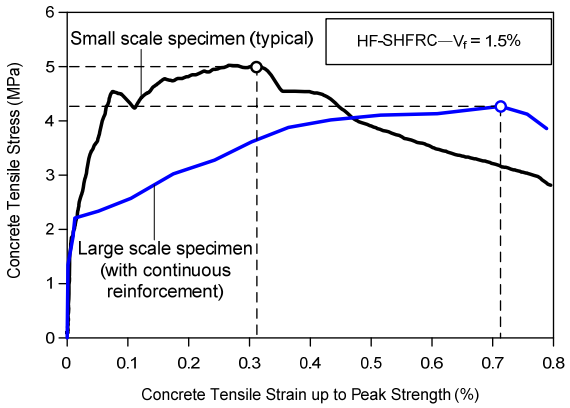

Fig.10 Comparison of stress-strain responses between dog-bone and long prismatic reinforced specimens made of HF-SHFRC mixture

4.3 In-plane Pure Shear Panel Test

The shear stress-shear strain response of HF-SHFRC panel is plotted in Figure 11. The behavior kept linear up to first cracking at the shear stress of 1.5 MPa. The panel failure occurred at a maximum shear stress of 4.3MPa and a corresponding shear strain of 6.20×10^{-3}. At the onset of panel failure, the applied load gradually declined and the major cracks opened up slowly. The failure of the panel was dictated by an aggregate interlock failure as there was no indication of concrete crushing or reinforcement rupture.

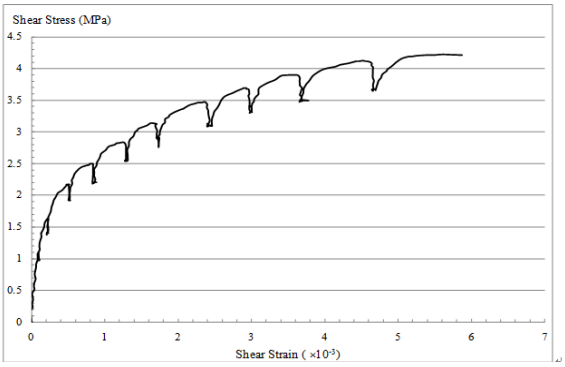

Fig.11 Shear stress - shear strain response of HF-SHFRC panel

The comparison of principal tensile stress-strain behaviors of HF-SHFRC and control panels is shown in Figure 12. The test data of the control panel was adopted from I Susetyo's previous work [6]. is noted that the control panel (f'_c= 50MPa), which was made of conventional concrete, has higher reinforcement ratios (x-direction: reinforcement area of 2061 mm², ρx= 3.31%; y-direction: reinforcement area of 260 mm²,ρy= 0.42%) compared to the HF-SHFRC panel. The principal tensile stress-strain relationships of HF-SHFRC and conventional concrete are conducted based on Mohr's circle method. Due to higher compressive strength of conventional concrete, the maximum principal tensile stress of conventional concrete is higher than that of HF-SHFRC as expected. However, in contrast to strain softening behavior of conventional concrete, HF-SHFRC exhibits tensile strain hardening until failure occurs at which the principal tensile strain of 4.1×10^{-3}. This can be deemed that the strain hardening behavior can be achieved with addition of fibers and that fiber addition can significantly improve the tensile carrying capacity of the concrete.

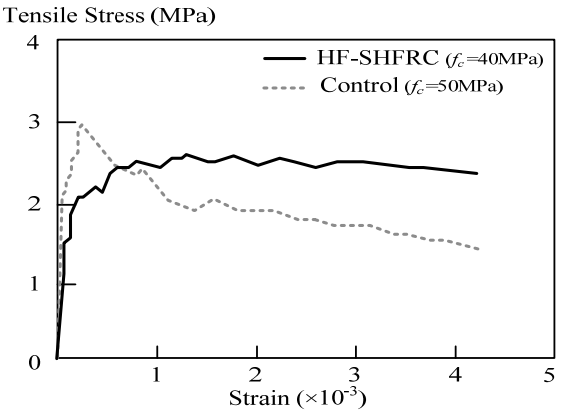

Fig.12 The principal tensile stress-strain relationships of HF-SHFRC and conventional concrete

4 CRACK CONTROL

By adding fibers into concrete can enhance the performance in many aspects. Cracking width control is also one of the most important advantages of addition of fibers. Not only plastic shrinkage cracking, other volumetric expansions caused by alkali-silica reaction, cyclic loading, or tensile forces can also be effectively controlled and minimized [7]. The resistance of crack opening of HF-SHFRC under tensile and shear forces respectively will be discussed in the following sections.

4.1 Long Prismatic Reinforced Tensile Test

Figure 13 shows that the HF-SHFRC exhibits multiple cracking. Compared to the crack distributions of conventional concrete, more extensive multiple cracks and no significant damage localization can be observed in the HF-SHFRC specimen.

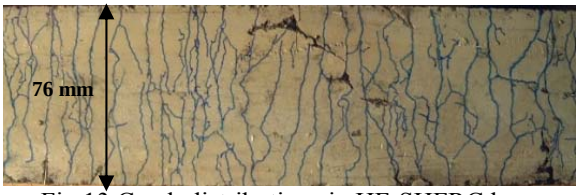

Fig.13 Crack distributions in HF-SHFRC long prismatic reinforced tensile test

The test results also showed that no primary crack opening localization occurred and additional secondary cracks can still develop with average crack width less than 50 μm under concrete tensile strain up to 0.7% as illustrated in Figure 14.

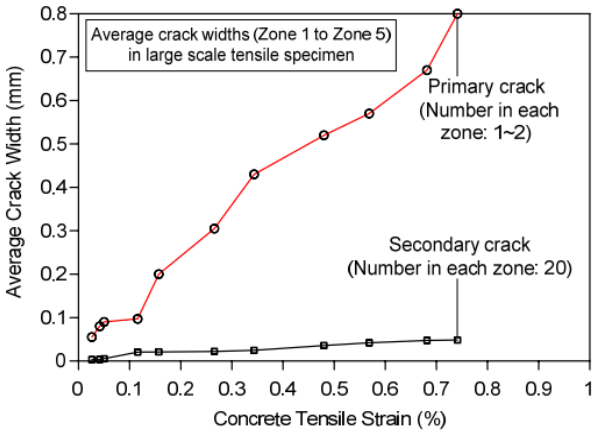

Fig.14 Average crack width of HF-SHFRC versus tensile strain

4.2 In-plane Pure Shear Panel Test

An important property of HF-SHFRC is its ability to control crack propagation due to addition of fibers.. In conventional RC, crack control is provided by the bonded steel reinforcement; without it, the concrete exhibits a brittle behaviour. In HF-SHFRC, the intrinsic fibers act as crack controllers and therefore, the behavior of the concrete is significantly improved. The comparison of crack pattern of HF-SHFRC and control panels at failure is shown in Figure 15. It was observed that the failure of the HF-SHFRC panel was caused by the inability of the concrete to transmit the load across the cracks (coarse aggregate interlock failure) instead of the yielding or fracture of the transverse reinforcement in the conventional concrete panel. The cracks in HF-SHFRC panel were significantly fine and well distributed across the face of the panel, with crack spacing smaller than those observed in the control panel.

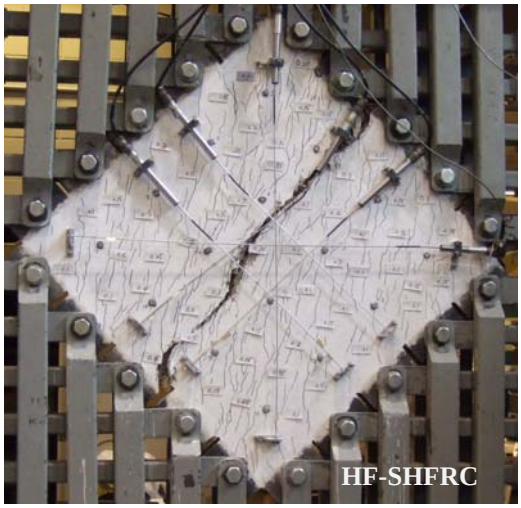

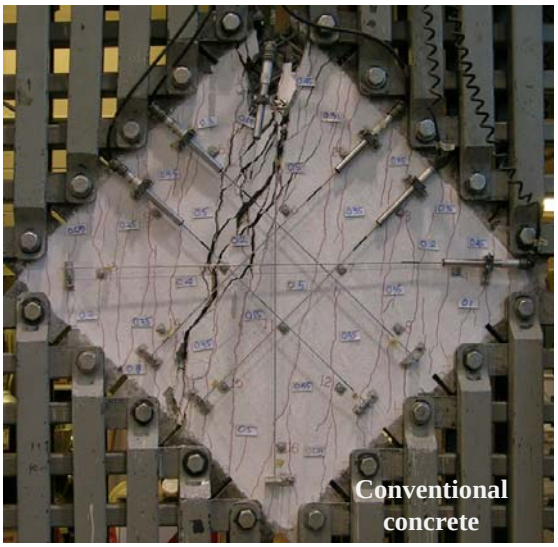

Fig.15 Crack pattern at failure stage of HF-SHFRC and conventional concrete

Maximum crack opening widths at different shear stress levels of HF-SHFRC and conventional concrete are also recorded as seen in Figure 15. It can be observed that even without the presence of transverse reinforcement, HF-SHFRC exhibits smaller crack opening widths at the same shear stress level by about 40% than conventional concrete. This signified the ability of fibers to control crack propagation.

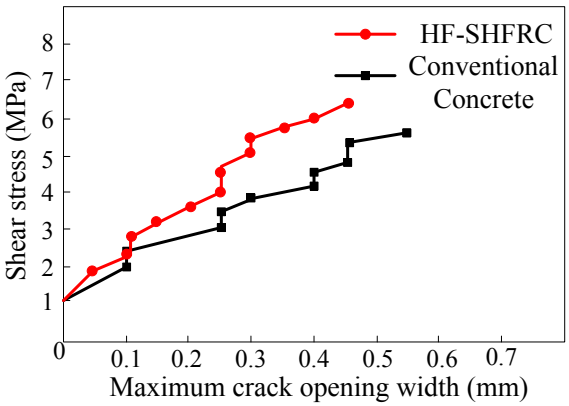

Fig.15 Comparisons of maximum crack opening width of HF-SHFRC and conventional concrete

5 CONCLUSIONS

(1) By modifying SCC mixtures recommended in previous studies and using locally available materials, HF-SHFRC mixtures for different strength demands can be easily manufactured.

(2) In terms of tensile behaviors of HF-SHFRC, the peak tensile strength obtained from dog-bone shaped specimens was generally higher than that of long prismatic reinforced specimens. The

tensile strain at the onset of damage localization in the long prismatic reinforced specimens was about twice that observed in the dog-bone shaped specimens where no reinforcement was used. The presence of continuous reinforcement leads to a significantly better crack development as well as a significant increase in energy absorption capacity.

(3) This paper also presents in-plane pure shear panel test results of HF-SHFRC, including shear stress-shear strain responses and principal tensile stress-strain behavior. Noticeable tensile strain hardening can be observed in HF-SHFRC. In terms of failure mode and crack pattern, HF-SHFRC showed fine and well distributed cracks with much smaller crack spacing than those observed in the conventional concrete panel. HF-SHFRC exhibits smaller crack opening widths at the same shear stress level by about 40% than conventional concrete. This signified the ability of fibers to control crack propagation.

ACKNOWLEDGEMENT

The research described herein was sponsored by the National Science Foundation under Grants Nos. CMS 0530383 and CMS 0754505, and the University of Michigan and the University of Toronto. Their support is gratefully acknowledged. The opinions expressed in this paper are those of the authors and do not necessarily reflect the views of the sponsor.

REFERENCES

[1] Naaman, A. E. “Strain Hardening and Deflection Hardening Fiber Reinforced Cement Composites,” High Performance Fiber Reinforced Cement Composites 4, Proceedings of the Fourth International RILEM Workshop, pp. 95-113. 2003.

[2] Liao W.-C., Chao, S.-H., and Naaman, A. E. “Experience with Self-Consolidating High Performance Fiber Reinforced Mortar and Concrete,” ACI Journal, Special Publication No. 247 “Fiber Reinforced Self-Consolidating Concrete - Research and Applications”, pp 79-94, 2010.

[3] Bui, V. K., Geiker, M. R., Shah, S. P., “Rheology of Fiber-Reinforced Cementitious Materials,” RILEM PRO30 High Performance Fibre Reinforced Composites HPFRCC4, pp. 221-232, 2003.

[4] Chao, S.-H., Liao, W.-C. and Naaman, A. E., Large Scale Tensile Tests of High Performance Fiber Reinforced Cement Composites, RILEM PRO53 High Performance Fibre Reinforced Composites HPFRCC5, pp. 77-86, 2007.

[5] Vecchio, F.J. “Shear Rig Design”, M.Eng. Thesis, Department of Civil Engineering, University of Toronto, 246 p, 1979.

[6] Susetyo J. “Fiber Reinforcement for Shrinkage Crack Control in Prestressed, Precast Segmental Bridges”, Ph.D. Thesis, Department of Civil Engineering, University of Toronto, 532 p, 2009.

[7] 9. Bektas, F., Turanli, L., and Ostertag, C. P., New Approach in Mitigating Damage Caused by Alkali-Silica Reaction,” Journal of Material Science, Vol. 41., pages 5760-5763, 2006.

[8] J. M. Davis: Simplified Diaphragm Analysis, Journal of Structural Div., ASCE, Vol. 103, pp.2098-2109, Nov. 1977

[9] F. R. Shanley: Basic Structures, John Willey & Sons Inc., pp.291-314,

Proceedings of the 3rd JCI-KCI-TCI Symposium on Recent Advancement of Technologies in Concrete Engineering
Japan Concrete Institute, July 2012

EVALUATING SHRINKAGE REDUCING ADMIXTURES ON THE EARLY-AGE CRACKING BEHAVIOR OF CEMENTITIOUS COMPOSITES USING RESTRAINED RING TEST

Shih-Tang Lin
Phoenix Material Company Ltd. Taipei, Taiwan, ROC
Nan Shing Color Co., Ltd. Taipei, Taiwan, ROC
Department of Engineering, Tatung University, Taipei, Taiwan, ROC

Ran Huang
Institute of Material Engineering, National Taiwan Ocean University, Keelung, Taiwan, ROC

Tsai-Lung Weng
Physics Division, Tatung University, Taipei, Taiwan, ROC

ABSTRACT

The effect of shrinkage reducing admixtures (SRA) on the shrinkage deformation of cementitious composites at an early-age is reported in this paper. Commercially available SRAs with different chemical compositions were employed in the cementitious composites with same mixing ratio. A restrained shrinkage test was conducted with a steel ring in accordance with ASTM C1581-04. In addition to the steel ring's strain, the surface tension, the hydration kinetics, compressive strength and drying shrinkage were also investigated. SRAs were found to be effective in reducing the crack tendency by extending the age at cracking in comparison to the control mixture. The test results also illustrated that the age at cracking significantly correlated with the peak of heat flow which might affect thermal stress and drying capillary stress. Nevertheless, the level of surface tension showed no linear relationship to the cracking tendency.
Keywords: *surface tension, heat flow, cracking tendencye, isothermal calorimeter, drying shrinkage*

1 INTRODUCTION

Concrete shrinkage is inevitable due to the volume of hydrated products is less than the volume of the un-hydrated constituents. When the shrinkage deformation is restrained, cracks may occur if concrete cannot withstand the tensile force induced by the restraints. Cracks would allow the aggressive agents to reach reinforcing steel and corrosion may occur, thus seriously affect the durability of reinforced concrete structure and reduce the service life [1]. Restraints can be boundaries, reinforcements, aggregates or different drying profiles. The major early shrinkage after final set of cementitious composite is assumed to be the result from drying [2]. At the beginning of the drying, cement and aggregate particles are covered by a layer of water. As evaporation continues, water level starts to retreat inside the particles pores. As a result, water menisci begin to form and produce capillary pressure [3]. When water evaporates from the menisci, the inner pore water would be transported by the capillary force to the drying front. By Laplace's equation ($P_{cap} = 2\gamma / r$), capillary tension is proportional to the surface tension (γ, dyne/ cm) of the fluid and inversely proportional to the radius (r) of the capillary pore. Therefore, The rate of water supply is inversely proportional to the size of pores (r). As a result, the larger the pore is, the faster the pore dries. As evaporation proceeds from large pores to smaller pores, hydrostatic tension increases. The exertion of hydrostatic tension on the capillary walls would result in volume shrinkage. Consequently early-age shrinkage occurs, so do the drying shrinkage. In the same way, given the same pore size, when the surface tension reduces, the capillary pressure reduces accordingly, thus the force exerts on capillary walls decreases and cracking potential reduces. When pressure of capillary pore is low,

stress to induce cracks may not bigger than the strength of early age concrete. Therefore, cracking could be prevented. Shrinkage reducing admixture (SRA) is a kind of chemical concrete admixture [4]. The major function of SRA is to lower the surface tension of pore solutions. From previous studies the change of surface tension in pore solution is significantly reduced with the addition of SRA [5-8]. The objective of this study is to evaluate the effectiveness of SRAs on the reduction of early age restrained shrinkage cracking.

Commercially available SRAs with different chemical compositions were employed in mortar specimens with same mixing ratio to evaluate their performance on reducing cracking tendency. Steel ring adhered with strain gauges was constructed to provide restraints to assess the age at cracking, maximum strain and strain evolution and to meet the designated specifications of ASTM C1581-04 [9]. Restrained shrinkage strains and age at cracking were recorded. Surface tension, kinetics of hydration by an isothermal calorimeter, compressive strength, and drying shrinkage were also investigated, and their potential relationships with the age at cracking were explored as well.

2 TEST PROGRAMS

2.1 Materials

(1) Shrinkage reducing admixture

One liquid and three solid SRAs from different producers were used. Basically, these SRAs are all ethylene oxide derivatives with different functional groups which can affect the pore water properties such as surface tension. The main active ingredients, chemical compositions, and physical properties are illustrated in Table 1.

Table 1 Characteristics of SRAs

Nota-tion	Appear-ance	Chemical composition	Active con-tent	Recommended dosage (wt. of binder)
S1	white coarse powder	methylene glycol based	100%	2-6%
S2	white coarse powder	propane glycol based	100%	2-6%
S3	yellowish liquid	mixture of glycols	100%	0.5-6%
S4	white to yellowish powder	Poly-alkylene glycol derivative	100%	0.5-6%

(2) Mixture proportion

Type I Portland cement with Blaine fineness of 360 m^2/g and silica sand with a size between 250-850 μm was used. Four types of commercially available SRA were included in the mortar mixtures. The water cement ratio fixed at 0.85. The dosage of SRA was 6 percent by weight of cement. The Mixture proportions are summarized in Table 2. SRA and other constituent materials were pre-weighted and a local jobsite 200 liter pan mixer (rpm 26) was used. Materials were mixed first for 2 minutes, then water was added gradually while mixing continuously for another 3~4 minutes until lump free, homogeneous creamy composites were obtained.

Table 2 Mixture proportion (by mass)

Notation	Type I OPC	Lime	Slag	Sand 20-60 mesh	SRA	Water
Co	20	1	5	73	0	17
S1-06	20	1	5	71.8	1.2	17
S2-06	20	1	5	71.8	1.2	17
S3-06	20	1	5	71.8	1.2	17
S4-06	20	1	5	71.8	1.2	17

2.2 Test methods and equipments

(1) Restrained ring test

The restrained ring test was performed following the specifications of ASTM C1581-04 and the schematic ring setup is depicted in Fig. 1. Ring specimen cast in the steel mold has a dimension of 426mm-outer diameter, 350mm-inner diameter and 150mm-height. The restrained shrinkage cracking sensitivity is determined by age of cracking. On the inside surface of steel ring, three uniaxial strain gauges were arranged in the central height at equal circumferential distance as illustrated in Fig. 2. Strains were collected by a data logger every 2 minutes. The specimens were cured in an environmental-controlled chamber (21±2℃, *RH* 65±10%). Specimens were de-molded 24 hours after casting. Top surface was sealed with paraffin wax to allow drying only from outer circumferential surface. Specimens were observed at constant interval for the verification of age of cracking.

(2) Surface tension measurement

Surface tension was measured by a Du Noüy Ring Tensiometer in the control temperature of 25℃. Surface tension is determined by the force that required to pull a platinum ring away from the contacting liquid surface. Detail operation procedures are described in ASTM D 971-99a [10]. Prior to test, tensiometer was calibrated using 20°C N-Butanol solution (24.6 dynes/cm) and de-ionized water (72.8 dynes/cm). Cementitious pore solution was sucked from the cementitious composite mixtures using water retention test apparatus specified by ASTM C1506-01 [11]

(3) Isothermal calorimeter

The temperature differences between specimens and the constant-temperature surrounding create heat flow which can be measured in terms of mille-watt (mW/g). The isothermal conduction calorimetry was performed using an eight channel TAM Air as shown in Fig. 3. All measurements were performed using 6 grams of fresh mixed mortar at a constant temperature of 25℃. The heat flow data were recorded at 1 minute intervals for 72 hours by a computer [12].

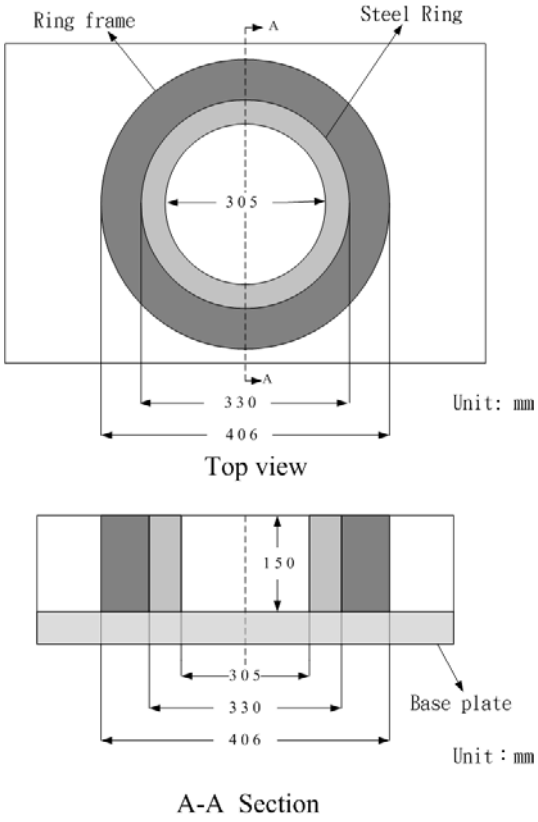

Fig. 1 Dimensions of restrained ring set up

(4) Drying shrinkage test

The drying shrinkage tests were conducted using 25x25x285-mm mortar prisms with two studs at each end following ASTM C596-09 Standard Test Method for Drying Shrinkage of Mortar Containing Hydraulic Cement specifications [13].

(5) Compressive strength

The compressive strength of mortar was determined on 50-mm cubes at the age of 3,7,28 days according to ASTM C109 standard method [14]. The cube specimens were cured at the same condition as restrained ring test.

3 RESULTS AND DISCUSSIONS

Test results of surface tension of pore solutions, isothermal calorimetry of cementitious composites, drying shrinkage, compressive strength and results of restrained shrinkage tests, such as age at cracking, and the restrained shrinkage strain when cracking occurred are summarized in Table 3.

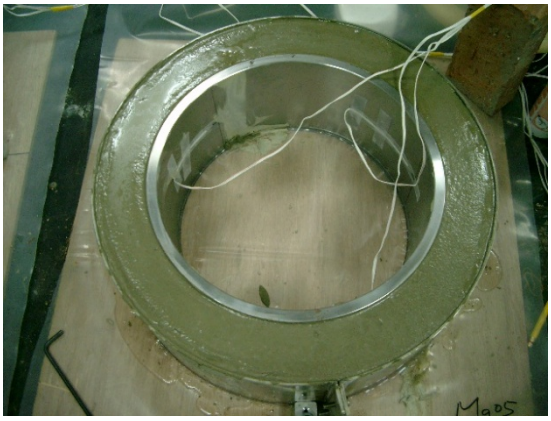

Fig. 2 Theee stain gauges are adhered along the center height with equal spacing

Fig. 3 Isothermal calorimeter

3.1 Influence of SRAs on the surface tension of pore solutions

Surface tension is the force pulling a platinum ring away from the contacting liquid's surface. The surface tension of solution is prominently affected by the SRA addition. Fig.4 displays the surface tension of solutions containing various type of SRA at various dosages. With the addition of 2% SRAs, the surface tensions of solutions reduced substantially from 72.8 dynes/cm to 59.7, 54.3, 43.9, and 62.2 dynes/cm for S1, S2, S3 and S4 respectively. S3(43.9 dynes/cm) appeared to be the most efficiency SRA, while S4 (62.2 dynes/cm) showed the least reduction ability. By adding more SRA to 4%, 6%, and 8%, the surface tensions values of S4 remained at its 2% level and the S1 and S3 reduced slightly and maintained at their 4% level regardless the dosage increase. However, for S2 the dosage effect on reducing the surface tension continued until 16%. Afterwards, the surface tension values leveled off (not shown in this paper). The surface tension values at 8% dosage were 54.8 (S1), 41.6(S2), 40.0(S3), and 62.3(S4) dynes/cm, respectively. Thus, it suggests that the reduction on the surface tension varies with chemical composition and dosages of SRAs.

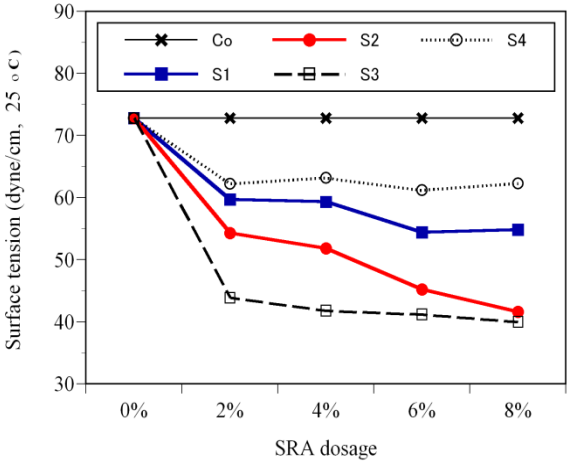

Fig. 4 The effect of SRAs' dosage on the surface tension of pore solutions

3.2 Influence of SRAs on the evolution of heat flow of cementitious composites

Cement hydration is an exothermic reaction, therefore, the heat flow of hydration of cementitious composite changes as reaction proceeds. In general, the initial set is assumed to occur some times after the dormant period and the final set corresponds to the time whenever the peak of the heat flow is reached [15]. The evolution hydration rate in terms of heat flow for the control mixture and SRA modified cementitious composites are presented in Fig. 5.

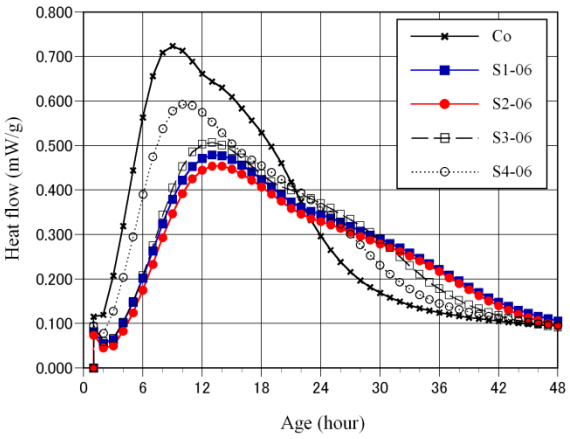

Fig. 5 The evolution of heat flow of cementitious composites with 6% SRAs and control mixture

The magnitude of heat flow and the time when the peak of the heat flow reached for the controlled mixture are seen to be much stronger and earlier than those for SRAs modified mixtures. Thus the influences of SRAs are clearly observed on reducing both the rate of heat flow and delaying the peak of the rate of heat flow by more than few hours, which suggested that the setting of cementitious composite were significantly affected by SRAs [4, 16].

Table 3 Summary of restrained shrinakge test results

Mixture designation	Co	S1-06	S2-06	S3-06	S4-06
Surface tension of pore solution (dyne/cm, 25° C)	72.6	54.4	41.6	41.2	60.2
3 d compressive strength (MPa)	22.6	12.5	11.4	15.0	10.0
7 d compressive strength (MPa)	29.1	19.5	19.5	24.1	17.8
28 d compressive strength (MPa)	38.9	33.0	32.0	39.6	26.9
Time of peak of heat flow (hour)	8	13	13	13	9
Peak of heat flow (mW/g) (	0.720	0.48	0.46	0.50	0.59
Age at cracking (day)	5	28	32	21	17
Maximum strain (micron)	-42.4	-29.0	-37.1	-29.0	-28.6
3 d drying shrinkage (micro ε)	100	200	200	200	100
7 d drying shrinkage (micro ε)	-520	-190	-500	-450	-180
14 d drying shrinkage (micro ε)	-980	-600	-520	-540	-470
21 d drying shrinkage (micro ε)	-910	-740	-660	-680	-560
28d drying shrinkage (micro ε)	-1010	-790	-660	-700	-710
Wet density (g/cm^3)	2.06	2.08	2.11	2.17	1.97

The heat flow curve of Co begin to ascend about 2 hours after it was mixed with water, and then followed by a sharp rise until 9 hours to reach the peak at 0.724 mW/g as shown in Fig.5. After the end of acceleration period or peak of heat flow, the rate of heat flow slows down. Nevertheless, a second kick (C3A hydration) [15] can be observed on hour 12, thereafter, the rate of heat flow decreases until it reaches a steady state at around 36 hours.

With the addition of SRAs, the heat flow curves were flattened and shifted to the right. The peak of heat flow extended form 9(Co) hours to 13(S1-06), 13(S2-06), 13(S3-06), and 10(S4-06) hours, respectively, and the magnitude of peak of heat flow reduced from 0.724(Co) mW/g to 0.479(S1-06), 0.454(S2-06), 0.507(S3-06), and 0.593(S4-06) mW/g, respectively. Moreover, the occurrences of second kick were much delayed for about 12 hour, in comparison with 3 hours of control mixture (Co) and the steady states begin after 48 hours.

The flattened heat flow curve and lowered peak of heat flow suggested that the reaction rates of hydration were smoother and slower, in other words, the thermal stresses resulting from exothermic hydration were lower for the SRA mixtures [17]. Since the hydration rates were lower, the consumptions of mixing water reduced accordingly. As a result, cementitious composites with SRAs retain more water which may reduce moisture gradient during drying. Among four types of SRAs, S1 and S2 induced a more significant retardation in the hydration rate than those of S3 and S4.

3.3 Influence of SRAs on the compressive strength of cementitious composites

The 3, 7 and 28 days compressive strengths of mortar cubes (50 mm) with and without SRAs are summarized in Table 3 and depicted in Fig. 6. Without the addition of SRAs, the 3, 7, and 28d compressive strengths of control mixture are 22.6, 29.14, and 38.9 (MPa), respectively. With the addition of SRAs, all the compressive strengths reduced except for the S3-06 at 28 days, which is about the same strength as that of the Co mixture.

The normalized compressive strength data are displayed in Fig. 7 for easier comparison. At 3 days, the compressive strength of SRAs modified composites were about 42-62 percent compared with the control mixture (Co). After 3 days, cementitious composites with SRAs increased their strength at faster rates. The normalized strengths of 7 days and 28 days increased to about 60-80 percent and 70-100 percent in comparison with Co mixture. Nevertheless, S4 mixtures had the lowest strength, which might be resulted from its smaller wet density caused by air entraining. On the contrary, S3 mixtures reached similar strength level as that of control at 28 days. In general, cementitious composites containing SRAs have lower compressive strength, especially for 3 and 7 day strength.

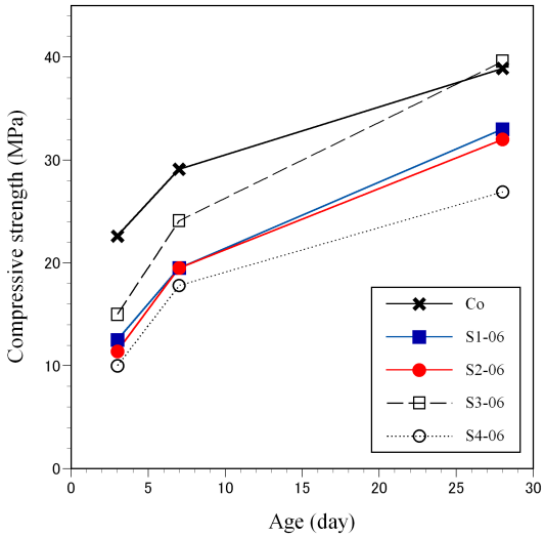

Fig. 6 Compressive strengths of cementitious composites at different ages

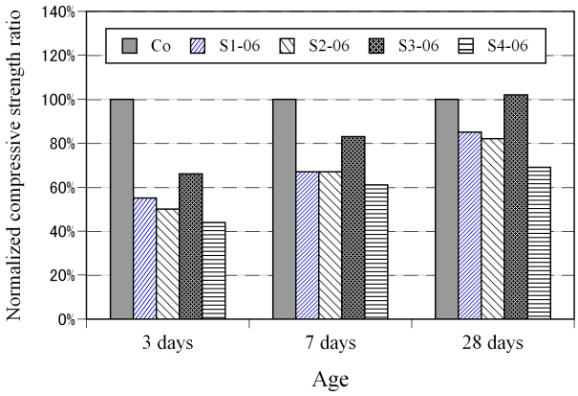

Fig. 7 Normalized compressive strength

3.4 Influence of SRAs on the drying shrinkage of mortar specimens

Drying shrinkage is the contracting of a hardened cementitious composite due to the loss of capillary water at the exposed surface of specimen. Drying shrinkage causes an increase in tensile stress, which may lead to cracking when restrained exists [18]. The drying shrinkage (micro-strain) is defined as micro $\varepsilon = (\Delta L/L) \times 10^6$. The drying shrinkage of mortar specimens are notably affected by SRAs addition. Fig.8 depicts the drying shrinkage of specimens with various types of SRAs at different ages.

For the control mixture (Co), the drying shrinkage increased significantly to around -1010 micro-strain during first 14 days of hydration. Thereafter, the drying shrinkage maintained. For S1, S2, and S3 mixtures, the magnitudes of drying shrinkage deviated from Co after 7 days and the rate of shrinkage decreased. The 28 days drying shrinkage results were -790(S1-06), -660(S2-06), and -700(S3-06) micro-strain, respectively, which were about 75% of the control mixture. For S4 mixture,

the drying shrinkage was lower and smoothly developed. The results showed that all the SRAs reduced the 28 days drying shrinkage to about 25% of that of control composite (Co).

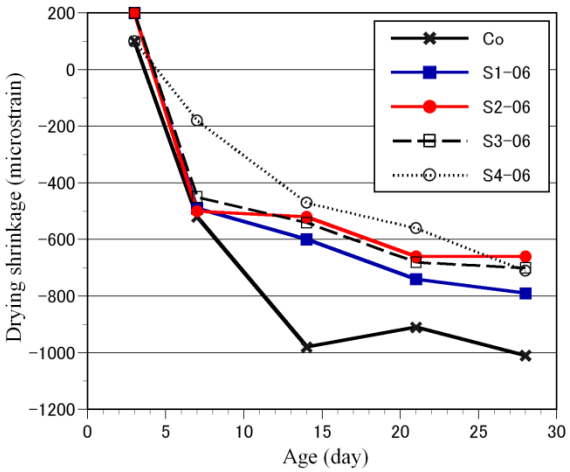

Fig. 8 Effect of SRAs on the drying shrinkage

The reduced drying shrinkage may result from the reduction of surface tension of pore solution when SRAs were added [4]. The reduction on the drying stresses may alleviate the occurrence of the early-age shrinkage cracking.

3.5 Influence of SRAs on the age at cracking and maximum restrained shrinkage strain

The evolution curves of compressive strain on the inner surface of steel ring are depicted in Figs. 9. The sharp change of strain is due to the release of compressive stress resulting from cracking of mortar ring; and the corresponding time is considered as the age at cracking [19, 20].

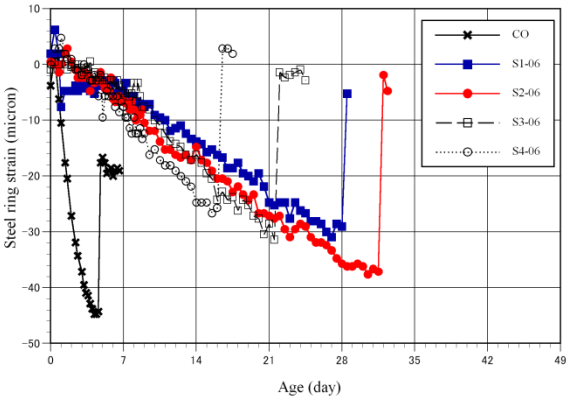

Fig. 9 Effect of SRAs on the development of compress strain on the inner steel ring

The maximum restrained shrinkage strain of inner steel (when cracking occurred) for the Co mixture was the lowest at -42.4 micro strain; followed by -37.1(S2-06), -29.0(S1-06), -29.0(S3-06), and -28.6(S4-06). On the contrary, the Co mixture cracked earliest at day 5, and all the SRAs specimens delayed their age at cracking. For SRAs composites the cracked age were 28(S1-06), 32(S2-06), 21(S3-06), and 17(S4-06) days as exhibited in Fig. 9. It seemed that there is no relationship between the cracked age and the restrained shrinkage strain when cracking occurred. Therefore, some other factors affecting cracking age should be existed and needed for further investigation [20].

3.5 Discussion on the properties of SRA affecting early-age shrinkage cracking behavior

Early-age shrinkage cracks would occur when the young cementitious composites have not yet developed enough strength to withstand the tensile stress induced by restraints, such as steel ring in this experiment. The cause of early-age shrinkage cracking are the combination of several factors, including thermal stress, internal drying stress (autogenous shrinkage or chemical shrinkage) and external drying stress (capillary stress). Thermal stress results from un-uniform temperature gradient due to the heat released by the cement hydration cannot liberate freely and quickly. Internal drying stress occurs because water is consumed by hydration and the volume of hydrated products is less than the original volume of cementitious material and water. External drying shrinkage is caused by loss of water through evaporation at the surface of specimen. Therefore, cement hydration is the underlying cause of early-age shrinkage, because it generates strength, liberates heat, consumes water, and induces chemical shrinkage.

Since different SRAs exhibited different degree of effectiveness on increasing age at cracking, and several effects were observed with the addition of SRAs. Surface tension of pore solution reduced, compressive strength development retarded, drying shrinkage decreased and progress of cement hydration changed.

The correlation between surface tension and cracked age are depicted in Fig. 10. It is clear to found that the reduction of surface tension might lead to a longer age at cracking. As surface tension of pore solution decreased, the age at cracking increased. Nevertheless, the degree of linear relation was low (R^2=0.67), which means the linear relationship between surface tension and cracked age was not good enough. Due to the extended age at cracking in SRAs specimens seemed not so consistent with the decreased magnitude of surface tension alone; some other factors might exist, such as hydration development or pore size distribution [4]. Yet similar results were found on the relationships between cracked age and mechanical strength, drying shrinkage and the time when peak of heat flow reached.

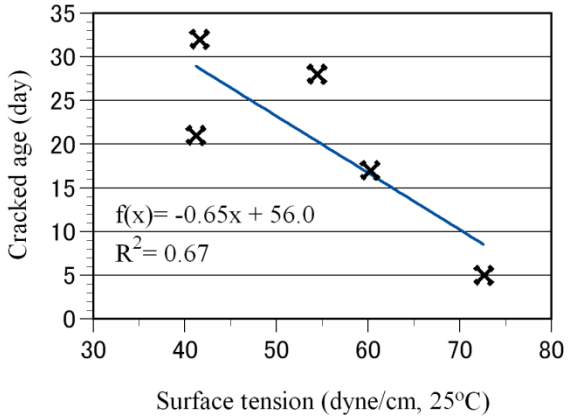

Fig.10 Correlation of surface tension and cracked age

The correlation between peak of heat flow and age cracked age are exhibited in Fig. 10. A power law relationship seems to exist with a correlation coefficient of 0.94. From the fitted curve shown, the slop gradually increased between 0.5-0.7, then increased sharply. It suggested that the peak of heat flow must be reduced to the level below 0.5mW/g so that the cracked age may be extended to more than 28 days, which is one of the requirements for cementitious repair materials by American Concrete Institute [21].

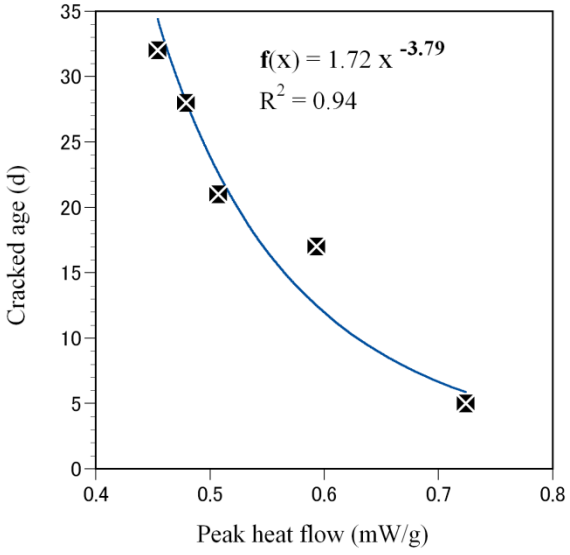

Fig. 11 Correlation of peak of heat flow and cracked age

5 CONCLUSIONS

This study has evaluated the effect of four kinds of SRAs on the early-age shrinkage cracking tendency induced by restrained steel ring. Several conclusions are drawn as follows:

(1) SRAs have significantly enhanced early-age cracking resistance so that cracked ages were lengthened.
(2) The mechanisms for SRAs to reduce early-age shrinkage were the combined effects of reducing surface tension of pore solutions, decreasing the peak of heat flow, and retardation of hydration heat development.
(3) Mixtures containing SRAs show lower compressive strength, lower drying shrinkage, lower and retarded peak of heat flow, and longer cracked age despite having lower strength at early-age.
(4) A power law relationship was found between the peak of heat flow and cracked age. It suggested that the peak of heat flow should below 0.5mW/g, so that the cracked age might be extended more than 28 days, which was one of the requirements for concrete repair materials in some countries.

ACKNOWLEDGEMENT

We would like to gratefully acknowledge the National Science Council (Taiwan) for the financial support (NSC98-2622-E-019-011-CC2).

REFERENCES

[1] H. Mihashi, and J.P. de B. Leite: State-of-the-Art Report on Control of Cracking in Early Age Concrete, Journal of Advance Concrete Technology (Japan Concrete Institute), Vol. 2, No. 2, pp.141-154, June 2004
[2] Y.Y. Mindess, J.F.Young, D. Darwin: Concrete, Peason Education Inc., pp.418-420, 2003
[3] G.W. Scherer: Theory of drying, Journal of American Ceramic society, Vol. 73, pp-3-14, 1990
[4] J. Weiss, N. Berke: Admixtures for reduction of shrinkage and cracking. In A. Bentur (ed) Early Age Cracking in Cementitious Systems, RILEM Report 25, Chapter 7, pp.323-335, 2003
[5] P. Lura, B. Pease, G.B. Mazzotta, F. Rajabipour, J. Weiss: Influence of shrinkage-reducing admixtures on development of plastic shrinkage cracks, ACI Material Journal, ACI, Vol. 104, pp-187-194, 2007
[6] D.P. Bentz: Curing with Shrinkage-reduction Admixtures: Beyond Drying Shrinkage Reduction, Concrete International, ACI, Vol.27, pp. 55-60, 2005
[7] D.P. Bentz, M.R. Geiker, K.K. Hansen: Shrinkage-reducing admixtures and early-age desiccation in cement pastes and mortars, Cement and Concrete Research, Vol. 31, pp.1075-1085, 2001
[8] A. B. Hossain, J. Weiss: The role of specimen geometry and boundary conditions on stress development and cracking in the restrained ring test, Cement Concrete Reserch, Vol.36, pp.189-199, 2006

[9] ASTM C1581-04, Standard Test Method for Determining Age at Cracking and Induced Tensile Stress Characteristic of Mortar and Concrete under Restrained Shrinkage
[10] ASTM D971 - 99a(2004) Standard Test Method for Interfacial Tension of Oil Against Water by the Ring Method
[11] ASTM C 1506-01 Standard Test Method for Water Retention of Hydraulic Cement-Based Mortar and Plasters
[12] ASTM C1702 - 09a Standard Test Method for Measurement of Heat of Hydration of Hydraulic Cementitious Materials Using Isothermal Conduction Calorimetry
[13] ASTM C596-09 Standard Test Method for Drying Shrinkage of Mortar Containing Hydraulic Cement
[14] ASTM C109 / C109M - 11b Standard Test Method for Compressive Strength of Hydraulic Cement Mortars (Using 2-in. or [50-mm] Cube Specimens)
[15] Y.Y. Mindess, J.F.Young, D. Darwin: Concrete, Peason Education Inc., pp.58-65, 2003
[16] D. P. Bentz: Influence of shrinkage-reducing admixtures on early-age properties of cement pastes, Journal of Advanced Concrete Technology, Vol. 4, pp.423-429, 2006
[17] D. A. Lange, S.A. Altoubat; Early therma changes, RILEM Report 25, Early Age Cracking in Cementitious Systems, Edited by A. Bentur, pp. 37-38, 2003
[18] S. P. Shah, M.E. Karagular. M. Sarigaphuti: Effects of shrinkage reducing admixtures on restrained cracking of concrete, ACI materials Journal, Vol. 89, pp. 289-295, 1992
[19] Shih-Tang Lin, R. Huang, and Chin-Yun Chang: Effect of water soluble polymers on the early age shrinkage of cementitious composites by using the ring test method, Material Chemistry and Physics., Vol. 121, Issue 3,pp. 440-446, 1 June 2010
[20] A. Radinska, J.H. Moon, F. Rajabipour, and J. Weiss: The Ring Test: A review of Recent Developments, RILEM Proceeding PRO 52. Volume Changes of Hardening Concrete: Testing and Mitigation, Edited by O.M. Jensen, P. Lura, and K. Kovler, pp.205-214, 2006
[21] ACI Committee 305: ACI 546.3R-06: Guide for the selection of materials for repair of concrete, 2006

Proceedings of the 3rd JCI-KCI-TCI Symposium on Recent Advancement of Technologies in Concrete Engineering
Japan Concrete Institute, July 2012

SHRINKAGE BEHAVIOR OF ULTRA HIGH PERFORMANCE CEMENTITIOUS COMPOSITE AT EARLY AGE

Sungwook Kim
Structural Engineering Research Division, Korea Institute of Construction Technology, Korea

Jungjun Park and Jaeheum Moon
Structural Engineering Research Division, Korea Institute of Construction Technology, Korea

ABSTRACT

Ultra high performance cementitious composite (UHPCC), characterized by a high strength and high ductility, is also subjected to large shrinkage due to its low water-to-binder ratio and its large content in high fineness materials. The large amount of autogeneous shrinkage of UHPCC at the early age can induce restrained stress by forms, and cracks can be developed when the restrained stress is higher than tensile strength of UHPCC at the same age. The most important issue in the process of manufacturing UHPCC structural members is to control cracks at early age. This study had focused on the early age shrinkage behavior in order to manufacture UHPCC structural members without crack. This study therefore evaluated free and restrained shrinkage behaviors of UHPCC. Elastic and residual tensile stresses of restrained UHPCC were investigated from a theoretical approach, and tensile strength at very early age was also evaluated.
Keywords: *UHPCC, Shrinkage behavior, Restrained shrinkage, Crack Control*

1 INTRODUCTION

Ultra high performance cementitious Composite (UHPCC), which has the characteristics of high strength and ductility, is highly vulnerable to premature shrinkage cracking because it has a low water to binder ratio and contains high fineness silica fume and filler without coarse aggregate. Accordingly, the shrinkage behavior of UHPCC should be assessed precisely and countermeasures to reduce shrinkage need to be prepared.

Since the shrinkage cracking behavior of concrete is influenced by the shrinkage development speed and size according to age as well as by the development of strength, stress relaxation and degree of restraint, this behavior is extremely complex. Therefore, the evaluation of the risk of shrinkage cracking should be accompanied by the execution of restrained shrinkage test and the evaluation of the mechanical characteristics [1,2]. The normal concrete structural member with large stiffness and low restrained stress can be endured crack without expansive admixture (EA) and shrinkage reducing agent (SRA) at manufacturing step. On the other hand, UHPCC structural member has normally a slim cross section. Therefore, EA and SRA can be used to fabricate UHPCC structural member in order to prohibit crack at that step. This study considered two types of mix proportion which one contains EA and SRA and another one doesn't contain them. The shrinkage behavior was analyzed by means of non-restrained shrinkage test, restrained shrinkage test, and ring test. Furthermore, research related to setting time of UHPCC was carried out in order to estimate autogeneous strain precisely.

2 PROPERTIES OF UHPCC

2.1 Materials and Mix Proportions

The test adopts type 1 Portland cement, fine aggregates with grain size smaller than 0.5 mm, filler of 2 μm, and silica fume (SF) with specific surface area of 200,000cm^2/g. Polycarbonate superplasticizer is admixed to secure workability and straight high-elastic steel fiber (density 7.8 g/cm^3, tensile strength 2,500 MPa, length 13 mm, diameter 0.2 mm, shape factor 65) is introduced at a ratio of 2% of the total volume of concrete to improve the tensile strength and ductility. The mix proportions of UHPCC used for all UHPCC test specimens reveal Table 1. These mix proportions were separated on two types. Mix.A didn't include with EA and SRA, however Mix.B included EA and SRA.

Table 1 Mix Proportion of UHPCC (by weight except for fibers)

Types	W/B	Cement	Silica fume	Sand	Filling powder	SP	SRA	EA	Steel Fiber
Mix.A	0.2	1	0.25	1.1	0.3	0.016	-	-	2%
Mix.B	0.2	1	0.25	1.1	0.3	0.016	0.01	0.075	

Table 2 Properties of fresh and hardened UHPCC

Nomen-clature	Flow (mm)	f_{ck} (MPa)				f_{fl} (MPa)				E_c (GPa)			
		1 day	3 days	7days	28days	1 day	3 days	7days	28days	1 day	3 days	7days	28days
Mix. A	235	78.8	105.6	126.2	152.4	26.3	28.7	33.8	34.1	28.2	40.3	41.2	43.3
Mix. B	240	70.7	98.7	127.3	152.2	24.1	25.1	32.5	33.4	30.9	41.1	44.6	46.0

2.2 Test Setup

Flow was determined according to ASTM C 1437. To measure the compressive strength (ASTM C 39), cylindrical specimens of Φ100 mm × 200 mm were tested using a universal testing machine (UTM) with a maximum load capacity of 3,000 kN. A compressometer for the average compressive strain measurement from three linear voltage differential transformers (LVDTs) was installed to obtain the elastic modulus. Flexural strength was estimated by a 4-point loading test.

2.3 Mechanical Properties

The flow and strength properties are represented in Table 2. It can be noticed that flow-ability was rarely affected by simultaneously adding EA and SRA. Compressive and flexural strengths at early age were slightly reduced as EA and SRA were applied, whereas they became similar to each other after 7 days. Secant elastic modulus was calculated by Eq. (1) and the results are listed in Table 2.

$$E_c = \frac{0.4 f_{ck} - f_1}{\varepsilon_2 - 0.00005} \quad (1)$$

Where, f_{ck} is the ultimate compressive strength (MPa), f_1 is the stress corresponding to a longitudinal strain of 50 με (MPa), ε_2 is the longitudinal strain produced by stress at 40% of f_{ck} (με).
Test results indicate that Mix.B represents slightly higher elastic modulus than that of Mix.A. The elastic modulus increased rapidly up to an age of approximately 3 days, but reached almost the same values thereafter. Since the experimental results were measured at specific times, regression function was used to obtain the time-dependent material properties and free elastic tensile stresses of UHPCC at other ages. The elastic modulus at arbitrary ages can be calculated by Eq. (2) and regression coefficients are shown in Table 3 [3].

$$E_c(t) = E_{c28} \exp\left(\frac{a}{b-t}\right) \quad (2)$$

Where, E_{c28} is the 28-day elastic modulus (GPa), and a and b are regression coefficients.

Table 3: Regression coefficients

Nomenclature	a	b	R^2
Mix. A	0.389	0.001	0.9948
Mix. B	0.381	0.001	0.9985

2.4 Time of Setting

Test of setting time of UHPCC was carried out by ASTM C 403. The penetration time and depth in order to measure setting time were 10 seconds and 25mm relatively. When vicat spindle reached at 25mm during on 10seconds, the setting time after casting UHPCC on test bowl was recorded. Generally, the initial setting time is defined when the internal stress of matrix by vicat spindle reach to 3.5N/mm^2. Hence the last setting time is defined when the internal stress of matrix will be reached to 28.5N/mm^2. In the case of UHPCC, the same measuring process applied.
Fig.1 shows test results of setting time of UHPCC.

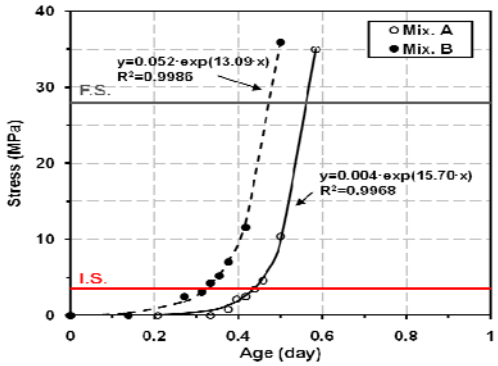

Fig.1 Test Results of Setting time of UHPCC

The initial setting time and final setting time of Mix.A revealed 11 h, 13.5 h after casting

respectively. In case of Mix.B contained with EA and SRA, the initial and final setting time was earlier shifted than Mix.A as 2.5 h and 4 h. That was 7.5 h, 11.5 h individually. The reason why the setting time of Mix.B was fastened would be based on ettringite from EA. The resistance stress penetrating on UHPCC was proportioned to the exponential time function.

3 SHRINKAGE BEHAVIOR OF OF UHPCC

3.1 Non-restrained Shrinkage of UHPCC

The test of non-restrained shrinkage of UHPCC carried with method recommended on Japan Concrete Institute [4]. The specimen was only exposed on the air to the direction of upper side. Generally, structural member such as beam, girder, and slab would be fabricated on the state of exposing upper side. The test specimen was exposed upper side (Fig.2). UHPCC has abundant binders, therefore the autogeneous shrinkage occupies most of shrinkages, and drying shrinkage quantity occurs small.

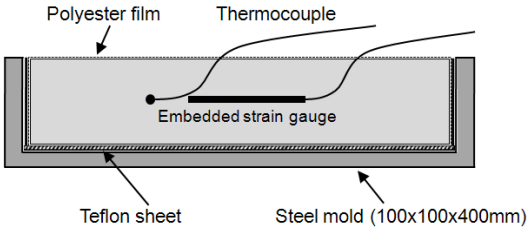

Fig.2 Test method of non-restrained shrinkage

Fig.3 shows test results of non-restrained shrinkage of UHPCC for 28days after casting. Test results were revised with thermo-strain.

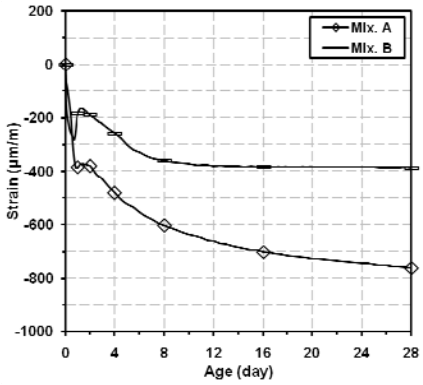

Fig.3 Non-restrained shrinkage of UHPCC (28days)

The non-restrained shrinkage of Mix.A converged on 800 με, and that of Mix.B converged on 400 με till 91 days. The shrinkage of Mix.B revealed smaller than that of Mix.A. In case of Mix.B, UHPCC was swelled between elapsed time 0.7 day and 1.2 days because ettringite generated by EA expanded UHPCC matrix. The shrinkage of Mix.A increased continuously according to time, however, the slope of shrinkage was come dull after 7 days in the Mix.B. Fig.4 reveals re-drawing of Fig.3 expanded with early 4 days. The shrinkage of Mix.B composed with EA and SRA in very early section was larger than that of Mix.A on the contrary. If the stress would be acted on UHPCC at that elapsed time, the mix proportion of Mix.B could be dangerous on crack.

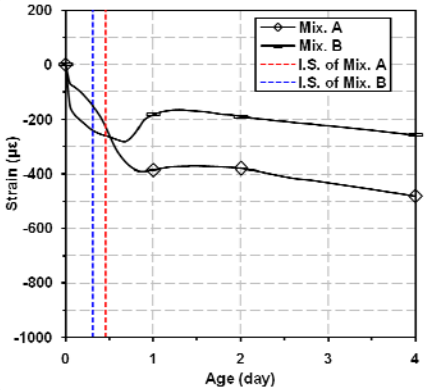

Fig.4 Non-restrained shrinkage of UHPCC (4days)

The dotted lines in Fig.4 explained initial setting times of Mix.A and Mix.B respectively. On following of research from JCI, the shrinkage before initial setting time can be considered as plastic deformation in normal concrete. We can assume that internal stress of UHPCC will not be generated in UHPCC too. Generally, crack can be occurred in the condition that internal stress is rather high than strength in hydrated matter as such concrete.

On the point view of crack control, the shrinkage before initial setting can be eliminated on the non-restrained shrinkage in UHPCC.

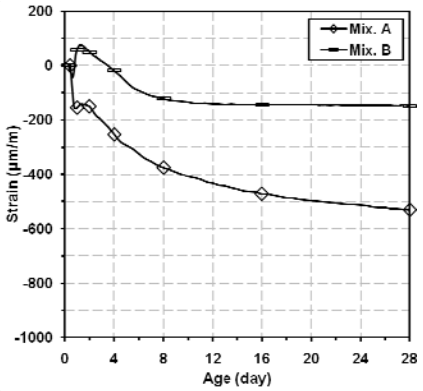

Fig.5 Non-restrained shrinkage after initial setting

Fig.5 shows the non-restrained shrinkage except shrinkage before initial setting time. The revised

shrinkage of Mix.A converged about 150 με and that of Mix.B converged 550 με. The shrinkage of 250 με before initial setting can be supposed to ignore influence of internal stress. However, can we ignore the shrinkage before initial setting time in the estimation of crack control? The former test results are not sufficient to prove assumption.

Fig.6 indicates a comparison of setting time and strain of steel ring at early age [5]. In case of Mix.A, strain increased rapidly after final setting time, and expansive behaviour occurred on Mix.B after that time. Hereby, a starting point of strength in UHPCC can be assumed after final setting time. In results of ring test, however, inner steel ring was deformed before initial setting time. That means occurrence of tensile stress in UHPCC. The issue of starting point of tensile stress in UHPCC could not be concluded in the study.

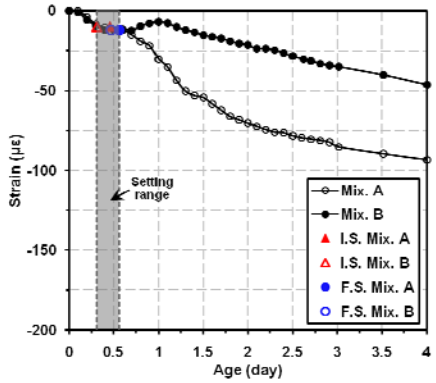

Fig.6 Comparison of setting time and stress of UHPCC

3.2 Restrained Shrinkage of UHPCC

According to previous research results [2], shrinkage cracking of UHPCC cannot be induced by conducting the ring-test as proposed in the specifications of AASHTO PP34-98 because of the outstanding tensile strength development of UHPCC and the effect of the tensile creep at early age. Therefore, in this study, the thickness of the concrete ring (t_c) is reduced from the previous 35 mm to 20 mm to improve the degree of restraint and tests were performed by applying various thickness and radius of the inner steel ring. The designation system according to the radius of the inner ring is illustrated at the bottom of Fig.7.

Moreover, the height of the ring-test was reduced from the previous 152 mm to 75 mm to induce uniform drying shrinkage in the section of the concrete ring. The circumference of the concrete ring was sealed using aluminum bond tape and test was carried out by exposing the upper and bottom sides. The test procedure followed the regulations of AASHTO PP34-98. The test was conducted at constant temperature of 23±1°C and constant humidity of 60±5% after placing.

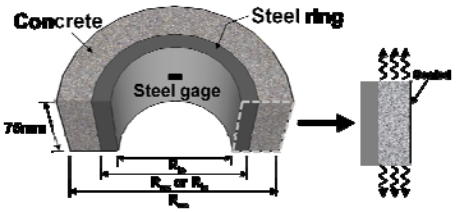

R-NS: R_{is}=127 mm, R_{os}=145.5 mm (t_s=18.5 mm),
R-MS: R_{is}=120 mm, R_{os}=145.5 mm (t_s=25.5 mm),
R-TS: R_{is}=115.5 mm, R_{os}=145.5 mm (t_s=30 mm)

Fig.7 Restrained ring-test specimens

For the purpose of comparison with the ring-test results, the free shrinkage strain and thermal variation of UHPCC were measured using dumbbell-shaped gages and a thermocouple embedded in the prismatic mold with dimensions of 20×75×285 mm. The mold was stripped 24 hours after concrete placing and the top, bottom and front sides of the specimen were sealed using aluminum bond tape as shown in Fig.8 to achieve a volume-to-exposed surface area ratio (V/S) identical to that of the concrete ring.

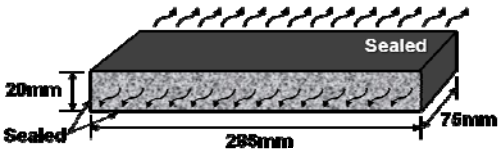

Fig.8 Prismatic free shrinkage specimen with sealing

Fig.9 plots the strain of the inner steel ring according to the age. For R-NS featured by the smallest thickness of the inner ring, the largest strain was observed at 4 days with value of about –31 με. The maximum strains of R-MS and R-TS ran around –19 με and –11 με, respectively, and indicate that the strain tends to decrease with larger thickness.

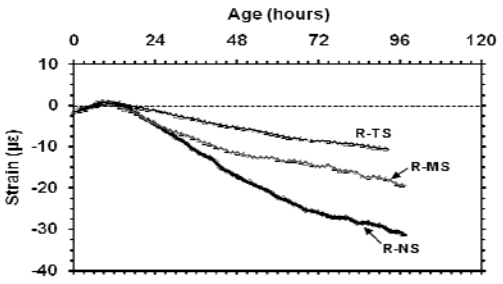

Fig.9 Measured average strains of the inner steel ring

Even if identical thickness of concrete ring and exposure conditions were applied, the decrease of the average strain measured in the inner ring with

larger thickness of the inner ring can be explained by the fact that the stress developed in the inner ring decreases with larger thickness of the inner ring while the interface pressure due to the shrinkage of concrete remains unchanged. Test was carried out on a free shrinkage specimen fabricated with identical sectional size and V/S for comparison purpose with the ring-test results.

As shown in Fig.10, the strain and temperature change were measured immediately after placing. The behaviors of the temperature and strain started to differ approximately 1 hour before early setting and, the shrinkage strain experienced sudden increase.

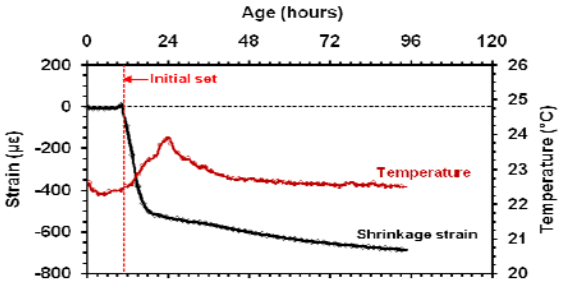

Fig.10 Total free shrinkage of the partially exposed specimen

The maximum temperature was 23.9°C at about 1 day and the maximum strain reached –686 με. The interface pressure (P_i) provoked by the restrained shrinkage of concrete due to the inner ring acts as a compressive force on the inner steel and causes tensile force of the same size on the concrete ring. Accordingly, assuming that concrete exhibits uniform and linear behavior and that uniform drying shrinkage occurs, the interface pressure can be calculated by the following Eq.(3) using the measured strain of the inner ring [5].

$$P_i = \frac{\left(r_{os}^2 - r_{is}^2\right)}{2r_{os}^2} E_{st}\varepsilon_{st} \qquad (3)$$

where r_{is} and r_{os} are respectively the inner and outer radii of the inner steel ring, and ε_{st} and E_{st} are respectively the strain and elastic modulus of the inner steel ring.

The maximum value of the stress in the circumferential direction occurs at the surface of the inner ring and concrete ring. If the interface pressure of Eq.(3) and r_{is} are substituted as the circumferential stress (σ_θ) and arbitrary value r, the equation can be reformulated as the product of the shape factor and elastic modulus and measured strain of the inner ring as expressed in Eq. (4).

$$\sigma_{t\max} = \frac{\left(r_{os}^2 - r_{is}^2\right)}{2r_{os}^2}\frac{\left(r_{ic}^2 + r_{oc}^2\right)}{\left(r_{oc}^2 - r_{ic}^2\right)} E_{st}\varepsilon_{st} \qquad (4)$$

where r_{ic} and r_{oc} are respectively the inner and outer radii of the concrete ring.

The average tensile strength of UHPCC at 28 days appears to be approximately 11.8 MPa. The tensile strength tends to increase suddenly as an exponential function at early placing to show reduced increase rate after 1 day and exhibit S-shaped variation to converge to a definite value (Fig.11). Therefore, the prediction model of the tensile strength expressed in Eq. (5) is applied as proposed in previous studies [4].

$$f_t(t) = f_{t28}\exp\left\{-a\left[\ln\left(1+(t-t_i)\right)^{-b}\right]\right\} \qquad (5)$$

Where f_{t28} is the tensile strength at 28 days (MPa), t_i is the time (days) when the penetration resistance reaches 1.5 MPa, and a and b are regression coefficients. From the regression analysis, a = 0.204 and b = 1.292.

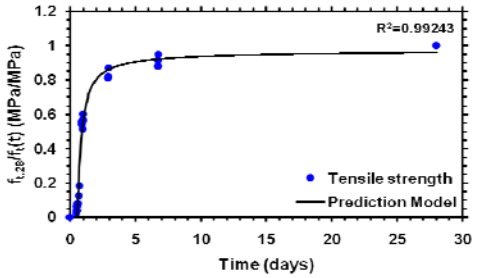

Fig.11 Tensile strength of UHPCC

Fig. 12 compares the residual stress calculated by Eq. (4), the tensile strength measured during the test and the tensile strength obtained by the prediction model (Eq. (5)). Moreover, the residual stress occurring due to the shrinkage restraint of the inner ring appears to be significantly smaller than the tensile strength of UHPCC. Accordingly, shrinkage cracking did not occur in all the specimens. In addition, the residual stress decreased with larger thickness of the inner ring. This can be explained by the fact that the tensile creep increases at early age for larger thickness of the inner ring despite of the action of identical interface pressure. In other words, insufficiently hardened concrete at early age cannot deform the inner ring when the thickness of the inner ring becomes thicker and induces the increase of the relaxed shrinkage, which causes increase of the tensile creep and stress relaxation.

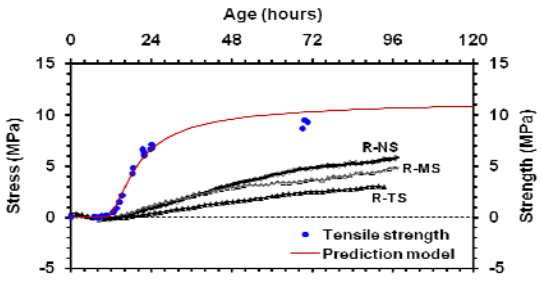

Fig.12 Comparison of residual tensile stress and

tensile strength of UHPCC

4 CONCLUSIONS

The initial setting time revealed between 7 hours and 11 hours although that could be gotten a little difference as following as mix proportion. In the study, the non-restrained shrinkage occurred till initial setting time was approximately 250 με. On the point view of crack control, the shrinkage before initial setting can be eliminated because UHPCC is supposed with a visco-plastic state. On the ring test, however, the strain in ring occurred earlier than initial setting.

This study compared the residual stress and tensile strength of UHPCC under restrained state by conducting ring-test considering the thickness and radius of the inner ring as variables. The following conclusions can be drawn from the results.

1) Even if identical thickness of concrete ring and exposure conditions are applied, the average strain measured in the inner ring decreases with larger thickness of the inner ring.

2) The results of the tests performed on the free shrinkage specimen fabricated to have sectional size and V/S identical to the concrete ring showed that the shrinkage strain experienced sudden increase about 1 hour earlier than the early setting. The maximum temperature was 23.9°C at about 1 day and the maximum strain reached –686 με.

3) The residual stress of UHPCC caused by the restraint of the inner ring appeared to be significantly smaller than the tensile strength. Shrinkage cracking did not occur in all the specimens. Moreover, the residual stress tended to decrease because tensile creep increased at early age with larger thickness of the inner ring.

ACKNOWLEDGEMENT

This work is the result of the research project, the Super Bridge 200 of Korea Institute of Construction Technology. The authors hereby express their appreciation for the support.

REFERENCES

[1] H.T. See, E.K. Attiogbe and M.A. Miltenberger: Shrinkage Cracking Characteristics of Concrete Using Ring Specimens, ACI Materials Journal, Vol. 100, No. 3, pp. 239-245, 2003

[2] D.Y. Yoo, J.J. Park, S.W. Kim and Y.S. Yoon: Characteristics of Early-Age Restrained Shrinkage and Tensile Creep of Ultra-High Performance Cementitious Composites (UHPCC), Journal of the Korea Concrete Institute, Vol. 23, No. 5, pp. 581-590, 2011

[3] Cha, , S. W., Kim, K. H., Kim, S. W., Park, J. J. and Bae, S. G., 'Models for hydration heat evelopment and mechanical properties of ultra high performance concrete', *J. KCI*, **22** (3) 389-397, 2010

[4] Committee of Autogeneous Shrinkage, Report for Autogeneous Shrinkage in Concrete, Japan Concrete Institute, 1996

[5] Korea Institute of Construction Technology: *Development of Ultra High Performance Concrete for Hybrid Cable Stayed Bridges*, Research Report, KICT 2011-067, 2011

Proceedings of the 3rd JCI-KCI-TCI Symposium on Recent Advancement of Technologies in Concrete Engineering
Japan Concrete Institute, July 2012

OUTLINE OF JCI GUIDELINES FOR CONTROL OF CRACKING OF MASS CONCRETE

Tsutomu Kanazu
Central Research Institute of Electric Power Industry, Japan
Ryoichi Sato
Department of Civil and Environmental Engineering, Hiroshima University, Japan
Shigeyuki Sogo
Department of Civil Engineering and Urban Design, Hiroshima Institute of Technology, Japan
Toshiharu Kishi
Institute of Industrial Science, the University of Tokyo, Japan
Takafumi Noguchi
Department of Architecture, the University of Tokyo, Japan
Toshiaki Mizobuchi
Department of Civil and Environmental Engineering, Hosei University, Japan
Shingo Miyazawa
Department of Civil Engineering, Ashikaga Institute of Technology, Japan

ABSTRACT

Japan Concrete Institute revised "Guidelines for Control of Cracking of Mass Concrete" in 2008 after 20 years interval. The guidelines follow the same idea for control of cracking as adopted in the original guidelines, and are composed corresponding to performance-based verification system. The following technological contents developed for the revised guidelines are incorporated; a relationship between thermal cracking index and thermal cracking probability established based on the past construction examples, design values of physical properties of concrete at early age applied to thermal stress analysis, an estimation equation of thermal crack width including thermal cracking index, etc.

Keywords: *mass concrete, performance based design, thermal cracking probability, thermal cracking index, three dimensional finite element method*

1 INTRODUCTION

Japan Concrete Institute revised "Guidelines for Control of Cracking of Mass Concrete" in 2008 after 20 years interval. The guidelines adopt a performance-based verification system that is based on the concepts for control of thermal cracking. The performance-based verification system was developed using information on the latest control and analysis technologies for thermal cracking. The major aspects of the guidelines are:

(1) Basic principles of control of thermal cracking are clarified.

(2) By using 3D-FEM (three dimensional FEM) as a standard analysis technique, a new diagram of thermal cracking probability relating to thermal cracking index is provided.

(3) By using the latest data, design values of concretes with different types of cement are provided, incorporating the physical properties at early age.

(4) A simple equation for predicting crack width is provided, which uses the reinforcement ratio as a parameter and the thermal cracking index.

(5) A simple equation for the thermal cracking index is provided.

In the guidelines, a "commentary" is added to provide details of the provisions. Reference data that provide the grounds for the contents of the guidelines are also appended. Furthermore, verification examples for thermal cracking are also appended, which are useful as reference in the design process.

2 OUTLINES OF JCI GUIDELINES

The outlines of JCI Guidelines are shown as

follows.

Chapter 1 GENERAL

1.1 Scope

This document provides standard guidelines for design, construction and inspection necessary to control thermal cracking due to heat of hydration of cement as well as autogenous shrinkage in concrete structures.

In the commentary of chapter 1, the following important matters related to the scope are described.

The guidelines provide methods to verify if thermal cracks develop, or whether thermal cracks satisfy the limit value of crack width in the design stage for thermal crack control, and if necessary, in the construction planning stage. Furthermore, the guidelines provide specific procedures relating to design, materials, mixture proportions of concrete, construction to control thermal cracking.

The provisions of the guidelines may be applicable to concrete structures whose concrete characteristic compressive strength is below 60N/mm^2 (60MPa), which are massive unreinforced and reinforced concrete structures. The guidelines also apply to reinforced and prestressed concrete structures that undergo large temperature drops from peak value as a result of high cement content or high concrete temperatures during construction, even if the structures are not massive in size. In general, mass concrete structures may be defined as reinforced walls having thicknesses greater than 50 cm restrained at the base or slabs with large surfaces having thicknesses greater than 80 cm.

The guidelines apply to mass concrete structures, and the period for verification of thermal cracking is from the time of completion of concrete placement to the time when concrete temperature equilibrates with the ambient temperature after the peak temperature. During this period, the effect of drying shrinkage is negligible and consequently is neglected in the verification procedure. Surface cracks, developed within one day after placing concrete due to drying and temperature drop in surface layer and cracks, developed within several days due to dominant internal restraint caused by a nonlinear distribution of temperature and shrinkage, are not the target of the verification. This implies that surface cracking can be avoided if construction, especially curing is conducted with appropriate care.

1.2 Definition

The terms related to thermal cracking are defined for general use in the guidelines.

1.3 Notation

The notations related to thermal cracking are explained for general use in the guidelines.

Chapter 2 BASIS OF THERMAL CRACK CONTROL

2.1 Basic principle

The target of thermal crack control shall be set and achieved so as to meet the performance requirements of the structures such as safety, serviceability, durability and aesthetic.

2.2 Target of thermal crack control

The target of thermal crack control shall be either the prevention of thermal cracking or the control of crack width. In the case of preventing thermal cracking of concrete structures of which airtightness or water-tightness should be secured only by the concrete material, thermal cracking probability is a reference index for control and verification. In the case of allowing thermal cracking, crack width is a reference index for control and verification. Thermal cracks shall not exceed the limit values of the control target and verification indices which are pre-defined based on the performance requirements and environmental conditions.

2.3 Control procedures

The control of thermal cracking shall be performed in the following procedures as shown in **Fig.1**. At design stage, setting the control target (Section 2.2), control planning (Chapter 3), analysis and verification (Chapter 4) and determination of the specifications (Chapter 4) are performed. Execution planning (Chapter 5), quality control (Chapter 5) and inspection (Chapter 6) are conducted before, during and after construction works, respectively. A flow chart of general procedure for control of thermal cracking is provided in the commentary.

Chapter 3 PLANNING FOR CONTROL OF THERMAL CRACKING

3.1 General

Proper plan shall be established to achieve control targets for thermal cracking. Thermal crack control planning shall include specifications for crack control joints and arrangement of reinforcing steel as well as specifications for materials, mixture proportions and execution (placement time, placement temperature limits, sequencing of concrete placements, curing method, etc.) taking into account environmental conditions, structure type and construction conditions.

3.2 Limit values for control target

3.2.1 Limit values for preventing thermal cracking

The limit value of thermal cracking probability shall be determined in consideration of performance requirements and environmental conditions of the structures. A relationship between thermal cracking probability ($P(I_{cr})$, %) and thermal cracking index (I_{cr}; splitting tensile strength/tensile stress) is derived as in the following equation (see **Fig.2**).

$$P(I_{cr}) = 1 - exp\left[-\left(\frac{I_{cr}}{0.92} \right)^{-4.29} \right] \times 100 \qquad (1)$$

The derivation of Eq.(1) is briefly explained. Sixty five mass concrete structures, whose information on

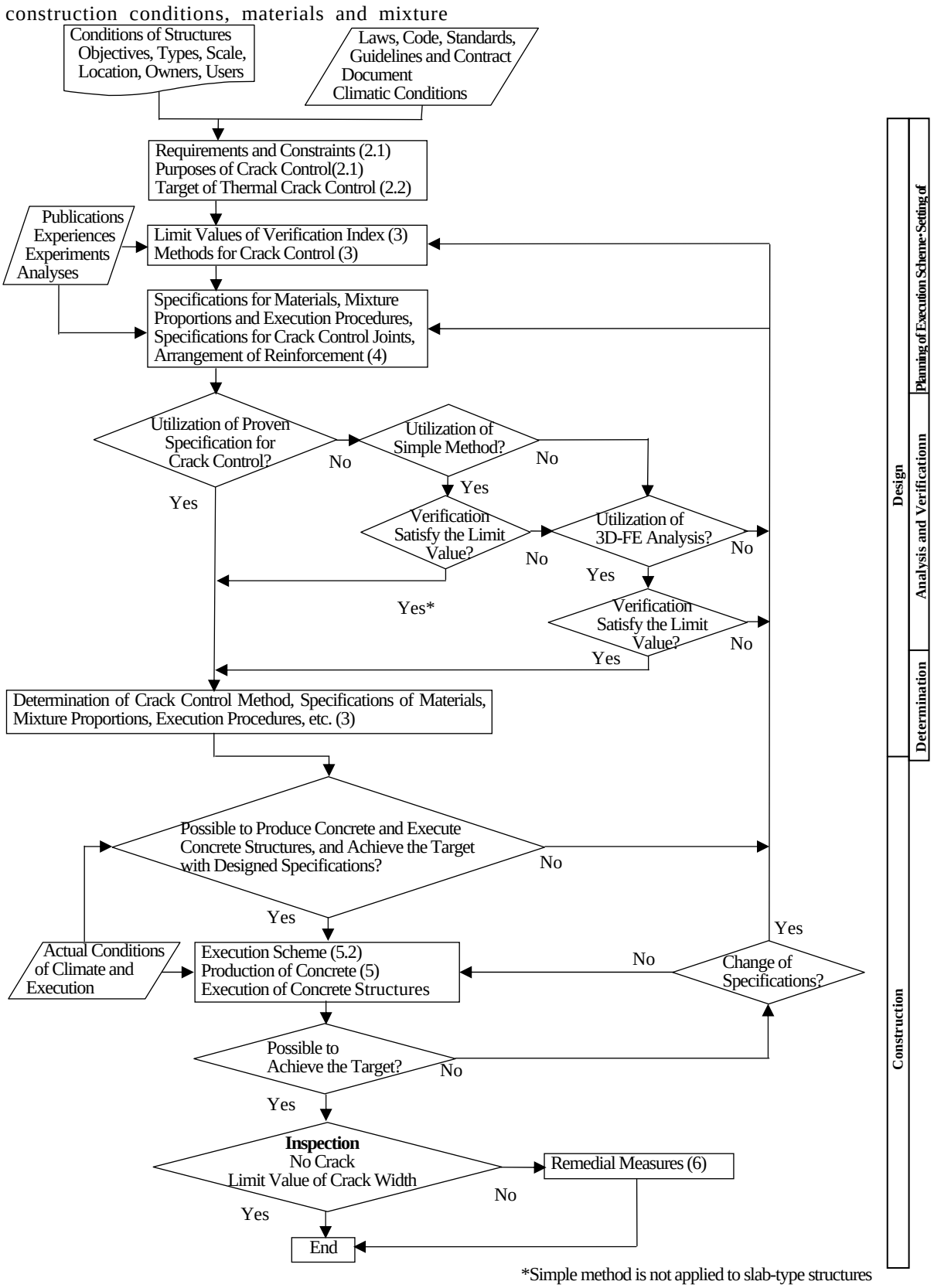

Fig. 1 General procedure for thermal crack control

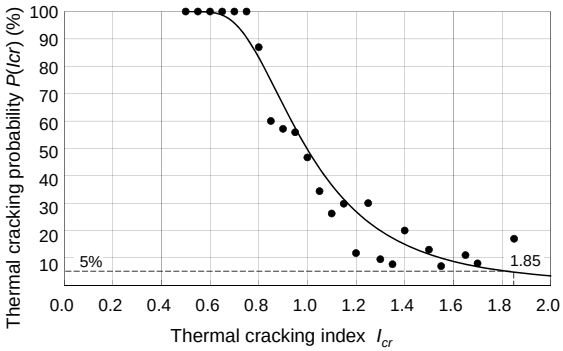

Fig. 2 Relationship between thermal cracking index and thermal cracking probability

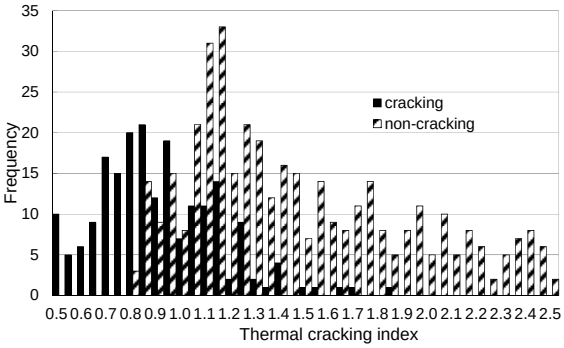

Fig. 3 Histogram of frequency on cracking and non-cracking in mass concrete structures surveyed

proportions conditions, and crack observation results had been obtained from the data survey of past construction examples, were selected and temperature and stress histories of each structure were analyzed by 3D-FE analysis. The histogram of frequencies on cracking or non-cracking of 728 members of sixty five structures, where we could judge the occurrence of cracks, was made in relation to the computed thermal cracking indices and is shown in **Fig.3**. The frequency on cracking or non-cracking corresponds to the number of the members whose computed thermal cracking indices are within numerical values with the interval of 0.05. The thermal cracking probability is defined as a ratio of the frequency of cracking to the number of total cases in each division of thermal cracking index. The investigated results on thermal cracking probability are plotted by black circles in **Fig.2**. The details of the analysis performed in the investigation conformed to the provisions in the guidelines.

The Weibull distribution function is adopted to estimate the thermal cracking probability. **Fig.4** shows the logarithmic expression of the data in **Fig.2** based on the Weibull distribution equation, where a good linear relation can be found. Eq.(1) is an exponential expression of this linear relation.

When thermal cracking is required to be prevented, the limit value of thermal cracking probability is given as 5%. The reason why the limit value of thermal cracking probability (5%) was adopted is

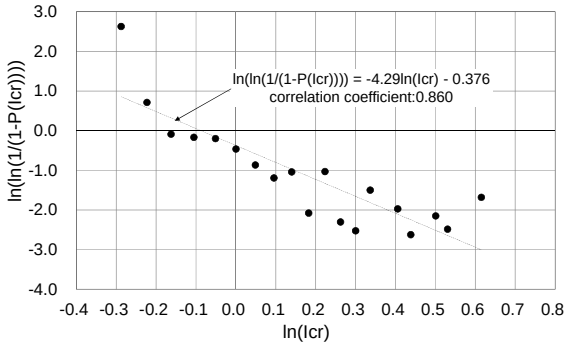

Fig. 4 Relationship between thermal cracking index and thermal cracking probability drawn in natural logarithm scale

that this value can be generally accepted as a limit for crack-free structures in view of probabilistic characteristics of thermal cracking, and that in practice crack controlling measures may be commonly available if thermal cracking probability is 5%. In the case when the structure is required to totally meet the crack-free criteria, a limit value lower than 5% needs to be specified. When a higher risk for thermal cracking can be tolerated, a value higher than 5% is allowed.

3.2.2 Limit values for controlling thermal crack widths

Limit values of crack widths on the surface of concrete shall be appropriately specified. When deterioration due to steel corrosion is considered, limit values of crack widths shall be specified considering the effects of thermal cracking on diffusion of chloride ion in concrete, carbonation rate, etc. When leakage constitutes a major concern, limit values of crack widths shall be specified in consideration of their effects on the amount of leakage. When the appearance of structures is considered, limit values of crack widths shall be specified considering the effects of thermal cracking on aesthetic appearance and sense of anxiety of nearby residents and users.

The limit values of crack widths are tabulated in the commentary.

3.3 Methods of controlling thermal cracks

3.3.1 General

To achieve the control targets, appropriate thermal crack controlling methods must be selected. To prevent thermal cracking, either or both of the two approaches shall be followed. One is to control volumetric change in concrete and the other is to reduce degree of restraint. To control thermal crack widths, proper arrangement of reinforcing steel shall be ensured if necessary, in addition to the methods for reducing thermal stress. The thermal crack controlling methods are summarized in **Table 1**.

3.3.2 Methods for controlling volumetric change in concrete.

In order to control volumetric change in concrete, materials, mixture proportions, production methods,

execution procedures, etc. for concrete shall be appropriately selected.

3.3.3 Methods to reduce external restraints

In order to control thermal cracking successfully, spaces, locations, types, constructions, etc. of crack control joints shall be specified so that the thermal stresses generated become as low as possible within the limit where the required performances for the concrete structures are satisfied.

3.3.4 Methods to control thermal crack widths

Adequate amount of reinforcing steel shall be arranged in appropriate positions in order to control thermal crack widths within the range of allowable value in addition to taking reasonable measures to reduce thermal stresses.

Table 1 Categorized crack control methods

	Category	Method
a-1	Methods to control volumetric change – mitigating temperature rise in concrete –	1. Use of cements with low hydration heat
		2. Use of admixtures
		3. Reduction of unit cement content
		4. Lowering material temperatures
		5. Time and period of concrete placement
		6. Methods of concrete placement
		7. Curing methods
a-2	Methods to control volumetric change – reducing shrinkage strains –	1. Selection of materials with lower thermal expansion coefficient
		2. Use of expansive additives
b	Methods to reduce external restraints	1. Employment of crack control joints
c	Methods to control thermal crack widths	1. Arrangement of reinforcements

Chapter 4 VERIFICATIONM OF THERMAL CRACKING

4.1 General

Thermal cracking is verified by computing the thermal cracking probability or thermal crack widths using an analysis method with proven reliability, and by applying limit values for control target. Three-dimensional FEM shall be utilized to analyze the thermal cracking index, but a simple method recommended in the guidelines may be used as well.

4.2 Design values of material properties

4.2.1 General

The design values of the material properties of concrete, steel, ground/bedrock and other materials to be used for temperature and thermal stress analyses shall be empirically determined. In the absence of experimental results, the design values may be determined based on reliable reference data, which are provided in the commentary.

4.2.2 Concrete

(1) Thermal properties of concrete

Heat conductivity of concrete may be 2.7W/m°C, thermal expansion coefficients may be recommended to be 10×10^{-6}/°C for portland cement, and 12×10^{-6} /°C for portland blast-furnace slag cement class B.

(2) Properties of adiabatic temperature rise in concrete

The properties of adiabatic temperature rise in concrete may be determined by the provided equation taking into consideration the type of cement, the unit cement content, and the concrete temperature at placement.

(3) Heat transfer coefficient of concrete

The reference values corresponding to the typical form and the curing method are provided in the commentary.

(4) Mechanical properties of concrete

The compressive strength of concrete may be determined by the provided equation, which can take into account the age, the temperature history dependence and so on. Equations of tensile strength and modulus of elasticity of concrete are provided as a function of the compressive strength. The tensile strength of concrete to be used for thermal stress analysis shall be the splitting tensile strength.

(5) Creep of concrete

The influence of creep of concrete may be evaluated by the effective modulus of elasticity, which is the product of the modulus of elasticity of concrete and a reduction constant.

(6) Autogenous shrinkage strain in concrete

The autogenous shrinkage strain in concrete may be determined by the provided equation taking into consideration the type of cement, water to cement ratio, and temperature history.

(7) Expansion strain in expansive concrete

The expansion strain in concrete mixed with expansive additive shall be determined taking into consideration the type of cement, the type and dosage of expansive additive, the temperature history dependence, the curing method and so on.

(8) Drying shrinkage of concrete

The drying shrinkage of concrete may be neglected.

4.2.3 Steel and 4.2.4 Ground and bedrock

The thermal and mechanical properties of steel, ground and bedrock are provided.

4.3 Verification based on three-dimensional FEM

4.3.1 Analysis method

Three-dimensional FEM is provided as the standard analysis method for verification of thermal cracking.

4.3.2 Verification method for preventing thermal cracking

The verification for preventing thermal cracking shall be implemented by the following equation.

$$\frac{P_c}{P_t} \le 1.0 \qquad (2)$$

where, P_t: limit value of the thermal cracking probability, to be regarded as 5 %, P_c: thermal cracking probability obtained by the provided method (%).

In practice, however, based on **Fig.2** the thermal cracking index which is equivalent to thermal cracking probability is applicable to the verification. In this case the limit value can be assumed as 1.85.

4.3.3 Verification method for controlling thermal crack widths

The verification for controlling the thermal crack

widths is implemented by the following equations.

$$\gamma_i \frac{w_c}{w_a} \le 1.0 \tag{3}$$

where, w_a: limit value of crack width (mm), w_c; thermal crack width obtained by the following equation (mm), γ_i: safety factor for verification, generally allowed to be 1.0.

$$w_c = \gamma_a \left(\frac{-0.071}{p} \right) \times \left(I_{cr} - 2.04 \right) \tag{4}$$

where, p: reinforcement ratio (%, the ratio of the reinforcement area perpendicular to the crack direction to the intended concrete area), the applicable range of which is 0.25 % to 0.93 %. I_{cr}: thermal cracking index, the applicable range of which is not more than 1.85. γ_a: safety factor to evaluate the thermal crack widths, which shall be 1.0 to 1.7 depending on the performance requirements.

The derivation of Eq.(3) is explained below. The maximum crack widths observed in the experiments are plotted as a function of the thermal cracking index in **Fig.5**. Three regression curves for the groups of specimens with reinforcement ratios of 0.25-0.28%, 0.57-0.66%, and 0.93% are also shown. All of the regression curves intersect at the point of maximum crack width of 0 mm with a cracking index of 2.04. The intersection point is determined by using the data group with a reinforcement ratio of 0.25-0.28% and the curve is regressed as it intersects a point of maximum crack width of 0.05 mm with a cracking index of 1.85. This maximum crack width of 0.05 mm conforms to the allowable crack width with less than 5% probability of thermal cracking. This regression curve crosses the x-axis at a cracking index of 2.04.

The tangent of each regression line can be a function of the reinforcement ratio as it is shown in **Fig.6** and the relationship is a hyperbola. Using this result, the equation for the evaluation of maximum crack width is derived.

4.4 Verification based on simple evaluation method

The simple equations to obtain the thermal cracking index, which have a well-defined scope of application and high reliability, are recommended for wall-type, layer-type and column-type structures.

The simple equation for wall-type structures is introduced as an example. The simple equation is derived from the following process: 1) compile thermal cracking indices with 3D-FEM for wall-type of structures from which the thermal cracking probability is obtained, 2) acquire a regression equation by multi-regression analysis for thermal cracking indices obtained by the 3D-FEM and with variables for the factors that affect strongly influence thermal cracking, and 3) shift the regression equations so as to give the lower limit values of thermal cracking indices obtained from 3D-FEM.

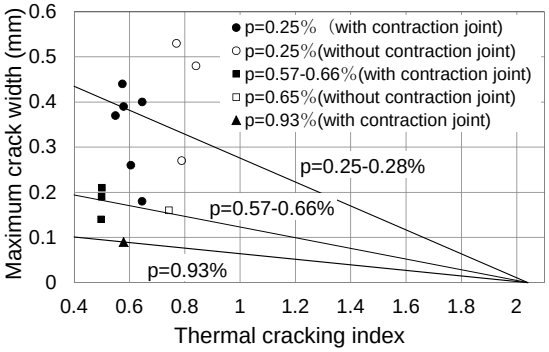

Fig. 5 Estimation method of crack width

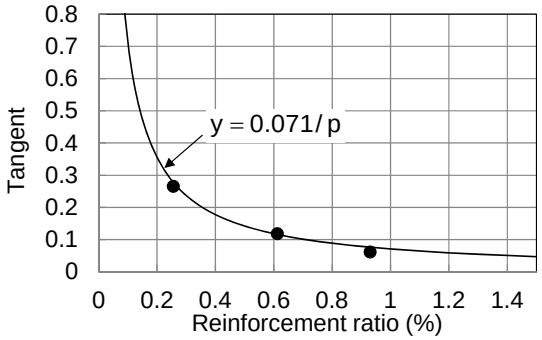

Fig.6 Relationship between reinforcement ratio and tangent of regression line

$$\begin{aligned} I_{mra-WT} &= -1.93\times10^{-2}T_a - 2.80\times10^{-3}D - 1.17\times10^{-2}Q_\infty \\ &+1.55\times10^{-2}r_{AT}{}^{s_{AT}} + 8.72\times10^{-2}log_{10}(H_R) + 0.476f_t \\ &-0.165log_{10}(L/H) + 0.224log_{10}(E_c/E_R) + 0.015 \end{aligned} \tag{5}$$

$$I_{cr} = I_{mra-WT} - I_b \tag{6}$$

where, the meanings of the variables are defined as follows.

$I_{mra\text{-}WT}$; thermal cracking index of wall-type structure calculated by the multi-regression equation

I_{cr}: thermal cracking index calculated by the simple equation

I_b; reduction constant introduced to keep the thermal cracking indices calculated by the simple equation on the safe side as compared with those computed by the 3D-FEM, I_b=0.3 in principle (see **Fig.7**).

T_a: concrete temperature at placement (°C)

D: minimum member thickness (m); wall thickness for wall-type structure

Q_∞: ultimate adiabatic temperature rise

$r_{AT}{}^{s_{AT}}$: constant representing the rate of adiabatic temperature rise, which may be determined in accordance with the provision in the guidelines.

H_R: value denoting the effect of heat radiation from the surface of a member; which is the product of the days up to removal of form and the heat transfer coefficient (W/m^2°C) during that period.

f_t: splitting tensile strength of concrete at 28 days or

91 days cured under water of 20 °C, which may be determined in accordance with the provision in the guidelines.

L/H: ratio of the length (*L*) of member consisting of both old and new concretes to the height (*H*) of the whole member from the bearing ground when the whole member is restrained by the bearing ground.

E_c/E_R: ratio of modulus of elasticity of restrained member concrete to that of restraining bearing ground. Modulus of elasticity of concrete should be that of the cylindrical specimens at 28 days or 91 days under water of 20 °C and may be determined by the equation prescribed in the guidelines.

Eq.(6) was obtained under the following conditions and therefore should not be applied if the actual conditions are beyond the applicable limits.

① Type of cement: ordinary portland cement, moderate-heat portland cement, low-heat portland cement, high-early-strength portland cement, portland blast-furnace slag cement class B, and portland fly ash cement class B

② D: 1.0-5.4m

③ T_a: 4.1-33.7°C

④ Q_∞: 38.5-53.9°C, (obtained from concretes with unit cement content of 245-324 kg/m^3)

⑤ $r_{AT}^{S_{AT}}$: 0.36-1.42

⑥ H_R: 24-232 W/m^2°Cday

⑦ f_t: 2.39-3.52 N/mm^2, (obtained from concretes with water to cement ratio of 42.8-60.0%) The strength control age is 28 days for ordinary portland cement, high-early-strength portland cement, and portland blast-furnace slag cement class B, and 91 days for moderate-heat portland cement, low-heat portland cement and portland fly ash cement class B.

⑧ *L/H*: 0.4-30 (*L*: 3.0-40m, *H*: 0.75-7.2m)

⑨ E_c/E_R: greater than 7

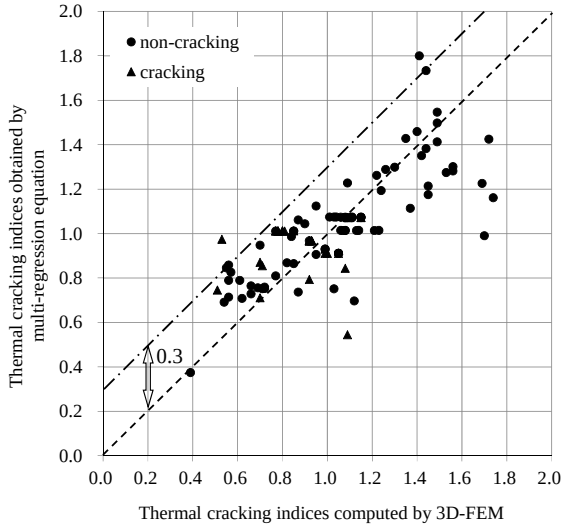

Fig.7 Relationship between thermal cracking indices of wall-type structures obtained by the simple evaluation method and those by the 3D-FEM

Chapter 5 CONSTRUCTION WORKS

5.1 General

The important items to be observed relating to plan and implementation for both execution and quality control are provided. The principles related to execution and quality control to achieve the control target of a mass concrete structure and those implementation procedures are prescribed. An emergency action for an obstacle due to unexpected matters that will lead to difficulties of the achievement of control target in the stages of execution is provided to be taken. The information obtained through execution and quality control shall be recorded and kept to judge the execution quality as well as to make a rational control plan for a similar execution in future.

5.2 Execution plan and quality control plan

Construction documents and quality control documents shall be compiled and the execution plan shall include standards for measures against unexpected rapid climate changes beyond assumptions during execution.

5.3 Implementation of execution

5.3.1 General

The general principles for implementation of execution are provided. Subsequently, the principles for the following each item necessary for mass concrete construction are provided.

5.3.2 Crack control joint

Methods to induce a crack at the planned section and materials to assure water tightness and durability for steel corrosion are introduced.

5.3.3 Production of concrete

Control of a temperature of fresh concrete is regarded as important.

5.3.4 Ready- mixed concrete

Ready-mixed concrete adapted to JIS A 5308 is applied to mass concrete construction in principle.

5.3.5 Transportation, placing and compaction of concrete

Control of temperature during transportation, and uniformity between upper and lower concrete layers during placing and compaction are regarded as important.

5.3.6 Construction joint

It is necessary to consider that the surface areas of vertical and horizontal construction joints are very large.

5.3.7 Curing

Proper materials for curing and measures for excessive weather change should be selected.

5.3.8 Pipe curing

Water leakage from pipe and breakage of pipe must be prevented, and effective control method of circulating water should be adopted.

5.3.9 Selection of forms

Proper form materials should be selected.

5.4 Implementation of quality control

5.4.1 General

The general principles for implementation of quality control are provided. Subsequently, the principles for the following each item necessary for the quality control are provided

5.4.2 Control by measurement

Placing temperature of concrete and temperature history of placed concrete must be controlled below the values determined in control plan.

5.4.3 Control at placing concrete

Rate of concrete placement, sequence of placing, and time interval of overlaying concrete should be managed.

5.4.4 Control of curing

Curing in accordance with execution plan must be implemented, time at form removal should be properly judged, and effective measures for unexpected measured results should be taken.

5.4.5 Control of structure

Realization of planed quality of mass concrete structure must be confirmed.

Chapter 6 INSPECTION

Inspection must be done to confirm whether a control target for thermal cracking determined in the stage of control pan is achieved or not after construction.

6.1 General

The general principles of inspection are provided for inspector, timing and method of inspection, judgment criteria, and countermeasures for rejection of inspection.

6.2 Inspection methods

The principles of inspection method are provided for inspection target relating to a control target, timing of inspection, and precision necessary for measuring crack widths.

6.3 Judgment of inspection results and countermeasures

The principles are provided for indices and their criteria to judge the achievement of control target, elucidation of the cracking causes and the subsequent countermeasures in case of rejection.

6.4 Recording of inspection results

Recording of inspection results as well as subsequent countermeasures is provided to utilize them for the maintenance management of the structure.

Appendices

Appendix A

Standards for various types of cement, which are specified in Japan, USA and EU, are summarized. Qualities of typical cements in Japan, which coincide with those of cement assumed for determining the design values of adiabatic temperature, are shown in comparison with the specified values in the standard. Standards for blast-furnace slag and fly ash specified in Japan and other countries are also summarized.

Appendix B (Reference materials)

Reference materials are provided in order to give detail information from which articles in the guidelines were derived. The reference materials include the following items.

(1) Derivation of relationship between thermal cracking index and thermal cracking probability by three-dimensional finite element method

(2) Derivation of simple evaluation equation for thermal cracking index

(3) Thermal cracking control tests of reinforced concrete wall structures subjected to continuous restraint at the bottom

(4) Relationship between thermal cracking index and maximum crack width

(5) Expansion strain of expansive concrete

(6) Simple method for thermal crack control of RC box culvert with crack control joint

(7) An investigation on thermal crack control of internal restraint predominant structure

(8) Estimation of representative values for adiabatic temperature rise

Appendix C (Case studies)

In case studies, two examples of verification for thermal cracking of a box culvert and a pier-type structure are provided. The verification was carried out in accordance with the guidelines.

3 CONCLUDING REMARKS

JCI guidelines are applicable to mass concrete structures in any country if the design values of concrete produced are determined in a similar way to the guidelines in accordance with the physical and thermal properties and the characteristics of materials in each country. Japan Concrete Institute hopes that the guidelines will be widely applied to mass concrete constructions in foreign countries.

The committee activities will be continued to revise the technological contents in the guideliens and to improve the practical use.

ACKNOWLEDGEMENT

The authors acknowledge the cooperation of the members of the technical committees on “English Version of JCI Guidelines for Control of Cracking of Mass Concrete” and “Revision of JCI Guidelines for Control of Cracking of Mass Concrete”.

REFERENCES

[1] Japan Concrete Institute: Guidelines for control of cracking of mass concrete 2008, ISBN978-4-86384-024-9-C3050, July 2011.

Proceedings of the 3rd JCI-KCI-TCI Symposium on Recent Advancement of Technologies in Concrete Engineering
Japan Concrete Institute, July 2012

EFFECTS OF ALKALI DOSAGE AND CURING TEMPERATURES ON ENGINEERING PROPERTIES OF ALKALI-ACTIVATED SLAG GEOPOLYMER

Tzong-Ruey Yang, Ta-Peng Chang, Ren-You Yang and Zih-Cian Chen

Department of Construction Engineering,
National Taiwan University of Science and Technology (Taiwan Tech), Taipei, Taiwan, R.O.C

ABSTRACT

Previous research results have shown that the alkali-activated slag geopolymer has an excellent early strength. But, after a long period, it is found that the interior of these hardened specimens are prone to produce the thermal cracks resulting from the heat of polymerization such that both the engineering properties and durability of geopolymer are declined. This study investigates the engineering properties of fresh and hardened geopolymer paste that is produced with a constant modulus of 0.6 for sodium silicate, three dosages of alkali activator (3, 5 and 7% of slag by weight), two water-solid ratios (0.33 and 0.36) and three low curing temperatures (5, 15 and 25^{o}C). The research results show that the compressive strength of 50×50×50 mm cubic specimen, dynamic elastic modulus of ϕ100×200 mm cylindrical specimen and drying shrinkage of 25×25×285 mm beam specimen will increase with the decrease of curing temperature. The cylindrical specimens of hardened geopolymer paste with higher values of alkali activator concentrations (5 and 7%) tend to gradually produce more internal and surface cracks after one week sitting in the ambient temperature such that its volumetric stability is hardly maintained.

Keywords: *geopolymer, low curing temperature, drying shrinkage, alkali-activated slag, alkali dosage*

1 INTRODUCTION

In recent years, the civil engineering industry, in response to the trend of environmental protection, began to develop research toward the target of energy saving, carbon emission reduction and reuse of waste such as ground granulated blast furnace slag (GGBFS) (slag)The slag is a by-product from the iron and steel industry with major components of SiO_2, CaO, Al_2O_3 and the other oxides. A large quantity of slag is produced every year in Taiwan and causes environmental problems. In general, the slag is commonly reused to replace a part of cement, especially for making high strength concrete (HSC) and high performance concrete (HPC), considering the improvement of workability and durability of concrete [1-3].

On the other hand, in recent years, a new material technology by using alkali and sodium silicate solution to activate mineral with rich Si, Al or Ca ion (such as metakaolin, fly ash and slag), to manufacture geopolymer after polymerization reaction. This new material, compared with the conventional Portland cement past, has lower energy consumption and low pollution. and exhibits high strength and good resistance to high temperatures, chemical attacks, etc. [4]. Geopolymer is an amorphous to semi-crystalline three-dimensional alumino-silicate materials developed by Davidovits in 1978, which has chemical compositions similar to those of zeolite [5, 6]. Its structure is composed of hydroxide ion of alkali solution precipitation, and Si and Al ion of aluminum silicate to form the polymer bond of Si-O-Al-O which is different from the hydration product of C-S-H gel by mixing water and Portland cement [7].

Previous studies show that the ratio of liquid to solid and the amount of alkaline solution are two significant factors to affect the mechanical properties of geopolymer.

For the influence of the amount of alkaline solution, Brough et al. [8] research results also show that an optimal high alkali hydroxide concentration

can significantly increase the strength and shorten the setting time, but it is liable to let the specimen becoming brittle and vulnerable to weathering, although this fault can be improved by adding other mineral or curing in water. Komnitsas et al. [9] indicate the hydroxide concentration is a vital control factor of strength. Their results show that a high alkali hydroxide concentration could obtain a high compressive strength, but when excess concentration is used, a decrease of the final strength occurs. Chen, G.-Y.[10] indicates an increase of the strength and ultrasonic speed, and a decline of setting time and thermal conductivity with the addition alkali hydroxide concentration. In addition, the drying shrinkage increases 32.7% with the increase of alkali concentration by 3 to 4 %,that leads to an inferior durability. Although geopolymer has good engineering properties, but it produces cracks due to the generation of high temperature from polymerization reaction and leads to the phenomenon of inferior volumetric stability and durability.

Ma et al.[11] indicate an appropriate ratio of liquid to solid assists the reduction of shrinkage due to a lesser emission of water from the polymerization and promotes the engineering properties and volumetric stability of geopolymer. Xu et al.[12] also indicate that the ratio of liquid to solid usually affects the reaction of cement polymerization and its engineering properties. Zheng et al.[13] show the increase of compressive strength from 58 to 110 MPa with decrease of liquid to solid ratio from 0.44 to 0.28, and the setting time increases from 95 min to over 24 hours when the liquid to solid ratio increases from 0.28 up to 0.44. Lin [14] shows that when the liquid to solid ratio increases from 0.45 up to 0.55, the flow value of 70~105 % increases to 115~150 %, and final setting time increases from 35 min to 185 min.

Summarizing the aforementioned research results, this study uses same sodium silicate (water glass) to investigate the effects of various percentages of sodium oxide by weight, ratios of liquid to solid by weight and curing temperatures on the engineering properties of geopolymer such as the compressive strength, dynamic modulus of elasticity and shrinkage of alkali-activated slag geopolymer. The details of experiment work are described at the following sections

2 EXPERIMENT WORK

2.1 Raw materials

The characteristics of raw materials of alkali-activated slag paste used in this study are described as follows:

(1) Sodium hydroxide (NaOH) solution :

The NaOH solution with 10M concentration was prepared by mixing the solid sodium hydroxide flake with deionized water in the laboratory with its chemical compositions shown in Table 1.

(2) Sodium silicate solution (water glass) (Na_2SiO_3):

A commercial sodium silicate solution produced in Taiwan has the chemical composition as shown in Table 1

(3) Ground granulated blast furnace slag (Slag):

A domestic product from CHC Resources Corporation, Taiwan, has the physic properties and chemical compositions as shown in Tables 2 and 3, respectively

Table 1 Chemical compositions of alkaline solutions

	Sodium hydroxide (NaOH)	Sodium silicate (Na_2SiO_3)
NaOH	98.2	---
$NaCO_3$	0.165	---
NaCl	0.0135	---
Fe	0.0004	<0.02
SiO_2	---	25.7
Na_2O	---	8.26

Table 2 Physic properties of slsg

Bulk density (g/cm^3)	Fineness (cm^2/g)	Activity index	
		7 days	28 days
2.8	6000	89.5	119.6

Table 3 Chemical compositions of slag

SiO_2	Al_2O_3	Fe_2O_3	CaO	All other oxides	L.O.I.
34.86	13.52	0.52	41.77	9.57	4.27

2.2 Specimen preparation and testing program

The mixtures of alkali-activated slag geopolymer with two liquid to solid ratio by weight (R_{LS} = 0.33 and 0.36), three percentages of sodium oxide (Na_2O) to slag solid (N = 0.3, 0.5 and 0.7) by weight and three low curing temperatures (5, 15 and 25^{o}C) are shown in Table 4.

The mix procedure is that the slag firstly placed in a mixer, then the 10 M NaOH sodium and silicate solution then was gradually added into the mixer and mixed for 10 minutes. The cubic specimens (50×50×50 mm), cylinder specimens (ϕ50×100 mm) and beam specimen (25×25×285 mm) with each mix proportion were cast. After one day, these specimens were demoulded and cured at room temperature until the ages to conduct the compressive strength test, dynamic modulus of elasticity test, drying shrinkage test, and test of coefficient of thermal conductivity.

The compressive strength test and dynamic modulus of elasticity test were conducted in accord

Table 4 Mix proportion of alkali-activated slag geopolymer

Designation	R_{LS}	N (%)	Solid	Liquid		
			Slag (kg/m^3)	Water glass (kg/m^3)	10M NaOH (kg/m^3)	Water (kg/m^3)
LS33N3	0.33	3	1463	103	149	339
LS36N3	0.36	3	1399	98	142	368
LS33N5	0.33	5	1463	171	248	243
LS36N5	0.36	5	1396	1631	236	278
LS33N7	0.33	7	1463	2391	347	147
LS36N7	0.36	7	1394	228	331	187

with ASTM C39, ASTM C215 and ASTM C593 Standards, respectively.

Finally, the microstructures of each specimen with different mix proportions were also investigated by using scanning electron microscope (SEM) and used to correlate the engineering properties of alkali-activated slag geopolymer

3 EXPERIMENT RESULT AND DISCUSSION

3.1 Workability

The flow test and setting time test were used to evaluate the workability of alkali-activated slag paste. Their results are shown in Table 5, Figs. 1. The smallest values of flow test between 49.5 and87.5 % occur at the highest N of 7 %. With the increase of R_{LS} from 0.33 to 0.36, a substantial increase of flow test value is observed. The smallest values of initial setting times between 29 and 101 minutes and final setting times between 46 and 148 minutes also occur at the lowest R_{LS} of 0.33. With the increase of R_{LS} from 0.33 to 0.36, increase of flow test value up to 30 to 208 minutes for initial setting time and 67 to 360 minutes for final setting time is observed. However, on the contrary, increasing the N values from 3 to 7 % tends to substantially decrease the both setting times for all three sets of mixtures (R_{LS} = 0.33 and 0.36).

Table 5 Flow value and setting of alkali-activated slag paste

	Flow value (%)	Initial setting time (min)	Final setting time (min)
LS33N3	106.3	101	148
LS36N3	150＊	208	360
LS33N5	116.3	45	75
LS36N5	150＊	58	109
LS33N7	49.5	29	46
LS36N7	87.5	30	67

* The fresh mix overflows the circumferential margin of round flow test table

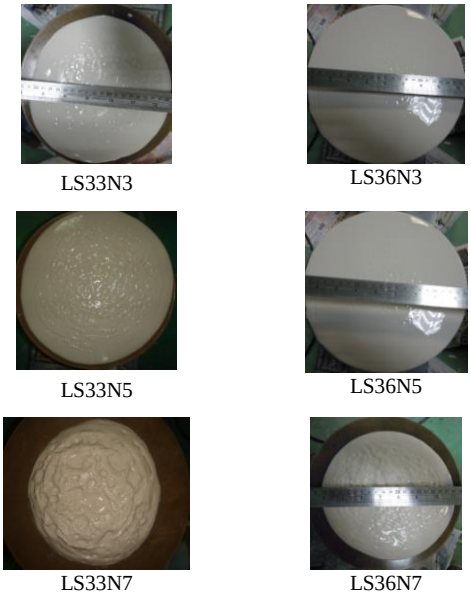

Fig. 1 Flow test of alkali-activated slag paste with each mix proportion

The reason for such opposite variation of these two workability indices could be attributed to the fact that the increase of R_{LS} means an increase of water in the fresh paste such that the flow test values apparently increase too. But too much water tends to dilute the concentration of alkali-activated solution and, subsequently, postpone the alkali-activating speed and increase setting time. On the other hand, increase N values from 3 to 7 % will thicken the concentration of alkaline solution to expedite alkali-activating reaction and reduce both setting times.

3.2 Compressive Strength

The results of compressive strengths for all mixtures at ages of 3, 7, 14, and 28 days are shown in Fig. 2. The highest values at age of 28 days occur at three mixture sets of R_{LS} of 0.33, rather than 0.36, in which an increase of strength from 80.1 to 121.9 MPa at 28 days with the increase of N values from 3 to 7 %. The increase ratios are 52.2 %. At a fixed value of N, it seems that the index of R_{LS} is the key parameter to control the strength. Thus there exists an optimal value of R_{LS} of 0.33 and strength increases

when the *N* value increases to 7 % for the mixture set of LS33N7.

On the other hand, the results of curing temperature test in 28 days shown in Table 6. Under different curing temperature with 5, 15 and 25°C, the compressive strength increase from 71.1 to 134.2 MPa with decrease temperature from 25 to 5 °C, all of mixture set to increase the compress strength with decrease of the curing temperature. The highest strength value of low curing temperature occur to mixture set of LS33N7 like the normal curing temperature condition, the average percentage of increase 1.07 to 21.94 % of all mixture sets.

Table 6 Compressive strengths in different curing temperature at 28 days

(unit: MPa)

	25 °C	15 °C	5 °C
LS33N3	80.1	87.3	94.8
LS36N3	71.1	71.3	86.7
LS33N5	121.7	123.6	123.0
LS36N5	96.5	106.7	108.3
LS33N7	121.9	130.3	134.2
LS36N7	113.4	115.6	119.0

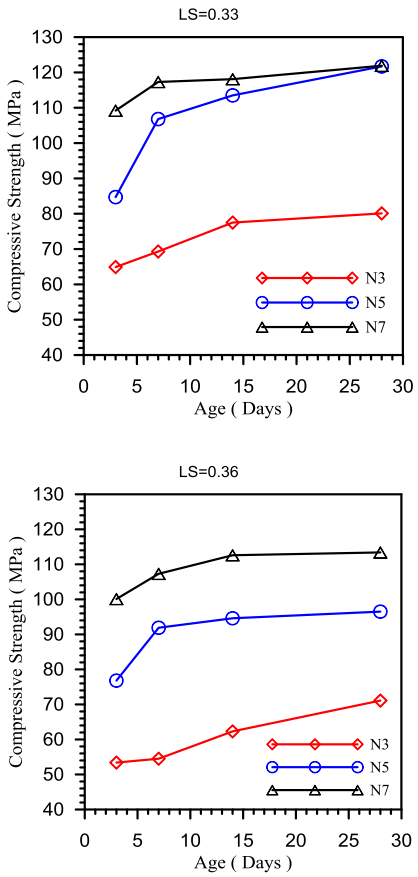

Fig. 2 Compressive strengths at 3, 7, 14, and 28 days

Unfortunately, Table 5 shows that the mixture set of LS33N7 also has a shortest setting time of 29 and 46 minutes. In practice, definitely, this mixture set is not the best choice for the practical application. Fig. 2 also shows that the mixture sets of *N* of 5 % have very high early strengths at 3 days of 76.8 to 84.7 MPa and a longer setting times of 58 and 109 minutes, respectively, for mixture set of LS36N5. This mixture is apparently suitable for repair work.

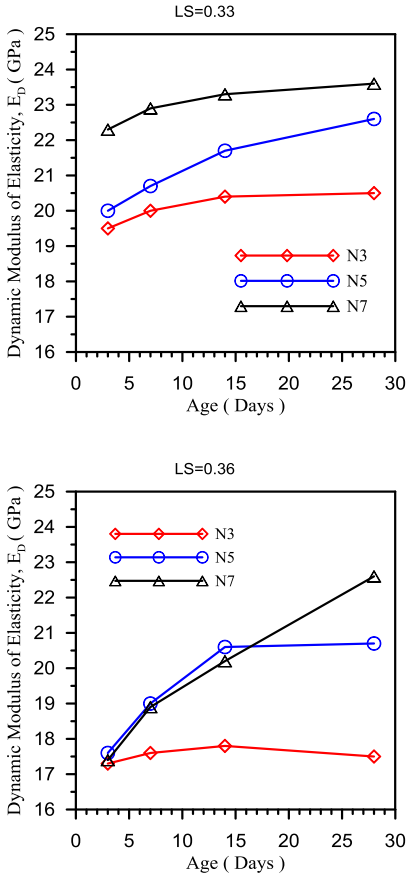

Fig. 3 Dynamic modulus of elasticity at 3, 7, 14, and 28 days

3.3 Dynamic Modulus of Elasticity

The results of dynamic modulus of elasticity tests on various mixes at ages of 3, 7, 14 and 28 days are shown in Figs. 3. Among three mixture sets of N = 3, 5 and 7 %, the highest values of dynamic moduli of elasticity of 23.6 and 22.6 GPa roughly occur at N = 7 %. On the other hand, among three mixture sets of R_{LS} = 0.33 and 0.36, the highest values of dynamic moduli of elasticity of 20.5, 20.0 and 23.6 GPa occur at R_{LS} = 0.33. Thus there exists an optimal combination of R_{LS} and N values to have a highest dynamic modulus of elasticity. But, unlike the considerable increase ratio of compressive strength, the increase ratios here are only between 18 and 29.14 %. In addition, indicate from the low curing temperature result in 28 days shown in Table 7, all mixtures increase dynamic modulus of elasticity when decrease the curing temperature from 25 °C to 5 °C in 28 days, the average percentage of increase 2.9 to 13.65 % of all mixture set.

Table 7 Dynamic modulus of elasticity at 28 days in different curing temperatures

(unit: GPa)

	25 °C	15 °C	5 °C
LS33N3	20.5	22.1	23.3
LS36N3	17.5	18.5	19.1
LS33N5	20.0	20.3	20.7
LS36N5	20.7	21.3	21.3
LS33N7	23.6	23.9	25.3
LS36N7	22.6	22.8	23.6

Table 8 Drying shrinkage at 28 days in different curing temperatures

(unit: mm/mm)

	25 °C	15 °C	5 °C
LS33N3	-0.002482	-0.004998	-0.006991
LS36N3	-0.002350	-0.004559	-0.003593
LS33N5	-0.006417	-0.009334	-0.008657
LS36N5	-0.006951	-0.009220	-0.007666
LS33N7	-0.006526	-0.008362	-0.012599
LS36N7	-0.009003	-0.011064	-0.014878

Table 9 Coefficient of thermal conductivity at 28 days with different R_{LS} and N

(Unit: W/m K)

	R_{LS} =0.33	R_{LS} =0.36
	average	average
N =3	0.675	0.609
N =5	0.639	0.619
N =7	0.643	0.637

Table 10 Thermal conductivity at 28 days in different curing temperatures

(Unit: W/m K)

	25 °C	15 °C	5 °C
LS33N3	0.675	0.623	0.629
LS36N3	0.609	0.607	0.609
LS33N5	0.639	0.632	0.606
LS36N5	0.619	0.617	0.603
LS33N7	0.643	0.642	0.599
LS36N7	0.637	0.633	0.610

3.4 Drying Shrinkage

The results of drying shrinkage tests on various mixes at ages of 3, 7, 14 and 28 days are shown in Fig. 4. The highest values at age of 28 days occur at three mixture sets of R_{LS} of 0.33, rather than 0.36, in which an increase of shrinkage from -0.002350 to -0.009003 at 28 days with the increase of N values from 3 to 7 %. This phenomenon occurs when the increase of R_{LS} makes the concentration of solution to decline that slows the polymer reaction and raises free water so that an increase of shrinkage happens due to an accumulated shrinkage of many pores with -water to vaporize after dehydration procedure of polymerization reaction. In addition, under the same R_{LS}, an increase of N values from 3 to 5 % and 7 % increases the percentage of shrinkage to 159 % and 163 %, respectively in 28 days.

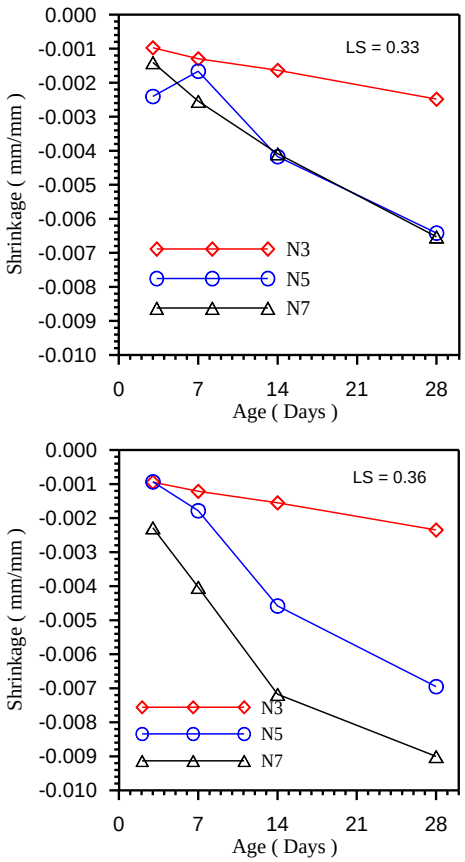

Fig. 4 Drying shrinkage at ages of 3, 7, 14, and 28 days

This result is similar to that of previous research [15]. The reason for this is that when the alkali-activated is the NaOH solution, the number of macropores of alkali-activated slag past is less than those of cement paste, but the numbers of mesopores and micropores are more than those of cement paste. Further, previous results [16, 17] indicate that the silica gel has a high water content and begins to shrink, expelling water from the mass. The shrinkage begins with this syneresis process, when free liquid trapped in the gel is spontaneously expelled. As a result, in this study, the specimen of mixture set of high N values (0.5 and 0.7), easily produces surface cracks after one week.

The results at different curing temperatures at 28 days are shown in Table 8 which indicate that all sets increase the drying shrinkage with the decrease of curing temperature with an average percentage of 10.3 to 181.6 % of increase for all mixture set.

3.5 Coefficient of thermal conductivity

Test results of the coefficient of thermal conductivity for alkali-activated slag geopolymer at

age of 28 days are shown in Tables 9. and 10. When N value is increased from 3 to 7 % and the R_{LS} from 0.33 to 0.36, the decrease ratio of coefficients of thermal conductivity is 5.63 % (from 0.675 to 0.637 W/m·K).

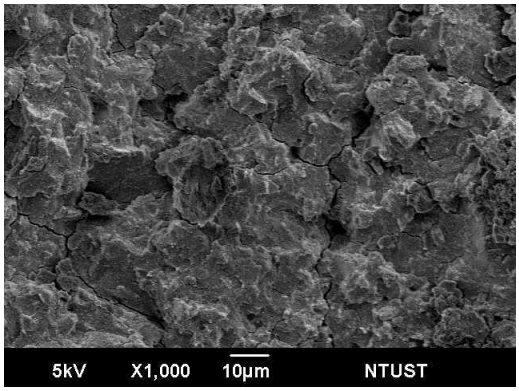

(a) 25 °C

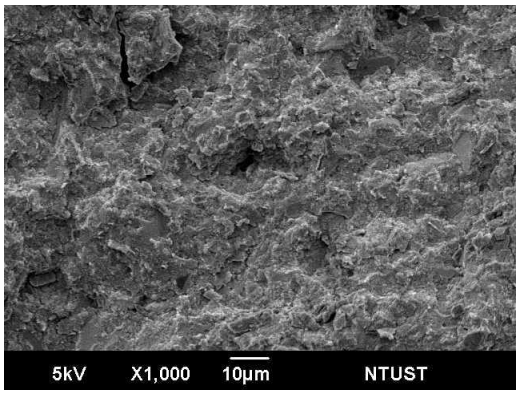

(b) 15 °C

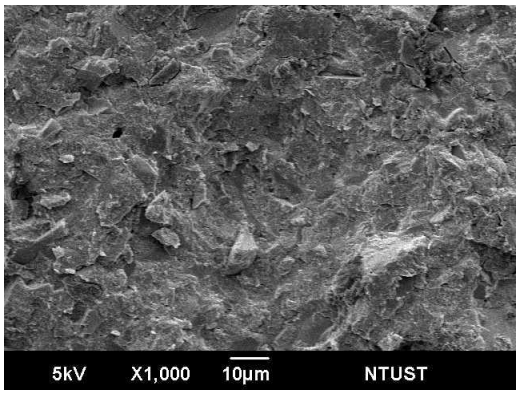

(c) 5 °C

Fig. 5. Typical microstructure of alkali-activated slag with R_{LS} of 0.33 and N of 3 % during curing temperature

The highest coefficients of thermal conductivity of 0.675 W/m·K is lower than that of 2.5 W/m·K for normal weight concrete [18]. Thus alkali-activated slag geopolymer paste can be used as a proper material for heat insulation and fire resistance of building construction. In addition, the coefficients of thermal conductivity of all mixture decrease from 2.58 to 6.81% with curing temperature decreases from 25 °C down to 5 °C. In summary, this result indicates that the influences of R_{LS} and curing temperature on the thermal conductivity are greater than that from N value.

3.6 Microstructure of alkali-activated slag

Typical microstructures of alkali-activated slag geopolymer with R_{LS} of 0.33 and N of 3 % , respectively, during different curing temperature are shown ins Fig. 5. At 25 °C, the coarse surface of alkali-activated slag geopolymer presented is Figure 4(a). As the curing temperature is decreasing to 15 and 5 °C, the coarse surface transform to smooth and denser surface in the microstructure of alkali-activated slag as shown in Figs. 5(b) and 5(c), respectively. Comparing the SEM results with the compressive strengths indicates that the low curing temperature tends to increase the compressive strength.

4 CONCLUSIONS

Based on the experimental results of alkali-activated slag paste presented in this study, the following conclusions can be drawn:

(1) A combined alkaline solution of sodium hydroxide and sodium silicate solution is necessary in the mixture to produce alkali-activated slag paste with good engineering properties.
(2) An optimal value of R_{SL} of about 33 % of the mixture was found to have the higher compressive strength of 121.9 MPa for the N of about 7 %.
(3) The dynamic moduli of elasticity of alkali-activated slag paste are not sensitive to the variations of the amount of sodium oxide and the liquid to solid ratio.
(4) Furthermore, drying shrinkage increase with raise amount of sodium oxide and lower curing temperature, moreover continued stable grow up with curing days.
(5) The alkali-activated slag geopolymer paste has better thermal properties compared with those of normal weight concrete and thus can be used as a proper material for heat insulation and fire resistance of building construction.

ACKNOWLEDGEMENT

This work was carried out under the financial supports of the Taiwan Building Technology Center (TBTC) of National Taiwan University of Science and Technology (Taiwan Tech) and the National Science Council, Taiwan. Courtesy of some experimental data from Mr. Ren-You Yang is also appreciated.

REFERENCES

[1] E. Vejmelková, Keppert, M., Grzeszczyk, S., Skaliński, B., and Černýa, R., "Properties of self-compacting concrete mixtures containing metakaolin and blast furnace slag," *Construction and Building Materials*, Vol. 25, No. 3, pp. 1325-1331 (2011).

[2] O. Boukendakdji, Kenai, S., Kadri. E. H., and Rouis, F., "Effect of slag on the rheology of fresh self-compacted concrete," *Construction and Building Materials*, Vol. 23, No. 7, pp. 2593-2598 (2009).

[3] S. Akyuz and Oner, A., "An experimental study on optimum usage of GGBS for the compressive strength of concrete," *Cement and Concrete Composites*, Vol. 29, No. 6, pp. 505-514 (2007).

[4] J. Davidovits, "Mineral Polymers and method of making them,"USA Paten, No.4, pp.349, 386 (1982).

[5] J. Davidovits, "Geopolymer Chemistry and Applications," Institut Géopolymère, Saint-Quentin, France, pp. 19-36 (2008).

[6] Y. Zhang., Wei, S., and Zongjin, L., "Composition design and microstructural characterization of calcined kaolin-based geopolymer cement," *Applied Clay Science*, Vol.47, No. 3-4, pp. 271-275 (2010).

[7] J. Davidovits, "Chemistry of geopolymeric systems terminology," *Proceedings of Geopolymere 99 Second International Conference*, edited by: Davidovits, J., Davidovits, R. and James, C., Institut Géopolymère, Saint-Quentin, France, pp. 9-40 (1999).

[8] A. R. Brough Holloway, M., Sykes, J. and Atkinson, A., "Sodium sili-cate-based alkali-activated slag mortars: Part II. The retarding effect of additions of sodium chloride or malic acid," *Cement and Concrete Research*, Vol. 30, No. 9, pp. 1375-1379 (2000).

[9] K. Komnitsas, Zaharaki, D. and Perdikatsis, V., "Effect of synthesis parameters on the compressive strength of low-calcium ferronickel slag inorganic polymers," *Journal of Hazardous Materials*, Vol. 161, No. 2-3, pp. 760-768 (2009).

[10] G.-Y. Chen, "Study on the Influence of Mixing Factors of Alkali-Activated Slag Pastes on Their Engineering Properties," (in Chinese) MS thesis, National Taiwan University of Science and Technology (2010).

[11] H.-W Ma, LING, F.-K., YANG, J.,WANG, G., "Preparation of Mineral Polymer from Potassium Feldspar Wastes," *Earth Science - Journal of China University of Geosciences*, Vol. 27, No. 5, pp. 576-583 (2002).

[12] H. Xu, and Van Deventer, J. S. J., "The geopolymerisation of alumino-silicate minerals," *International Journal Minerals Process*, Vol.59, No. 3, pp. 247-266 (2000).

[13] J.-R. Zheng, Zhou, T.-H., Liu, L.-N., "Study on Setting and Hardening of Alkali-Metakaolin-Slag Cementing Material," *Bulletin of The Chinese Ceramic Society*, Vol. 26, No. 6, pp. 1064-1067 (2007).

[14] W.-L. Lin, "Study on Engineering Properties of Alkali-Activated Slag Pastes," (in Chinese) MS thesis, National Taiwan University of Science and Technology (2009).

[15] F. Collins, and Sanjayan, J.G., "Effect of pore size distribution on drying shrinkage properties of alkali - activated slag concrete, " *Cement and Concrete Research*, Vol. 30, No. 9, pp. 1401-1406 (2000).

[16] C. Shi, and Xie, P., "interface between cement paste and quartz sand in alkali-activated slag mortars," *Cement and Concrete Research*, Vol. 28, No. 6, pp. 1619-1625 (1998).

[17] D. Krizan and Zivanovic, B.,"Effects of dosage and modulus of water glass on early hydration of alkali-slag cement," *Cement and Concrete Research*, Vol. 32 , No. 8, pp. 1181-1188 (2002).

[18] S. Mindess, Young, J. F. and Darwin, D., "Concrete," 2nd Edition, Prentice Hall (2002).

Proceedings of the 3rd JCI-KCI-TCI Symposium on Recent Advancement of Technologies in Concrete Engineering
Japan Concrete Institute, July 2012

MATERIAL DESIGN OF CEMENT FOR INCREASED WASTE USAGE AND REDUCTION OF CO_2 EMISSIONS

Etsuo Sakai
Department of Metallurgy and Ceramics Science, Tokyo Institute of Technology, Japan

Eiji Maruya
Technical Development Center, Ube Industries, Ltd., Japan

ABSTRACT

Cement industry contributes to the recycling of resources by using various industrial wastes and by-products in Japan. Furthermore, the industry must facilitate efforts to prevent global warming. Therefore, the comprehensive materials design of cement, in consideration of both environmental impacts and properties, is expected to become increasingly important. This paper describes the influence of mineral admixtures on the paste fluidity and the adiabatic temperature rising characteristic of cement containing high aluminate phase content. The fluidity of the cement paste containing aluminate phase of 12 mass% was improved by adding of mineral admixtures such as granulated blast furnace slag or limestone powder. By increasing of aluminate phase of cement and addition of mineral admixtures, it is possible to enlarge waste usage and reduce CO_2 emission without changing the performance of cement in cement industry.

Keywords: *ordinary Portland cement, aluminate phase, industrial wastes, reduction of CO_2 emission, mineral admixture*

1 INTRODUCTION

The cement industry contributes to recycling by utilizing various industrial wastes and by-products as raw materials or fuels. However, with no hope of increasing the demand for cement in Japan, it is necessary to increase the volume of waste per unit mass in order to maintain the amount of waste consumed. In such cases, increase in heavy metals and changes in setting time by minor components such as fluorine or phosphorus become problems. Industrial waste and byproducts, such as incinerated garbage ash, sewage sludge, construction emission soil and coal ash, contain relatively large amounts of Al_2O_3. The possibility of utilizing wastes is suggested by increasing the aluminate phase content or the interstitial phase content (the total amount of aluminate phase (C_3A) and ferrite phase (C_4AF)) in the clinker [1, 2].

The interstitial phase of cement clinker has a higher rate of initial reaction. Hence, it is feared that an excessive increase in the interstitial phase content of cement clinker could produce concrete with lower fluidity [3, 4] or higher heat evolution. In this case, it will become more important to control the fluidity and the heat liberation of cement, with a growing the use of industrial wastes. A decline in fluidity causes poor concrete works, and increased heat evolution encourages thermal cracking that is harmful to reinforced concrete. It is important to grasp an adiabatic temperature rise of concrete to prevent the thermal cracking of concrete.

However, there have been few studies on the relationship between the properties, such as the fluidity or the adiabatic temperature rise, and various characteristics, such as the composition of the interstitial phase, and the amount of mineral admixtures, in cement in which the interstitial phase content exceeds that in ordinary Portland cement. This paper describes the influence of the interstitial phase composition and the addition of mineral admixtures on the fluidity and adiabatic temperature rise properties of the cement which contained a greater interstitial phase than ordinary Portland cement. In addition, this paper discusses the reduction of CO_2 emission and the usage of industrial wastes and by-products of cement with high C_3A content and mineral admixtures. And this paper proposes cement compositions for increased waste usage and the reduction of CO_2 emission.

Table 1 Mineral composition of cement clinker

Sample		Mineral composition (by Bogue's eq., mass%)				
		C_3S	C_2S	C_3A	C_4AF	Interstitial phase
Control	A9F9	59.2	19.6	9.4	9.0	18.4
High C_3A	A12F9	56.6	19.4	12.1	9.1	21.2
	A15F9	57.9	15.5	15.2	8.6	23.8
High C_4AF	A9F12	59.7	16.5	9.1	11.8	21.0
	A9F14	58.2	15.4	9.1	14.4	23.5

2 INFLUENCE OF INTERSTITAL PHASE CONTENTS ON THE PROPERTITS OF CEMENT

2.1 Synthesis of clinker

Clinker samples with different interstitial phase (C_3A+C_4AF) contents were prepared using special grade reagents and industrial materials including limestone, silica-stone, coal ash, blast-furnace slag, and ferrous slag. These materials and reagents were mixed at specified ratios. The mixture was mixed by adding water, and the dried mixture was molded into a cubic form. Clinkers were sintered in an electric furnace for 30 min at a maximum temperature of 1550°C, and then removed from the furnace at a temperature of 1350°C. Table 1 shows the mineral composition of clinkers calculated by Bogue's equation. These samples were ground using a ball mill until the Blaine specific surface area became 320±5 m^2/kg. Cement samples were prepared by adding gypsum and hemihydrate to clinker and adjusting the SO_3 content to 2%.

2.2 Fluidity

(1)Measurement of fluidity of cement paste

To prepare the paste, the water-cement ratio (W/C) was fixed at 0.32 by mass. The dosage of superplasticizer was 0.048 to 0.192 mass% (as determined by the ratio of solid polymer content to cement). De-ionized water, in which the superplasticizer had been initially dissolved, was added to the cement, and a paste was prepared in a thermostatic chamber set to 20°C. The paste was prepared using a hand mixer for a mixing time of 10 min. After mixing, the fluidity of the paste was evaluated using a concentric-cylinder rotational viscometer (Rotovisco RT20 made by Haake, Inc.; radius of the inner cylinder, 20.71 mm; clearance between the inner and outer cylinders, 0.99 mm; with smooth surface). The time from filling to measurement was minimized to minimize the effect of segregation. The shear stress was increased from 0 to 200 Pa over 3 min, and the apparent viscosity was then measured at 200 Pa.

(2) The influence of content and composition of interstitial phase

Fig.1 shows relation between the interstitial phase content of cement and the apparent viscosity of cement paste. And the relationship between the C_3A or C_4AF content and the apparent viscosity, when the dosage of superplasticizer was kept constant at 0.15 mass%, for cements with or without blast-furnace slag are shown in Fig.2 and Fig.3. The apparent viscosity of the samples with increased C_4AF was roughly constant regardless of the C_4AF content. However, the apparent viscosity tended to increase with increasing C_3A content. These results

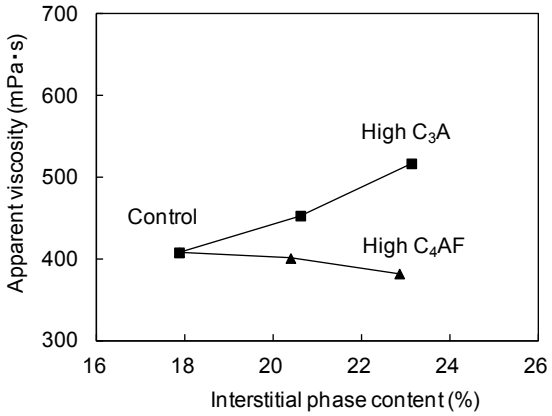

Fig.1 Fluidity of cement paste

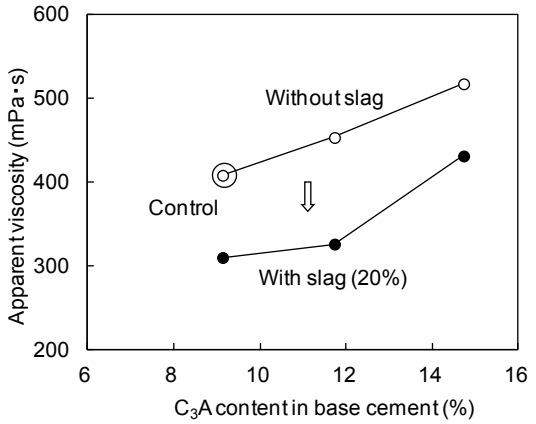

Fig.2 Influence of C_3A content

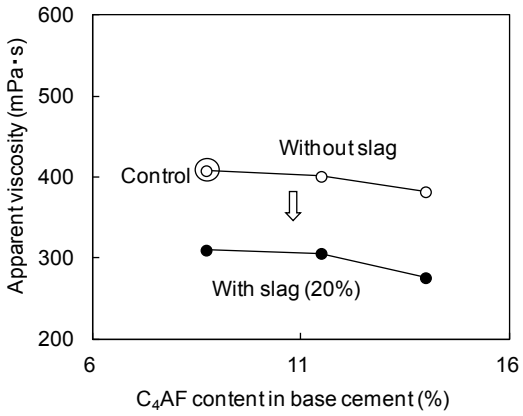

Fig.3 Influence of C_4AF content

were similar to those of previous works [6, 7]. For all samples, the apparent viscosity of paste was decreased by adding blast-furnace slag of 20 mass%. When the C_3A content in the original cement was 12 mass%, the apparent viscosity of cement paste with 20 mass% blast-furnace slag was less than that of the control sample containing no blast-furnace slag. This result indicates that adding blast-furnace slag could be an effective way to control the fluidity of cement with increased interstitial phase content.

2.3 Adiabatic temperature rise of mortar

(1)Measurement of temperature rise of mortar

The adiabatic temperature rise of mortar containing with different C_3A contents was measured by small sample adiabatic calorimeter (Tokyo Riko Corp. Ltd.) as shown in Fig.4. This equipment uses a 30 ml sample in a film case, which is used as a sample container [7]. The adiabatic state can be controlled by adjustment of the temperature of surrounding air to follow that of sample. The fewer the samples, the harder it is to maintain exact adiabatic control. The measurement time was set over 3 days in such a way that the temperature rise becomes moderate. The water-cement ratio (W/C) and sand-cement ratio (S/C) of mortar was fixed at 0.5 and 2.5, respectively. The mortar was prepared by hand mixing because the volume of samples was small. After mixing the cement and water with a mixing time of 2 min, sand was added into the mixture and then stirred for 3 min. The mortar was prepared in a thermostatic chamber set to 20±1°C. After mixing, the mortar sample was set into the sample container, and then thermocouples were inserted for measuring and controlling the temperature. Silicon grease was applied around the insertion site to prevent water dissipation.

This equipment includes temperature control circuit which combines a zener diode and a supersensitive direct amplifier, and has maximum control sensitivity of 5×10^{-3} °C. Four copper-constantan thermocouples are used for local temperature measurement. The adiabatic container is made from aluminum and the insulating material surrounding the film case is polyurethane.

The adiabaticity and responsiveness of this equipment was tested prior to the examination for mortar, by checking the adiabatic temperature rise when Joule heat was supplied electrically. An aluminum block (ϕ25 mm×h 30 mm) wrapped in manganin wire (70 Ω of resistance) was set in the film case, and then applied a voltage of 1.0, 1.3, 1.6 and 2.0 V for 24 hours. The changes in center temperature of aluminum block with time when the supply voltage is changed. It was confirmed that the temperature climbed during Joule heat supplying, and slightly decreased with time after cessation of supplying. This result showed that the equipment was slightly short of adiabaticity. Therefore, the observation data were corrected by calculating the amount of reduction in temperature per unit time from Newton's cooling equation expressed as follows:

$$dT/dt = - k (T - T_0) \qquad (°C/h)$$

T = sample temperature, °C

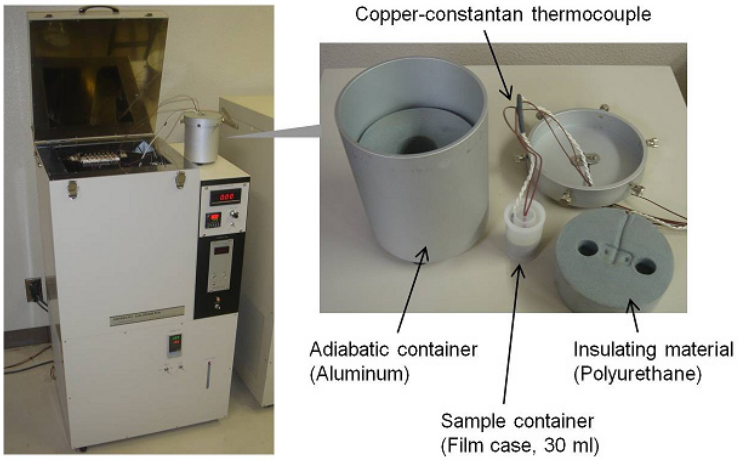

Fig. 4 Description of prototype equipment

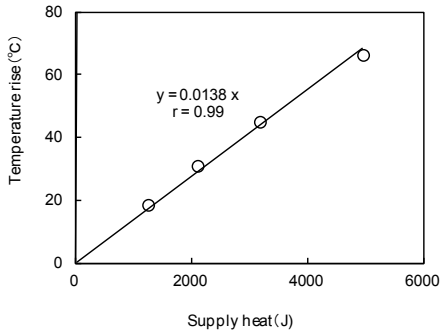

Fig.6 Relation between supply heat and temperature rise

t = time, h
k = coefficient of heat loss, h^{-1}
T_0 = ambient temperature, °C (20°C)

In reference to the amended data, the relationship between supply heat and temperature rise of aluminum block as shown in Fig. 6. It was confirmed that the two had linear relation, and this calorimeter had sufficient ability to evaluate the temperature rise with high accuracy.

(2)Influence of interstitial phase

The change in the adiabatic temperature rise with increasing of the interstitial phase content differed between high C_3A cements and high C_4AF cements. For the mortar sample of high C_3A cements prepared with S/C=2.5, the adiabatic temperature rise curves are shown in Fig.7. When the C_3A content was increased, the temperature rise of samples was equal to that of control sample until 0.6 day. However, since then, the temperature rise increased depending on the C_3A content. Especially with the sample containing C_3A of 15 mass%, the temperature rise in the period of one day reached the same level with control sample obtained in the period of three days, and ultimate temperature rise appeared rapidly.

In contrast, when the C_4AF content was increased, the temperature rise of samples after 0.6 day increased with increasing of C_4AF content, but the differences between samples were small. It was confirmed that changes in adiabatic temperature rise were negligible even when the C_3A content of cement was increased from 9 mass% to 12 mass%, or the C_4AF content of cement was increased from 9 mass% to 14 mass%.

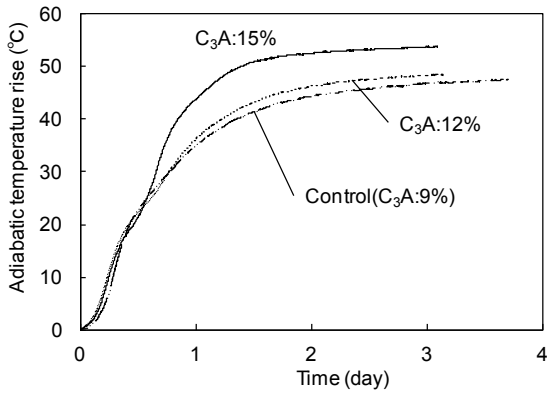

Fig.7 Influence of C_3A content on adiabatic temperature rise of mortar

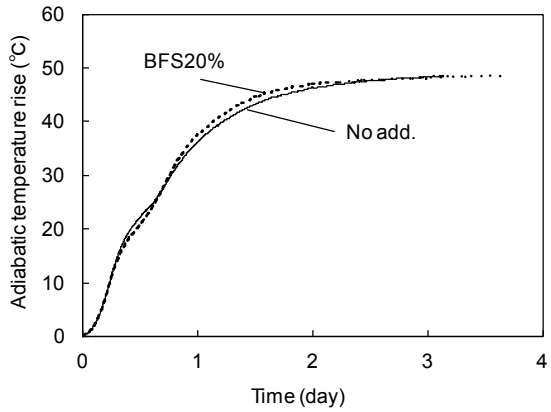

Fig.8 Adiabatic temperature rise of mortar with blast furnace slag

Fig.8 shows the effect of blast-furnace slag on the adiabatic temperature rise for cements with C_3A content of 12%. In case of samples containing large amount of C_3A, the temperature rise of mortar was decreased by adding blast-furnace slag of 20 mass%.

3 THE EFFECT OF MINERAL ADMIXTURES

3.1 Fluidity

In this series, clinker with C_3A content of 9% and 12% were prepared as shown in Table 2. Synthesis condition of these clinker is describes in 2.1.Clinker with C_3A of 9% (control in Table 2) is average mineral composition of commercial OPC in Japan. C_3A content of high C_3A cement is 12%. Table 3 shows the chemical composition of mineral admixtures.

Fig.9 shows the apparent viscosity of the paste

Table 2 Mineral composition of cement

Sample	C_3S	C_2S	C_3A	C_4AF	SO_3	Interstitial phase
Control	52.5	23.1	9.2	8.8	1.84	18.0
High C_3A	47.8	23.8	11.6	8.8	2.36	20.4

(mass%)

Table 3 Physical and chemical properties of mineral admixtures

Symbol	Blaine (m^2/kg)	CaO	MgO	Al_2O_3	Fe_2O_3	Unburned Carbon	Mean Diameter (μm)
LSP5000	494	55.5	0.30	0.01	0.02	-	11
LSP9000	912	55.6	0.31	0.01	0.02	-	4
BFS	424	42.9	5.62	14.8	0.30	-	12
FA	340	3.0	0.75	29.7	6.25	2.86	20

(LSP: Limestone powder, BFS: Blast furnace slag, FA: Fly ash)

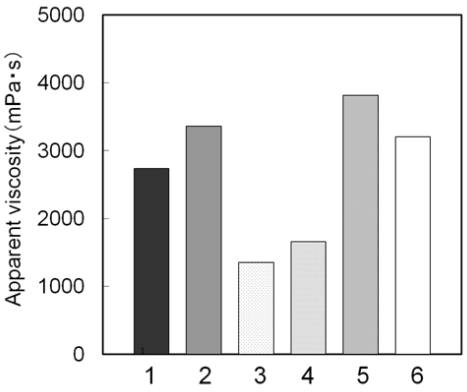

Fig.9 Fluidity of cement paste with various mineral admixtures (1:Control (C_3A9%), 2:High C_3A(12%), 3-6:High C_3A cement with mineral admixtures , 3:LSP5000, 4:LSP9000, 5:FA, 6:BFS)

for cements with or without mineral admixtures. For the high C_3A sample, the apparent viscosity of the paste was decreased by adding blast-furnace slag or limestone powder of 10 mass%. When the limestone powder was added, the apparent viscosity of the paste was less than that of the control sample (C_3A 9%, without mineral admixture), regardless of the fineness of the limestone powder. The fluidity of cement paste with high C_3A content was improved by adding of blast furnace slag more than 20 mass% as shown in 2.1. This is the dilution effect of C_3A by adding of mineral admixture. The fluidity of cement paste is generally expected to improve with the addition of mineral admixture because of the dilution effect. However, the vast improvement by limestone powder could not be explained as resulting from only the dilution of C_3A.

The amount of adsorption of superplasticizer per unit surface area (determined by BET specific surface area) of the hydrated cement with various mineral admixtures is not changed. It was contemplated that paste fluidity would increase with increasing amounts of adsorption of superplasticizer per unit surface area of hydrated cement [8]. However, the apparent viscosity of the paste in this test couldn't be explained by this index. Paste fluidity is often evaluated by the adsorption of the superplasticizer. However, the amount of adsorption calculated from the residual concentration (as mentioned above) also contains the amount of superplasticizer incorporated into hydrates; therefore, it does not represent the true amount of adsorption on the surface. Considering that the superplasticizer incorporated into the cement hydrates could not contribute to improving fluidity, the apparent viscosity of the paste might indicate a large value even when the amount of adsorption of superplasticizer is large. Therefore, we examined the initial heat liberation governing the production of hydrates.

3.2 Relationship between initial heat liberation and paste fluidity

The C_3A of cement reacts rapidly with water.

Fig. 10 Description of prototype equipment

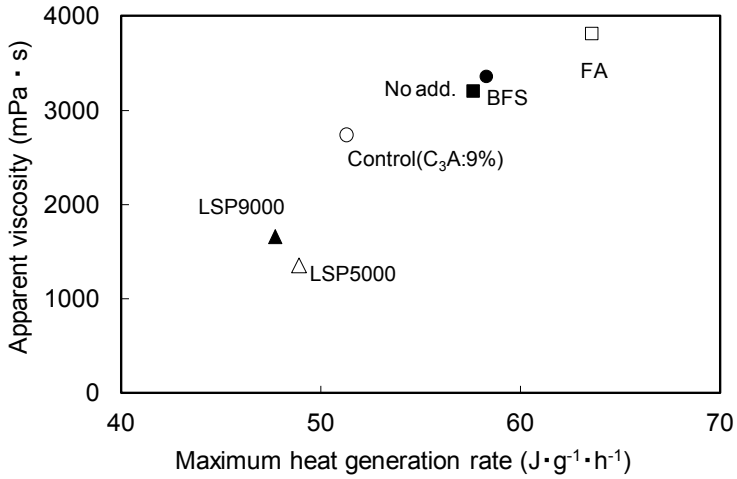

Fig. 11 Relationship between the maximum rate of heat liberation and the apparent viscosity of paste (with 0.048% superplasticizer)

Hence, the measurement of the initial heat liberation of high C_3A cement requires special equipment that has a higher response speed than a conventional conduction calorimeter. Furthermore, such cement paste with low W/C is difficult to mix in an apparatus. Thus, we modified existing equipment (isothermal calorimeter; IC-20 made by Tokyo Riko Corp. Ltd.) by changing the temperature sensor from a thermo module to a thermocouple and by converting the inner agitating blade from a propeller type to a comb type (Fig.10). This equipment to compare the very early reaction rate of the cement sample was used [9].

When the mineral admixture was not added, the rate of heat liberation of high C_3A cement exceeded that of the control sample as expected. When limestone powder of 10 mass% was added, the rate of heat liberation decreased below that of the control sample, as did the apparent viscosity. These results indicate that the very early hydration of high C_3A cement is inhibited by adding limestone powder, and the amount of hydrates is significantly decreased. Limestone powder is known to inhibit the hydration of C_3A because it forms gel-like hydrates containing carbonate ions and the hydrates act as a dense layer on the surface of C_3A [10]. Similarly, the very early hydration of high C_3A cement in this test could have been efficiently inhibited by carbonate ions supplied from limestone powder.

The relationship between the maximum rate of heat liberation of paste and the apparent viscosity of the paste is shown in Fig.11. The apparent viscosity of the paste tended to decrease with a decrease of the maximum rate of heat liberation of paste, and they were well correlated. It would appear that the high C_3A cement rapidly produced hydrates in the very early stage of hydration, so the superplasticizer adsorbed on the surface of cement was incorporated into the hydrates. When limestone powder is added, such action is impaired, and good fluidity could be obtained with less absorption of superplasticizer. There is also more superplasticizer per unit mass of clinker so dispersion will be better assuming it is more important to disperse cement than limestone.

It was found that analysis of fluidity must consider not only the adsorbed amount of superplasticizer but early hydration for the high C_3A cement, and that the rate of very early heat liberation corresponds with the fluidity of paste containing superplasticizer. These results suggested that quality control for fluidity of high C_3A cement could be practiced reasonably by measuring the very early heat of hydration.

3.3 The effect of lime

Limestone powder is very useful for the improvement of fluidity of cement paste with high C_3A. In JIS of ordinary Portland cement, the content of LSP is limited less than 5%. In addition, the problem of thaumasite sulfate attack for limestone Portland cement is indicated [11]. It is necessary that the content of lime stone powder is decreased less than 5% from these points. In our previous report, it was reported that the early hydration of C_3A can be controlled by adding of lime [12].

Fig.12 shows the influence of lime and limestone powder on the fluidity of cement paste with high C_3A. Lime is prepared by the calcination of $CaCO_3$ at 900°C. The apparent viscosity of cement paste with high C_3A is decreased by adding of lime until the dosage of 1%. The fluidity of cement paste with high C_3A is improved further by adding of lime and limestone powder. The fluidity of cement with high C_3A is as same as that of cement with C_3A of 9% by combination of 1% lime and 5% of lime stone powder. If free-CaO in clinker can be controlled, the

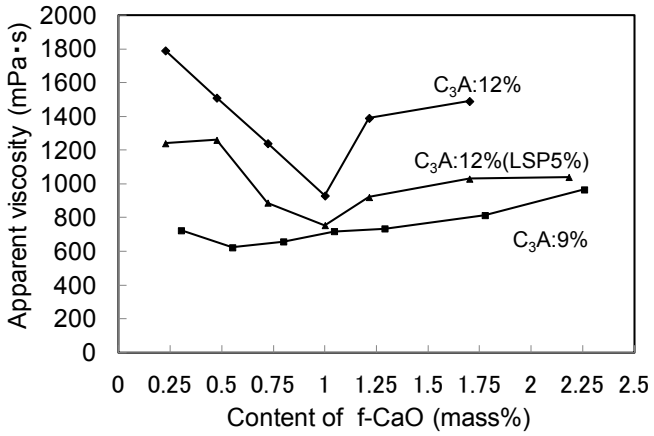

Fig. 12 Influence of lime and limestone powder on the fluidity of cement paste.

fluidity of high C_3A cement can be improved and can be used practically in current JIS.

4 CO_2 EMISSION AND USAGE OF WASTE IN HIGH C_3A CEMENT WITH MINERAL ADMIXTURES

By adding of mineral admixtures, the fluidity and the adiabatic temperature rise of cement with 12% C_3A is as same as that of cement with 9% C_3A which is commercial ordinary Portland cement in Japan. For the improvement of fluidity of cement with 12% C_3A, it is necessary that the dosage of blast furnace slag is over 20 mass% and that of limestone powder is over 10 mass%. Fig.13 shows the CO_2 emission and the waste usage in cement with different C_3A content. For example, the symbol <A9F9> represents 9% C_3A and 9% C_4AF content in mineral composition of cement. These values were calculated based on the data and raw materials of actual cement plant. By adding of mineral admixtures, the CO_2 emission is reduced with replacement ratio of mineral admixtures. Waste usage of cement production can be increased by increasing of interstitial phase (C_3A and C_4AF content). For example, in the case of A12F11 (C_3A 12%, C_4AF 11%) and the additional of mineral admixture, waste usage is 1.12 to 1.4 times of A9F9 that is commercial product in Japan. Compressive strength and length change of mortar are shown in Table 4. Compressive strength and length change of mortar was measured by JIS R 5201 and JIS A 1129-1, respectively.

For compressive strength, A12F11 and A12A9 cement with mineral admixtures meet in 42.5 class cement of ISO. Length change of mortar with A12F11 cement is slightly increased by adding of blast furnace slag cement. But, there are small different in length change of mortar with high C_3A content cement and mineral admixtures compared with that of A9F9. By using these cements, the reduction of CO_2 emission and the increase of waste usage can be realized. These cements are available as soft environmental cement. But, the standard of cement in Japan is different from ISO, and we have no standard for strength class type of cement. More

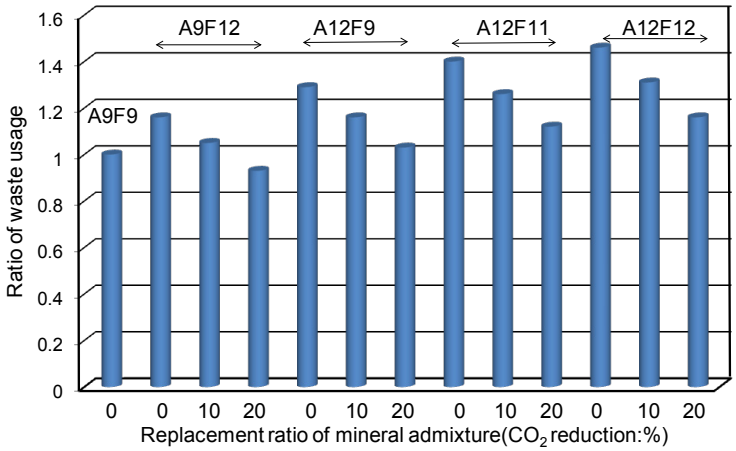

Fig. 13 Example of waste usage and the reduction of CO_2 emission of cement
(A9F9: Average mineral composition of commercial OPC in Japan, Waste: Blast furnace slag, coal ash, sludge, construction emission soil and bunt residue)

Table 4 Properties of mortar containing cement with high C_3A content and mineral admixtures

Cement	Mineral admixture	Compressive strength (N/mm^2)	Length change (10^{-6}) 112d
A9F9	0	52.3	-729
A12F9	BFS 20%	50.3	-793
A12F11	BFS 20%	45.8	-807
A12F11	LSP 20%	42.9	-657

detail investigations containing the investigation for standard of cement are necessary for practical use of these cements.

5 CONCLUSIONS

This study investigated the influence of the interstitial phase composition and the addition of mineral admixtures on the fluidity and adiabatic temperature rise properties of the cement which contained a greater interstitial phase than ordinary Portland cement. And this paper discusses the reduction of CO_2 emission and the usage of industrial wastes and by-products of cement with high C_3A content and mineral admixtures.

Changes in adiabatic temperature rise were negligible even when the C_3A content of cement was increased from 9 mass% to 12 mass%, or the C_4AF content of cement was increased from 9 mass% to 14 mass%. In case of samples containing large amount of C_3A or C_4AF, the adiabatic temperature rise of mortar was decreased by adding blast-furnace slag of 20 mass%.

By adding of mineral admixtures such as blast furnace slag and limestone powder, the fluidity of cement with high C_3A content can be improved. Limestone powder exhibited much more improvement in fluidity than blast-furnace slag and fly ash. For the heat liberation in the very early stage of hydration, the hydration of cement was found to be inhibited by the addition of limestone powder using equipment modified to respond to thermal change more rapidly than a conventional conduction calorimeter. The rate of very early heat liberation was highly correlated with the apparent viscosity of paste containing superplasticizer. This result indicates that adding limestone powder could be an effective way to control the fluidity of cement with increased C_3A content.

By using cements containing 12% C_3A and 9-12%C_4AF contents and mineral admixtures such as blast furnace slag and limestone powder, it is possible to enlarge waste usage and reduce CO_2 emission without changing the performance of cement in cement industry. More detail investigations are necessary for thaumasite formation of sulfate attack of cement with limestone powder.

REFERENCES

[1] H. Uchikawa and H. Obana,: World Cement, Vol.26(11), pp.33-pp36,1995.

[2] M.Osaki: Proceedings of Annual Meeting of the Ceramic Society of Japan, pp.265,2000, in Japanese

[3] N.Spiratos, M.Page., N.P.Mailvaganam, V.M. Malhotra and C. Jolicoeur, “Superplasticizers for Concrete: Fundamentals, Technology, and Practice”; Supplementary Cementing Materials for Sustainable Development Inc., Ottawa.2000

[4] E.Sakai, K.Yamada and A. Ohta, J. Advanced Concrete Technology, Vol.1 (1), pp.16-pp.25.2003

[5] E. Maruya, M. Osaki, E. Sakai and M. Daimon:Cement Science and Concrete Technology, Vol.57, pp.38-pp44,2003 in Japanese.

[6] E. Maruya, M. Osaki and H. Igarashi: Transactions of the Materials Research Society of Japan, Vol.31, No.2, pp.329-pp.332.2006

[7] E. Maruya, E. Sakai, S. Hagiwara and M. Daimon: J. Advanced Concrete Technology., Vol.7(3), pp.367-pp.373.2009

[8] K. Yamada and S. Hanehara: Proceedings of the 11th International Congress on the Chemistry of Cement, Durban, pp.538-pp.549, 2003.

[9] E. Maruya, R. Ichinose and E. Sakai: Proceedings Ninth ACI International Conference on Superplasticizers and Other Chemical Admixtures, Seville, pp.347-pp.356, 2009.

[10].M. Daimon and E. Sakai: Proc. Shigeyoshi Nagataki Symposium on Vision of Concrete: 21st Century, pp.41-pp.54.1998.

[11] N.J. Crammond, Cement & Composite,Vol.25, pp.809-pp.818, 2003.

[12] E. Sakai, J.K.Kang and M.Daimon: Cement Science and Concrete Technology, No.56,pp36-pp.41,2002

Proceedings of the 3rd JCI-KCI-TCI Symposium on Recent Advancement of Technologies in Concrete Engineering
Japan Concrete Institute, July 2012

CRACK SELF-HEALING CONCRETE INTRODUCING SEMI-CAPSULATION EFFECT BY GRANULATION OF INGREDIENTS

Toshiharu Kishi and Tae-Ho Ahn
Institute of Industrial Science, The University of Tokyo, Japan

Takao Koide
Cement & Concrete Research Laboratory, Sumitomo Osaka Cement Ltd., Japan

ABSTRACT

A fundamental study on whether improvements in performance of self-healing agent whose main component is geo-materials can be achieved by mixing it into granules instead of that in powder form, for the purpose of preventing leakage of water through cracks was conducted. The points of concern are the rapid slump loss compensation by the granulation of self-healing agents and the long-term retention of the self-healing capability. It was found that semi-capsulation by granulation of self-healing ingredients improved the slump retention capability and the water leakage prevention effect through cracks.

Keywords: *Crack, Self-healing concrete, Water leakage, Granules*

1 INTRODUCTION

In this study, in order to apply materials with self-healing capability to the field application, the essential fresh properties of ready-mixed concrete with self-healing capability are examined and the recovery of water tightness to the leakage through penetrating cracks are examined in the laboratory. Cementitious composite materials with self-healing capability were prepared in order to develop autogenous healing concrete based on the basic design concept as reported in the previous paper [1]. Concretes including several self-healing ones and plain one for control were produced at a ready-mixed concrete plant for the other field test and the only experimental investigations conducted in the laboratory is reported in this paper. This study focused on the following issues, such as improvement of workability on self-healing concrete by granules and performance evaluation of crack self-healing concrete incorporating various granules.

2 EXPERIMENTAL PROGRAMS

2.1 Materials

The self-healing agents were prepared based on self-healing performance as reported in the previous research [1]. A crack with a width of 0.2 mm was induced in hardened self-healing cementitious paste with 45% W/C at the curing age of 120 days, and from the 3 days after water immersion, re-hydration products formed in the crack and crack healing was confirmed. This self-healing agent includes expansive agent, geo-materials and chemical agent and they are commercial products produced in Japan. These ingredients were selected to fabricate granules in this research.

2.2 Preparation of granules based on self-healing agents

Fig. 1 shows the concept of crack self-healing in hardened concrete incorporating granules. When a crack occurs in hardened concrete, granules break up, crystals precipitate through the reaction, dissolution, diffusion, etc., of components contributed to the self-healing agent through water supply in the cracked parts, and the crack closes. The two challenges of slump loss compensation and long-term preservation of the self-healing capability of ready mixed concrete are thought to be solvable through the use of such granules. An additional issue is that self-healing agent is traditionally incorporated in concrete through partial substitution of cement, so that mixing in large quantities of self-healing agent in powder form in ready mixed concrete causes reduced compressive strength besides slump loss. By contrast, in the case of granules, the self-healing agent is done through fine aggregate substitution, which is thought to improve compressive strength also.

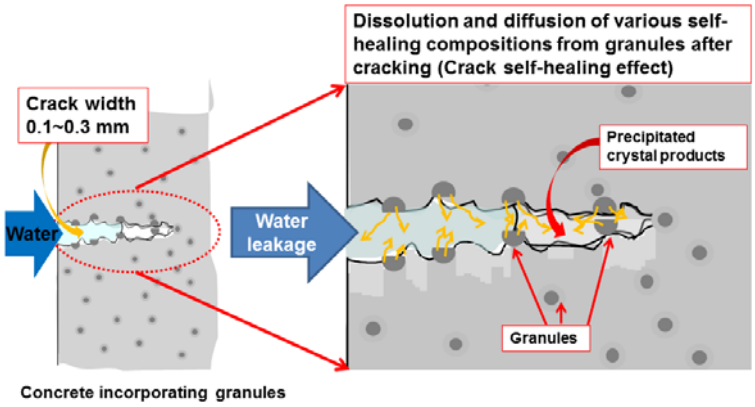

Fig. 1 Application concept of self-healing concrete incorporating granules for the water tightness

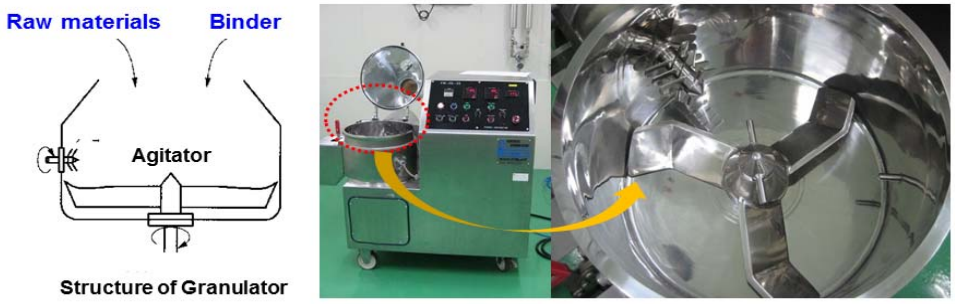

Fig. 2 Outline of the granulator

Table 1 Mix-proportions of granules (Unit: %)

Sample	Self-healing agent			Binder		*PVA fiber (kg/m^3)
	Expansive agent	Geo-materials (A, B type)	Chemical additives	Low-heat portland cement	Water + Ethanol	
EG	O	O	O	42	18	0.08
	42					
NEG	-	O	O	49	18	0.08
	33					

The diameter of most of the granules manufactured with the mortar mixer was on the order of 300 μm or approximately 5 mm, greatly differing from the particle size distribution of fine aggregate used for concrete. This is thought to be due to the shape of the blades of the mortar mixer and other factors not being well suited for granulation. It was thus decided to use a granulator of the type used to produce pharmaceutical and food products (capacity: 25 l, processing amount: 12 kg/batch, processing time: 10 minutes/batch) to produce granules as shown in Fig. 2.

Table 1 shows the mix-compositions of the granules. Two types of granules, with and without expansive agent (EG and NEG) were fabricated. Low-heat portland cement, which has self-healing capability, was used as the cement for binding purposes. With regard to the NEG mix, the reduction in expansive agent in the self-healing agent was made up with low-heat portland cement. For the liquid binder, a mixture containing 70 vol% water and 30 vol% ethanol, based on the above-mentioned previous results [2], was used. As fiber, PVA short fibers (27 μm diameter × 6 mm length, 1.3 /cm^3 density), which have been reported to contribute to self-healing of cracks in the ECC (Engineered Cementitious Composites), were added in the proportion of 0.08 kg/m^3. [3]

Fig. 3 shows the manufacturing process of granules. Following curing under sealed condition for 7 days, the manufactured granules were impregnated with a fatty acid saturated ethanol solution and then underwent air drying outdoors to evaporate the ethanol, leaving a thin impermeable membrane of fatty acid on the surface of the granules.

Fig. 4 (a) and (b) show the powder and granules of self-healing agent and Fig. 4 (c) shows the sieve analysis results.

The granules manufactured with the granulator shown in Fig. 2 were within the normal size range for fine aggregate of JIS A 5308 and confirmed to have a size distribution equivalent to that of fine aggregate.

2.3 Fabrication of new self-healing concrete incorporating granules

In order to fabricate the self-healing concrete (SHC) incorporating granules, various concretes were mixed at the actual ready-mixed concrete plant. Table 2 shows the mix proportions of concretes; a W/C ratio of 57.9% and an S/A ratio of 45.2% were applied to all concretes (target strength of plain control concrete = 24 N/mm^2, target slump = 12 cm, and target air content = 4.5%). The three self-healing agents such as one powder type and two granules types were substituted for fine aggregate in the amount of 40 kg/m^3 for each type. The dosage of super plasticizer (SP) was C×0.8% for plain concrete and C×3.0% for the three types of SHC.

By measuring the slump and air content of concrete before and after discharge, the slump improvement effect obtained through the use/non-use of granules was investigated. Concrete 10Φ x 20 cm cylinders were prepared after conducting the concrete slump test for the compressive strength test and the water tightness test of cracked concrete in the laboratory. The compressive strength was measured by JIS 1108 after 7, 28, and 270 days.

2.4 Verification methods for the recovery of water tightness on fabricated self-healing concrete

In case of the water tightness test, the specimens

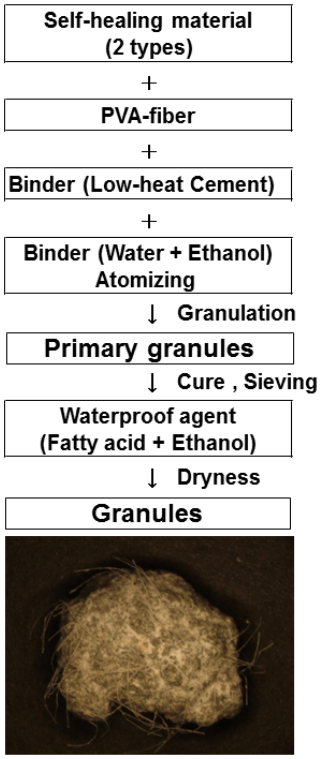

Fig. 3 Manufacturing process of granules with PVA fiber

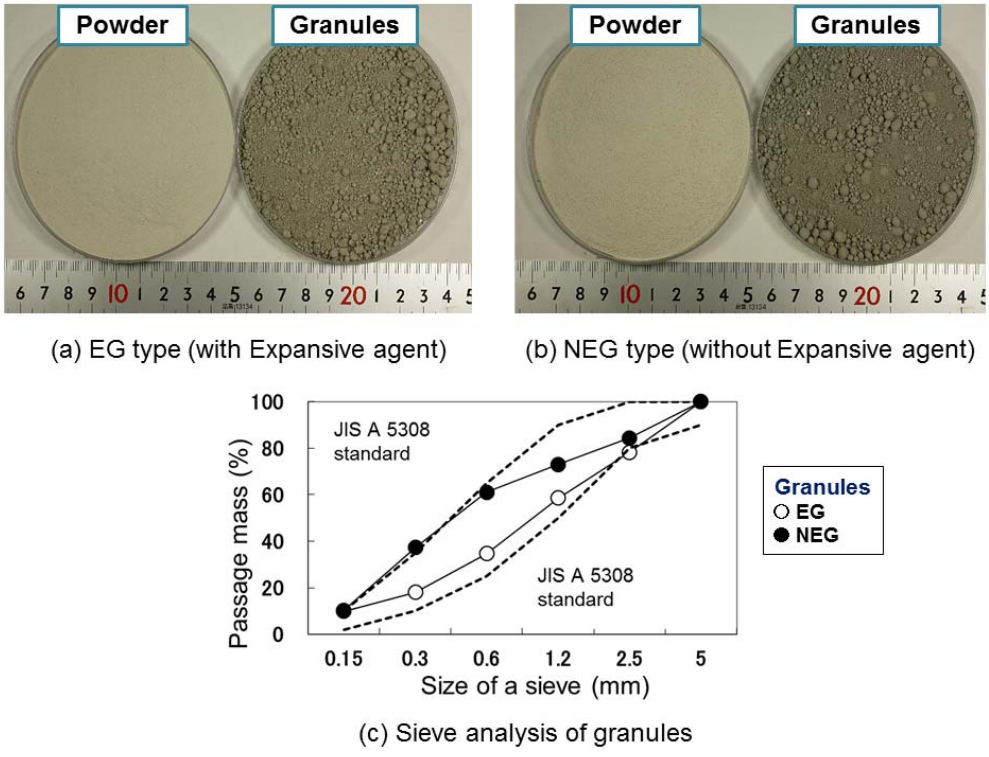

(a) EG type (with Expansive agent)

(b) NEG type (without Expansive agent)

(c) Sieve analysis of granules

Fig. 4 Fabrication of EG and NEG type granules (a) EG type (with expansive agent) (b) NEG type (without expansive agent) (c) Sieve analysis of granules

Table 2 Mix-proportions of concrete

Sample	W/C (%)	S/A (%)	Air (%)	Unit (kg/m^3)					
				Water	Cement	Self-healing agent	Fine Aggregate	Coarse Aggregate	SP
Plain	57.9	45.2	4.5	168	290	-	826	1019	2.3
P-SHC						40	786		8.7
EG-SHC									8.7
NEG-SHC									8.7

(P: powder type self-healing agent of EG, EG & NEG: granules type self-healing agent)

(a) Water permeability test (b) Measurement of water leakage

Fig. 5 Permeability test setups (a) Water permeability test (b) Measurement of water leakage

were split longitudinally using a compression tester. The fractured surfaces of the split specimens were cleared of fine particles through the use of high pressure air to suppress the occurrence of clogging favorable to self- healing (in order to make severe condition). Then, using two steel hose clamps to restrain each specimen, the crack width was adjusted between 0.2 mm and 0.3 mm under digital microscope observation. Crack width measurement was done at a total of six points, three at the top end face and three at the bottom end face of the specimen. A vinyl chloride pipe measuring 100 mm in diameter and 100 mm in height was attached to the top end of the specimen to provide a water head of approximately 80 mm, and the space between the specimen and vinyl chloride tube as well as the cracked areas along the side of the specimen were closed up with silicone resin. The laboratory water permeability test was done by pouring tap water into the vinyl chloride tube in a 20°C environment and comparing the degree of self-healing of the cracks yielded by the granules of self-healing material by recording water leakage over time.

The water tightness test in the laboratory was conducted by maintaining a constant pressure, continuous flow state in the vinyl chloride pipe as shown in Fig. 5 (a), and measuring for five minutes the amount of water leaking from the bottom end face of the cracked specimens on days 0, 1, 3, 7, 14, 21, and 28, counting from the time the vinyl chloride pipe was filled with water. As shown in Fig. 5 (b), measurement was done by attaching a funnel to the bottom end face of the specimens and attaching this assembly over a graduated cylinder to allow measurement of the amount of water leaked from the cracked bottom end face only. The water pressure applied to the specimens when the vinyl chloride pipe was filled with water was calculated to be around 0.8 kPa. The relationship between changes in the water leakage amount and changes in pH was determined through measurement of the pH of the leaked water with pH test paper. The water leakage prevention effect of the granules and powder of self-healing agent was also investigated on a comparative basis before and after the permeability test by checking for the presence of precipitates in the cracks and cross-sections of the specimen with a digital microscope.

3. RESULTS AND DISCUSSION

3.1 Effect of granules on the workability and compressive strength of self-healing concrete

Table 3 shows the effect of granules on the workability of self-healing concrete. Compared to P-SHC, which does not incorporate granules of self-healing agent, EG granules and NEG granules present improved slump values. In case of EG granules, material segregation was occurred partially, because of an excessive dosage of superplasticizer (SP). From these results, the addition of self-healing

Table 3 The effect of granules on the workability of self-healing concrete

Sample	Slump (cm)		Air content (%)		Temperature (℃)	
	Initial (5 min)	Final (30 min)	Initial (5 min)	Final (30 min)	Initial (5 min)	Final (30 min)
Plain	14.0	12.0	5.0	3.5	14	15
P-SHC	16.5	14.5	10.2	5.2	14	15
EG-SHC	23.5	SF40	3.8	3.4	14	15
NEG-SHC	19.0	19.0	2.0	3.4	14	15

SF: Slump Flow

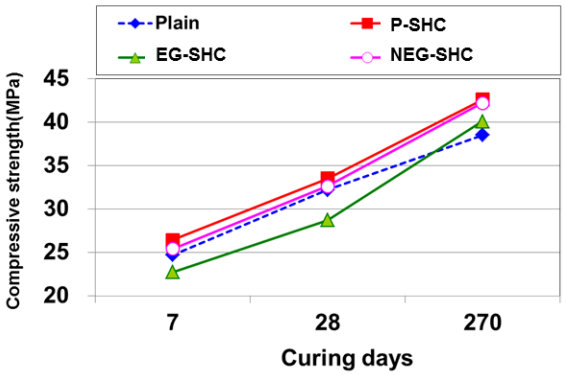

Fig. 6 Effect of granules on the compressive strength

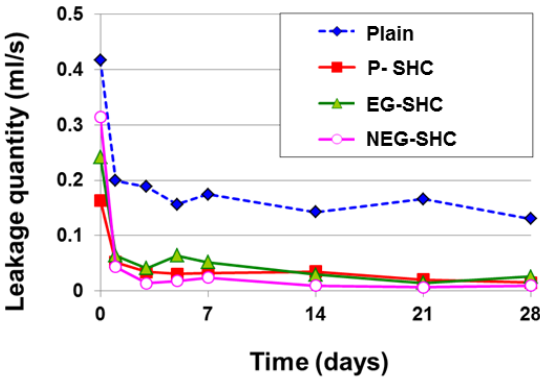

Fig. 7 Effect of granules on the recovery of water tightness under water leakage

agent in the form of granules to concrete is considered to compensate slump loss. With regard to air content, while the incorporation of self-healing agent in powder form tends to cause excessive air content at the initial stage, the incorporation of granules keeps air content at a level comparable to that in plain concrete.

Fig. 6 shows the results of the compressive strength of the various concretes. No differences in compressive strength caused by the use or non-use of granules were observed at 7 days curing. Neither was a decline in compressive strength observed at 28 days and 270 days curing; on the contrary, a slight increase in strength compared to the plain concrete was seen. Based on these results, it was found that the substitution of self-healing agent for fine aggregate in the amount of 40 kg/m^3 does not have an adverse effect on compressive strength.

In the case of EG granules, compressive strength was lower than that of plain concrete, which is thought to be due to an excessive slump value (material segregation). However, at 270 days curing, the compressive strength was somewhat higher than that of plain concrete, suggesting that the strength decrease is only in the initial stage.

3.2 Effect of granules on the recovery of water-tightness in cracked concrete

Fig. 7 shows the time-dependent changes in water leakage amount observed in the laboratory test and these date are the averages of three specimens for each mix proportion.

One can see in Fig. 7 that although the crack width of the specimens was adjusted between 0.2 mm and 0.3 mm, there is disparity among the initial leakage values. This is thought to be due to the differences not only in the topography of the crack surfaces (fracture surfaces resulting from splitting) but also in the chemical characteristics among the specimens.

Compared to plain concrete, SHC incorporating self-healing agent showed a tendency to have lower initial leakage values, whether or not granules of self-healing agent were included, and whether or not the granules contained expansive agent. This is considered to be due to the water cutoff effect obtained from the initial phase through the expansion and the swelling effects of the geo-materials included in the self-healing agent. Examination of the subsequent time-dependent changes in leakage reveals a large drop in leakage in the first day of permeation through the effect of water absorption, etc., even in the plain concrete, and the continuation of this effect until the fifth day, but no major change was seen after that and the leakage value never became nil. On the other hand, for SHC too, the leakage value greatly dropped in the first day of permeation, whether or not the concrete included granules, and the leakage value went on declining on the 14th and 21st day of permeation. The leakage value was finally observed to become almost nil on the 28th day after water permeability test.

Fig. 8 shows the time-dependent changes of the pH value of the leaked water immediately after leakage measurement and these data are the averages of three specimens for each mix proportion. In Fig. 8

plain concrete shows that the pH value of the leaked water dropped sharply from approximately 12 immediately after permeation to approximately 8 on the first day, and went on to decline to approximately 7. On the other hand, in the case of SHC, the changes in pH were less pronounced whether or not granules of self-healing agent and expansive agent were included. The pH value of the leaked water was approximately 11 on the first day of permeation, went on to decline to 8 on the 14th day, and remained level after that.

From these results, it is thought that in the case of SHC, the movement of water inside the cracks was suppressed by the expansion of the swelling materials, leaving the other self-healing components, cement hydrates, etc., in place rather than flushing them out and thus allowing them to heal the cracks, thus demonstrating a high water cutoff effect.

Moreover, based on the fact that similar changes were observed for SHC up to the 14th and 21st day after water permeability test as shown in Fig. 7 and Fig. 8, it is considered possible to evaluate the retention of self-healing components and the water cutoff performance through measurement of the pH of the leaked water. In order to confer to SHC the full water cutoff effect, it is important to suppress leakage from the initial leakage phase through the use of swelling materials, etc. This allows the long-term retention of the self-healing components in order to obtain a strong water leakage prevention effect.

Fig. 9 shows the changes in the cracks before and after water permeability test of specimens. In the case of plain concrete any product was not observed as shown in Fig. 9 (a). On the other hand, in the case of P-SHC, EG-SHC and NEG-SHC the precipitation of self-healing products were clearly observed in cracks as shown in Fig. 9 (b), (c) and (d), respectively.

Fig.10 shows a cross-section of samples after water permeability test. Surfaces of the cross section 10 cm, 15 cm, and 20 cm from the water inflow site (from top and bottom) were investigated by the digital microscopy.

From these results, it was found that in the case of P-SHC, which has high water leakage prevention capacity, ample crystals precipitated so as to cover the surface of the fine aggregate exposed at the split surfaces. The amount of crystal precipitation tended to be particularly pronounced for SHC-granules, compared to SHC-powder. This suggests that the use of self-healing agent in the form of granules makes it possible to reduce the amount of self-healing agent for obtaining the requisite water leakage prevention performance, compared with the use of self-healing agent in powder form.

Based on the laboratory test results, specimens for 8 months demonstrated ample water leakage prevention effect whether or not they included granules of self-healing agent and expansive agent. Therefore, at the approximately 8 months curing, the long-term retention effect of the self-healing component in the form of granules could not be confirmed.

However, the fact that the concrete specimens that incorporated the self-healing agent whose principal component was geo-materials used in this study

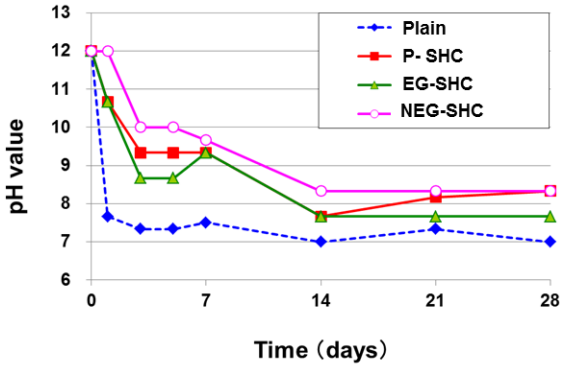

Fig. 8 Effect of granules on the pH of water after permeability test

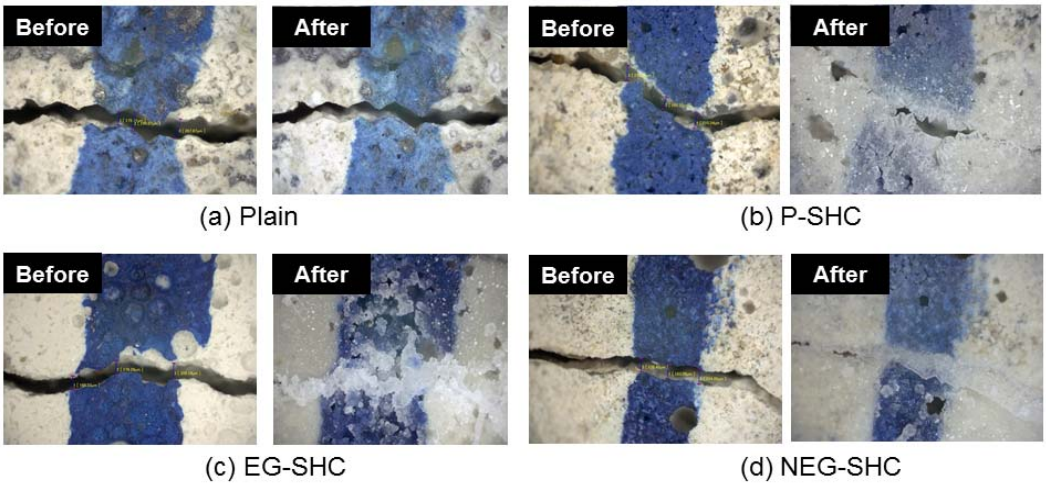

Fig. 9 Self-healing behavior of concrete incorporating various self-healing agent

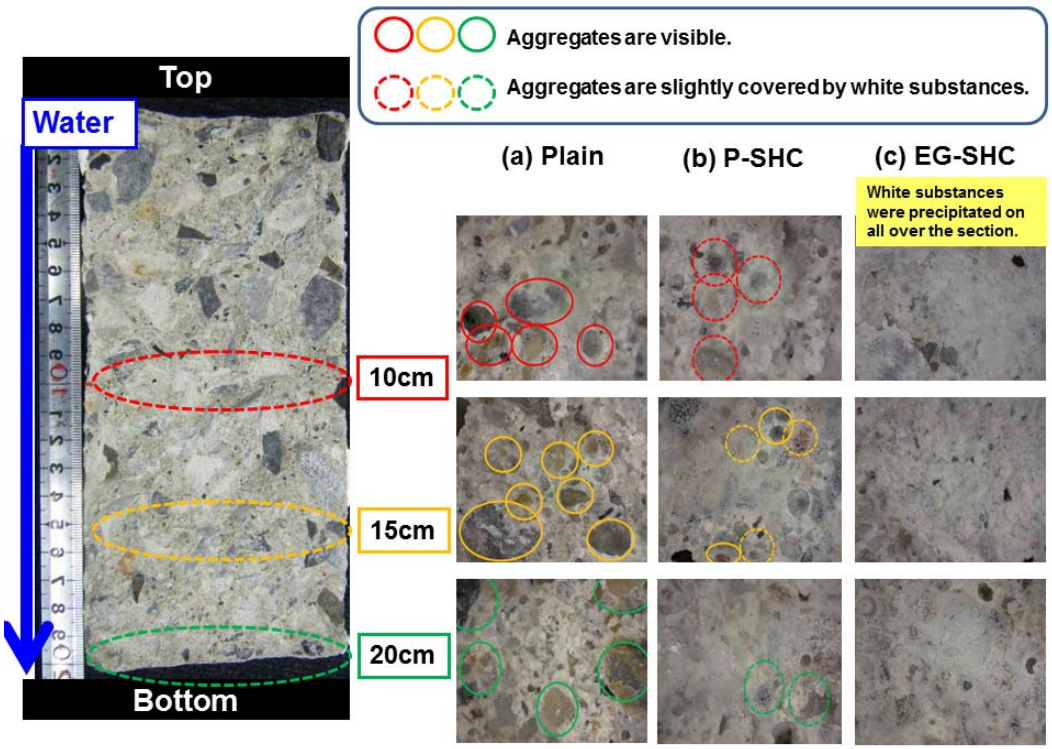

Fig. 10 Cross section of specimen after water permeability test

processed in the form of granules rather than powder exhibited a larger amount of crystalline precipitate on their cross-sections even though the amount of self-healing agent was lesser, indicates that the performance of SHC can be improved by processing self-healing agent into granules.

4 CONCLUSIONS

In this study, the new method of self-healing design to improve water tightness in cracked concrete was suggested, and the self-healing properties of cracked concrete using various self-healing agent (powder and granules) were investigated. The following conclusions can be drawn from the experimental study.

(1) Binder such as low-heat cement, water, and ethanol was added to powder of self-healing agent consisting principally of geo-materials that have high reactivity with water to achieve granulation, yielding granules with a size distribution comparable to that of fine aggregate used for concrete.
(2) The 40 kg/m^3 admixture of self-healing agent in granule form as a fine aggregate replacement was found to improve the workability of ready mixed concrete without lowering compressive strength, compared with using self-healing agent in powder form.
(3) Investigation of performance of the self-healing agent in terms of preventing water leakage from cracks through laboratory tests found that the use of granules of self-healing agent as a fine aggregate replacement improved the slump of ready mixed concrete and produced a high water leakage prevention effect through self-healing of cracks even at the 8 months curing.

ACKNOWLEDGEMENT

The authors acknowledge the advices of Dr. K. Kobayashi and Dr. Y. Matsuda at East Japan Railway Company (JR) and the contribution on experimental works of Mr. M. Morita, the past graduate student.

REFERENCES

[1] Ahn, T.H. and Kishi, T. (2010). "Crack self-healing behavior of cementitious composites incorporating various mineral admixtures, Journal of Advanced Concrete Technology, 8(2), 171-186.
[2] Morita, M., Koide, T., Ahn, T.H. and Kishi. T. (2011). "Feasibility study of crack self-healing concrete incorporating inorganic granulated materials for the water-leakage", Proceedings of Japan Concrete Institute, Osaka, Japan, 33(1), 1457-1462.
[3] Yang, Y., Lepech, M.D., Yang, E., Li, V.C. (2009). "Autogenous healing of engineered cementitious composites under wet–dry cycles" Cement and Concrete Research, 39, 382–390.

Proceedings of the 3rd JCI-KCI-TCI Symposium on Recent Advancement of Technologies in Concrete Engineering
Japan Concrete Institute, July 2012

Applications of Synchrotron X-ray Radiation on Structural Materials Research in Nano/Micro-scale

Jae-Eun Oh, Ph.D.
School of Urban and Environmental Engineering,
Ulsan National Institute of Science and Technology (UNIST),
Ulsan Metropolitan City, Korea

Paulo J.M. Monteiro, Ph.D.
Department of Civil and Environmental Engineering,
University of California, Berkeley, CA, US.

ABSTRACT

The world consumes over 17 billion tons of portland cement concrete per year. While its embodied energy of 1.3 MJ/kg for a 30 MPa concrete is smaller than the 9 MJ/kg for recycled steel and 32 MJ/kg for new steel, the 2.3 billion tons production of portland cement is responsible for 1.7 billion tons per year of emissions of CO_2. Therefore, it is important to characterize and improve the mechanical properties of calcium silicate hydrate (C-S-H), the most important hydration product of portland cement, to achieve optimized sustainable concrete with lower cement consumption. A major limitation to our understanding of this material is our poor understanding of its atomic structure due primarily to the experimental difficulties in dealing with a poorly crystalline material. Each leap forward in our understanding of the nature of C-S-H has come about with the application of new experimental techniques. Atomistic simulations mark the forefront in our attempts to understand C-S-H. Unfortunately, there are few experimental probes that can be used to test the results of these simulations. One parameter that can be calculated and can be measured is the bulk modulus. Here we report the determined bulk modulus of 14Å tobermorite and C-S-H(I), a set of semicrystalline materials used to model C-S-H by measuring the unit cell volume change with pressure up to 4.8 and 3.7 GPa respectively. Our results allow us to distinguish between different approaches to the modeling of C-S-H, provide key experimental observations that future simulations need to match and suggest an appropriate strategy for future simulation studies.

Keywords: *synchrotron X-ray radiation, nano- and micro-structural study, 14Å tobermorite, C-S-H, alkali-activated slag, C-S-H(I)*

1 INTRODUCTION

The manufacturing and processing of portland-cement concrete (PC) consists of about 12% cement, 8% mixing water, 80% aggregate by mass, and, in some cases, chemical admixtures. Although concrete is an extremely versatile material, it suffers a few major critical sustainable drawbacks [1].

First, a huge amount of natural resources are consumed up for the concrete production. The world has annually consumed over 1.5 billion tons of portland cement, 9 billion tons of aggregates with one billion tons of potable water, corresponding 110,000 times volume of potable water more than the whole seawater in the San Francisco Bay, resulting in production of 17 billion tons of structural concrete per year. The portland-cement concrete has been placed second after water for human resource consumption [1].

Secondly, the cement production emits 1.7 billion tons of huge CO_2 gas, which accounts for at least 5-7% of world-wide man-induced CO_2 emission [2]. Generally, one tone of cement production generates nearly one tone of CO_2 emission.

Moreover, the aging of infrastructures made of concrete became economically serious. Service life of major concrete infrastructures such as dams, buildings, bridges, roads is largely shortened by corrosion, climate action, chemical attacks and alkali-silica reaction. These drawbacks render the status of cement and concrete production 'not' sustainable [1].

Two significant achievements must be prerequisite to resolve these drawbacks as the following: (1) largely enhancing essential mechanical properties of concrete, resulting in considerable reduction of consumption of concrete for an equivalent degree of construction purpose; and (2) fully understanding of the mechanism of concrete deterioration, leading to development of proper repair strategies. However, traditional approaches of civil engineering based on macro-scale testing of concrete researches have already faced the limit in resolving these problems because most of overall material behaviors are governed by micro- and nano-scale of materials properties. At present, further inherent solutions can be made only by nano- and micro-scale of studies. Therefore, nano-scale of research should be accompanied with the traditional macro-scale of approaches.

Natural rare mineral 14Å tobermorite and synthetic C-S-H (I) are closely related to each other and analogous to C-S-H with respect to the crystal structure [3][4]. Schematic representation of the relationship between tobermorite, C-S-H(I) and C-S-H is shown in Fig. 1 and Fig. 2. The tobermorite is a layered calcium silicate hydrate. It exists in three forms with different interlayer spacings (14Å, 11Å and 9Å). The interlayer spaces contain water and various cations such as Ca^{2+}. Some level of disorder is always found in the tobermorite crystal structure. It has a strong basal diffraction peak near at d = 14Å in X-ray diffraction. C-S-H(I) is thought to be similar to tobermorite, but with higher disorder. Usually it is considered to have missing bridging tetrahedra. It exists on a micro to nano scale. It has a broad basal diffraction peak. C-S-H is thought to be made up of nano sized particles. The structure is close to that of tobermorite, but more disordered with shorter silicate chains. Water molecules exist in between the atomic layers and adsorbed on surfaces. It has no basal diffraction peak in X-ray diffraction pattern [3][4].

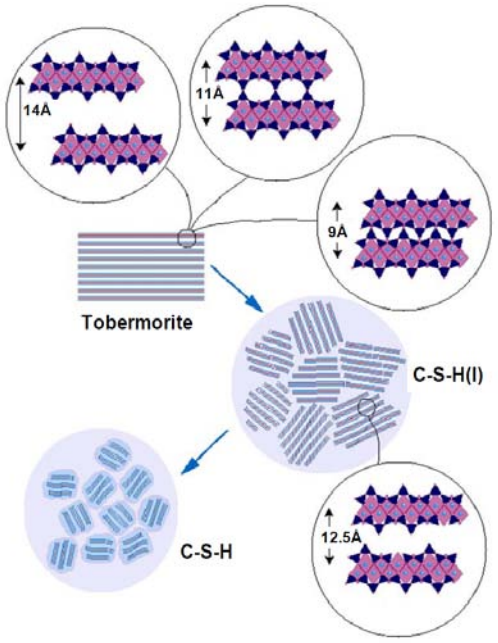

Fig. 1 Schematic structural representation of the relationship between tobermorite, C-S-H(I) and C-S-H

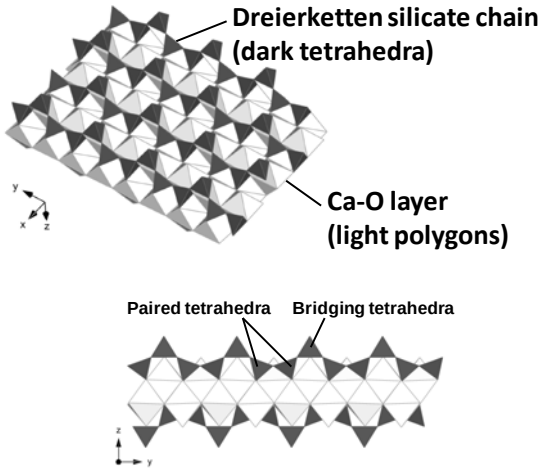

Fig. 2 Common structure of Ca-O layer and silicate chain of calcium silicate hydrates [tobermorites and C-S-H(I)s]

Although 14Å tobermorite and C-S-H (I) have been one of the major active issues in C-S-H research, experimental measurements of bulk modulus, which is one of the fundamental mechanical properties of structural materials, have been very difficult. Mostly the theoretical estimations of bulk modulus of these materials have been reported based on molecular dynamics or Monte-Carlo simulations [5-9].

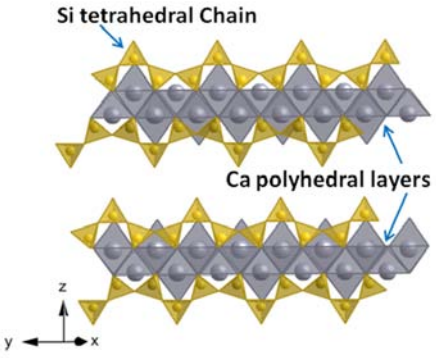

(a) SYN C-S-H(I) structure

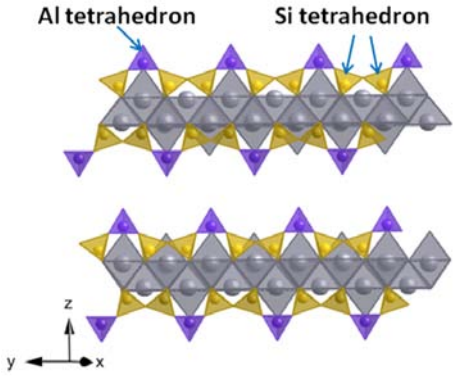

(b) AAS C-S-H(I) structure

Fig. 3 Schematic view of the structural difference between SYN C-S-H(I) and AAS C-S-H(I).

Alkali-activation of aluminosilicate raw materials using alkaline solution, including Ca-rich materials, was first discovered by Glukhovsky [10] in the Ukraine in the 1950s. In his extensive study, he designated the binders as 'soil cements'. In 1979, Davidovits introduced the term 'geopolymer' for the activation of metakaolin by alkali metal silicate solution [11]. Until the 1990s, most of the research on the subject of alkali-activation focused on an activation of ground blast furnace slag called 'alkali-activated slag cement' (AAS). From the 1990s onward, the trend of research has migrated to studying geopolymers.

The main reaction product of alkali-activated slag cement is agreed to be calcium silicate hydrate I [= C-S-H(I)] with Ca/Si = ~ 1. It is regarded as a structural model for C-S-H of hydration product of portland cement [hereafter we denote this C-S-H(I) as SYN C-S-H(I)]and it usually does not contain Al in its structure, but the C-S-H(I) of alkali-activated slag cement [hereafter we denote this C-S-H(I) as AAS C-S-H(I)] has been generally reported to contain high amount of Al at bridging tetrahedral sites in its structure with Al/Si ratio of 0.11 ~ 0.34 [13, 15] (see Fig. 3).

Here we report the determined bulk modulus of 14Å tobermorite, SYN C-S-H(I) and AAS C-S-H(I) samples by measuring the unit cell volume change with pressure up to 4.8 and 3.7 GPa respectively

2 TEST PROGRAMS

2.1 Materials

The 14Å tobermorite sample used in this study was obtained from Los Angeles County Museum of Natural History, which has the origin of Crestmore, California.

Two synthesized C-S-H(I) samples [i.e., SYN C-S-H(I) and AAS C-S-H(I)] were prepared. The SYN C-S-H(I) sample was purchased from Construction Technology Laboratories. The Ca/Si ratio of this sample was determined using electron microprobe to be 0.975. The AAS C-S-H (I) sample was synthesized using alkali activation of blast furnace slag with 10M NaOH solution cured at 80°C for 40 days. The SYN C-S-H(I) sample contained no Al, whereas the AAS C-S-H(I) sample had an Al/Si atomic ratio of 0.34 (the Al substitution ratio was examined using energy-dispersive spectroscopy of scanning electron microscope).

Note that the SYN C-S-H(I) sample is a chemically synthetic sample, but the AAS C-S-H(I) sample is an actual alkali-activation product and the alkali-activated slag sample showed a compressive strength of 49MPa at 14 days of curing.

2.2 Tests

Angle dispersive, X-ray diffraction measurements were made on beamline 12.2.2 of the Advanced Light Source [12]. An X-ray wavelength of 0.6199Å for the measurement of 14 Å tobermorite and 04959Å for the C-S-H(I) samples were used. A symmetric type diamond anvil cell (DAC) with 500μm culet size diamonds was used to generate high pressures (see Fig. 4). 200μm thick stainless steel gaskets pre-indented to about 65μm with 180μm diameter holes drilled in them where used to contain the samples between the diamonds. Samples were finely ground and loaded into the gasket hole together with a pressure transmitting fluid (4:1 Methanol/Ethanol solution) and a few chips of ruby which acted as pressure markers [15].

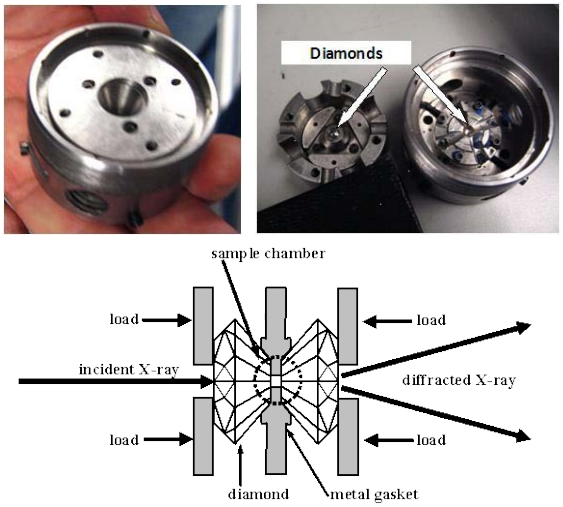

Fig. 4 Diamond anvil cell

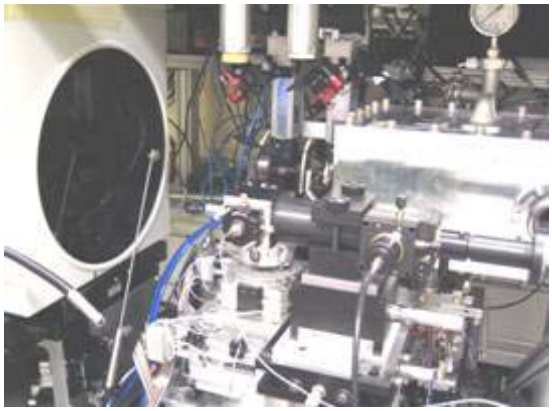

Fig. 5 MAR345 image plate detector and an experimental set-up at beamline 12.2.2.

Diffraction patterns were recorded using a MAR345 image plate (see Fig. 5 and Fig. 6) with typical exposure times of about 300s. Three dimensional diffraction data were processed using the Fit2D [16] software package to give conventional two dimensional patterns. Peak positions were determined using the XFIT [17] program.

3. RESULTS AND DISCUSSION

The whole procedure of measuring a bulk modulus using a DAC is quite simple. As the hydrostatic pressure applying to a material increases, the unit cell of the material experiences changes in its lattice parameters (usually, the unit cell shrinks under pressure. See Fig. 7).

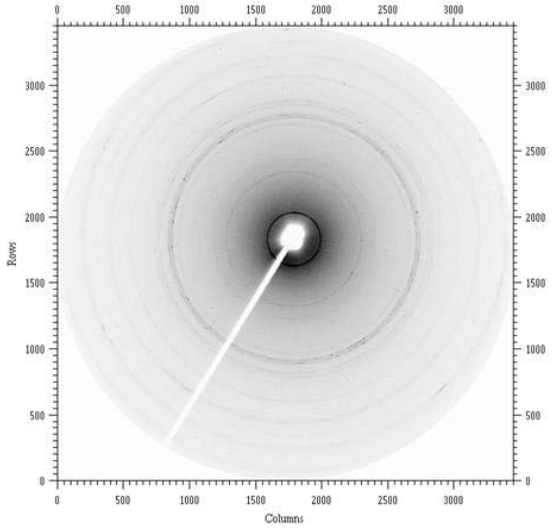

Fig. 6 Synchrotron X-ray diffraction image of 14 Å tobermorite taken under an ambient pressure (no DAC).

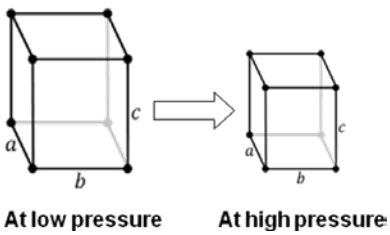

Fig. 7 Volume change of a unit cell under increasing pressure

By analyzing the X-ray diffraction patterns collected under pressure, the lattice parameters (e.g., ***a***, ***b***, ***c*** and angles between edges in Fig. 7) at a certain pressure can be calculated based on crystallographic knowledge. Using the lattice parameters, a volume of the unit cell can be calculated [e.g., for an orthorhombic system, the unit cell volume (=**V**) is obtained simply by **V** = ***a***×***b***×***c***, where ***a***, ***b***, ***c*** are the lattice parameters of the unit cell], resulting in a set of pressure-volume data.

In the experiment, a third-order Birch-Murnaghan (B-M) equation of state was fitted to the normalized pressure-volume data to calculate a bulk modulus of 14Å tobermorite, SYN C-S-H(I) and AAS C-S-H(I). The equation is expressed as the following [21]:

$$P = \frac{3}{2}K_o\left[(V/V_o)^{\frac{-7}{3}} - (V/V_o)^{\frac{-5}{3}}\right]\left[1+\frac{3}{4}(K_o'-4)\left((V/V_o)^{\frac{-2}{3}}-1\right)\right]$$

, where, V = volume of the unit cell, V_o = initial volume of unit cell at ambient pressure, P =

pressure applied to material, K_o = bulk modulus at zero pressure and K_o' = the derivative of bulk modulus at zero pressure.

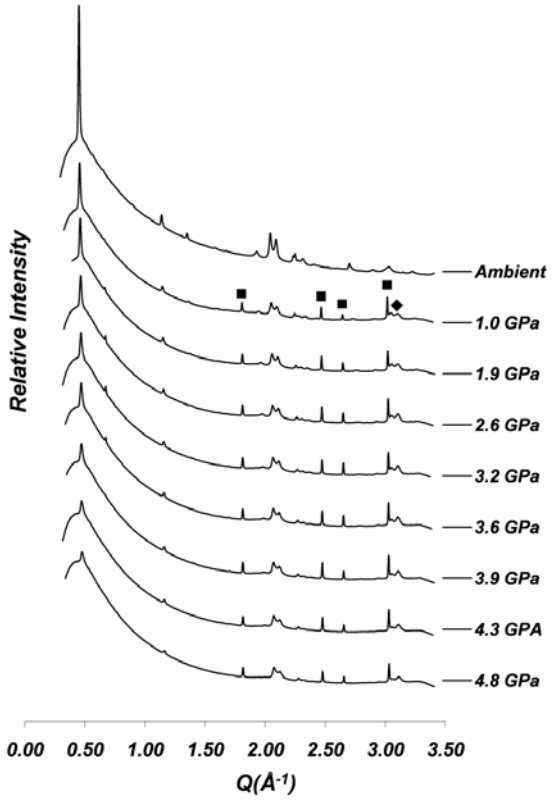

Fig. 8 Observed one-dimensional X-ray diffraction patterns of 14 Å tobermorite. The solid square (■) designates the corundum peaks and the solid diamond (◆) indicates a diamond peak.

The two dimensional high pressure X-ray diffraction patterns of 14Å tobermorite are integrated into one-dimensional diffraction profiles as seen in Fig. 8. All peaks except for the peaks labeled with solid squares and a diamond belong to 14Å tobermorite.

For an analysis of the 14Å tobermorite sample, since the crystal structure has been confirmed [19], the Rietveld analysis was applied to calculate more exact unit cell parameters using the MAUD software for all pressure range of X-ray diffraction profiles (see an example shown in Fig. 9) [20].

By newly defining the normalized pressure, $F = P/\{1.5[(V/V_o)^{-7/3} - (V/V_o)^{-5/3}]\}$, and the Eulerian strain, $f = 0.5 \cdot ((V/V_o)^{-2/3} - 1)$, the third order Birch Murnaghan equation of state is reorganized into the linear form: $F(f) = K_o - 1.5K_o(4 - K_o')f$.

In the plot of F versus f, the y-intercept and slope of weighted least-squares fit gave the bulk modulus Ko and its derivative Ko´. In this study, the pressure derivative of the bulk modulus was fixed to 4 since the restricted range of pressure over which the diffraction peaks used to determine the lattice parameters and volumes were clearly measurable made the determination of the pressure derivative of the bulk modulus unreliable.

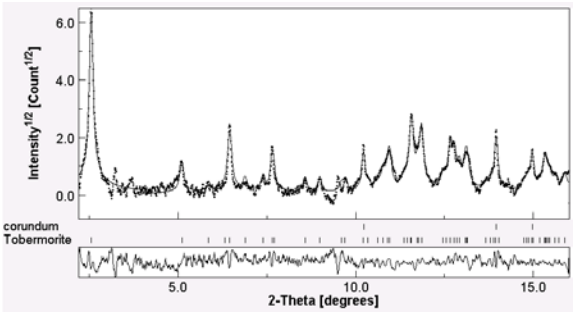

Fig. 9 An example of refined (solid line) and original experimental (dashed line) profiles from Rietveld analysis of 14Å tobermorite under an ambient pressure.

For the two C-S-H(I) samples, to refine the unit cell parameters, the CELREF [18] software was used because the Rietveld refinement cannot be applied because the crystal structure of C-S-H(I) has not been cleared (in this paper, the X-ray profiles are not included).

Fig. 10 shows the f-F plots used to determine the bulk modulus of 14Å tobermorite, SYN C-S-H(I) and AAS C-S-H(I) samples and Table 1 summarizes the results.

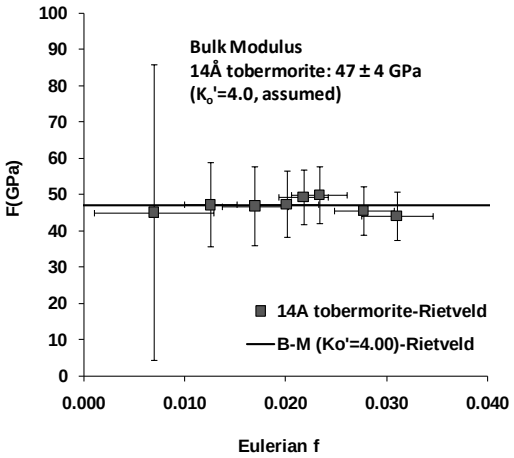

(a) 14Å tobermorite

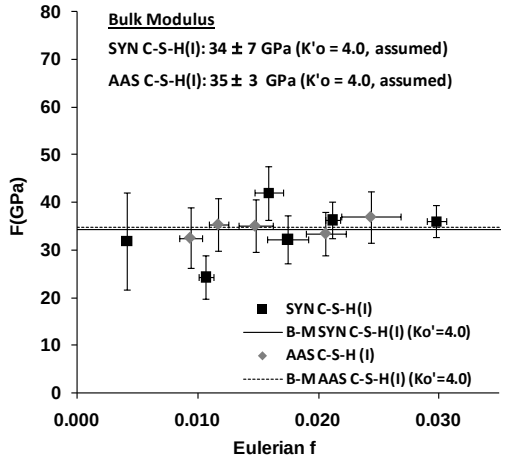

(b) SYN C-S-H(I) and AAS C-S-H(I)

Fig. 10 Plot of normalized pressure ***F*** versus of Eulerian strain ***f*** of 14Å tobermorite, SYN C-S-H(I) and AAS C-S-H(I). Note that B-M in the label indicates the linearly reorganized B-M curve and its y-intercept shows the bulk modulus.

The fitted curve of the equation of state with experimental data for 14Å tobermorite, SYN C-S-H(I) and AAS C-S-H(I) are depicted in Fig. 11, where the normalized pressure-volume data are fitted to the third order of Birch Murnaghan (B-M) equation of state.

Table 1 Measured bulk modulus values of 14Å tobermorite, SYN C-S-H(I) and AAS C-S-H(I)

Phase	Bulk modulus K_o(GPa)	Pressure derivative K'_o(GPa)	R-squared value (R^2) of EOS to the data
14Å tobermorite	47 ± 4	4	0.991
SYN C-S-H(I)	34 ± 7	4	0.967
AAS C-S-H(I)	35 ± 3	4	0.992

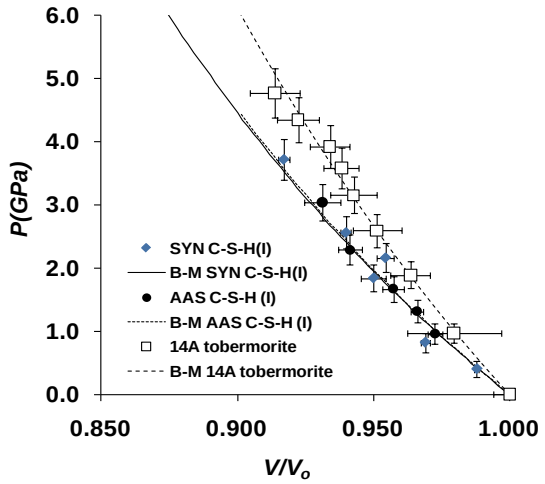

Fig. 11 Pressure vs. normalized volume data of 14Å tobermorite, SYN C-S-H(I) and AAS C-S-H(I) with curve fitted third order Birch-Murnaghan (B-M) equation of state (dashed and solid lines).

The bulk modulus of 14Å tobermorite is found to be higher than that of C-S-H(I) by ~24%, which is agreed with the earlier atomic simulation studies and explained by the higher order of disorder in C-S-H(I) structure [5-9].

It is interesting that the compression curves of the unit cell parameters ***a*** and ***b*** for both 14Å tobermorite and C-S-H(I) are clearly very similar (see Fig. 13), implying they are possibly made up of very similar Ca-O layers that are parallel to the ***a-b*** plane.

However, the linear incompressibility of ***c*** of 14Å tobermorite is significantly higher than those of SYN C-S-H(I) and AAS C-S-H(I) samples, implying the compression behaviors of 14Å tobermorite and C-S-H(I) are dominated by the characteristics of the interlayer spacing in [001] direction (see Fig. 12).

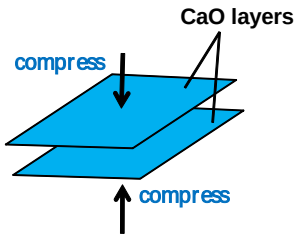

Fig. 12 Schematic view of incompressibility of layered structure of calcium silicate hydrates.

The 14Å and C-S-H(I) have quite different characteristics of interlayer space along [001] (e.g., different interlayer spacing, interlayer water molecules, degree of disorders in the silicate chains, or additional Ca ions). It is worth to note that the bulk modulus values are approximately proportional to their linear incompressibility of the lattice parameter c.

Although the AAS C-S-H(I) sample contained a large amount of Al-substitution (Al/Si = ~ 0.34 for the current sample by EDS), which does not exist in SYN C-S-H(I) at all, the pressure-normalized volume compression curves and bulk modulus values for the two C-S-H(I) samples are seen to be very similar (see Fig. 11). In addition, the incompressibility of lattice parameter ***a***, ***b*** and ***c*** are seen almost identical between two C-S-H(I) samples in Fig. 13, indicating that the Al-substitution seems to have little effect on the incompressibility of C-S-H(I).

5 CONCLUSIONS

The bulk moduls values of the selected representatives [= 14Å tobermorite, SYN C-S-H(I) and AAS C-S-H(I)] of calcium silicate hydrate, which is a main hydration product of portland cement, are expreimentally measured by measuring the unit cell volume change with pressure up to 4.8 and 3.7

GPa respectively by means of high pressure synchrotron X-ray diffraction technique.

Our results allow us to distinguish between different approaches to the modeling of C-S-H, provide key experimental observations that future simulations need to match and suggest an appropriate strategy for future simulation studies.

ACKNOWLEDGEMENT

All these experimental results were published in the following paper:
(1) Jae Eun Oh, Simon M. Clark, Hans-Rudolf Wenk and Paulo J.M. Monteiro, " Experimental Determination of Bulk Modulus of 14Å Tobermorite Using High Pressure Synchrotron X-ray Diffraction", Cement and Concrete Research 42(2) (2012) 397-403.
(2) Jae Eun Oh, Simon M. Clark, Paulo J.M. Monteiro. "Does the Al substitution in CSH (I) change its mechanical property?", Cement and Concrete Research. 41(1) (2011) 102-106.

The Advanced Light Source is supported by the Director, Office of Science, Office of Basic Energy Sciences, of the U.S. Department of Energy under Contract No. DE-AC02-05CH11231

This report was based on work supported in part by Award No. KUS-l1-004021, made by King Abdullah University of Science and Technology (KAUST) and by NIST grant 60NANB10D014.

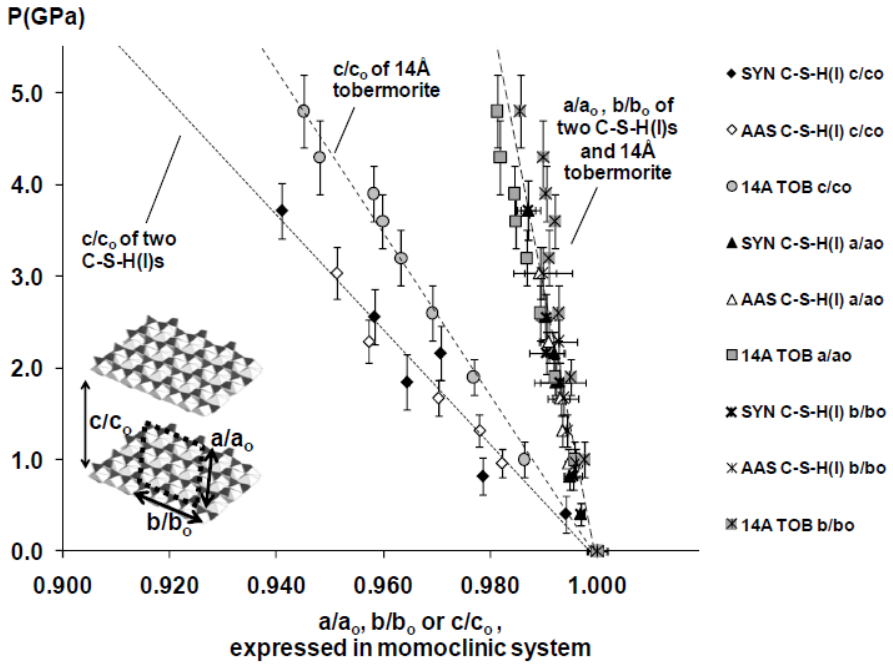

Fig. 13 Incompressibility of normalized lattice parameters a, b, and c of 14Å tobermorite, SYN C-S-H(I) and AAS C-S-H(I).

REFERENCES

1. P.L. Mehta and P.J.M. Monteiro: Concrete: Structure, Properties and Materials. , McGraw-Hill, 2005
2. E. Gartner: Industrially Interesting Approaches to "low-CO2" Cements. Cem. Concr. Res., 34(9), pp. 1489-1498, 2004
3. I.G. Richardson: The calcium silicate hydrates. Cem. Conc. Res. 38. pp.137-158, 2008.
4. D. Viehland, J. Li, L. Yuan and Z. Xu: Mesostructure of Calcium Silicate Hydrate (C-S-H) gels in Portland cement paste: short-range ordering, nanocrystallinity, and local compositional order. J. Am. Ceram. Soc. 79[7]. pp. 1731-44, 1996
5. H. Manzano, J.S. Dolado, A. Guerrero, A. Ayuela: Mechanical properties of crystalline calcium-silicate-hydrates: comparison with cementitious CSH gels, Phys. Status Solidi (a) 204, pp. 1775-1780, 2007.
6. R.J.M. Pellenq, N. Lequeux, H. Van Damme: Engineering the bonding scheme in CSH: the iono-covalent framework, Cem. Concr. Res. 38 , pp.159-174, 2008.
7. H. Manzano, J.S. Dolado, A. Ayuela, Elastic properties of the main species present in Portland cement paste, Acta Mater. 57,pp. 1666-1674, 2009.
8. R. Shahsavari, M.J. Buehler, R.J.M. Pellenq, F.J. Ulm: First-principles study of elastic constants and interlayer interactions of complex hydrated oxides: case study of tobermorite and jennite, J. Am. Ceram. Soc. 92, pp. 2323-2330, 2009.

9. A. Al-Ostaz, W. Wu, A.H.-D. Cheng, C.R. Song: A molecular dynamics and microporomechanics study on the mechanical properties of major constituents of hydrated cement, Composites Part B Eng 41, pp. 543-549, 2010.
10. V. D. Glukhovsky, Gosstroiizdat Publish.Kiev, USSR, 127, 1959.
11. J. Davidovits, "Synthesis of New High-Temperature: Geo-Polymers for Reinforced Plastics." Composites, SPE PACTEC, 79, pp. 151-154, 1979.
12. M. Kunz, A.A. MacDowell, W.A. Caldwell, D. Cambie, R.S. Celestre, E.E. Domning, R.M. Duarte, A.E. Gleason, J.M. Glossinger, N. Kelez, D.W. Plate, T. Yu, J.M. Zaug, H.A. Padmore, R. Jeanloz, A.P. Alivisatos, and S.M. Clark: A beamline for high pressure studies at the Advanced Light Source with a superconducting bending magnet as the source. J. Synch. Rad. 12, pp. 650-658, 2005.
13. I. Richardson, A. Brough, G. Groves, C. Dobson:The Characterization of Hardened Alkali-Activated Blast-Furnace Slag Pastes and the Nature of the Calcium Silicate Hydrate(C-S-H) Phase, *Cem. Concr. Res.*, 24(5), pp. 813-829, 1994.
14. S.D. Wang, K.L. Scrivener: Hydration products of alkali activated slag cement, Cem.Concr.Res. 25, pp. 561-571, 1995.
15. R.J. Angel, M. Bujak, J. Zhao, G.D. Gatta, S.D. Jacobsen: Effective hydrostatic limits of pressure media for high-pressure crystallographic studies, J. Appl. Crystallogr. 40, pp. 26-32, 2007.
16. A.P. Hammersley, Fit2d version 12.040, ESRF, Grenoble, France, 2006.
17. R.W. Cheary, A.A. Coelho. Programs XFIT and FOURYA, deposited in CCP14 Powder Diffraction Library, Engineering and Physical Sciences Research Council, Daresbury Laboratory, Warrington, England, 1996 (http://www.ccp14.ac.uk/tutorial/xfit-95/xfit.htm).
18. J. Laugier, B. Bochu. CELREF. Version 3. Cell parameter refinement program from powder diffraction diagram. Laboratoire des Matériaux et du Génie Physique, Ecole Nationale Supérieure de Physique de Grenoble (INPG), France, 2002.
19. E. Bonaccorsi, S. Merlino, A.R. Kampf: The Crystal Structure of Tobermorite 14Å(Plombierite), a C–S–H Phase, J. Am. Ceram. Soc. 88, pp. 505-512, 2005.
20. L. Lutterotti, D. Chateigner, S. Ferrari, J. Ricote: Texture residual stress and structural analysis of thin films using a combined X-ray analysis, Thin Solid Films 450, pp. 34 - 41, 2004.
21. F. Birch. Elasticity and internal constitution of the Earth's interior, J. Geophys. Res.. 57, pp. 227-286, 1952.

Proceedings of the 3rd JCI-KCI-TCI Symposium on Recent Advancement of Technologies in Concrete Engineering
Japan Concrete Institute, July 2012

CARBON DIOXIDE UPTAKE DURING CONCRETE LIFE CYCLE

Yasuhiro Kuroda and Toshifumi Kikuchi
Institute of Technology, Shimizu Corporation, Japan

ABSTRACT

This paper reports the research on quantification of CO_2 uptake during concrete life cycle. Various laboratory tests and analysis of nationwide survey results were carried out. The major findings are as follows. 1) the amount of CO_2 uptake increases remarkably when the particle size is small and when crushed material is alternately wetted and dried. 2) the nationwide survey on the CO_2 uptake of concrete rubbles gave rise to the quantification that the amount of CO_2 uptake in one ton of recycled crusher-run is estimated to be approximately 24kg-CO_2. 3) the $LCCO_2$ calculation result when considering CO_2 uptake during demolition and recycling was found to be about 12% less than the case when the CO_2 uptake is not taken into account.

Keywords: *CO_2 uptake, $LCCO_2$, carbonation, concrete rubbles, demolished and crushed concrete*

1 INTRODUCTION

The production of Portland cement leads to the release of significant amounts of carbon dioxide (CO_2), a greenhouse gas. It is said that the production of 1 ton of Portland cement clinker creates approximately 1 ton of CO_2(Naik and Moriconi 2005[1]). Approximately half of the CO_2 emissions from cement production stem from the calcination of limestone, i.e. the process where limestone is burnt and CO_2 gas is released to the atmosphere. Theoretically, hardened concrete binds approximately the same account of CO_2 in a carbonation process (Engelsen et al. 2005[2]).

Carbonation of concrete is a well-known process, where cement hydrates of concrete react with atmospheric CO_2 to form calcium carbonate ($CaCO_3$) as shown in Table 1[3].

Table 1 Carbonation of Cement Hydrates[3].

$3CaO \cdot 2SiO_2 \cdot 3H_2O + 3H_2CO_3 \rightarrow 3CaCO_3 + 2SiO_2 + 6H_2O$
$Ca(OH)_2 + H_2CO_3 \rightarrow CaCO_3 + 2H_2O$
$3CaO \cdot Al_2O_3 \cdot 3CaSO_4 \cdot 32H_2O + 3H_2CO_3 \rightarrow 3CaCO_3 + 2Al(OH)_3 + 3CaSO_4 + 32H_2O$
$3CaO \cdot Al_2O_3 \cdot CaSO_4 \cdot 12H_2O + 3H_2CO_3 \rightarrow 3CaCO_3 + 2Al(OH)_3 + CaSO_4 + 12H_2O$
$3CaO \cdot (Al_2O_3 \cdot Fe_2O_3) \cdot 3CaSO_4 \cdot 32H_2O + 3H_2CO_3 \rightarrow 3CaCO_3 + 2Al(OH)_3 + 2Fe(OH)_3 + 3CaSO_4 + 29H_2O$

It is a process that occurs from the surface of the concrete and the amount of carbonated concrete is related to exposure time as well as surface area. When concrete structures are demolished and crushed, the surface area per unit weight of concrete increases significantly. Therefore, the CO_2 uptake rate per unit mass of concrete and thus the total amount of CO_2 uptake increase after the demolishing stage.

In Northern Europe, the CO_2 emission as well as the CO_2 uptake during the life cycle of concrete has been considered in the assessment of the life cycle CO_2 ($LCCO_2$) of reinforced concrete structures. In a project called "CO_2 uptake during the concrete life cycle" of the Nordic Innovation Center (e.g. Lagerblad 2005[4]), the carbonation rates of different types of concrete under various conditions, including the rate of carbonation during secondary life, i.e. after demolition of the concrete, have been assessed. That project also estimated the annual production of various concrete types and products. "Guidelines - Uptake of carbon dioxide in the life cycle inventory of concrete" (Pommer and Pade 2005[5]) represents, based on the findings of the project, an attempt to establish a general procedure of CO_2 life cycle inventory that adequately includes all phases in the life and secondary life of any concrete product.

The above-mentioned studies were based on many assumptions and there has not been enough experimental data to verify. Quantification of CO_2 uptake based on experiments and surveys on the

carbonation of actual concrete in structures before demolition work and also in recycling plant would go a long way toward overcoming these shortcomings.

This paper introduces the research were to quantify the amount of CO_2 uptake during concrete life cycle.

2 PRESENT SITUATION OF CONCRETE RECYCLING IN JAPAN

In Japan, the amount of waste concrete exceeds 30million tone a year, and the recycling and reused rates of concrete rubbles are about 97% as shown in Table 2[6]

Most recycling plants produce recycled crusher-run for use as roadbed material and backfill by crushing concrete rubbles. An example of the recycled crusher-run is shown in Photo 1. In most cases, the primary crushing is carried out using a jaw crusher as shown in Fig.1 and secondary crushing implemented by using an impact crusher as shown in Fig.2[7].

Table 2 Change in Waste Concrete and Recycling[6]

Year	Waste concrete million ton/year	Recycling and reused rates %
1990	25.0	48
1995	36.5	65
2000	35.3	96
2002	35.1	97.5
2005	32.2	98.1
2008	31.3	97.3

Photo 1 Example of Recycled Crusher-run

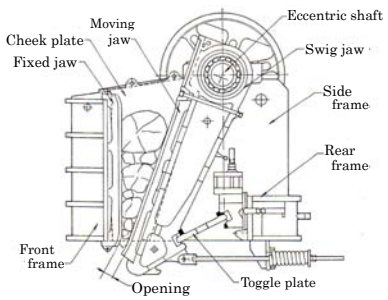

Fig.1 Example of Jaw Crusher[7]

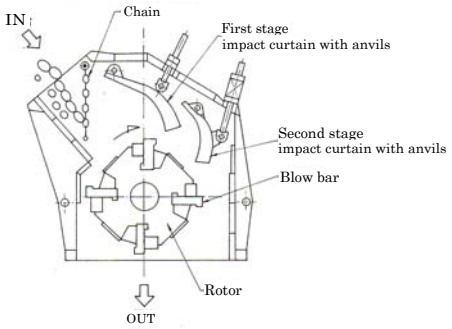

Fig.2 Example of Impact Crusher[7]

3 EXPOSURE EXPERIMENT WITH CRUSHED MORTAR IN LABORATORY

This section describes the exposure experiment [8] with crushed mortar to identify the conditions that promote CO_2 uptake after demolition.

3.1 Outline of Experiment

Table 3 shows the factor and the level of the exposure experiment with crushed mortar in laboratory.

Table 3 Factor and Level of Experiment [8]

Factor		Level
Mortar Mixture	Type of Cement	OPC, BB
	Water-Cement Ratio	0.60, 0.40
Crushed Mortar	Range of Grain Size	0-0.5, 0.5-2, 2-5mm
	Exposure Condition	D, WD

(1) Materials and Mix Proportions

The types of cement used in the experiment were ordinary Portland cement (OPC) and Portland blast-furnace slag cement B class (BB). In addition, silica sand and ion-exchange water were also used. The water-cement ratio was 0.6 or 0.4, and the sand-cement ratio was 3.0.

(2) Mortar Specimens

The mortar specimens were mixed using a Hobart mixer and casted onto a plastic mold. The mortar specimens were seal-cured by maintaining them at a constant room temperature (20°C) for a year. Subsequently, each of the mortar specimens were crushed to a particle size of less than 5 mm using a jaw crusher.

(3) Exposure Condition

The specimens (0–5 mm) were placed in a room where temperature and humidity were maintained at 20°C and 65%, respectively. The two exposure conditions used were dried (D) and alternately wetted and dried (WD). Measurements were carried out after 0, 28, and 91 days. The alternately wetted and dried specimens were homogeneously mixed and sprayed with water twice a week (number of rainy days is 100 per one year in Tokyo) in such a

way that the moisture content was about 15%. The dried specimens were also homogeneously mixed. The examination and adjustment of the moisture condition of crushed mortar are shown in Photo 2.

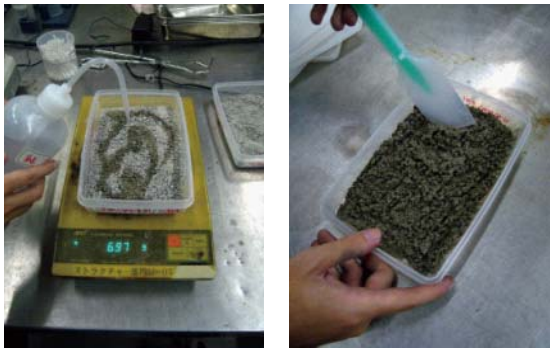

Photo 2 Examination and Adjustment of Moisture Condition[8]

(4) Test Methods

After being exposed for the required period of time, the specimens were soaked in acetone, and their particles were screened out according to their sizes (0–0.5 mm, 0.5–2 mm, and 2–5 mm). Then, they were crushed to particle size less 0.15 mm using a disk mill. Then, an insoluble residue test was carried out by dissolving the specimens in hydrochloric acid in order to determine the amount of insoluble residue that is required for an aggregate content. Thermogravimetry - differential thermal analysis (TG-DTA) was carried out in order to determine the $Ca(OH)_2$ and $CaCO_3$ contents of the specimens. The temperature was increased at a rate of 10°C/min from room temperature to 850°C. The endothermic peak from about 450–500°C during DTA was regarded to be due to the dehydration of $Ca(OH)_2$ and that at about 600–750°C was regarded to be due to the decarboxylation of $CaCO_3$. The $Ca(OH)_2$ and $CaCO_3$ contents of the specimens were calculated from the mass loss during TG. Using these results, the $Ca(OH)_2$ and $CaCO_3$ contents per cement paste were calculated. The molecular weights used in the calculation are as follows:

$Ca(OH)_2$ = 74.1, $CaCO_3$ = 100.1, H_2O = 18.0, CO_2 = 44.0

3.2 Results and Discussions

The results of the experiment on crushed mortar are listed in Table 4, and the content of $CaCO_3$ in the cement paste of the mortars of different sizes is shown in Fig.3.

Regarding the effect of the water to cement ratio, the $CaCO_3$ content of the mortar with water to cement ratio of 0.6 was higher than that in the mortar with water to cement ratio of 0.4. This is due to the fact that the hydration product of the mortar with high water to cement ratio is more porous, resulted in a higher carbonation rate.

Regarding the effect of cement type, the $CaCO_3$ content in the case of OPC use was found to be higher than in the case of BB cement use, possibly due to the fact that the $Ca(OH)_2$ content in mortar using BB cement is smaller than in the case of mortar using OPC.

Table 4 Results of Experiment on Crushed Mortar[8]

Type of cement	W/C	Exposed condition	Particle sizes	0 days			28 days			91 days		
				insol.	$Ca(OH)_2$	$CaCO_3$	insol.	$Ca(OH)_2$	$CaCO_3$	insol.	$Ca(OH)_2$	$CaCO_3$
			mm	%	%	%	%	%	%	%	%	%
OPC	0.40	D	0.5-0	68.4	10.8	2.0	58.9	11.5	9.4	61.8	7.4	17.3
			2-0.5				73.3	9.3	3.1	77.5	9.0	10.5
			5-2				69.5	12.4	3.0	70.5	11.2	8.4
		WD	0.5-0				61.7	-	53.6	64.0	-	67.7
			2-0.5				60.6	-	17.2	76.0	3.1	30.0
			5-2				66.2	6.8	8.8	68.5	6.9	14.2
OPC	0.60	D	0.5-0	68.3	12.6	2.2	57.2	11.5	19.2	58.4	8.0	32.9
			2-0.5				79.7	12.2	6.8	79.5	-	26.2
			5-2				70.3	14.8	3.8	70.5	7.5	32.1
		WD	0.5-0				54.0	-	55.4	57.5	-	66.0
			2-0.5				72.6	-	34.0	73.2	-	33.7
			5-2				69.4	5.9	17.0	68.2	5.3	25.3
BB	0.60	D	0.5-0	69.6	7.7	0.9	56.2	6.2	9.1	58.0	-	22.4
			2-0.5				74.2	4.8	5.6	77.5	-	17.4
			5-2				68.8	4.4	5.5	69.5	-	13.7
		WD	0.5-0				54.9	-	45.2	57.6	-	51.0
			2-0.5				71.5	1.0	18.2	72.1	-	29.4
			5-2				71.0	3.0	10.7	69.3	2.8	15.6

"-" means that the endothermic peak was indeterminable.

As for the influence of particle size, it was found that the smaller particle size, the faster carbonation rate was, even in the case of low water to cement ratio. This is because of the larger surface area (in contact with the atmosphere) per unit mass of small particles compared to that of larger particles. Regarding the effect of the exposing condition, it was confirmed that the carbonation rate of specimens in the alternately wetted and dried condition was higher than that of specimens in the dried condition.

The $Ca(OH)_2$ content of specimens in the alternately wetted and dried condition, which had small-sized particles, decreased significantly while the $CaCO_3$ content increased significantly. It was speculated that the $Ca(OH)_2$ consumption of specimens in the alternately wetted and dried condition was accelerated.

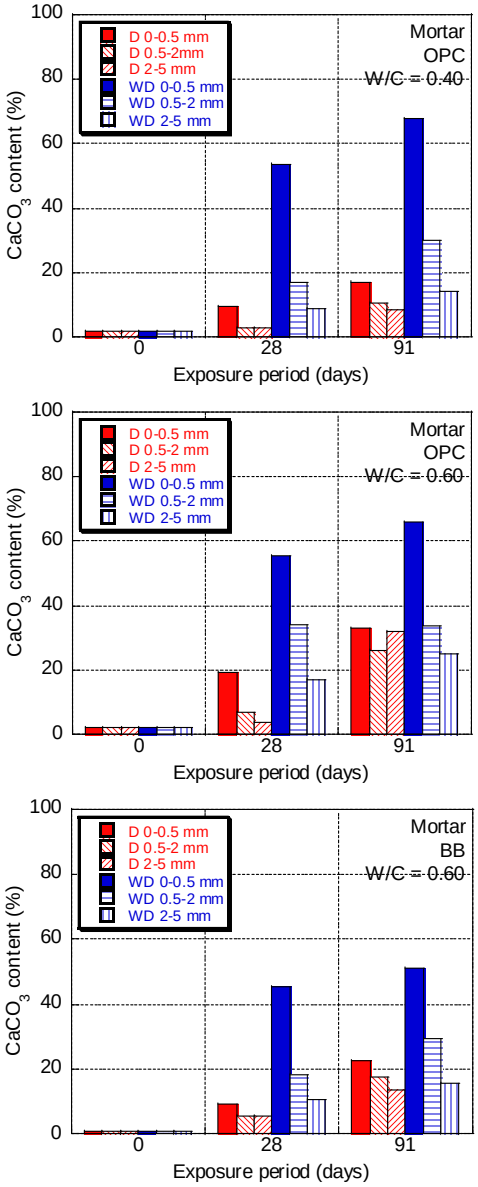

Fig.3 $CaCO_3$ Content in Cement Paste

Further, despite the fact that all of the $Ca(OH)_2$ contents in specimens has been consumed, the $CaCO_3$ content will continue to increase, because not only $Ca(OH)_2$ but also other cement hydrates (i.e. calcium silicate hydroxide and calcium aluminate hydroxide) have been carbonated.

4 NATIONWIDE SURVEY ON CO_2 UPTAKE OF CONCRETE RUBBLES BY NILIM

This section introduces the nationwide survey[9] to quantify the amount of CO_2 uptake in demolished and crushed concrete.

4.1 Outline of Survey

National Institute for Land and Infrastructure Management (NILIM) has conducted a nationwide survey on the amount of the CO_2 uptake through recycling of concrete rubbles. 46 specimens of recycled crusher-run around the nation were collected.

Each specimen was divided into two parts. The amount of CO_2 was measured immediately for one part (denoting uptake during service period of concrete structures), and after 28-day exposure to the environment for the other. The exposure period is similar to that in a recycling site. During the exposure, the specimens were watered twice a week. CO_2 uptake was quantified by TG-DTA analysis. In actual situations, the demolished concrete at the recycling plants are usually stored in open space and usually mixed up during transportation

The measurement methods are shown in Table 5.

Table 5 Test Methods[9]

Items*	Test Object	Method	Information obtained
Grain size	0-day (0-40mm)	JIS A 1102, Japan Road Assoc. method	Influence on CO_2 uptake
Insoluble residue	0-day (0-5mm,5-20 mm)	Japan Cement Assoc. method F-18	Cement content, influence on CO_2 uptake
C			
CC	0-day/28-day (0-5mm,5-20 mm)	TG-DTA	Amount of CO_2 uptake
CH			

* C : CO_2, CC : $CaCO_3$, CH : $Ca(OH)_2$,

4.2 Results and Discussions

The results of sieving test are shown in Fig. 4. The percentage passing was remarkably different in each sample. However, it did not depend on the region. On average, the ratio of 0-5 mm particles was about 32% and that of 5-20 mm particles was about 44%.

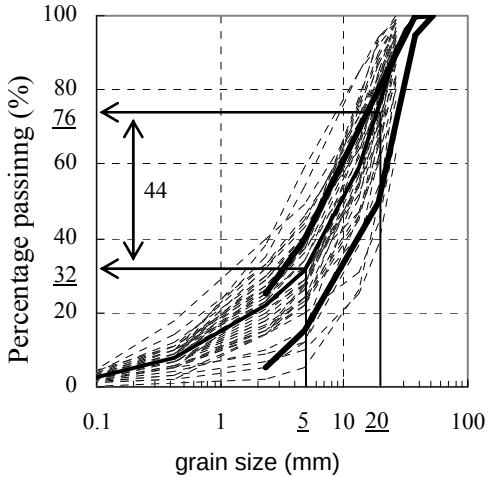

Fig.4 Grading Chart of Recycled Crusher-run[9]

The cement content estimated by Japan Cement Association method F-18 are shown in Table 6. The average cement content in 0-5mm and 5-20mm particles were 16.7% and 11.4%, respectively. It means that the small particles seems to contain more cements compared with large particles. The average cement content of 0-20mm particles was 13.6%, one can see that there is not much difference in this value between regions.

Table 6 Cement Content[9]

	Cement content %		
Grain size	0-5mm	5-20mm	0-20mm
Hokkaido area and Tohoku area	16.4	11.0	13.5
Kanto area	17.5	12.5	14.5
Hokuriku area	14.9	10.7	12.7
Chubu area	17.0	10.6	12.9
Kinki area	17.5	12.1	14.0
Chugoku area	17.5	11.0	13.9
Shikoku area	14.0	9.3	11.5
Kyushu area and Okinawa area	17.7	12.9	14.3
National average	16.7	11.4	13.6

The amount of CO_2 uptake is shown in Fig.5. Initially, recycled crusher-run absorbed 15.2kg-CO_2/t on average. That increased to 23.6 kg-CO_2/t after 28-day exposure. The amount of CO_2 uptake through recycling was about 8.5kg-CO_2/t on average (minimum: 3, maximum 17), calculated as the increment between 28-day exposures. The smaller the grain size was, the more CO_2 the specimen absorbed.. These results lead to the suggestion that the carbonation rate of demolished and crushed concrete is relatively-rapid under the actual environment.

Based on the result of this survey, if the period after crushed concrete rubbles is about one month, the amount of CO_2 absorbed in one ton of demolished concrete was estimated to be about 24 kilograms.

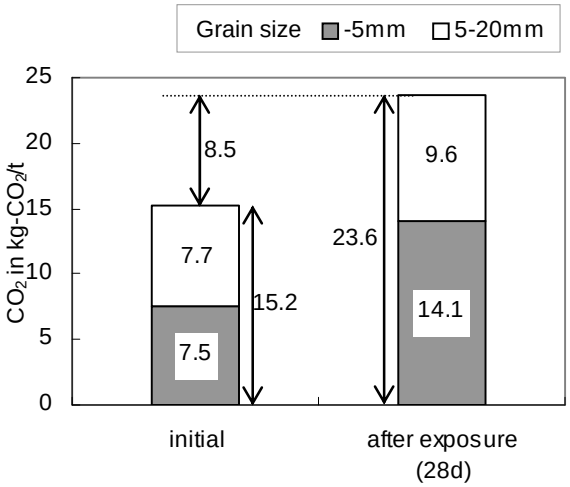

Fig.5 Amount of CO_2 in Recycled Crusher-run

5 CALCULATION OF $LCCO_2$ IN CONCRETE STRUCTURE

This section describes calculated results of $LCCO_2$ with using the result (the amount of CO_2 uptake of 1 ton recycled crusher-run: 23.6kg-CO_2) obtained in Chapter 4 during the service life of a reinfoced concrete structure.

5.1 Outline of Calculation

Assuming the volume of reinfoced concrete to be 100 m^3, inventory analysis was carried out, and their $LCCO_2$ values were calculated. The CO_2 emission inventory data and amount of materials used are shown in Table 7. The water-cement ratio in concrete was 55%, and the sand content was 44%. Inventory analysis included the following processes: material process, concrete and costruction process, demolition process, recycling process, and transport process.

Table 7 Inventory data and amount of materials[10]

Items	Specific CO_2 emission	Amount used (ton/100m^3)
Water	-	16.5
Cement(OPC)	765.5kg-CO_2/t	30
Fine aggregate	3.4kg-CO_2/t	80
Coarse aggregate	2.8kg-CO_2/t	105
Reinforcement	755.3kg-CO_2/t	20

The amount of CO_2 emission during each process was calculated, and these results are also reported. The amount of CO_2 emission during the material

process, the concrete and construction process, the demolition process, and the transport process was quoted from data listed in reference 10.

On the other hand, for calculating the CO_2 emission during the recycling process as shown Fig.6(Case of production capacity:80ton/h), total rated power output of electromotors was assumed to be 215 kW and its load factor was assumed to be 80% as shown in Table 8. Assuming CO_2 emission coefficient was 0.561kg-CO_2/kWh[11], specific CO_2 emission of these equipments is 1.21kg-CO_2/ton as follows.

$$\frac{\left(0.8\times 215^{kW}\times 0.561^{kg-CO_2/kWh}\right)}{80^{ton/h}} = 1.21^{kg-CO_2/ton}$$

In addition, based on past record of similar recycling plants of this scale, the specific CO_2 emission of heavy equipments(1 excavator and 2 wheel loaders) was assumed to be 0.99kg-CO_2/ton. Therefore, specific CO_2 emission during the recycling process is totally 2.2 kg-CO_2/ton. However, this is the comparatively ideal situation.

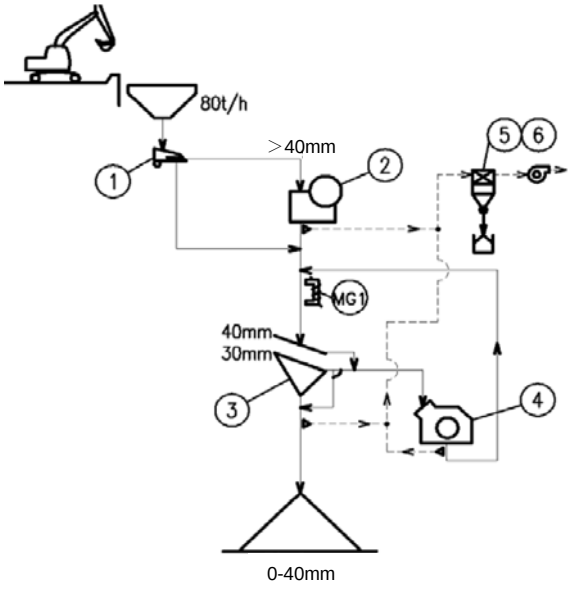

Fig.6 Work flow of recycling plant

Table 8 List of Equipments and Electromotor

No.	Equipment	Electromotor
1	Vibratory feeder	5.5kW 4P
2	Jaw crusher	75kW 6P
3	Vibrating screen	5.5kW 4P
4	Impact crusher	75kW 6P
5	Dust collector	22.0kW
6	Compressor	3.7kW
MG1	Magnetic ore separator	5.0kW 4P
Rest	6 conveyor belts	23.3kW
Total rated power output		215kW

4.2 Results and Discussions

The results of $LCCO_2$ calculation are shown in Fig.7, and a comparison between the exclusion and inclusion of CO_2 uptake in calculating $LCCO_2$ is shown in Fig.8.

One can find that the amount of CO_2 uptake is much lower than the amount of CO_2 emission during the material process but it is higher than the amount of CO_2 emission during the construction, demolition, recycling, and transport processes. Therefore, it can be said that the amount of CO_2 uptake almost compensates for the amount of CO_2 emission during the demolition and recycling processes. Moreover, the value of $LCCO_2$ with consideration of CO_2 uptake is about 12% lower than the case without consideration of CO_2 uptake.

Simple calculation shows that if 30 million tons of demolished concrete are discharged every year and 29 million tons of recycled crusher-run are used, the amount of CO_2 uptake by the recycled crusher-run is approximately 0.68 million tons per year. Consequently, the contribution of the construction industry to net CO_2 emissions might have been overestimated.

5 CONCLUSIONS

At present, reduction in carbon dioxide (CO_2) emission in the construction industry is required for the prevention of global warming. Concrete is one of the major construction materials, and carbonation of concrete is a well-known process, where cement hydrates of concrete react with atmospheric CO_2 to form calcium carbonate ($CaCO_3$). Therefore, concrete absorbs atmospheric CO_2 during the service life of a concrete structure and as well as after its demolition and recycling.

This paper reports the research on quantification of CO_2 uptake during concrete life cycle The following conclusions are drawn.

(1) The amount of CO_2 uptake increases remarkably when the particle size is smaller and when crushed material is alternately wetted and dried.

(2) The nationwide survey on the CO_2 uptake of concrete rubbles gave rise to the quantification that the amount of CO_2 uptake in one ton of recycled crusher-run (0 to 40 millimeters) is estimated to be approximately 24 kilograms.

(3) The $LCCO_2$ calculation result when considering CO_2 uptake during demolition and recycling was found to be approximately 12% less than the case when the CO_2 uptake is not taken into account.

(4) When calculating the $LCCO_2$, taking into account not only the CO_2 uptake during demolition and recycling processes but also the CO_2 uptake of the in-service period may lead to more accurate result.

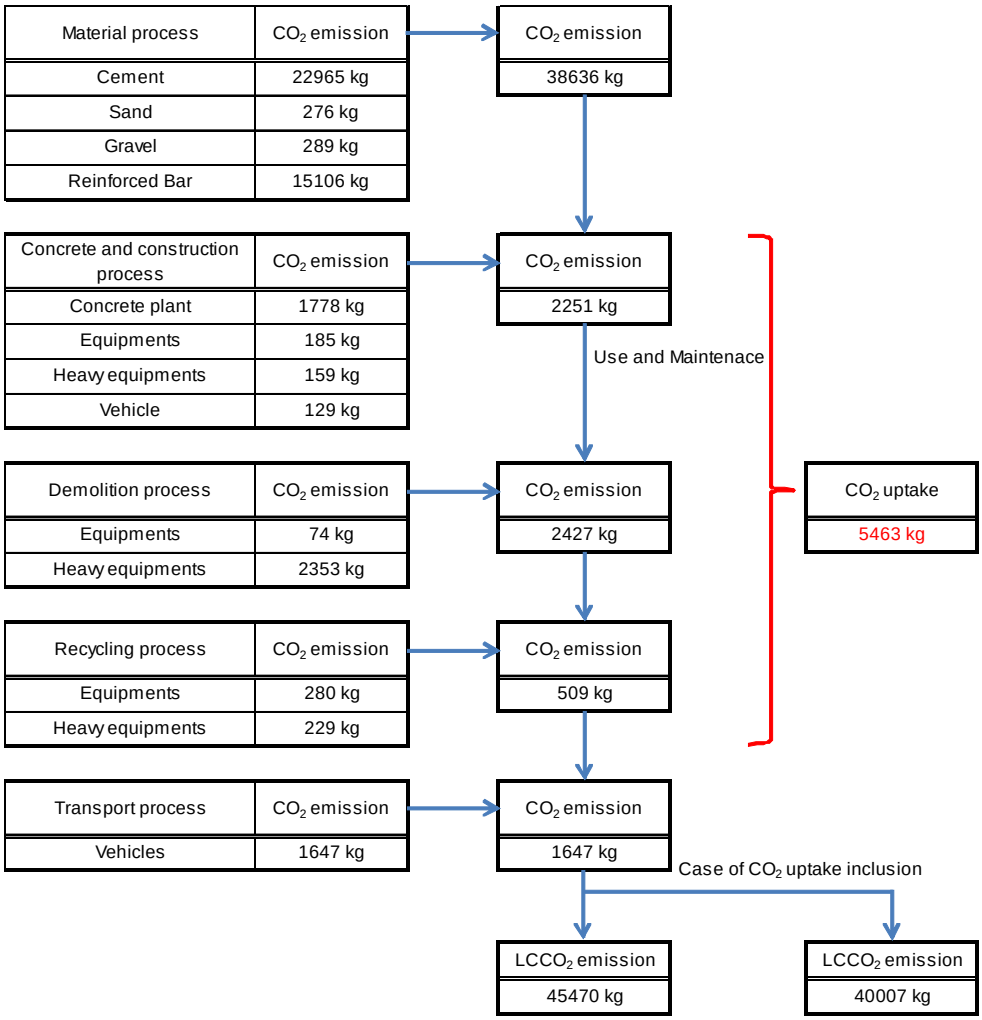

Fig.7 Results of $LCCO_2$ Calculation with Inclusion of CO_2 Uptake

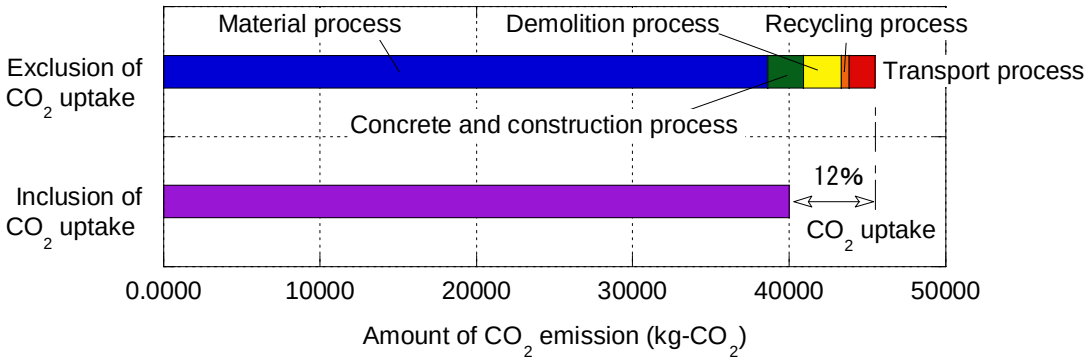

Fig.8 Comparison between exclusion and inclusion of CO_2 uptake in calculating $LCCO_2$

ACKNOWLEDGEMENT

The authors would like to express their sincerely gratefulness to Mr. Kanda and Mr. Sone at National Institute for Land and Infrastructure Management for offering precious survey data..

REFERENCES

[1] Naik, T. R. and Moriconi, G., "Environmental-friendly durable concrete made with recycled materials for Sustainable concrete construction." In: V. M. Malhotra and K. Sakai, Eds.

Sustainable development of cement, concrete and concrete structure, Proceedings of CANMET/ACI/JCI three-day international symposium, Toronto, Canada, pp.485-505, 2005.
[2] Engelsen, C. J., Mehus, J., Pade, C. and Sæther, D. H., "Carbon dioxide uptake in demolished and crushed Concrete." Nordic Innovation Centre project number 03018, Norwegian Building Research Institute, 2005.
[3] Japan Concrete Institute, "Technical Committee Report on Carbonation of Concrete", 1993.(in Japanese)
[4] Lagerblad, B., "Carbon Dioxide Uptake during Concrete Life Cycle – State of the Art." Nordic Innovation Centre project number 03018, Swedish Cement and Concrete Research Institute, CBI, 2005.
[5] Pommer, K. and Pade, C., "Guidelines - Uptake of carbon dioxide in the life cycle inventory of concrete." Nordic Innovation Centre project number 03018, Danish Technological Institute, 2005.
[6] Japan Ministry of Land, Infrastructure, Transport and Tourism, "Survey on Recycling of Construction By-product in The Year 2008", 2010.(in Japanese)
[7] Takahashi H., "Recycling of Concrete-rubble, - Feature Issue - Technology Status of Recycling of Construction By-product and Future Prospects", Mechanization of Construction, No.613, pp.6-10, Japan Construction Machinery and Construction Association, 2001.(in Japanese)
[8] Kikuchi, T. and Kuroda, K., "Carbon Dioxide Uptake in Demolished and Crushed Concrete", Journal of Advanced Concrete Technology, Volume 9, No. 1, pp.115-124, 2011.
[9] Kanda, T., Sone, S. and Kishida, H., "CO_2 Uptake over Service Period of Concrete Structures and Recycling Process of Concrete Rubbles", Concrete Journal, Vol.49, No.8, pp.9-16, 2011.(in Japanese)
[10] Japan Society of Civil Engineers, "Environmental assessment of Concrete (Part 2)", Concrete engineering series No.62, pp.32-40, 2004.
[11] http://law.e-gov.go.jp/htmldata/H18/H18F15002002003.html.(in Japanese)

Proceedings of the 3rd JCI-KCI-TCI Symposium on Recent Advancement of Technologies in Concrete Engineering
Japan Concrete Institute, July 2012

CYCLIC BEHAVIOR OF REINFORCED CONCRETE BEAMS WITH CORRODED TRANSVERSE REINFORCEMENT

Yu-Chen Ou
Assistant Professor, Department of Construction Engineering, National Taiwan University of Science and Technology, Taipei, Taiwan.
E-mail: yuchenou@mail.ntust.edu.tw

Hou-Heng Chen
Formerly Master student, Department of Construction Engineering, National Taiwan University of Science and Technology, Taipei, Taiwan

ABSTRACT

The seismic performance of reinforced concrete beams with corroded transverse reinforcement was examined using cyclic loading on full-scale specimens. Seven beams were constructed. One beam was used as control without corrosion. The other six beams were subjected to six different levels corrosion. The corrosion was induced by imposing a constant current on the transverse reinforcement in the potential plastic hinge region. Each corroded beam was accompanied by a specimen for corrosion observation. The specimen for corrosion observation was intended to simulate the corrosion condition of the beam. After the corrosion process, the beam was tested using cyclic loading to examine the seismic performance. The specimen for corrosion observation was demolished to investigate the corrosion condition of transverse reinforcement. Test results showed that as the corrosion level increased, the failure mode changed from flexural-shear failure due to crushing of core concrete to flexural-shear failure due to fracture of transverse reinforcement. Corrosion of transverse reinforcement did not have a significant effect on the peak applied load the beams. However, it had a significant detrimental effect on the deformation capacity of the beams. The ultimate drift, the ductility and the plastic rotation capacities greatly decreased as the corrosion level increased.

Keywords: *Reinforced concrete beams; corrosion; transverse reinforcement, cyclic loading; seismic.*

1 INTRODUCTION

Due to humid weather and wind born salts, steel reinforcement in reinforced concrete structures located near the ocean are prone to corrosion. Fig. 1 shows two corroded school buildings in Taiwan. Severe corrosion of steel reinforcement and spalling of cover concrete can be observed, significantly damaging the structural capacity. Many research activities have been paid to study the effects of steel reinforcement corrosion on the structural performance [1-7]. However, very little effort was devoted on the study of seismic performance of corroded structural members using cyclic loading [8-9], particularly on the effects of transverse reinforcement corrosion. Previous research carried out by Ou et al. [10] has shown that the failure mode of a beam with corroded longitudinal and transverse reinforcement can change from flexural failure to flexural-shear failure. However, only one specimen exhibited flexural-shear failure. This research carried out cyclic tests on beams with corrosion only induced in the transverse reinforcement. Six different levels of corrosion were examined. The objective of this research is to better understand the effects of transverse reinforcement corrosion on the seismic performance of reinforced concrete beams.

Figure 1. Corroded members of reinforced concrete buildings

2 EXPERIMENTAL PROGRAM

2.1 Specimen Design

The specimen is designed conforming to the ACI code [11]. Fig. 2(a) shows the side view of the specimen. The specimen contains a beam connected to a block. The end of the beam connected to the block is referred to as fixed end while the other end referred to as free end. The cross-sectional view of the beam is shown in Fig. 2(b). The beam was designed with three #9 bars in the top and bottom sides of the beam and with #4 hoops having a horizontal spacing of 10 cm. The beam has a tension longitudinal reinforcement ratio of 1.5% and volumetric ratio of transverse reinforcement (hoops) to the concrete core of 1.8%. Shear strength of the beam was designed according to shear demand corresponding to moment strength assuming 1.25 yield stress in the longitudinal reinforcement. Concrete shear strength is ignored in the shear strength calculation. Fig. 2(c) shows the corrosion observation specimen. The specimen is the replication of the portion of the beam from fixed end extending 60 cm towards to the free end. Fig. 2(d) shows the photo of rebar cages of the beam and corrosion observations specimens. There are in total seven sets of the specimens. One set is the control without corrosion while the other six sets are subjected to different levels of corrosion.

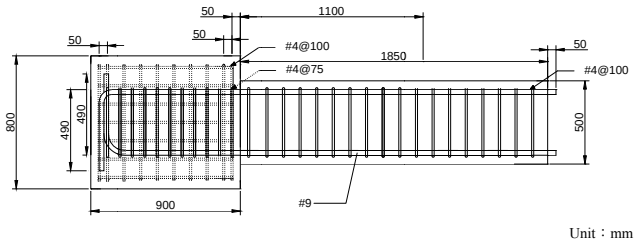

Unit：mm

(a)

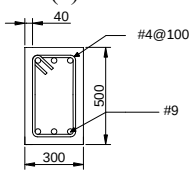

Unit：mm

(b)

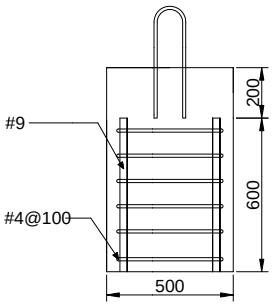

(c)

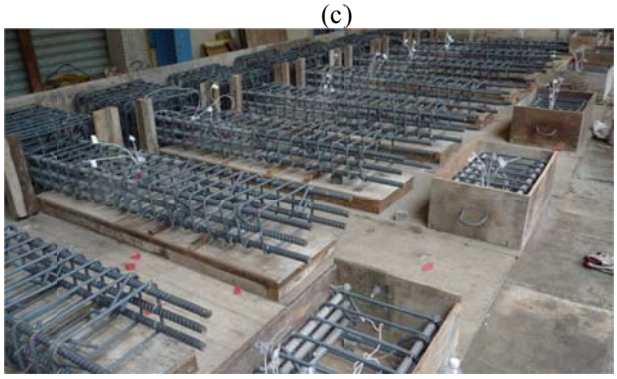

(d)

Figure 2. Specimen design: (a) side view; (b) cross-sectional view; (c) corrosion observation specimen; and (d) photo.

2.2 Test setup

Corrosion of transverse reinforcement (hoops) was induced by imposing electrical current to the reinforcement. Corrosion is assumed to occur only in the potential plastic hinge region of the beam, from the fixed end extending 50 cm to the free end of the beam (one full depth of the beam). To accelerate the corrosion process, six hoops from the fixed end of the beam were imposed with electrical current by connecting the ends of the hoops to the anodes of D.C. power supplies. The 50-cm region was enclosed with a water tank infilled with 5% NaCl solution. Four copper plates were placed against the four sides of the beam in the water tank. The cathodes of the power supplies were connected to the copper. Figs 3(a) and 3(b) show the elevation view and cross-sectional view of the test setup. Fig. 3(c) shows the photo of the acceleration corrosion process. The beam specimen and the corrosion observation specimen in each set were subjected to the corrosion process starting from the same time and lasted for the same period.

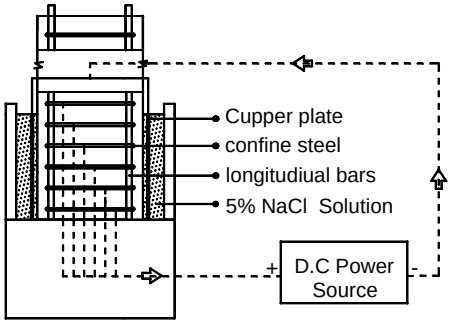

(a)

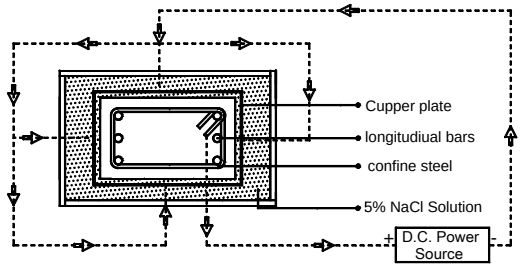

(b)

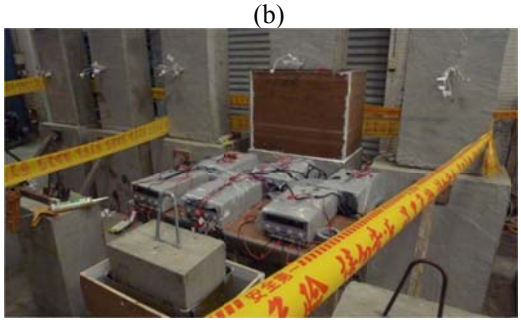

(c)

Figure 3. Accelerated corrosion process: (a) elevation view; (b) top view; and (c) photo.

After the corrosion process, the corrosion observation specimen was demolished and the reinforcement was removed for corrosion measurement. The beam specimen was subjected to cyclic loading to test the seismic performance. The block of the specimen was fixed to the strong floor. Cyclic load was applied using a hydraulic actuator attached to the beam at 120 cm from the fixed end. The beam was cyclically loaded up to drift levels of 0.25%, 0.375%, 0.5%, 0.75%, 1.0%, 1.5%, 2.0%, 3.0%, 4.0%, 5%, and 6%. Each drift level was repeated twice. The actuator was real-time controlled using the relative displacement between the loading point and the fixed end of beam measured during testing to achieve the precisely prescribed drift levels.

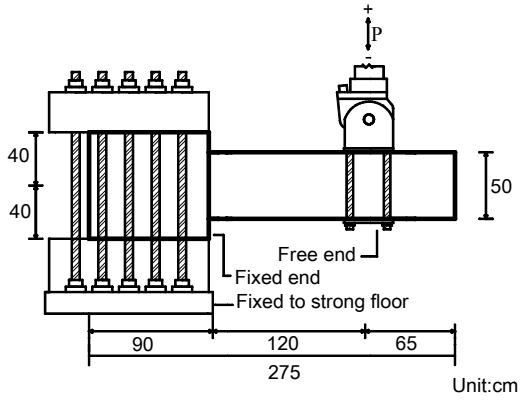

(a)

(b)

Figure 4. Cyclic loading setup: (a) details; and (b) photograph

3 RESULT AND DISCUSSION

3.1 Weight Loss and Minimum Residual Cross-Sectional Area

Table 1 lists the corrosion weight loss and the minimum residual cross-sectional area for all the specimens. The values listed in the table are the average of the values from the six hoops subjected to accelerated corrosion. The minimum residual cross-sectional area was calculated based on the average of three diameters measured at the smallest cross section. It can be seen from the table that as the corrosion level increases, the weight loss increases while the minimum residual cross-sectional decreases. When the weight loss reaches approximately 35%, the accelerated corrosion process could not be continued due to extraordinary high electrical resistance. It was later confirmed that the high resistance was due to the fact that the hoops were broken.

Figure 5 shows the distribution of cracks on the four faces of the corrosion observation specimens. The red line in each plot represents the cross section which has the maximum total crack width. It is interesting to note that the cracking directions of most of the cracks are along the longitudinal direction of the beam rather than along the hoop direction. The corrosion crack distribution and maximum total crack width were found to be similar between the corrosion observation specimen and the beam specimen. This implies the corrosion conditions between the two types of specimens are similar.

Table 1: Weight loss and minimum residual cross-sectional area

Specimen	Weight loss (%)	Minimum residual cross-sectional area (mm^2)
B_t-0	0.0	127
B_t-3	2.9	99
B_t-6	5.9	84
B_t-11	11.7	70
B_t-12	12.4	78
B_t-16	15.7	59
B_t-35	35.1	0

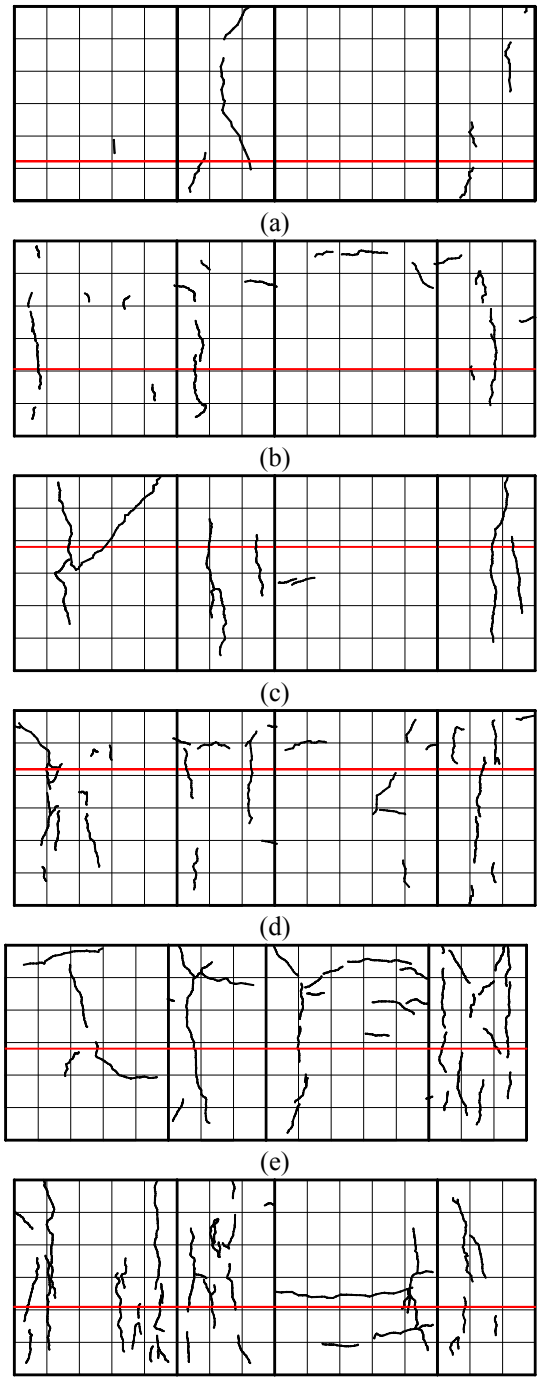

Figure 5. Corrosion crack pattern: (a) Bt-3; (b) Bt-6; (c) Bt-11; (d) Bt-12; (e) Bt-16; and (f) Bt-35

3.2 Cyclic Test Results

Figure 6 shows the damage distribution of the specimens at selected drift levels. Figure 7 illustrates the hysteretic behavior of all the specimens with the instances of spalling of cover concrete and fracture of hoops indicated. Table 2 lists various performance indicators for the specimens. The symbols used in Table 2 as defined as follows: Δ_y denotes yield drift; Δ_u denotes ultimate drift, defined when the applied load declines more than 20% from the maximum value; P_{max} denotes maximum applied load; μ denotes ductility, defined by the ratio of Δ_u to Δ_y; Δ_p denotes plastic rotation, defined as the difference between Δ_y and Δ_u. Definitions of Δ_y, P_{max}, and Δ_u are illustrated using an envelope response of the hysteretic behavior of a specimen in Fig. 8. To calculate the yield point, the nominal applied load P_n is calculated first using the reinforced concrete beam theory. Next, a line in Fig. 8 can be formed by connecting the origin and the point on the envelope curve corresponding to 75% P_n. Finally, the line is extended to P_n. The drift on the line corresponding to P_n is the yield drift Δ_y.

The specimen without corrosion (Bt-0) showed a typical flexural-domindated beahvior until the first cycle of the 5% drift (Fig. 6(a)). Flexural-shear cracks were well distributed within the 70-cm region from the fixed end. Significant spalling of concrete started at 5% drift. At the second cycle of the 5% loading, the core concrete near the fixed end of the beam started to spall off. As a result, the beam lost its shear capacity, showing significant shear deformation in the 40-cm region of the beam from the fixed end. The applied load dropped drastically. This specimen failed in a flexural-shear failure mode. For specimen Bt-3, the beam showed flexual-domindated behavior until the first cycle of 4% drift. At the second cycle of 4% drfit loading, significant spalling of cover concrete occurred. At 5% drift, most of the cover concrete of the 40-cm region spalled off (Fig. 6(b)). A significant part of the core concrete also spalled off. The beam failed with significant shear deformation in the 40-cm region from the fixed end. The failure mode is a flexural-shear type same as the specimen Bt-0. Specimen Bt-6 showed a flexural-shear failure mode with a similar failure process to the previous two specimens except that the hoop closest the fixed end of the beam fractured at the second cycle of the 4% drift loading. Comparison among specimens Bt-0, Bt-3 and Bt-6 at 5% dirft as shwon in Figs. 6(a), 6(b) and 6(c), respectively, revealed that as the coroosion level increases, the extent of spalling of cover concrete increases. In adition, the peak applied load and ultimate drift decrease as the corrosion level increases (Table 2). However, the corroded beams (Bt-3 and Bt-6) still possess a drift capacity more than 4% with a fairly ductile behavior (Figs. 7(b) and 7(c)) similar to the control specimen. This suggests that a beam designed based on the current design code is able to sustain 6% corrosion weight loss in the hoops without significantly impairing the seismic capacity.

Specimens Bt-11, Bt-12 and Bt-36 also showed a flexural-shear failure mode but with a different failure process. The failure of these specimens was

preceded with a major diagonal shear crack as shown in Figs. 6(d), 6(e) and 6(f), respectively. Subsequently, a large portion of cover concrete spalled and then fracture of transvers reinforcement occurred as indicated in Figs. 7(d), 7(e) and 7(f), respectively. Note that negative drift loading was applied before positive drift loading in each cycle of loading. It appears that with a corrosion weight loss in between 11% and 16%, the corroded hoops were not able to restrain the diagonal shear cracking. The beams failed soon after the diagonal cracking formed. The peak applied loads of these specimens are similar to that of specimen Bt-6 (Table 2). However, the drift capacities were reduced significantly with ultimate drifts ranging between 2% to 3%. The higher the corrosion level, the lower the drift capacity. These three beams show a hysteretic behavior much less ductile than the previous three specimens (Bt-0 to Bt-6).

The hoops of specimen Bt-35 were corroded to fracture prior to cyclic testing. Several major diagonal cracks formed at the first negative 2% drift loading (Fig. 6g). When the load was reversed to the positive 2% drift, a large portion of cover concrete spalled, exposing several fractured hoops and leading to failure of the beam as shown in Fig. 7(g).

All the specimens were able to develop yielding of longitudinal reinforcement as evident by the clear softening of the hysteretic behavior (Fig. 7) before failing in shear. It appears that the concrete shear strength is sufficient in resisting shear demand in the elastic response region of the specimens. Corrosion of hoops took effect on the beam response after the concrete cracked and started to lose its shear capacity. Since the longitudinal reinforcement of all the specimens had yielded before failure, the peak applied load did not decrease significantly as the corrosion level increased. The reduction of the peak applied load in specimen Bt-35 is only 13% compared to the control specimen. On the other hand, the ultimate drift, the ductility and plastic rotation capacity decreased considerably as the corrosion level increased. This is because corrosion decreased the ability of the hoops to confine the core concrete (specimens Bt-3 and Bt-6) and to restrain shear cracks (specimens Bt-11, Bt-12, Bt-16, and Bt-35), accelerating failure of the beams and hence reducing deformation capacity.

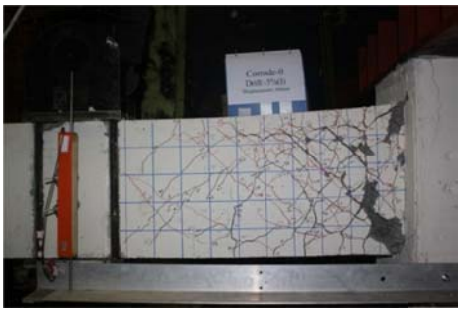
(a)

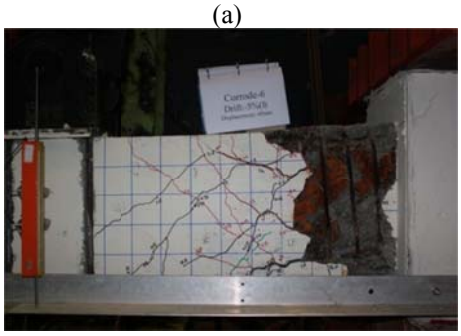
(b)

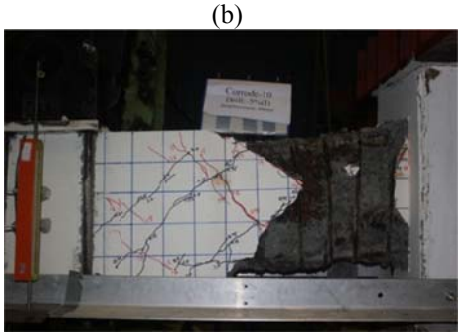
(c)

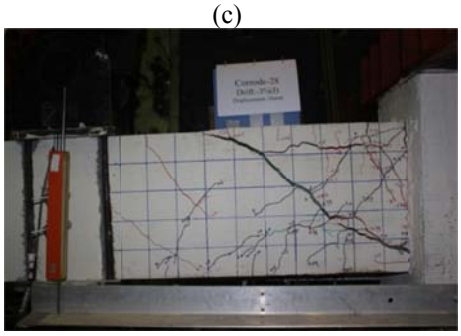
(d)

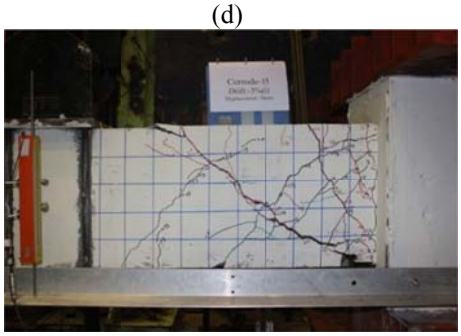
(e)

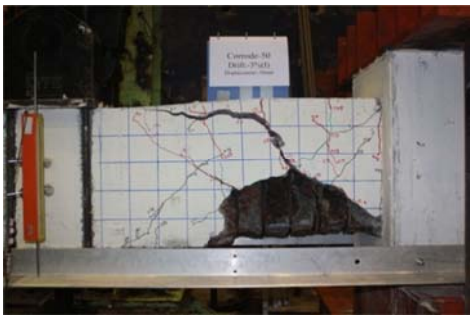

(f)

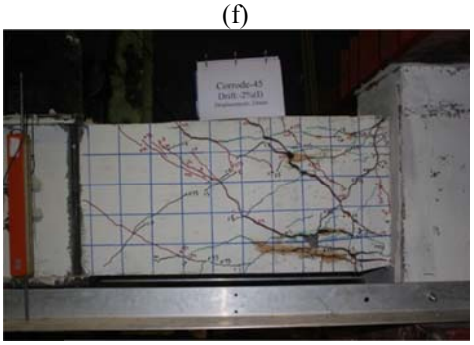

(g)

Figure 6. Damage distribution: (a) Bt-0 at -5% drift; (b) Bt-3 at -5% drift; (c) Bt-6 at -5% drift; (d) Bt-11 at -3% drift; (e) Bt-12 at -3% drift; (f) Bt-16 at -3% drift; and (g) Bt-35 at -2% drift.

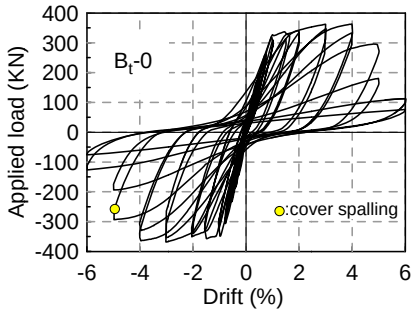

(a)

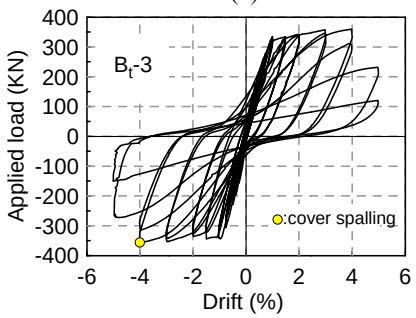

(b)

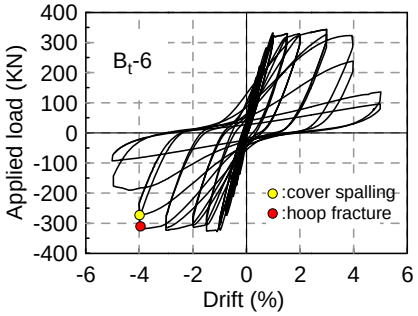

(c)

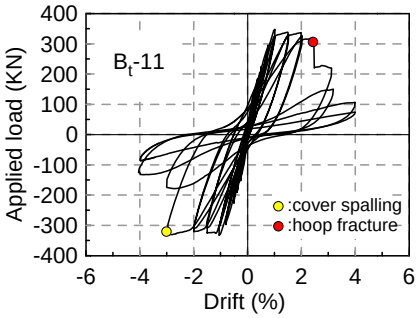

(d)

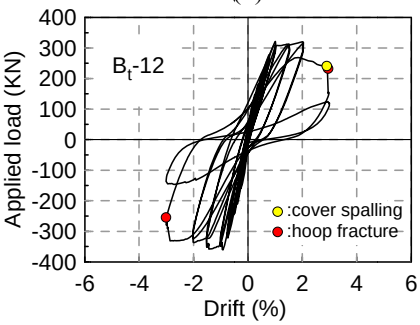

(e)

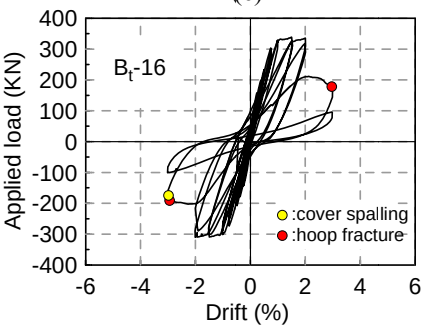

(f)

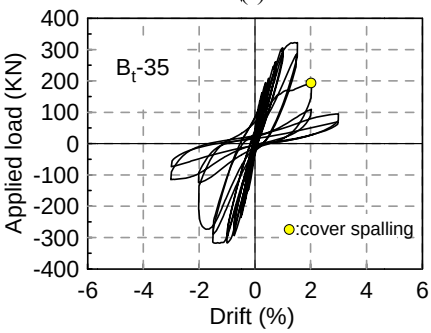

(g)

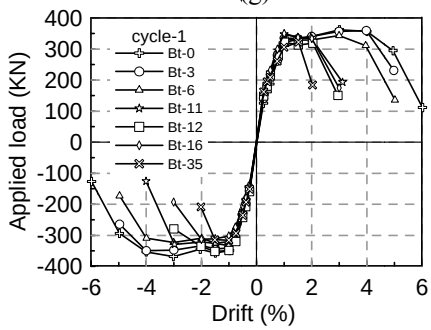

(h)

Figure 7. Hysteretic behavior: (a) Bt-0; (b) Bt-3; (c) Bt-6; (d) Bt-11; (e) Bt-12; (**f**) Bt-16; (g) Bt-35; and (h) envelope responses of all specimens

Table 2. Performance indicators

Specimen	Δ_y(%)	P_{max}(kN)	Δ_u(%)	μ	Δ_p(%)
B_t-0	0.89	365	4.97	5.6	4.08
B_t-3	0.81	355	4.67	5.7	3.86
B_t-6	0.84	333	4.27	5.1	3.43
B_t-11	0.80	336	2.87	3.6	2.07
B_t-12	0.77	337	2.66	3.4	1.89
B_t-16	0.81	332	2.43	3.0	1.62
B_t-35	0.83	318	1.78	2.2	0.95

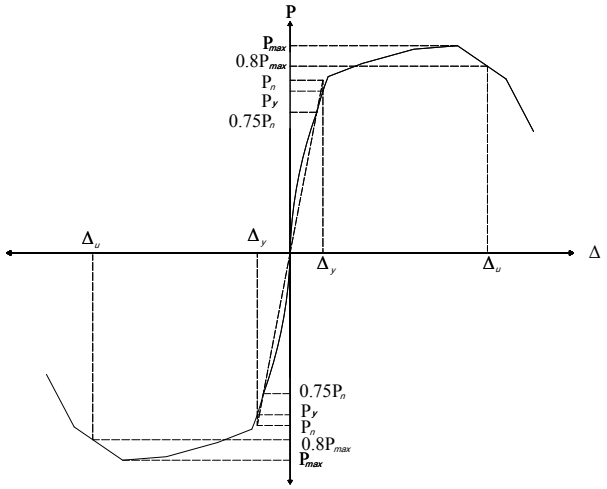

Figure 8. Idealization of the envelope response

4 CONCLUSION

Reinforced concrete beams with corroded transverse reinforcement were tested using cyclic loading to examine the seismic performance. Test results showed that as the corrosion level increased, the failure mode changed from flexural-shear failure due to crushing of core concrete to flexural-shear failure due to fracture of transverse reinforcement. Corrosion of transverse reinforcement did not have a significant effect on the peak applied load of the beams. However, it had a considerable detrimental effect on the deformation capacity of the beams. The ultimate drift, the ductility and the plastic rotation capacity decreased significantly as the corrosion level increased.

ACKNOWLEDGEMENT

The authors would like to thank the National Science Council of Taiwan and Taiwan Building Technology Center of NTUST for financially supporting this research..

REFERENCES

[1] Al-Sulaimani, G. J., Kaleemullah, M., Basunbul, I.A., and Rasheeduzzafar. (1990), "Influence of corrosion and cracking on bond behavior and strength of reinforced concrete members," *ACI Structural Journal*, Vol. 87, No. 2, 220-231.

[2] Rodriguez, J., Ortega, L. M., and Casal, J. (1997), "Load Carrying Capacity of Concrete Structures with Corroded Reinforcement," *Construction and Building Materials,* Vol. 11, No. 4, 239-248.

[3] Huang, R., and Yang, C. C. (1997), "Condition assessment of reinforced concrete beams relative to reinforcement corrosion," *Cement and Concrete Composites,* Vol. 19, 131–137.

[4] Mangat, P. S., and Elgarf, M. S. (1999), "Flexural strength of concrete beams with corroding reinforcement," *ACI Structural Journal*, Vol. 96, No. 1, 149–58.

[5] Castel, A., François, R., and Arliguie, G. (2000), "Mechanical behaviour of corroded reinforced concrete beams—Part 1: Experimental study of corroded beams," *Materials and Structures,* Vol. 33, No. 9, 539-544.

[6] Maaddawy, T.E.l., Soudki, K., and Topper, T. (2005), "Long-term performance of corrosion-damaged reinforced concrete beams," *ACI Structural Journal*, Vol. 102, No. 5, 649-656.

[7] Higgins, C., and Farrow, III W.C. (2006), "Tests of reinforced concrete beams with corrosion-damaged stirrups," *ACI Structural Journal,* Vol. 103, No. 1, 133-141.

[8] Kato, E., Iwanami, M., and Yokota, H. (2006). "Deterioration in Ductility of RC Beams with Corroded Reinforcement," *Proceedings of the 2nd fib International Congress*, Naples, Italy, pp.1-8.

[9] Kobayashi, K. (2006). "The Seismic Behavior of RC Member Suffering from Chloride-induced Corrosion," *Proceedings of the 2nd fib international congress,* Naples, Italy.

[10] Ou, Y. C., Tsai, L. L., and Chen, H. H. (2011). "Cyclic performance of large-scale corroded reinforced concrete beams," *Earthquake Engineering and Structural Dynamics*. (Published Online)

[11] ACI Committee 318. (2008), *Building Code Requirements for Structural Concrete (ACI 318-08) and Commentary (ACI 318R-08)*, American Concrete Institute, Farmington Hills, MI, U.S.A.

SIMULATION OF SHRINKAGE RELATED BEHAVIOR OF CONCRETE STRCTURES BASED ON DURABILITY MECHANICS

Takumi Shimomura
Department of Civil and Environmental Engineering, Nagaoka University of Technology, Japan
Kenichiro Nakarai
Department of Civil and Environmental Engineering, Hiroshima University, Japan
Ippei Maruyama
Department of Environmental Engineering and Architecture, Nagaya University, Japan

ABSTRACT

Shrinkage related problems are vigorously discussed in recent years in Japan from the viewpoint of shrinkage of aggregate and excessive concrete shrinkage. However, influences of excessive shrinkage on mechanical performance of concrete structures have not been enough clarified. The technical committee on evaluation of effect of shrinkage based on durability mechanics (JCI-TC-105A) analyzed previous studies and design methods in this field as coupling problem between material and structure on the basis of concept of systematization which had been proposed by the working group on durability mechanics in JCI-TC-061A. Based on the investigation of the influences of shrinkage on mechanical performance and durability of structures, the committee aimed to find the direction of research in this field and to contribute to re-establishment of design system of structures.

Keywords: *shrinkage, durability, creep, crack, numerical simulation*

1 INTRODUCTION

1.1 Background

Since excessive cracks and deformation due to large shrinkage of concrete in the PRC bridge were reported, studies on the mechanism of shrinkage and the influence of shrinkage on structural performance became one of the important topics in concrete engineering in Japan. For example, the characteristic of drying shrinkage of concrete to be used in structural design was strictly regulated in the standard specifications by Japan Society of Civil Engineers (JSCE) and Architectural Institute of Japan (AIJ). In Japan Concrete Institute (JCI), a special technical committee was established to discuss this topic. It has not been clarified, however, the influence of shrinkage on structural performance or long-term durability of concrete structures so far.

The Technical Committee on Shrinkage Effect Evaluation based on Durability Mechanics (JCI-TC-105A) was established in JCI in 2010 to investigate the influence of concrete shrinkage on structural performance including long-term durability. The chair of the TC was Prof. Ryoichi Sato of Hiroshima University. The TC inherited the approach based on the Durability Mechanics proposed from the Working Group on Durability Mechanics within the Technical Committee on Time-Dependent Behavior of Cement-Based Materials (JCI-TC-061A) was used. The chair of this WG on Durability Mechanics was also Prof. R. Sato.

JCI-TC-105A consists of two working groups. One is the working group on the influence of shrinkage on structural performance chaired by A. Prof Takumi Shimomura of Nagaoka University of Technology. This WG summarized the structural influence from the point of the view of the mechanism, modeling and design code. The other was the working group on the influence of cracks on durability chaired by Prof. Isao Ujike of Ehime University. This WG summarized the material influence from the point of the view of the mechanism and modeling.

1.2 Approach to shrinkage issue based on durability mechanics

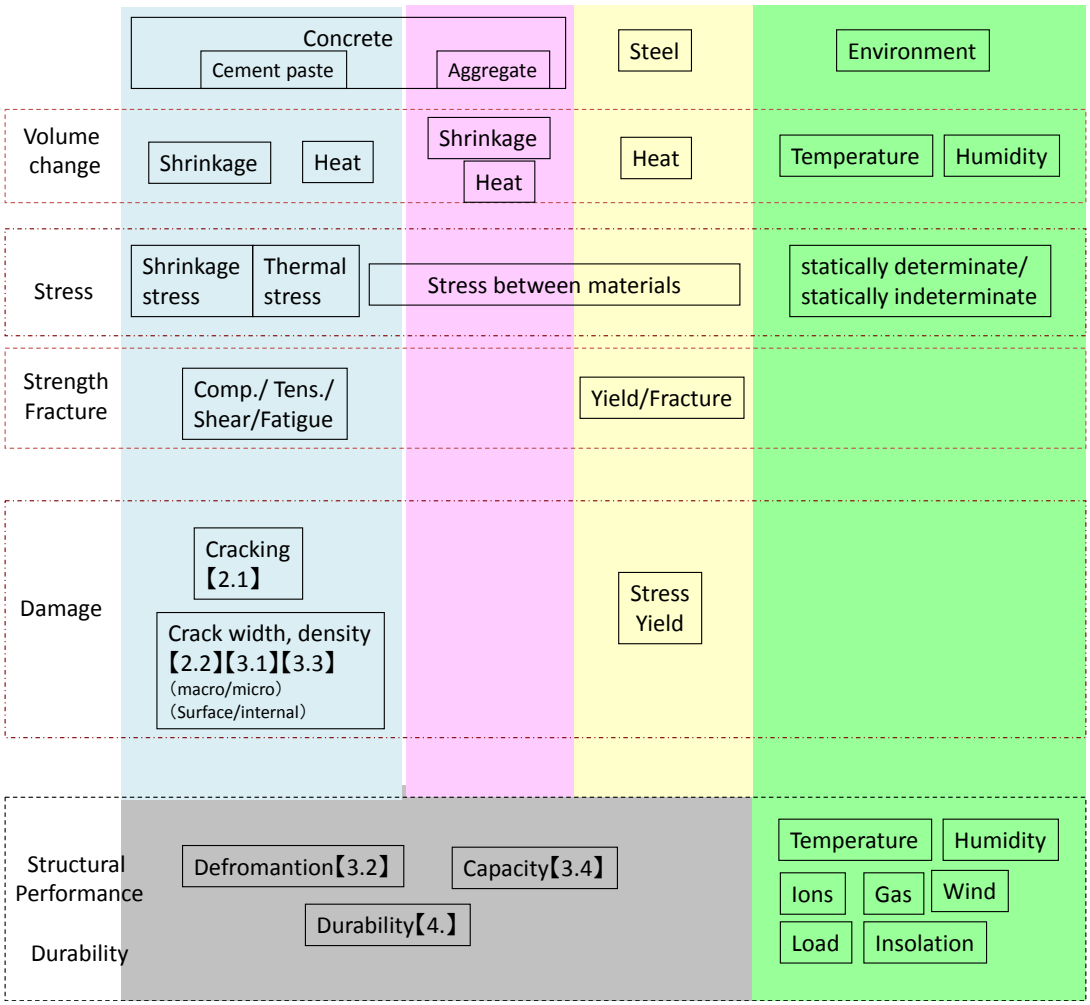

Fig. 1 Approach to shrinkage issue based on Durability Mechanics

Durability Mechanics was firstly proposed in the 6th CONCREEP in 2001 by Prof. Ulm as a new discipline of Engineering Mechanics concerned with early-stage degradation and a number of critical problems related to safe and economic hazardous waste storage [1]. Durability Mechanics includes three sub-fields: 1) degradation kinetics, 2) chemo-mechanical couplings at the materials level and 3) prevention, diagnosis/prognosis on the structural level. Inspired by Ulm's proposal and based on stocks of related studies in Japan, the Durability Mechanics WG of JCI-TC-061A defined again Durability Mechanics as a discipline where performance evaluation of concrete structures is dealt with by micro/macroscopic chemo-physical models taking account of complex couplings of materials and structures in space-time continua.

The WG on Durability Mechanics of JCI-TC-061A proposed the following redefinition of durability mechanics based on the proposal of Coussy & Ulm [1] in order to systematize each deterioration factor so as to lead finally to the prediction and evaluation of the structural performance of concrete structures: "Durability Mechanics for concrete structures is one of the academic disciplines of Engineering Mechanics for the systematic prediction and evaluation of time-dependent behavior of concrete materials and structures, in which the chemo-mechanical deterioration of cementitious materials over time due to chemical reaction, environmental action, and external load, can be described by physicochemical models of reaction, transport, fracture and their coupling, and the performance of concrete structures over time can be also predicted by constitutive models of deteriorating materials."

Figure 1 shows the outline of the research activities of JCI-TC-105A and the related contents in this paper. The volumetric change of concrete is caused by temperature change and autogenous/ drying shrinkage. Then, restraint of shrinkage by the reinforcement or another part of the structure causes tensile stress in the structure. When the stress reached the fracture criterion, cracks are generated. The width and number of the cracks and the induced stress affects the structural performance and durability of the structure. Here, the boundary conditions such as environmental temperature,

humidity and external load also affect the performance. The committee tried to extract the essential physicochemical phenomenon governing the performance of concrete structures damaged by shrinkage.

2 INDUCEMENTS OF STRESS AND DAMAGE BY SHRINKAGE OF CONCRETE

2.1 Initial crack due to shrinkage

One of the significant influences by concrete shrinkage on structures is that shrinkage causes cracks in structures. Drying shrinkage crack in structure is simulated through moisture transport analysis, stress analysis due to drying shrinkage and analysis of development and propagation of crack in structures. However, there has been no general method for numerical simulation of shrinkage crack in structures so far although it has analogy with simulation of thermal crack in structures as mathematical problem. In the committee, following methods were investigated.

(1) Numerical simulation of shrinkage crack in structures.

Time-dependent stress analysis considering creep and crack propagation analysis were focused among the technical problems in numerical prediction of shrinkage crack in structures.

Since drying shrinkage of concrete proceeds very slowly except around the surface at the initial stage of drying, consideration of concrete creep is necessary to evaluate shrinkage stress adequately. There are various methods for consideration of creep in stress analysis depending on type of creep model and computational procedure. Approximated method such by time-dependent effective elastic modulus is sometimes adopted to avoid complicated calculation.

In the committee report, creep analysis based on integration of stress history is introduced. In addition, methods for stress analysis and crack propagation analysis after the first crack in generated are also described.

(2) Consideration of autogenous and drying shrinkage in thermal crack analysis

Stress due to autogenous shrinkage of concrete sometimes contributes thermal stress in mass concrete structures. It is reported that consideration of autogenous shrinkage in thermal stress analysis does not only improve accuracy in stress evaluation but also makes prediction of crack location and direction possible [3].

(3) Crack prediction in beam and wall members based on shrinkage stress analysis

Since shrinkage crack likely occurs thin members that can be simply modeled as beam or wall, prediction method based on stress analysis with simplified analytical dimension and boundary condition is sometimes used.

(4) Analysis of crack in actual bridges

If shrinkage crack in structures can be predicted in high accuracy by numerical simulation before construction, countermeasure to avoid crack can be taken at design and construction stage. In order to develop numerical prediction method for shrinkage crack in structures, it is necessary to explain the pattern, location and size of crack observed in actual structures. There are many influencing factors on crack in actual structures. In case of super structure of bridge, cracks are affected not only by shrinkage characteristic of concrete but also many factors such as size and thickness of structures, arrangement of reinforcement and PC sheath, reduction of cross sectional area of concrete due to PC sheath, order of concrete casting, prestress and drying condition. The committee investigated several cases of crack in actual structures including PC bridges. Some hypotheses on reason of observed crack were assumed. Their verification shall be done in the further study.

2.2 Influences of creep and shrinkage on crack width in RC and PRC structures

In most cases, performance of structures is not degraded immediately even if crack is developed. In case of RC and PRC structures, crack width during service life is controlled within the limit value which assures the necessary structural performance instead of avoiding crack. Therefore, prediction of crack width is of importance in structural design. It is apparent that creep and shrinkage of concrete affect time-dependent change of crack width in structures.

(1) Previous studies on effect of shrinkage on crack width

Many studies have been done on crack width in concrete structures. Ishibashi proposed evaluation method for crack width, in which shrinkage of concrete between flexural cracks in the member is regarded as free shrinkage after the crack is developed as shown in Fig. 2 [4]. Thereafter, Seki experimentally clarified that the fact that shrinkage of concrete between cracks can be regarded as free shrinkage is attributable to greater shrinkage of concrete near cracks [5].

Though effect of creep and shrinkage on crack width is often discussed together, effect of creep on crack width is not as apparent as that of shrinkage. Several effects can be considered, namely compression creep in flexural member, tensile creep between cracks and boding creep which is time-dependent reduction of bonding between concrete and reinforcement. It should be noted that these phenomena affect crack width by different mechanisms.

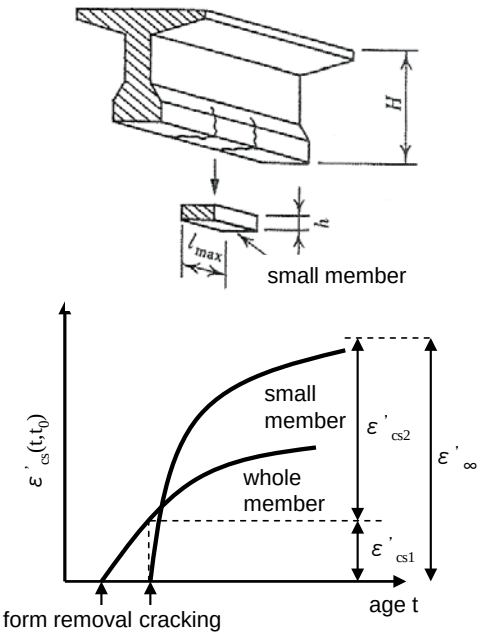

Fig.2 Evaluation method of shrinkage of concrete between cracks [4]

(2) Recent experimental and analytical studies on crack width

Accurate prediction of crack width is still needed as an index in structural design and as a parameter for prediction of deterioration process in long time. Recent experimental and analytical studies on crack width done by committee members are introduced in the committee report.

3 EFFECT OF SHRINKAGE OF CONCRETE ON STRUCTURAL PERFORMANCE

3.1 Effect of creep and shrinkage on deformation and stress in road and railway structures

Effect of creep and shrinkage of concrete has been considered in terms of various ways in design of road and railway structures such as bridges. There are some provisions and design values whose origin is not clear in current design code. For example, it is recommended in JSCE standard specification and several other design codes that shrinkage may be set as 150μ when redundant force in rigid frame structures is calculated by means of elastic analysis. This provision was adapted in the first edition of the standard specification in 1931 and has been succeeded in the present edition. Since the value of shrinkage 150 μ is apparent value including the effect of creep, it does not mean that the shrinkage of unrestrained specimen is this value. In addition, the value 150 μ is standard one though it varies in reality according to mix proportion of concrete, size of cross section, environmental condition, reinforcement arrangement and age at start of drying. It is, therefore, regarded that 150 μ shrinkage may be used when these conditions are within standard range.

There has been no fatal inadequacy in using 150 μ of shrinkage in design. However, since important structural dimension is determined by this provision in some cases, it is necessary to clarify the ground and applicable range of this provision. Effect of creep and shrinkage on redundant stress and crack width in actual structures has been vigorously investigated in railway structures.

3.2 Recent topic on long-term deflection of PC bridge

Long-term deflection of prestressed concrete bridges is one of the creep and shrinkage related structural problems to which researchers and engineers pay attention recently. It was pointed out that calculated long-term deflection by means of prediction equation for creep and shrinkage for design varies with respect to equations used and underestimates actual deflections. The reason of this is considered as follows.

Deflection of PC bridges constructed by cantilever method is affected by not only final value of creep coefficient but also its time-dependent development, because loading age of each segment is different. The time-dependent change of creep coefficient varies with prediction equations. In addition, temperature and humidity conditions of inside and outside surfaces of upper slab, webs and bottom slab in box cross section of PC bridge are different with each other. The prediction equations for creep and shrinkage in the standard specifications fail to produce accurate results because they evaluate mean value of creep and shrinkage in cross section. Moreover, prediction equation for creep and shrinkage had been proposed mainly to be adopted to evaluate short term creep and shrinkage such as prestress loss.

To overcome these problems, a multi-scale numerical simulation was applied, in which moisture transport and heat transfer in the structure is considered as actual condition and enhanced creep and shrinkage models based on microscopic physicochemical mechanisms are incorporated [6].

3.3 Effect of shrinkage of concrete on building elements

In this section, effects of shrinkage and creep of concrete on deformation and stress in building elements are summarized. Especially, related parts in lows and standards regarding building structure, effect of volume change of concrete on an earthquake response, potential problem of ultra-high-strength concrete which has large autogenous shrinkage, and CFT structure are dealt and explained.

(1) Regulations and standards regarding crack width and deformation.

In Building Standards Act in Japan, there is no

description about crack width. In "Recommendations for Design and Construction of Partially Prestressed Concrete (Class III of Prestressed Concrete) Structures (1986)" by AIJ, maximum crack width is shown as a function of environmental conditions and acting forces. Regarding "AIJ Standard for Structural Calculation of Reinforced Concrete Structures (revised 2010)" (hereafter AIJ RC-standard), long-term allowable stress of rebars is defined and increase of crack width is controlled in an indirect manner. Limit value of crack width is 0.2 - 0.25mm in member subjected to outer environmental condition and 0.3 - 0.4 mm in member located in a building. Regarding shear cracks, generally it is prohibited under permanent loadings, but in RC beam, it is allowed to use the allowable stress of RC member including the contributions of rebars. It is recommended to determine the limit value of deflection of slabs and beams in AIJ RC-standard, and Lx/250 is shown as a recommended limit value. Long-term deflection δ_L of slabs is 12 - 16 times of elastic deflection in the case of both ends fixed condition, and is 6 - 12 times of elastic deflection in the case of simply-supported condition. AIJ RC-standard includes more precise prediction formula in appendix.

(2) Stress evaluation in an indeterminate structure and earthquake response

Aoyama [7] proposed an evaluation method for stress and force in reinforced concrete member in indeterminate structures. And he did numerical and experimental works regarding self-induced stress due to concrete volume change, and he concluded that self-induced stress does not have any effect on the strength of structures in the case of total failure mode but it has effect on the strength of structures in the case of local failure mode. In addition, he indicated that volume change of concrete has large effect on a stiffness of structure and formulated prediction equations. They are validated by the experiments.

From the numerical approach, it is confirmed that drying shrinkage and creep of concrete produces indeterminate stress in RC member and it can exceed the cracking strength of concrete. And such cracking in reinforced concrete member decrease the stiffness of structure and resultantly, performance of earthquake response is altered.

(3) Shrinkage and creep of ultra-high-strength concrete

Nowadays, using concrete whose design strength concrete is over 100 MPa is commonly applied for ground and under-ground structures of high-rise residence with more than 40 stories [8]. It is important to control the axial strain in the reinforced concrete member because large axial force. And it has been experimentally confirmed that the surface cracking, cracking around rebar (sometimes, they are connected), and lateral cracking in the center part of member can be produced due to combination of temperature distribution, enhancement of hydration process and resultant autogenous shrinkage [9]. And it has been pointed out that these shrinkage-induced cracks may jeopardize the structural performance of reinforced concrete members [10].

(4) Concrete-Filled-steel-Tube structure

Concrete-filled-steel-Tube (CFT) member is one of the solutions for high-rise buildings. Recently, combination of high-strength steel and ultra-high-strength concrete has been applied to those members. Generally, this combination increases the structural performance, but when we focus on the inhomogeneous behavior among components, especially the effect of autogenous shrinkage of concrete, some risk can be emerged. At this moment, stress distribution among components under permanent loading and seismic loading is not cleared, therefore, development of detail against such inhomogeneous behavior and monitoring and experiments of frame structure to grasp overall performance of CFT are desired.

3.4 Influences of shrinkage on ultimate strength of structural members

It has been considered conventionally that shrinkage of concrete has an effect on the deformation, deflection, and loss of prestress but does not much influence on the failure process of structures. Indeed, in case of the bending failure mode, shrinkage of concrete has an effect only on the cracking moment, stiffness, and no effect on the ultimate moment and the ductility.

Recently, Sato et al. confirmed that shear cracking strength of reinforced concrete beam without stirrups is decreased due to autogenous shrinkage and resultant self-induced stress as shown in Fig.3 [11], and he indicated that shrinkage effect on the shear capacity of reinforced concrete beam cannot be ignored.

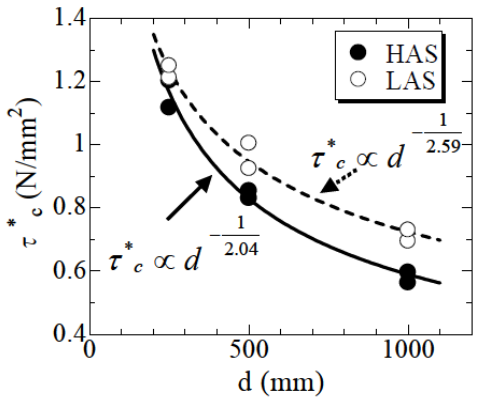

Fig. 3 Effect of shrinkage on the shear strength of reinforced concrete beam without stirrups [11] (HAS: high autogenous shrinkage, LAS: Low

autogenous shrinkage)

Maekawa et al. successfully simulated the experiments by Sato et al. [11] by his numerical simulation system[12].

4. SUMMARY

Effect of shrinkage of concrete has been considered in design of structures in various ways. On the other hand, new problems related with shrinkage have arisen, such as excessive long-term deflection of PC bridges, shear strength of RC members, shrinkage of ultra-high-strength concrete and problems in composite members. In order to estimate them and to take countermeasure effectively based on understanding of their mechanisms, it is essential to treat objective phenomena as coupling problems between material and structure and to analyze them from microscopic physicochemical viewpoint. Durability Mechanics is expected as suitable methodology for this purpose.

ACKNOWLEDGMENT

The authors wish to acknowledge the dedicated cooperation of Prof. Ryoichi Sato of Hiroshima University, who is the chair of the technical committee (JCI-TC-105A), and the members of the committee.

REFERENCES

[1] Coussy, O. and Ulm, F. -J., Elements of Durability Mechanics of Concrete Structures, International Conference on Creep, Shrinkage, and Durability Mechanics of Concrete and other Quasi-Brittle Materials, edited by F. -J. Ulm, Z. P. Bazant, and F. H. Wittmann, Elsevier Science Ltd.: 393-409, 2001

[2] Sato, R., Shimomura, T., Maruyama, I., and Nakarai, K., Durability mechanics of concrete and concrete structures - Re-definition and A New Approach, 8th International Conference on Creep, Shrinkage and Durability of Concrete and Concrete Structures, 2008.

[3] Sato, H., Miyazawa, S. and Yatagai, A., Influences of autogenous shrinkage on thermal stress in dam concrete, Proceedings of the JCI, Vol.30, No.2, pp.181-186, 2008.

[4] Ishibashi, T. and Tsuyoshi, T., A Study on the Estimation of Bending Crack Width on the Surfaces of Concrete Girders, Journal of Materials, Concrete Structures and Pavements, No.484/ V-22, pp.33-40, 1994.2

[5] Seki, T., Sakurai, T. and Shimomura, T., Influence of drying shrinkage on time-dependent change of crack width of reinforced concrete, Proceedings of the JCI, Vol.32, No.2, pp.211-216, 2010.7.

[6] Maekawa, K., Chijiwa, N. and Ishida, T. : Long-term deformational simulation of PC bridges based on the thermo-hygro model of micro-pores in cementitious composites, Cement and Concrete Research, 2011.5

[7] Aoyama, Y.: "Research on self-induced stress in reinforced concrete frame buildings", The University of Tokyo, 1959.12

[8] Architectural Institute of Japan: State of the art of high-strength concrete 2009, Maruzen, pp.379-401, 2009

[9] Maruyama, I., Sato, R., and M. Suzuki: Verification of soundness of HPC in RC members, Proc. of AIJ, Vol. A, pp. 625-626, 2005.9

[10] Takamo, N, et al. :An Experimental Study on the Influence of Shrinkage and Creep on Seismic Performance of R/C Column using Ultra-High Strength Materials, Fujita Research Report, Vol. 45, pp. 49-54, 2009

[11] Sato, R. and Kawakane, H.: A new concept for the early age shrinkage effect on diagonal cracking strength of reinforced HSC beams, Journal of Advanced Concrete Technology, 6(1) 45-67, 2008.

[12] Gebreyouhannes, E. and Maekawa, K.: Numerical simulation on shear capacity and post-peak ductility of reinforced high-strength concrete coupled with autogenous shrinkage, Journal of Advanced Concrete Technology, 9(1), 73-88, 2011.

Proceedings of the 3rd JCI-KCI-TCI Symposium on Recent Advancement of Technologies in Concrete Engineering
Japan Concrete Institute, July 2012

An Analytical Study of Long-term Deformation in SRC Columns Considering Differential Moisture Distribution

Jin-Keun Kim and Gyeong-Hee An
Department of Civil Engineering, KAIST, Korea

ABSTRACT

Steel Reinforced Concrete (SRC) columns, which have been widely employed in high-rise buildings, exhibit a time-dependent behavior due to creep and shrinkage of the concrete. This long-term behavior may cause serious serviceability and stability problems in structural systems, thus it is very important to predict the long-term deformation for proper maintenance of structures.

Moisture diffusion in SRC column is disturbed by the flange of H-shape steel. Consequently, the moisture distribution of SRC columns is different from RC columns and moisture distribution can affect the amount of drying shrinkage and drying creep. Therefore, differential moisture distribution should be taken into account in order to predict column shortening of SRC columns reasonably.

In this study, some factors like steel shape and size of the section are considered as parameters to affect moisture distribution in SRC columns. Also, an analysis method and a shrinkage prediction program are developed to involve the characteristics of moisture distribution. Finally, a modified shrinkage model for SRC is suggested so that we can easily predict column shortening for SRC.

Keywords: *long-term deformation, column shortening, creep, drying shrinkage, differential moisture diffusion, Steel Reinforced Concrete*

1 INTRODUCTION

Long-term deformation of concrete such as drying shrinkage and creep varies depending on lots of factors like concrete mixing, size and environmental conditions. These inelastic and time-dependent characteristics of concrete make it hard to predict exact amount of deformation but it should be counted properly.

Creep and drying shrinkage lead shortening of vertical elements in the structure. For columns, this phenomenon called as column shortening. The column shortening can cause undesirable problems related to serviceability and safety especially when each column has a different level of shortening. This differential column shortening causes additional stress to a system, distortion of wall or finishing materials and other structural problems. Therefore, accurate prediction of column shortening is quite important especially for high-rise buildings because small errors of shrinkage prediction can be accumulated and become a critical issue in the high-rise buildings.

SRC(Steel Reinforced Concrete) columns are widely employed nowadays as high-rise building construction increases. Consequently, being well aware of long-term deformation of the SRC columns will be helpful for reducing structural problems and economical designs of high-rise buildings.

From the previous studies, it has shown that SRC column shortening tends to be overestimated when a general method to predict RC column is used. It means that a new analysis method is necessary to analyze long-term behavior of SRC more accurately.

The difference between RC and SRC columns is mainly from the existence of H-shape steel. The flange of H-shape steel disturbs the moisture diffusion in concrete and makes the long-term deformation such as drying shrinkage and drying creep related to the moisture diffusion different. Therefore, differential moisture distribution should be taken into account in order to predict the column shortening of SRC columns reasonably.

In this study, some factors like steel shape and size of the section are considered as parameters to affect moisture distribution in SRC columns. Also, shortening analyzed from the relative humidity at every point in the concrete section which is the result of moisture diffusion analysis. Finally, a modified shrinkage model for SRC is suggested so that we can

easily predict column shortening for SRC columns.

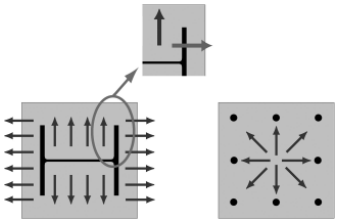

Figure 1 Obstruction of the moisture diffusion route in SRC columns

2 ANALYTICAL PROGRAM

In this study, finite-element analyses were imployed to estimate the moisture diffusion and differential drying shrinkage.

2.1 Analysis of moisture diffusion progress

The progress of moisture diffusion was calculated using nonlinear moisture diffucion equation, as given in Eq.(1).

$$\frac{\partial H}{\partial t}=[\frac{\partial}{\partial x}(D\frac{\partial H}{\partial x})+\frac{\partial}{\partial y}(D\frac{\partial H}{\partial y})+\frac{\partial}{\partial z}(D\frac{\partial H}{\partial z})] \quad (1)$$

A numerical step by step procedure at any time t and the Newmark integration method were used. The Newmark β intergration method assumes the following equations.

$$\dot{H}^{t+\Delta t}=\dot{H}^{t}+[(1-\delta)\ddot{H}^{t}+\delta\ddot{H}^{t+\Delta t}]\Delta t \quad (2)$$

$$H^{t+\Delta t}=H^{t}+\dot{H}^{t}\Delta t+[(\frac{1}{2}-\beta)\ddot{H}^{t}+\beta\ddot{H}^{t+\Delta t}](\Delta t)^{2} \quad (3)$$

2.2 Relationship between local shrinkage and relative humidity

In the free shrinkage case, the rate of local shrinkage strain is [8]

$$d\varepsilon_{sh}=k_{sh}dh \quad (4)$$

$$k_{sh}=\varepsilon_{s}^{0}g_{s}(t)\frac{df_{s}(h)}{dh} \quad (5)$$

where k_{sh} is the shrinkage coefficient; ε_{s}^{0} is the ultimate shrinkage; $g_{s}(t)=E(t_{0})/E(t)$.

There are a lot of researches to identify $f_{s}(h)$. In this paper, we use the equation suggested by Bazant.[8]

$$f_{s}(h)=1-h^{3} \quad (6)$$

2.3 Analysis of drying shrinkage considering the differential moisture distribution.

Analysis is performed in the order shown in figure 2.

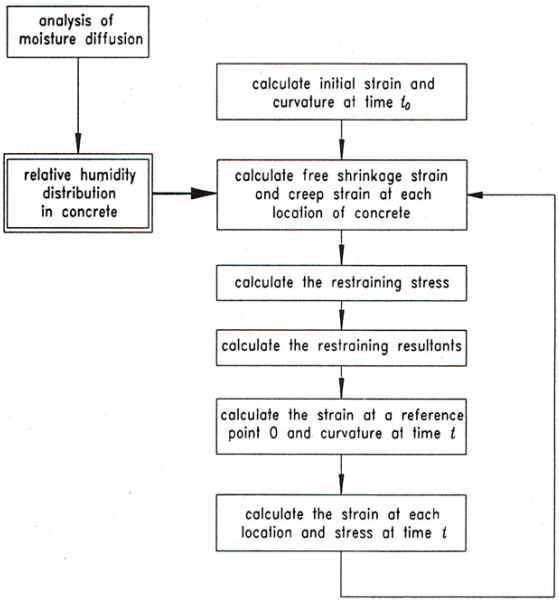

Figure 2 Analysis procedure for differential drying shrinkage of concrete [1]

If the time we are interested in splits n steps, we can express time as t_{i}, $i=1,...,n$. Initial strain of section can be calculated from the equation (7).

$$\varepsilon_{c}(t_{1})=\frac{1}{E_{c}(t_{1})}\frac{N}{A} \quad (7)$$

where A is the area of transformed section and N is the axial force applied on the cross-section.

At time t, if the moisture distribution in concrete is non-uniform, the restraining force($\Delta\sigma_{r}$) is introduced at each location of concrete. And the strain change due to differential drying shrinkage and creep is restrained. Thus the strain increment due to differential drying shrinkage and creep during time t_{i-1} to t_{i} plus the strain due to restraining force is zero. That is, the compatibility condition is satisfied with equation (8).[1]

$$(\varphi(t_{i},t_{1})-\varphi(t_{i-1},t_{1}))\varepsilon_{c}(t_{1})+\sum_{j=1}^{i-2}\frac{\Delta\sigma_{c}(t_{j})}{E_{c}(t_{j})}(\varphi(t_{i},t_{j})-\varphi(t_{i-1},t_{j})) \quad (8)$$
$$+\Delta\varepsilon_{sh}(t_{i},t_{i-1})+\frac{\Delta\sigma_{r}(t_{i},t_{i-1})}{E_{c}(t_{i-1})}[1+\chi\varphi(t_{i},t_{i-1})]=0$$

Local shrinkage strain during time t_{i-1} to t_{i} can be calculated from equation (9).

$$\Delta\varepsilon_{sh}(t_{i},t_{i-1})=\varepsilon_{s}^{0}g_{s}(t_{i})(1-h(t_{i},x,y)^{3})-\varepsilon_{s}^{0}g_{s}(t_{i-1})(1-h(t_{i-1},x,y)^{3}) \quad (9)$$

From equation (8), restraint stress $\Delta\sigma_{r}$ is obtained during time t_{i-1} to t_{i} and the resultant forces($\Delta N,\Delta M$) are calculated by integrating restraint stress over the area of cross-section, as follows.

$$\Delta N = \int_A \Delta\sigma_r(t_i, t_{i-1})dA \qquad (10)$$

The opposite force $-\Delta N, -\Delta M$ are applied on the cross-section of concrete to remove the restraint. Then, the strain increment($\Delta\varepsilon_c(t_i, t_{i-1})$) is calculated by equation(11).

$$\Delta\varepsilon_c(t_i, t_{i-1}) = \frac{1+\phi(t_i, t_{i-1})}{E_c(t_{i-1})}\frac{(-\Delta N)}{\overline{A}} \qquad (11)$$

Finally, the strain of concrete at time t_i is as follows.

$$\varepsilon_c(t_i) = \varepsilon_c(t_{i-1}) + \Delta\varepsilon_c(t_i, t_{i-1}) \qquad (12)$$

2.4 Input parameters

The mix proportion of all analyses is as below.

Table 1 Mix proportion of analysis

w/b: %	Fine aggre-gate ratio: %	Unit weight: kg/m^3						
		Water	Cement	Fly ash	Slag	Fine aggre-gate	Coarse aggreg-ate	Super-plast-iciser
33.9	43.0	161	403	48	24	720	976	6.65

Mechanical properties of specimen of analysis is in Table 2.

Table 2 Mechanical properties of concrete

Age: days	Elastic modulus: GPa	Strength: MPa
28	24.0	43.0

Environmental conditions used for analysis are temperatue 20℃ and relative humidity 60%. Initial drying of specimen starts at 7 days.

The maximum moisture diffusion coefficient, D_1, and the surface factor, f, were determined from an experiment.[2] This experiment was performed with the same conditions we use in this analytical study. Details of the experiment are written in the paper.[2] In this study, we simply use $D_1 = 1.8\times10^{-6}\,\mathrm{m}^2/\mathrm{hr}$ and $f = 12\times10^{-6}\,\mathrm{m}^2/\mathrm{hr}$ according to the test results. Also, the final shrinkage value was determined in [2], and we use the value of the paper, $\varepsilon_s^0 = -1000\times10^{-6}$. Because all the experment conditions are same as those used in this analysis, this anaylsis can have consistency.

To get the results to identify the effects of steel arrangements and flange length, we set the cross-section as follows.

First, three kinds of square sections with different steel arrangements as shown in figure 3 are used to compare the effects of steel arrangements and sizes. Let the name of the section 'Plain', 'H', 'Cross' from the left. Each section has five kinds of sizes, one side length of the sections are 300mm, 600mm, 900mm, 1200mm, 1500mm. Every 'H' section and 'Cross' section, the covering depth is fixed as 100mm. The flange length of 'H' section is same as web and the flange length of 'Cross' section is three fourth of web length.

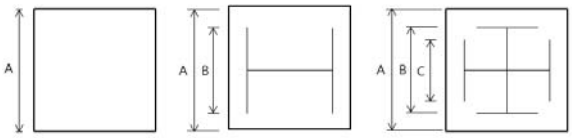

Figure 3 Sections with different steel arrangement

In this study, elastic modulus of steel is set at zero and the thickness is set very thinly to ignore the effect of steel to drying shrinkage, thus we can only consider concrete.

Details of section dimension are represented in Table 3. In Table 3, sections of the same size are indicated in the same group to represent all sections constrictively. A, B and C means the length of sections as marked in figure 3.

Table 3 Dimensions of sections (Unit: mm)

Group	A	B	C
1	300	100	75
2	600	400	300
3	900	700	525
4	1200	1000	750
5	1500	1300	975

Second, four kinds of square 'Cross' sections with different lengths of flange as shown in figure 4 are used to compare the effects of flange length and section size. Flange lengths are decided to be 1/4, 2/4, 3/4, and 4/4 of the web length at each size of the section. Let the name of the section 'Cross_1/4', 'Cross_2/4', 'Cross_3/4' and 'Cross_4/4' from the first in figure 4. Each section has five kinds of sizes, one side length of the sections are 300mm, 600mm, 900mm, 1200mm, 1500mm. The covering depth of all sections is fixed as 100mm.

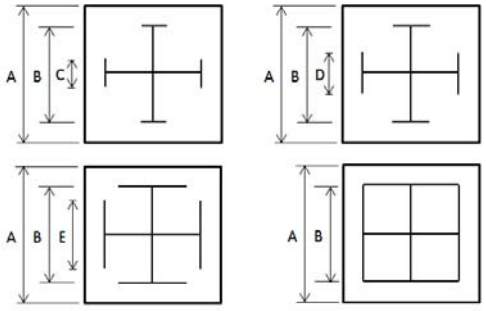

Figure 4 Sections with different flange length

Also, elastic modulus of steel is set at zero and

the thickness is set very thinly to ignore the effect of steel to drying shrinkage, thus we can only consider concrete .

Details of section dimension are represented in Table 4. Again, sections of the same size are indicated in the same group to represent all sections constrictively. A, B, C, D and E means the length of sections as marked in figure 4.

Table 4 Dimensions of sections (Unit: mm)

Group	A	B	C	D	E
1	300	100	25	50	75
2	600	400	100	200	300
3	900	700	175	350	525
4	1200	1000	250	500	750
5	1500	1300	325	650	975

3 ANALYSIS RESULTS

3.1 Drying shrinkage of sections with different steel arrangement.

From the moisture diffusion analyses, we can obtain the information of relative humidity at each time step and each node on the sections. As an example, moisture distributions of each kind of 1.2m sections after 1000 days are in figure 5.

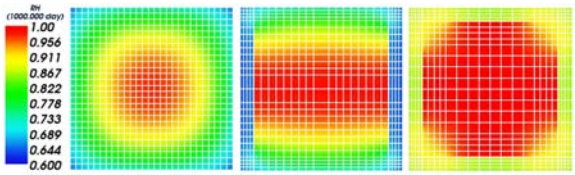

(a) Plain (b) H (c) Cross

Figure 5 Result of moisture diffusion analysis (1000 days)

Through the sectional analysis explained in 2.3, developments of drying shrinkage with time are obtained. Figure 6 shows the strains of each section.

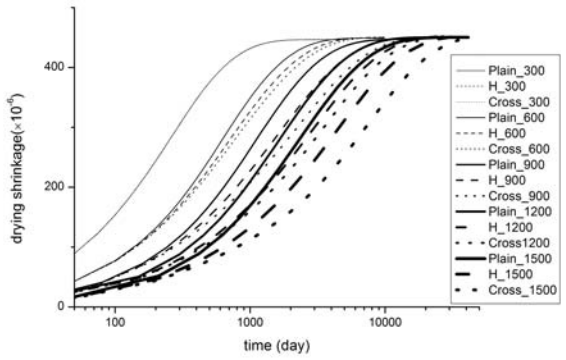

Figure 6 Comparison of drying shrinkage of sections with three kinds of steel arrangements

In figure 6, solid lines represent 'Plain' sections, dashed lines are 'H' sections, and dotted lines mean 'Cross' sections. Then, line thickness shows the size of the section. The thicker line means the bigger size.

When it comes to the same size sections with different steel arrangements, 'Cross' section shrinks relatively slowly than 'H' and 'Plain' sections. That's because the speed of moisture diffusion of each section is different. For the same reasons, the bigger section shrinks slowly than the small section.

3.2 Drying shrinkage of sections with various lengths of flanges of steel

From the moisture diffusion analyses, we can obtain the information of relative humidity at each time step and each node on the sections. As an example, moisture distributions of each kind of 1.2m sections after 1000 days are in figure 7.

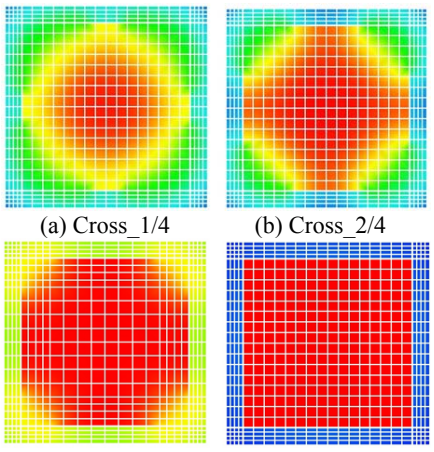

(a) Cross_1/4 (b) Cross_2/4

(c) Cross_3/4 (d) Cross_4/4

Figure 7 Result of moisture diffusion analysis

Through the sectional analysis explained in 2.3, developments of drying shrinkage with time are obtained. Figure 8 shows the strains of each section. The legend '300_1/4' in Figure 8 means the 'Cross_1/4' section with the size of 300mm. Other legends mean sizes and lengths of flanges in the same way.

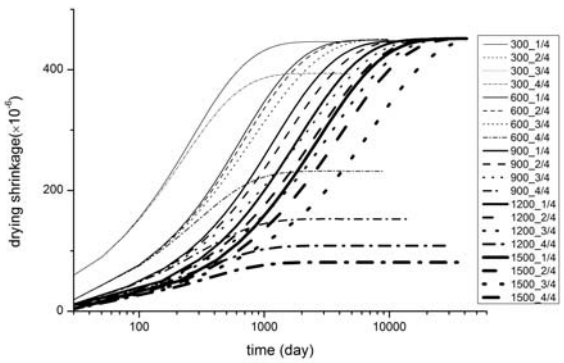

Figure 8 Comparison of drying shrinkage of sections with four kinds of flange lengths

The results presented in figure 8 show that drying shrinkage development is delayed when the length of flange becomes longer. Especially for the 'Cross_4/4' section, the amount of ultimate

shrinkage decreases because moisture in the middle of the section is not diffused at all. Final shrinkage decrement is proportional to the ratio of the middle part to the whole area. Because we have fixed covering depth, the largest section has the biggest decrement as shown in Figure 8.

In conclusion, the arrangement of steel and the flange length affect drying shrinkage. The effects are proportional to the effect of disruption of moisture diffusion.

4 SUGGESTION OF DRYING SHRINKAGE EQUATION

4.1 Regression of analysis results of 'Plain' sections by CEB-FIP model

Modified CEB-FIP drying shrinkage model is suggested from the analysis results. The basic hypothesis is that CEB-FIP drying shrinkage model provides fairly good results for plain concrete. CEB-FIP drying shrinkage model is as follows.

$$\varepsilon_{sh}(t,t_0) = \varepsilon_{sho}\sqrt{\frac{\frac{(t-t_0)}{t_1}}{\beta_{SH}+\frac{(t-t_0)}{t_1}}} \qquad (13)$$

On this hypothesis, we find the best parameters, ε_{sho} and β_{SH}, in the drying shrinkage model to explain the analysis result of plain concrete through the regression analysis. Then, some factors are multiplied to the equation of plain concrete to reflect the characteristics of SRC column sections. Finally, we find the coefficients which make the equation fit well to the analytical the results by regression analysis.

Figure 9 shows the regression result of program analysis result for the 120mm 'Plain' section. Results of regression analysis seem that shrinkage from a CEB-FIP model and a program suggested in this study are not perfectly fitted, but our goal is to find relative relationship between 'Plain' sections and other SRC sections and to give an advice to estimate shrinkage of SRC, it can be acceptable.

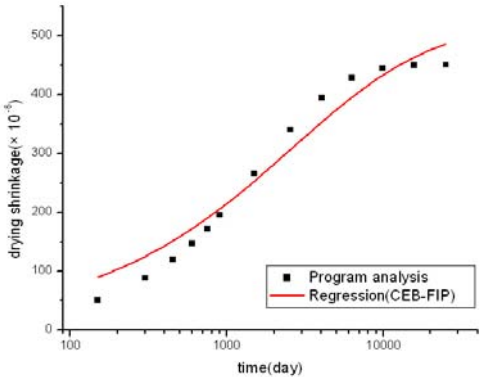

Figure 9 Regression result of 1200mm plain section

Table 5 gives the best regression results at each size of sections while using the CEB-FIP model to fit analytical result of the plain concrete.

Table 5 Regression result for 'Plain' concrete

Size of section(h)	ε_{sho}	β_{SH}
300x 300(150)	526.4	747.6
600x 600(300)	531.1	1918.8
900x 900(450)	531.6	3373.7
1200x 1200(600)	534.1	5186.1
1500x 1500(750)	521.2	6497.7

4.2 Modified drying shrinkage model for 'H' sections.

From the analysis results shown in 3.1, we need to add a coefficient to β_{SH} related with the shape of the section to explain the drying shrinkage of 'H' sections. The equation has form written in (14).

$$\varepsilon_{sh}(t,t_0) = \varepsilon_{sho}\sqrt{\frac{\frac{(t-t_0)}{t_1}}{\alpha_H\beta_{SH}+\frac{(t-t_0)}{t_1}}} \qquad (14)$$

When we perform regression analysis for 'H' sections, we fix other variables, ε_{sho} and β_{SH}, as we got from plain concrete regression for each size of sections what mentioned in Table 5. Only α remains a regression parameter to fit the program results of 'H' sections. It means that we modify the drying shrinkage model is based on the 'Plain' concrete section and the difference between shrinkage of 'Plain' and 'H' sections are reflected by the coefficient α_H. Figure 10 shows the regression analysis for the 'H' section of 1200mm size. Other sections give similar results. Table 6 includes all the regression results of α_H for all the sections of various sizes.

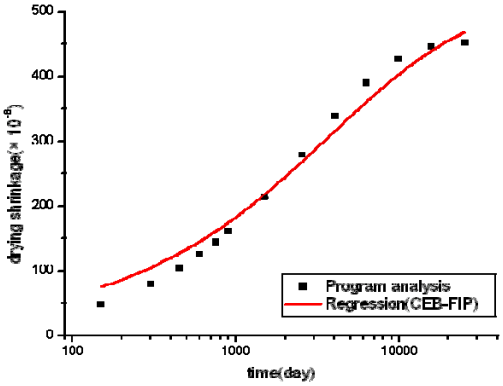

Figure 10 Regression result of 1200mm H section

Table 6 Regression results for coefficients of 'H'

Size of section(h)	α_H
300x 300(150)	1.0
600x 600(300)	1.1
900x 900(450)	1.3
1200x 1200(600)	1.45
1500x 1500(750)	1.6

We can relate α_H with notional thickness h(mm). Figure 10 represents the regression results with h(mm). The relationship can be fitted by a linear function, equation (15).

$$\alpha_H = 0.00102h + 0.8334 \quad (15)$$

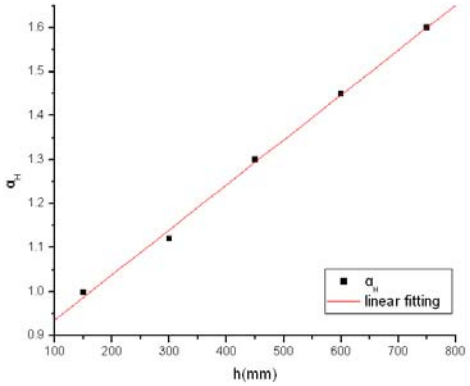

Figure 11 Relationship between α_H and h

To sum up, drying shrinkage of 'H' section can be estimated by the equation (16).

$$\varepsilon_{sh}(t,t_0) = \varepsilon_{sho}\sqrt{\frac{\frac{(t-t_0)}{t_1}}{(0.00102h+0.8334)\beta_{SH}+\frac{(t-t_0)}{t_1}}} \quad (16)$$

4.3 Modified drying shrinkage model for 'Cross' sections.

Modification procedure is same as for 'H' sections. However, we should consider one more parameter for 'Cross_4/4', because the final shrinkage value of it is different from other sections.

Regression equation is same as (14), but the coefficient is represented α_{c_ratio} for the 'Cross' sections.

For the 'Cross_1/4', 'Cross_2/4', and 'Cross_3/4', α_{c_ratio} got from regression analysis are as follows.

Table 7 Regression results for coefficients of 'Cross_1/4'

Size of section(h)	$\alpha_{c\_1/4}$
300x 300(150)	1.0
600x 600(300)	1.01
900x 900(450)	1.04
1200x 1200(600)	1.10
1500x 1500(750)	1.11

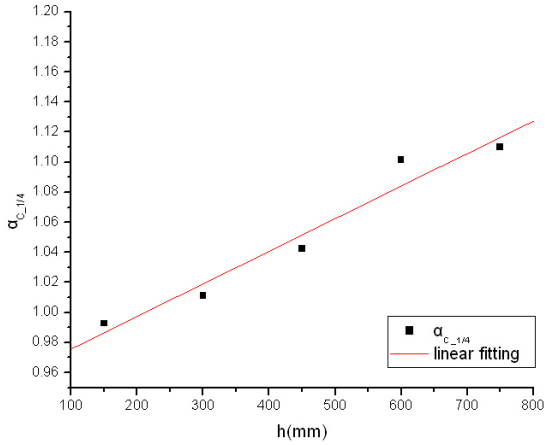

Figure 12 Relationship between $\alpha_{c\_1/4}$ and h

The relationship between $\alpha_{c\_1/4}$ and notional thickness h is as follows.

$$\alpha_{c\_1/4} = 0.000217h + 0.954 \quad (17)$$

Table 8 Regression results for coefficients of 'Cross_2/4'

Size of section(h)	$\alpha_{c\_2/4}$
300x 300(150)	1.0
600x 600(300)	1.07
900x 900(450)	1.21
1200x 1200(600)	1.39
1500x 1500(750)	1.52

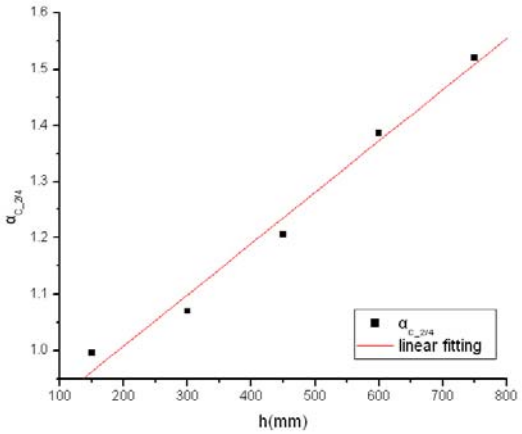

Figure 13 Relationship between $\alpha_{c\_2/4}$ and h

The relationship between $\alpha_{c\_2/4}$ and notional thickness h is as follows.

$$\alpha_{c\_2/4} = 0.000911h + 0.825 \quad (18)$$

Table 8 Regression results for coefficients of 'Cross_3/4'

Size of section(h)	$\alpha_{c\_3/4}$
300x 300(150)	1.0
600x 600(300)	1.21
900x 900(450)	1.56
1200x 1200(600)	1.68
1500x 1500(750)	2.39

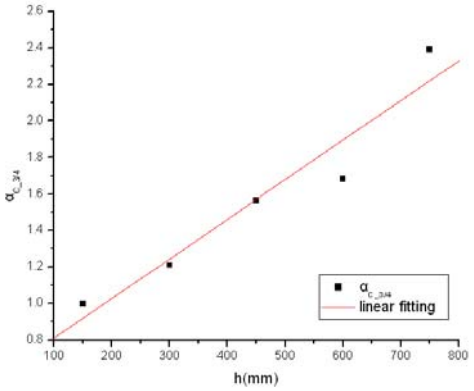

Figure 14 Relationship between $\alpha_{c\_3/4}$ and h

The relationship between $\alpha_{c\_3/4}$ and notional thickness h is as follows.

$$\alpha_{c\_3/4} = 0.00217h + 0.592 \quad (19)$$

For the 'Cross_4/4', regression equation is (20) which includes two factors. One is $\alpha_{c\_4/4}$ related with the speed of drying shrinkage development, the other is $\beta_{c\_4/4}$ related with the amount of drying shrinkage.

$$\varepsilon_{sh}(t,t_0) = \beta_{c\_ratio}\varepsilon_{sho}\sqrt{\frac{\frac{(t-t_0)}{t_1}}{\alpha_{c\_ratio}\beta_{SH} + \frac{(t-t_0)}{t_1}}} \quad (20)$$

Table 8 Regression results for coefficients of 'Cross_4/4'

Size of section(h)	$\alpha_{c\_4/4}$	$\beta_{c\_4/4}$
300x 300(150)	0.79	0.87
600x 600(300)	0.32	0.48
900x 900(450)	0.16	0.31
1200x 1200(600)	0.08	0.21
1500x 1500(750)	0.06	0.16

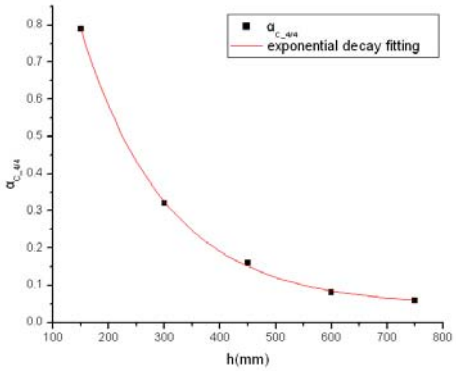

Figure 15 Relationship between $\alpha_{c\_4/4}$ and h

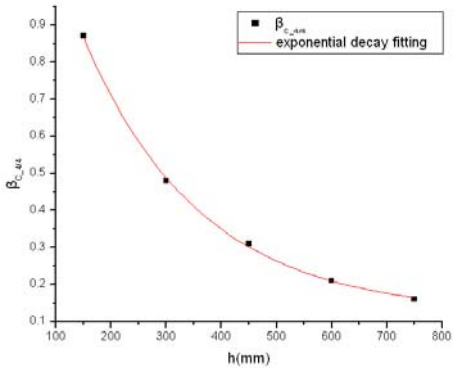

Figure 16 Relationship between $\beta_{c\_4/4}$ and h

$$\alpha_{c\_4/4} = 1.975\exp(-h/153.74) + 0.0445 \quad (21)$$

$$\beta_{c\_4/4} = 1.523\exp(-h/210.9) + 0.121 \quad (22)$$

After those factors for 'Cross' sections substitute into the original equation (14) and (20), these equations become the drying shrinkage model for SRC column.

5 CONCLUSIONS

(1) Flange of H-beam in SRC column disturbs moisture diffusion of concrete, thus the moisture diffusion progress is different from that of RC.
(2) Moisture diffusion properties affect long-term behavior of concrete such as drying shrinkage. Drying shrinkage of SRC column is developed slowly and the value of drying shrinkage becomes less when the steel obstructs moisture diffusion too much.
(3) Through the analysis results, modified equations are suggested to be adoptable for SRC columns. Using the modified equations, we can simply predict column shortening.
(4) More studies are required to use the equation broadly. Also, a consideration of differential drying creep will enhance the reliability of shortening prediction.

ACKNOWLEDGEMENT

This work was partly supported by the Nuclear Research & Development of the Korea Institute of Energy Technology Evaluation and Planning (KETEP) grant funded by the Korea government Ministry of Knowledge Economy (20111520100090). The authors wish to express their gratitude for the financial support that has made this study possible.

REFERENCES

[1] C.S. Lee. (1998). “Moisture Diffusion and Differential Drying Shrinkage of Concrete”, Ph.D. Thesis, Korea Advanced Institute of Science and Technology, Daejeon, Republic of Korea, 130 pages.

[2] H.C. Seol. (2005). “Column Shortening of SRC Columns Considering the Differential Moisture Distriubtion”, Master’s Thesis, Korea Advanced Institute of Science and Technology, Daejeon, Republic of Korea, 56 pages.

[3] Comite Euro-International Du Beton, (1990). CEB-FIP Model Code 1990, Thomas Telford.

[4] A.M. Neville et al. (1983). Creep of plain and structural concrete, Construction Press, London and New York, 356 pages.

[5] S.H. Kwon., J.K. Kim., H.W. Jung. (2003). "Experimental Study on Long-term Behavior of RC and SRC Columns", KCI Spring convention, 2003, South Korea, Vol.15, No.1, pp. 481-486.

[6] Sakata, K. (1983). "A study on Moisture Diffusion in Drying and Drying Shrinkage of Concrete" Cement and Concrete Research, Vol.13, No.2, pp. 216-224.

[7] Z.P. Bazant. (1995). "Creep and Shrinkage Prediction Model for Analysis and Design of Concrete Structures-Model B3", Materials and Structures, Vol.28, pp. 357-365.

[8] Z.P. Bazant., Y. Xi., (1994). "Drying creep of concrete: constitutive model and new experiments separating its mechanisms", Materials and Structures, Vol.27, pp. 3-14.

[9] H.C. Seol., S.-H. Kwon et al., (2008). "Effect of differential moisture distribution on the shortening of steel-reinforced concrete columns", Magazine of Concrete Research, Vol.60, No.5, pp.313-322.

Proceedings of the 3rd JCI-KCI-TCI Symposium on Recent Advancement of Technologies in Concrete Engineering
Japan Concrete Institute, July 2012

RELATIVE HUMIDITY AND DRYING SHRINKAGE OF HARDENING CONCRETE CONTAINING NORMAL- AND LIGHT-WEIGHT COARSE AGGREGATE: A COMPARATIVE EXPERIMENTAL STUDY

Seongcheol Choi and Young Soo Chung
School of Civil and Environmental Engineering, Urban Design and Studies, Chung-Ang University, South Korea

ABSTRACT

In this study, the effect of moisture contents in coarse aggregates on the variation of internal relative humidity (RH) and the drying shrinkage of hardening concrete was experimentally investigated. The concrete prisms were cast with normal-weight and light-weight coarse aggregates having different absorption capacities, in which the nonlinear distribution of RH and drying shrinkage were measured at the same time. Test data indicated that light-weight concrete had less RH drop than normal-weight concrete and it was due to the additional moisture in light-weight coarse aggregate. The development of drying shrinkage over time was closely related to the sectional average of RH variation. By introducing the shrinkage coefficient, the drying shrinkage was quantitatively expressed in terms of RH changes. The difference in drying shrinkage between normal-weight and light-weight concretes was discussed based on the measured RH differentials and shrinkage coefficient.

Keywords: *drying shrinkage, light-weight concrete, relative humidity (RH), shrinkage coefficient*

1 INTRODUCTION

Drying shrinkage of hardening concrete is affected not only by the rate of moisture loss in concrete but also by the stiffness of hardened materials including aggregates [1,2]. The lightweight aggregates are known to be efficiently used in the high-performance/strength concrete with the low water-to-cementitious ratio because the extra moisture in aggregate can be provided to such chemical process as the hydration of cement, i.e., internal curing [3]. Due to the negligible moisture contents in the normal aggregates, the existing models evaluate drying shrinkage of concrete in terms of strength or stiffness of cementitious materials.

In order to measure drying shrinkage, the existing test method simply measured the length change of specimen over time in accordance with ASTM C 157. In evaluating drying shrinkage of concrete containing lightweight aggregate, however, two conflicting factors affecting drying shrinkage of concrete coexist. One factor is extra moistures in lightweight aggregate. As the absorption capacity of the lightweight aggregates is very large compared to normal aggregates, the moisture in lightweight aggregate may reduce moisture loss, which results in the reduction of drying shrinkage of concrete [4]. The other factor is the stiffness of aggregate. The lightweight aggregate is known to have lower stiffness than normal aggregate. This provides less restraint to the shrinkage of cement paste and thus more drying shrinkage will be produced in concrete [2]. The evaluation of drying shrinkage of lightweight concrete, therefore, requires considering not only the extra moisture contents in the aggregate but also the stiffness of aggregate.

Drying shrinkage results from moisture loss in pore structures through diffusion and evaporation. The shrinkage coefficient can be used to model free drying shrinkage in terms of RH changes [1,5]. Free drying shrinkage is defined as shrinkage measured in idealized conditions, in which there is no restraint or stress, and a whole specimen shrinks uniformly [1]. It is difficult to measure free drying shrinkage in the experiment. Because an outer exposed surface will dry quicker than an inner core, the nonlinear differential of RH will exist in a cross-section of a

specimen [6]. This differential will be internally restrained by the plane of specimen and thus, tensile stress will build up at the exposed surface, which may induce micro-cracking [7]. In order to avoid internal restraint and surface micro-cracking in free drying shrinkage measurements, Bažant and Raftshol1 [8] limited the specimen thickness, which resulted in a smaller RH differential between the core and surface. Bissonnette et al. [9] measured the drying shrinkage of paste and mortar specimens with 4 mm thickness. Ayano and Wittmann [10] sliced mortar and concrete specimens with 3 mm thickness and free drying shrinkage was expressed in terms of RH changes. Bentz et al. [11] modified Mackenzie's equation [12] to theoretically predict drying shrinkage due to capillary pressure for a partially saturated porous medium. Physicochemical and mechanical equilibriums exist at the interface between liquid and vapor phases in the pore. Drying shrinkage is predicted in a bulk scale with capillary pressure, and capillary pressure can be estimated from RH through the Kelvin-Laplace equation. Bentz's model holds very well for saturations of 80% or above and decreases in accuracy for lower saturations. Bažant [1,8,13] modeled drying shrinkage in bulk scale rather than in infinitesimal scale. The drying shrinkage in bulk scale is defined as the average value of drying shrinkage in a cross-section, which was approximately proportional to average RH. It may not be a practical way to measure free drying shrinkage of concrete in infinitesimal scale because of the coarse aggregates in concrete. Rather, it would be more feasible to set up the relationship between the average RH and drying shrinkage in bulk scale. In order to model drying shrinkage of concrete, this study adopted the practical approach, in which the relationship between the average RH and drying shrinkage in bulk scale was identified.

The purpose of this study is to quantitatively evaluate the effect of stiffness and moisture contents of coarse aggregates on the development of drying shrinkage of concrete. The development of drying shrinkage and internal relative humidity (IRH) of concrete were measured at the same time. By introducing shrinkage coefficient considering the stiffness development of hardening concrete, the drying shrinkage was quantitatively evaluated in terms of RH variation.

2 SHRINKAGE COEFFICIENTS

The free shrinkage of small specimens is proportional to the water loss, and according to the desorption isotherm, the water loss is approximately proportional to the RH drop. Therefore, the free drying shrinkage can be approximately modeled as follows [1]:

$$\Delta\varepsilon_i^{fsh} = \alpha^{sh}\Delta h_i \qquad (1)$$

where $\Delta\varepsilon_i^{fsh}$ is the change of free drying shrinkage during time step $\Delta t_i = t_{i+1} - t_i$; α^{sh} is the shrinkage coefficient; and Δh_i is the change of RH during time step. Bažant and Xi modeled the shrinkage coefficient in terms of ultimate drying shrinkage and development of elastic modulus of cementitious materials as follows [1]:

$$\alpha^{sh} = \frac{E(t_\infty)}{E(t)}\varepsilon_\infty^{sh} \qquad (2)$$

where $E(t)$ is elastic modulus [MPa, psi] at time t [day]; and ε_∞^{sh} is the ultimate drying shrinkage. In their model [1], the ultimate shrinkage was material constant representing the magnitude of the final shrinkage value and left as a free empirical constant because it was very difficult to directly measure. It is worth noting that the shrinkage coefficient in Eq. (2) is a function of the development of elastic modulus, which depends on the hydration process. The RH gradient will exhibit high nonlinear distribution near the exposed surface as shown in Fig. 1 even in thin sections, because moisture diffusion occurs at very slow rates [14,15].

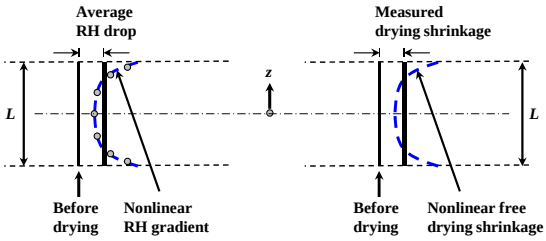

Fig. 1 Nonlinear distribution of RH and free shrinkage

Measured drying shrinkage with embedded gauges can be considered as the average value of free drying shrinkage in cross-sections in bulk scale [1, 13]

$$\Delta\varepsilon_i^{sh,m} = \frac{1}{A}\int \Delta\varepsilon_i^{sh}(z)dA \qquad (3)$$

where $\Delta\varepsilon_i^{sh,m}$ is the increment of measured drying shrinkage [μ mm/mm]; A is the cross-sectional area [mm^2]; $\Delta\varepsilon_i^{sh}(z)$ is the distribution of free drying shrinkage increment over the section [μ mm/mm]; z is the depth in section [mm]. Substitution of Eq. (2) into Eq. (3) leads to Eq. (4)

$$\Delta\varepsilon_i^{sh,m} = \alpha_{sh}(t)\Delta h_i^{avg} \qquad (4)$$

in which

$$\Delta h_i^{avg} = \frac{1}{A}\int \Delta h_i(z)\, dA \qquad (5)$$

where Δh_i^{avg} is the sectional average of RH change [-]; and $\Delta h_i(z)$ is the distribution of RH changes over the section [-]. Eq. (4) means that the measured drying shrinkage in bulk scale is proportional to the sectional average of RH changes [13]. Eq. (5) requires the distribution of RH over the section. Power curves can be assumed for RH distribution based on nonlinear diffusion theory as follows [13,15]:

$$h(z) = A - B\left(1 - \frac{z}{L/2}\right)^{\gamma} \qquad (6)$$

where A and B are the fitting parameters [-] obtained from measured RH data through nonlinear regression; γ is the radius of NC [mm, in]; and is the empirical constant [-].

The symmetric drying condition has such advantage that the strain component by bending moment is eliminated and the difference caused by the installation position of strain gauges in the specimen can be removed in the test because the measured drying shrinkage is constant along the depth of the specimen.

Once the shrinkage coefficient in Eq. (4) is derived from measured data, Eq. (2) can be used to estimate free drying shrinkage of other concrete elements at different depths from measured RH data.

3 EXPERIMENTS

3.1 Materials

Two different types of coarse aggregates such as siliceous river gravel and lightweight coarse aggregates were used in concrete. Table 1 shows the mixture proportions of concrete in the experiments. With the exception of coarse aggregates, all the materials were set the same in the proportions of concrete mixture.

Fig. 2 indicates test results on the absorption capacity of lightweight coarse aggregate, suggesting that the large amount of water can be absorbed in the aggregate over time. The difference in absorption capacity between siliceous river gravel and lightweight coarse aggregate resulted in the different amount of water contained in the coarse aggregate as shown in Table 1.

Table 1 Mixture proportion of concrete

Materials	Unit	SRGC[a]	LWC[b]
Cement	kg/m^3	282.0	282.0
Water	kg/m^3	141.0	141.0
w/c	-	0.5	0.5
AC[c] of CA[d]	%	1.5	20.5
CA[e]	kg/m^3	1121.0	583.2
Water in CA	kg/m^3	17.4	119.4
FA[f]	kg/m^3	753.0	753.0

[a]Siliceous river gravel concrete
[b]Lightweight concrete
[c]Absorption capacity
[d]Coarse aggregate
[e]Weight of CA dried completely.
[f]Fine aggregate
[g]Air entrained agent
[h]Water reducing agent

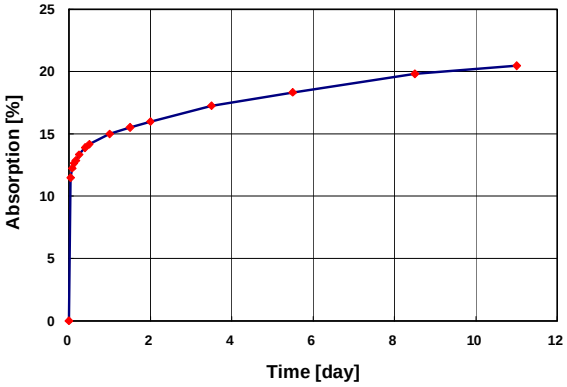

Fig.2 Rate of water absorption of lightweight coarse aggregate over time

3.2 Measurements

In order to quantitatively evaluate the effect of moisture contents in coarse aggregates on the rate of moisture loss and the corresponding drying shrinkage of concrete, seven capacitive type RH sensors were symmetrically installed at the difference depths from the exposed surface of concrete prism specimen as shown in Fig. 3. At the same time, vibrating wire strain gages (VWSGs) were also embedded into the center of the specimen.

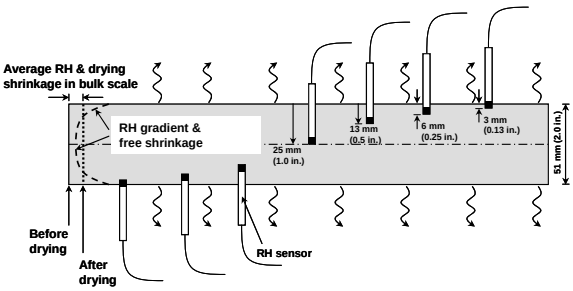

Fig. 3 RH measurement scheme of a prism subject to symmetric drying

Wood form was removed at one day from

concrete casting and placed at the environmentally controlled room with constant 23±1 ° C (73±2 ° F) temperature and 50±5 % RH. Only two side surfaces were exposed to the drying environment and all the other surfaces were sealed with adhesive-backed aluminum tape as shown in Fig. 4 so that the symmetric drying conditions could be imposed to the specimen.

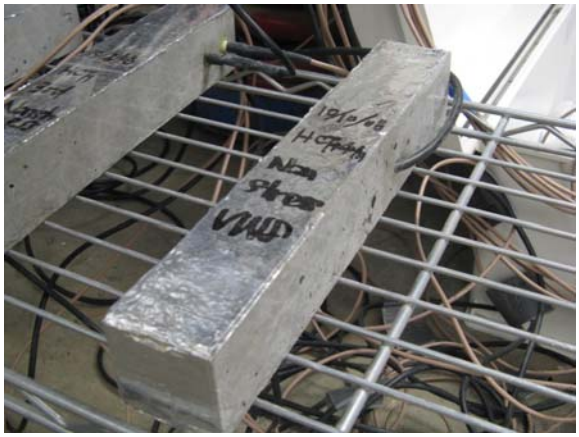

Fig. 4 RH prism specimen placed in the environmental room

In order to measure the drying shrinkage of specimen over time, another prism specimen was cast and one embedment type concrete strain gauge was installed at the center of specimen as shown in Fig. 5. As in a RH prism specimen, drying shrinkage specimen was placed in the same environmental room.

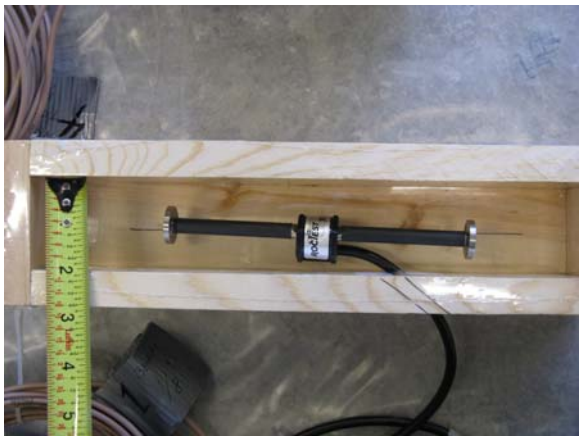

Fig. 5 Shrinkage prism specimen placed in the environmental room

Fig. 6 illustrates the RH gradient of the specimen at different ages. The RH sensors produced the symmetric distribution of RH under the symmetric drying condition, indicating that the RH sensor installed produced accurate measurement of internal RH level in concrete. Noted is that the internal RH distribution was nonlinear and symmetric under symmetric exposure condition. The distribution of free drying shrinkage will be similar to that of the RH because free drying shrinkage is approximately proportional to RH changes in porous material [1,8] (see Eq. (1)). The distribution of free drying shrinkage, however, will be restrained by the translation symmetry as shown in Fig. 1 and thus the longitudinal strain is constant across the cross-section [1,8]. This shrinkage can be measured in bulk scale with a strain gage, which was installed longitudinally at the center of prism.

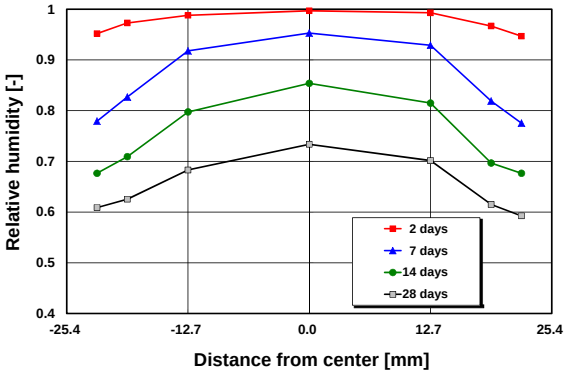

Fig.6 RH gradient exposed to symmetric drying conditions

3.3 Test results

(1) Elastic modulus

Fig. 7 shows the elastic modulus of concrete tested. Compared to siliceous river gravel concrete, lightweight concrete had smaller elastic modulus due to the lower stiffness of aggregates. For given volume change of cement paste in concrete due to RH drop, the reduced stiffness of lightweight coarse aggregate will provide less restraint, resulting in more drying shrinkage of lightweight concrete.

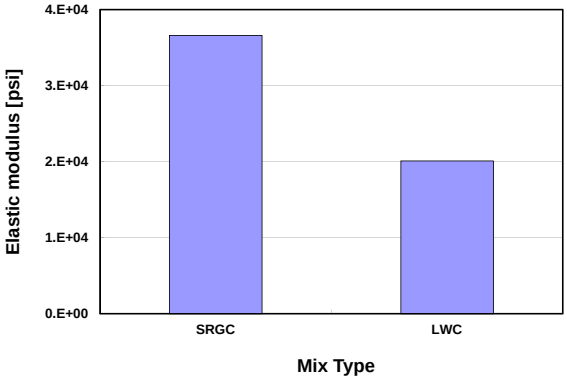

Fig. 7 Elastic modulus of SRGC and LWC

(2) Internal relative humidity

Figs. 8 and 9 depict the variation of internal relative humidity of siliceous river gravel concrete and lightweight concrete, respectively, over time at different depths from exposed surface. As expected, the drying of concrete slowly progressed with time and the RH drop was higher at surface regions than

at core regions.

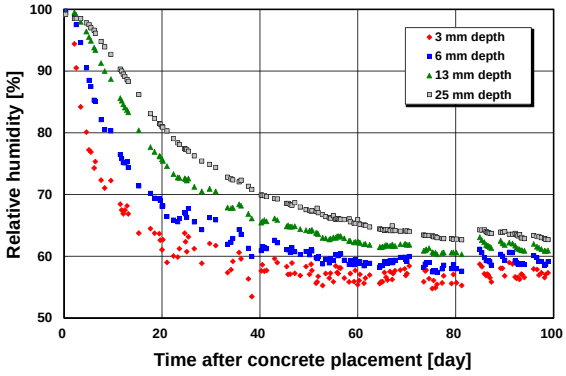

Fig.8 Variation of internal RH of SRGC over time

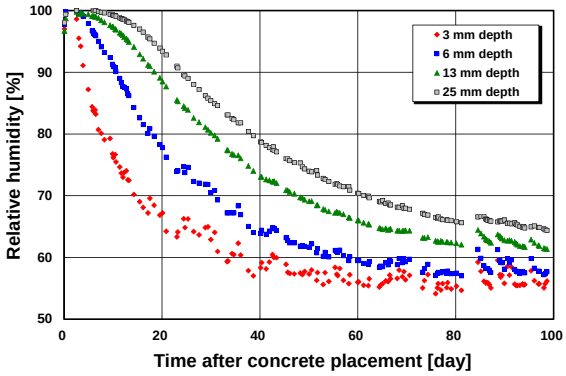

Fig.9 Variation of internal RH of LWC

The RH variations of SRGC and LWC at 13 mm and 25 mm depth were compared and shown in Figs. 10 and 11, respectively. LWC had less RH drop than SRGC because the extra moisture in lightweight coarse aggregates. The extra moisture in lightweight coarse aggregate decreased RH drop of about 10% at 20 days from concrete casting. This result indicates that the saturated lightweight aggregate can be used as the internal curing materials.

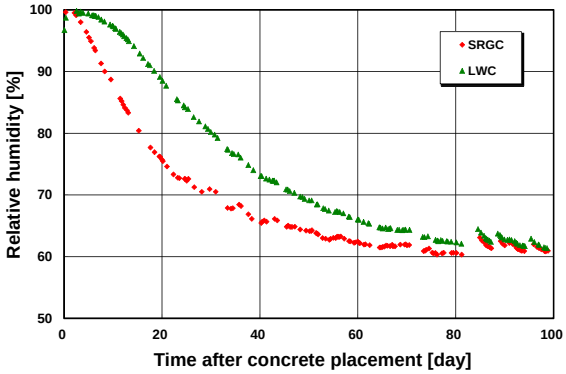

Fig.10 Variation of internal RH
of SRGC and LWC at 13 mm depth

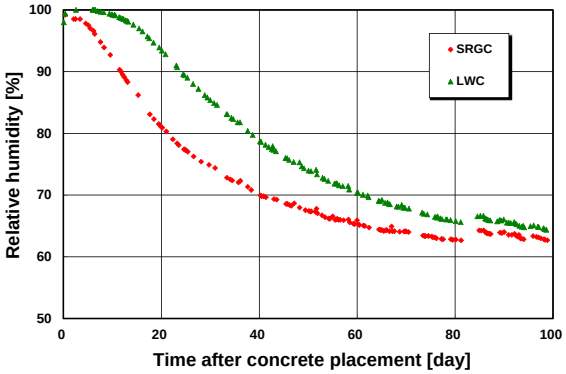

Fig.11 Variation of internal RH
of SRGC and LWC at 1.0 in. depth

(3) Drying shrinkage

Fig. 12 shows the variation of drying shrinkage of SRGC and LWC over time. From casting to about 20 days, the drying shrinkage of LWC was less than SRGC. However, this trend turned around after 20 days, exhibiting more drying in LWC than SRGC. It indicates that the extra moisture by lightweight coarse aggregate reduced the development of drying shrinkage at early stages, whereas the stiffness of siliceous river gravel aggregates made more restraint to the volume change of SRGC and reduced the drying shrinkage in long-term.

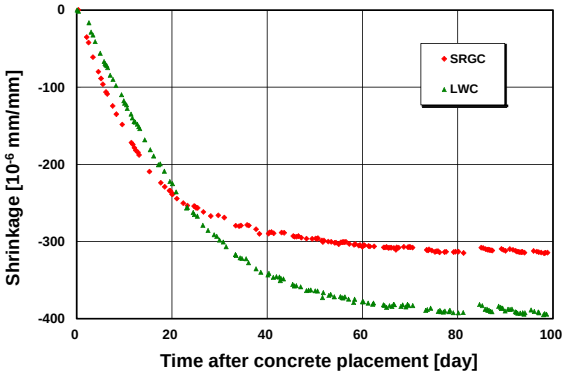

Fig.12 Variation of drying shrinkage
of LWC and SRGC

4 ANALYSIS OF RESULTS AND DISCUSSION

Fig. 13 average RH of LWC and SRGC calculated through Eqs. (5) and (6). As in Figs. 10 and 11, the average RH of LWC was higher than that of SRGC.

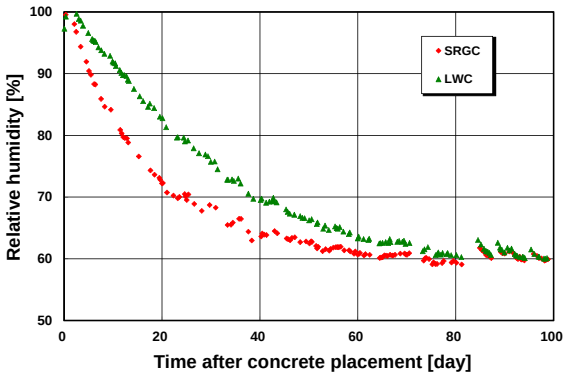

Fig.13 Variation of average RH of LWC and SRGC

Figs. 14 and 15 show the variation of measured drying shrinkage along with average RH of SRGC and LWC. It indicates that the variations of average RH were correlated very well with the variations of drying shrinkage.

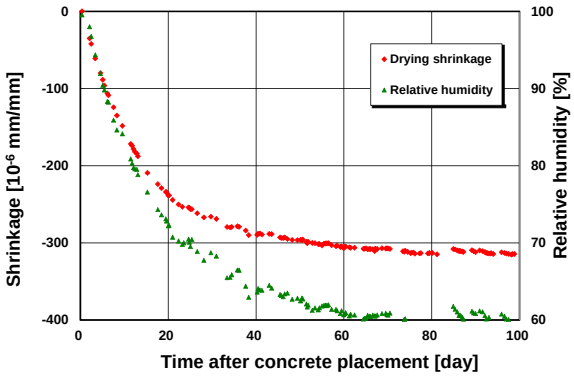

Fig.14 Variations of average RH and drying shrinkage of SRGC

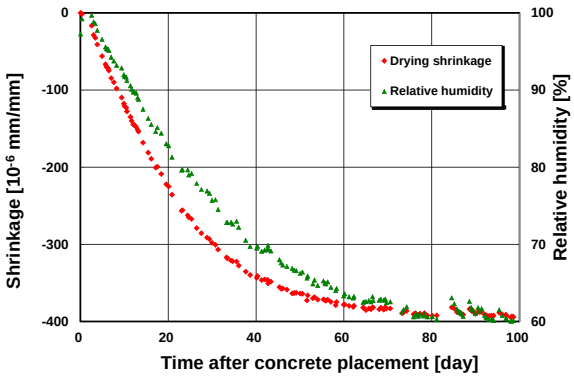

Fig.15 Variations of average RH and drying shrinkage of LWC

Fig. 16 shows the experimentally identified shrinkage coefficient. It indicates that the shrinkage coefficient, which is the slope of curve, was greater at early ages. This is because the prism started to be exposed to symmetric drying conditions at one day from casting. The solid microstructure was being hydrated at early ages and thus the paste drying shrinkage was less restrained by solid microstructure [1,11]. As the hydration of concrete progressed, however, the coefficient decreased to constant.

Noted is that the drying shrinkage of SRGC was larger than that of LWC from casting to about 20 days as shown in Fig. 12. For a given change of RH, however, drying shrinkage of LWC was larger than that of SRGC even at early ages. It indicates that the development of drying shrinkage of concrete over time may be different from the development of drying shrinkage over RH change if extra moisture in aggregate exists.

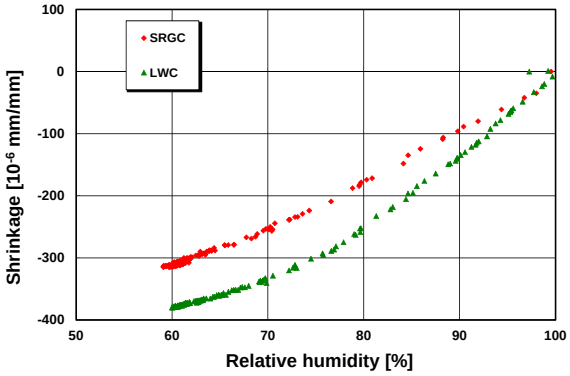

Fig. 16 Shrinkage coefficient of specimens

It is known that not only thermal stress but also drying shrinkage stress strongly affects the cracking potential of cast-in-place concrete structures [16-19]. In order to estimate the cracking potential of cast-in-place concrete structures, the spatial distribution of RH in concrete and its variations over time is numerically predicted first. The free shrinkage resulting in drying shrinkage stress when restrained was estimated from the shrinkage coefficient and the RH changes.

Because the governing equation of moisture diffusion and boundary conditions of surface drying were mathematically well-formulated, the spatial distribution of moisture in concrete and its variations over time can be easily predicted with accuracy and expressed in terms of RH. However, there are huge discrepancies in the values of shrinkage coefficient in the existing studies [4,5,20-22]. The coefficient was constant [5,20] because it originated from the test data of hardened concrete, which would be not directly applicable to hardening concrete. With the help of recent advancement of RH measurement technology, the shrinkage coefficient of hardening concrete was proposed by measuring autogenous shrinkage due to self-desiccation [4,21,22]. However, these coefficients may have the limitation of applicability because they were based on the data measured in limited ranges of time and RH values.

5 SUMMARY AND CONCLUSIONS

The difficulties in the testing imposed certain

limitation on the testing method proposed. The RH drop due to self-desiccation will exist in high strength/performance concrete [21]. In this case, the measured strain with the VW gage may include the autogenous shrinkage of concrete [20,21], especially at early ages. The surface micro-cracking due to differential shrinkage and creep was not considered in the proposed method. As the thickness of specimen increases, the surface micro-cracking and creep may affect measurement of drying shrinkage and RH [10,13,14]. Further study is still needed in this area.

In this study, an experimental testing method was developed in order to measure shrinkage coefficient of hardening concrete. The proposed method involved vibrating wire (VW) strain gages, and RH sensors. The test results confirmed the validity of RH sensor employed in this study. Unlike the existing studies, the shrinkage coefficient had an age-dependency, indicating that it was large at early age and decreased as the concrete hardening progressed. It is expected that this study can be effectively used in evaluating drying shrinkage of hardening concrete and allow realistic assessments of drying shrinkage stress development of cast-in-place concrete structures, including cracking potential.

REFERENCES

[1] Z. P. Ba?ant, Y. Xi: Drying Creep of Concrete: Constitutive Model and New Experiments Separating Its Mechanisms, Materials and Structures, V. 27, No. 1, pp. 3-14, 1994

[2] D. W. Hobbs: Influence of Aggregate Restraint on the Shrinkage of Concrete, ACI Journal, Proceedings V. 71, No. 9, pp. 445-450, 1974

[3] P. Lura, O. M. Jensen, S. Igarashi: Experimental Observation of Internal Water Curing of Concrete. Materials and Structures, pp. 211-220, 2007

[4] J. Ye et al.: Effect of Pre-Wetted Lightweight Aggregate on Internal Relative Humidity and Autogenous Shrinkage of Concrete," Journal of Wuhan University of Technology-Materials Science Edition, V. 21, No. 1, pp. 134-137, 2006

[5] A. M. Alvaredo: Drying shrinkage and crack formation, Building Materials Reports, No. 5, Lab. For Building Materials, Swiss Federal Institute of Technology, Zurich (Switzerland), 102 pp., 1994

[6] Z. P. Ba?ant: Mathematical Modeling of Creep and Shrinkage of Concrete, John Wiley and Sons, Chichester and New York, 459 pp., 1988

[7] C.-L. Hwang, J. F. Young: Drying Shrinkage of Portland Cement Pastes I. Microcracking During Drying, Cement and Concrete Research, V. 14, No. 4, pp. 585-594, 1984

[8] Z. P. Ba?ant, W. J. Raftshol: Effect of Cracking in Drying and Shrinkage Specimens, Cement and Concrete Research, V. 12, No. 2, pp. 209-226, 1982

[9] B. Bissonnette, P. Pierre, M. Pigeon: Influence of Key Parameters on Drying Shrinkage of Cementitious Materials, Cement and Concrete Research, V. 29, No. 10, pp. 1655-1662, 1999

[10] T. Anayo, F. H. Wittmann: Drying, Moisture Distribution, and Shrinkage of Cement-based Materials," Materials and Structures, V. 35, No. 3, pp. 134-140, 2002

[11] D. P. Bentz, E. J. Garboczi, D. A. Quenard: Modelling Drying Shrinkage in Reconstructed Porous Materials: Application to Porous Vycor Glass, Modelling and Simulation in Materials Science and Engineering, V. 6, No. 3, pp. 211-236, 1998

[12] J. K. Mackenzie: The Elastic Constants of a Solid containing Spherical Holes, Proceedings of the Physical Society. Section B, V. 63, No. 1, pp. 2-11, 1950

[13] Z. P. Ba?ant Z. P: Prediction of Concrete Creep and Shrinkage: Past, Present and Future, Nuclear Engineering and Design, V. 203, No. 1, pp. 27-38, 2001

[14] J. K. Kim, C. S. Lee: Moisture Diffusion of Concrete Considering Self-desiccation at Early Ages, Cement and Concrete Research, V. 29, No. 12, pp. 1921-1927, 1999

[15] Z. P. Ba?ant, L. J. Najjar: Nonlinear Water Diffusion in Nonsaturated Concrete, Materials and Structures, V. 5, No. 25, pp. 3-20, 1972

[16] R. Springenschmid, ed.: Prevention of Thermal Cracking in Concrete at Early Ages, State of the Art Report by RILEM TC 119, E&FN Spon, New York, 348 pp., 1998

[17] M. Emborg: Thermal Stresses in Concrete Structures at Early Ages, Lule? University of Technology, Lulea, Sweden, 285 pp., 1989

[18] S. Choi: Thermo-hygro-mechanical Behavior of Early-age Concrete Deck in Composite Bridge under Environmental Loadings. Part 1: Temperature and Relative humidity, Materials and Structures, V. 44, pp. 1325-1346, 2011

[19] S. Choi: Thermo-hygro-mechanical Behavior of Early-age Concrete Deck in Composite Bridge under Environmental Loadings. Part 2: Strain and Stress, Materials and Structures, V. 44, pp. 1347-1367, 2011

[20] H. Sadouki, J. G. M. van Mier: Simulation of Hygral Crack Growth in Concrete Repair Systems, Materials and Structures, V. 20, pp. 518-526, 1997

[21] J. Zhang, H. Dongwei, S. Wei: Experimental Study on the Relationship Between Shrinkage and Interior Humidity of Concrete at Early Age, Magazine of Concrete Research, V. 62, No. 3, pp. 191-199, 2010

[22] S. Lim, J.-H. Jeong, D. G. Zollinger: Moisture Profiles and Shrinkage in Early-age Concrete Pavements, International Journal of Pavement Engineering, V. 10, No. 1, pp. 29-38, 2009

Proceedings of the 3rd JCI-KCI-TCI Symposium on Recent Advancement of Technologies in Concrete Engineering
Japan Concrete Institute, July 2012

RELIABILITY-BASED DESIGN FOR CONCRETE-COVER THICKNESS CONSIDERING THE CORROSION HAZARD OF REINFORCING STEEL BARS: COASTAL REGIONS IN TAIWAN

Chien-Kuo Chiu and Fung-Chung Tu
Department of Construction Engineering, National Taiwan University of Science and Technology, Taiwan

ABSTRACT

The main purpose of this work is to propose an estimating procedure that building designers can use to choose an appropriate concrete-cover thickness with a specified durability performance. At first, the authors build equations for estimating airborne chloride concentrations in coastal regions in Taiwan by regressing measurement data. Then, an analytical model incorporates these data into a deterioration model for chloride-induced corrosion and to estimate corrosion of reinforcing steel bars. This work also presents a novel computational procedure for calculating the hazard of corrosion of reinforcing steel, while considering uncertainties in environmental conditions, material properties, and model error. Using the hazard curve of corrosion of reinforcing steel, building designers can set an allowable durable reliability to determine the needed thickness of a concrete cover for reinforced concrete members. Finally, this work adopts coastal regions in Taiwan as an example to determine the minimum needed concrete-cover thicknesses.

Keywords: *concrete-cover, reliability, chloride, corrosion, hazard curve*

1 INTRODUCTION

Many steel and reinforced concrete (RC) buildings near the coastline have suffered chloride-induced damage in Taiwan. As the service period of buildings increases, their safety and serviceability decrease. Restated, the original designed service life and safety reliability depreciate when buildings are deteriorated by such environmental factors as chloride concentration and carbonation. However, due to frequent earthquakes in Taiwan, repairing or retrofitting buildings is mainly based on seismic performance. Unless corrosion damages the structural safety of building, "pre-damage" repairing work is seldom considered to prevent the serviceability from being deprived by corrosion. Moreover, in Taiwan only few engineers consider the hazard of the corrosive environment and mechanical models of corroded reinforcing steel bars in concrete when evaluating seismic performance. Therefore, in structural design, unlike the case in terms of actions that are usually considered (e.g., probabilistic seismic hazard analysis), there has been a lack of research on marine environmental hazard assessment in Taiwan. Restated, a method that engineers can use to quantify the hazard of corrosion induced by marine environment is an urgent need in the sustainable development of a country or city.

Many codes and specifications use the compressive strength of concrete as a measure of durability. Although compressive strength may give some indication of potential durability, it is not a valid criterion for several reasons [1]. For instance, the compressive strength of a concrete cube or cylinder constitutes the mean value of a property for the entire cross section of a specimen, whereas concrete durability is governed primarily by concrete-cover properties. Concretes with the same strength grade may have different durability and resistance against chloride ingress, carbonation, and sulphate attack. Concrete durability is largely governed by the resistance of a concrete cover to ingress of aggressive media. Therefore, the focus should be on the means of achieving a good-quality concrete cover and determining the needed thickness of a concrete cover. This work focuses on how to identify the appropriate thickness of a concrete cover to protect against environment-induced deterioration. Additionally, an estimating procedure is needed, such that building designers can choose an appropriate concrete-cover thickness to meet a specified durability performance.

2 AIRBORNE CHLORIDE CONCENTRATIONS IN TAIWAN'S COASTAL REGIONS

2.1 Test points for chloride deposits in Taiwan's coastal regions

Taiwan's Institute of Transportation inspected 203 bridges in 2002 to identify and analyze chloride environments in coastal regions [2][3]. Inspection results indicated that the amount of chloride adhering to the bridges decreased as distance between a bridge and the coastline increased. Moreover, when a structure and the coastline is separated by a distanced exceeding 3 km, the amount of chloride adhering to concrete surfaces is very low; therefore, the impact of chloride ions on steel structures or RC structures can generally be ignored. That is, the distance used by Taiwan's Institute of Transportation during its investigations of chloride-induced corrosion was 3 km from the coastline. Test points for chloride deposits were arranged along inland lines, which run vertical to the coastline. Test points in each measurement line were set at 100 m, 300 m, 1 km, and 3 km from the coastline (Fig. 1). Moreover, collectors of chloride deposits use the wet-candle method (CNS 13754 1996), which exposes wet fibers to air in a given area for a set duration; a chemical analysis is then conducted to measure the deposits (mg/m^2/day). This work acquired data from test points along measurement lines from Taiwan's Harbor and Marine Technology Center. These data are for chloride deposits and corrosion rates of carbon steel exposed to air (CNS 13753 2005) between August 2009 and December 2010 [2][3].

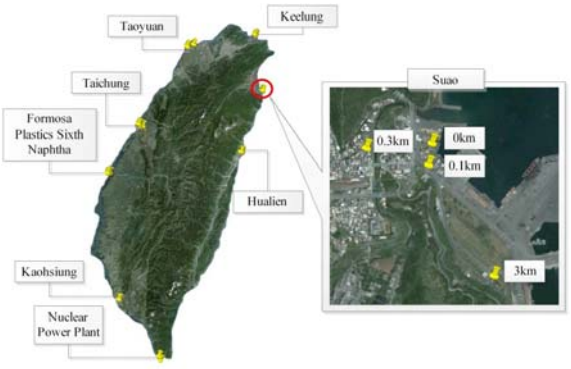

Fig. 1 Test points for chloride deposits in each measurement line in Taiwan

2.2 Equation for estimating airborne chloride concentrations in Taiwan

This work applies the estimation equation established by JSCE [4] for estimating airborne chloride concentrations (Eq. (1)), and considers influential parameters, including the ratio of sea wind r (defined as the percentage of time during one day when the wind is blowing from sea toward load), mean wind speed u, and distance to the nearest coastline d to develop the equations for estimating airborne chloride concentrations in Taiwan's coastal regions. No measurement data exist for the ratio of sea wind; thus, this work includes this ratio in model error. The data for wind speed, including its mean value and standard deviation, were obtained from the website maintained by Taiwan's Central Weather Bureau.

$$C_{air} = 1.29 \times r \times u^{0.386} \times d^{-0.952} \quad (1)$$

where C_{air} is the airborne chloride concentration (mdd); r is the ratio of sea wind ratio; u is mean wind speed (m/s); and d is distance to the nearest coastline (km).

The equation for estimating airborne chloride concentrations, Eq. (1), was applied and simplified as Eq. (2) to account for measured chloride deposits in Taiwan. In Eq. (2), the given values are the chloride concentration at a test point, C_{air}; the chloride concentration at the test point nearest the coastline, C_{star}; mean wind speed, u; and distance between a test point and the nearest coastline, d. Equation (3) was formed taking the logarithm of Eq. (2), and then undefined coefficients a and b were obtained via data regression. Table 1 shows the regression equations of measurement lines, including the model error with the mean value and coefficient of variation for each regression equation. Figure 2 shows measured values and regression results. In the case study, we only discuss the regression equations for the cities of Suao, Taichung, Kaohsiung and Hualien, which locate in the northern, middle, southern and eastern zones of Taiwan, respectively.

$$C_{air} = C_{star} \times u^{a} \times d^{b} \quad (2)$$

$$\log C_{air} = \log C_{star} + a \log u + b \log d \quad (3)$$

$$C_0 = 13.137 \times C_{air}^{0.6394} \quad (4)$$

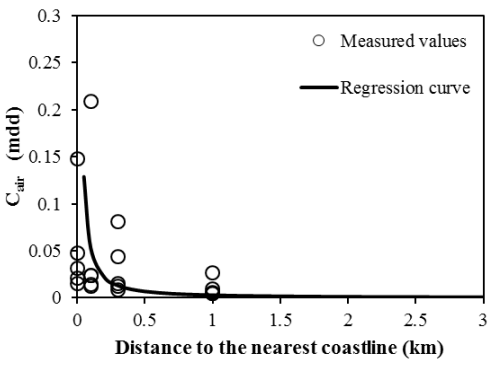

Fig. 2 Regression equation for air-borne chloride concentration in Suao

Table 1 Regression equations for air-borne chloride concentration
(*Model error = measured data / regression data)

Measurement line	Air-borne chloride concentration	*Mean value of model error	*COV of model error
Taoyuan	$C_{air} = 0.4606 \times u^{-3.9654} \times d^{-1.9076}$	1.4660	0.7521
Suao	$C_{air} = 0.0526 \times u^{-4.0179} \times d^{-1.2749}$	2.5504	0.9029
Taichung	$C_{air} = 0.1588 \times u^{-5.5253} \times d^{-0..9235}$	3.2964	0.5521
Hualien	$C_{air} = 0.0992 \times u^{-2.5298} \times d^{-1.3061}$	2.8766	0.7061
Yunlin (Mailiao)	$C_{air} = 0.3089 \times u^{-3.8131} \times d^{-1.3932}$	4.5039	0.6429
Kaohsiung	$C_{air} = 0.0539 \times u^{-2.916} \times d^{-1.0454}$	4.4166	0.5790
Maanshan nuclear power plant	$C_{air} = 0.1111 \times u^{-2.3821} \times d^{-1.1637}$	3.4957	0.7420

Because not all chloride deposits remain on concrete surfaces, airborne chloride concentrations should be modified to include the chloride concentrations on concrete surfaces, which are needed in a diffusion simulation of chloride ions in concrete. Therefore, this work uses data for the chloride concentration on concrete surfaces investigated in the past research [5] and the equations for estimating airborne chloride concentrations stated above to figure out the relationship between the chloride deposits and chloride concentrations on concrete surfaces, as shown in Eq. (4) (Fig. 3).

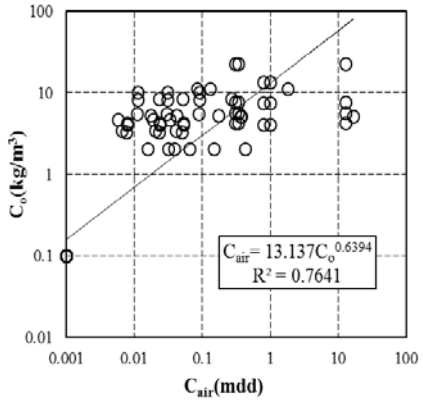

Fig. 3 Regression equation for the relationship between the chloride deposits and chloride concentrations on concrete surfaces

3. MODEL FOR CHLORIDE-INDUCED DETERIORATION

3.1 Corrosion process

The carbonation- or chloride-induced corrosion process for reinforcing steel bars can be divided into four stages: the initiation stage, propagation stage, former period of acceleration stage, and latter period of acceleration stage. Definitions of stages and evaluation methods are as follows:

(a) Initiation stage

This stage spans the time of building completion to corrosion of reinforcing steel bars. As indicated in previous studies, corrosion of reinforcing steel bars can be defined as diffusion of chloride ions on concrete surfaces to the surface of reinforcing steel bars or the carbonation front invading the surface of reinforcing steel bars. Due to uncertainties in environmental and concrete conditions, reliability theory and Monte Carlo simulation (MCS) can be applied to evaluate the occurrence time of corrosion. Carbonation is taken as an example. Generally, uncertainties in environmental conditions, material properties of concrete, and construction quality are considered by the carbonation coefficient when determining the appropriate thickness of a concrete cover. When corrosion probability that can be calculated using MCS reaches 10% (ASTM C876 1991), this time point is regarded as corrosion initiation.

For chloride-induced corrosion in Taiwan's coastal regions, based on mean wind speed and distance to the nearest coastline, the airborne chloride concentration, C_{air}, is determined using the regression equations (Table 1), and it is substituted into Eq.(4) to determine the chloride concentration on concrete surfaces, C_0. Fick's second law can then be applied to estimate the time when chloride ions diffuse from concrete surfaces to a passive film on the surface of reinforcing steel bars, as in Eq. (5).

$$Cl = C_0 \left[1 - erf\left(\frac{0.1 \times c}{2\sqrt{D_c t}} \right) \right] \quad (5)$$

$$\log D_c = -6.77\left(W/C\right)^2 + 10.1\left(W/C\right) - 3.14 \quad (6)$$

where Cl is the chloride concentration on the surface of reinforcing steel bars (kg/m^3); C_o is the chloride concentration of the concrete surface (kg/m^3); c is diffusion distance, which is the thickness of the concrete cover (mm); D_c is the apparent diffusion coefficient of chloride ions (cm^2/year); t is a specified service period (year); and *erf* is the error function.

Based on observation results obtained by Kato and Uomoto [6], we assume corrosion initiates when the chloride concentration on the surface of reinforcing steel bars reaches a threshold, which is a random variable distributed uniformly in the range of 1.0 – 1.2 kg/m^3. This work accounts for uncertainties in chloride-induced deterioration analysis of this stage that are related to the apparent diffusion coefficient, concrete-cover thickness, and the chloride concentration on concrete surfaces caused by environmental and construction conditions [4].

(b) Propagation stage

The propagation stage is the period from corrosion initiation to cracking of the concrete cover. Based on an existing deterioration model [13], we assume the rate of corrosion (mg/cm^2/year) in the propagation stage is treated as a lognormal random variable with a mean value, which can be derived using Eq. (7), and a coefficient of variation of 0.5. The effect of corrosion on material degradation is assessed according to the degree of corrosion of reinforcing steel bars, where weight loss is typically used as a quantifiable measure, as in Eq. (8).

$$V_{corr} = \frac{78}{\sqrt{c}}\left(0.578 \times Cl + 0.023(W/C) - 1.52\right) \quad (7)$$

$$\Delta W_{avg} = \frac{4V_{corr}}{\gamma \times d_{bi}} \quad (8)$$

where γ is the density of reinforcing steel bars (mg/cm^3; approximately 7850), and d_{bi} is the diameter of reinforcing steel bars (mm).

(c) Former period of acceleration stage

This period ranges from concrete-cover cracking to concrete-cover spalling. Most studies used experimental field-exposure results to determine the relationship between degree of corrosion of reinforcing steel bars and occurrence of corrosion-induced cracking. Additionally, according Tottori and Miyagawa [7], we assume the corrosion rate in the propagation stage and former period of acceleration stage is the same. In the future, more reliable experiments or theoretical achievements can replace this assumption.

(d) Latter period of acceleration stage

This period occurs after spalling of a concrete cover. According to AIJ [8], spalling of a concrete cover is caused by the formation of cracks with widths exceeding 0.5 – 1.0 mm. The corresponding initiation threshold of the latter period of acceleration stage is difficult to define. In this work, the empirical result obtained by [9] is used to set the threshold as the weight loss percentage of corroded reinforcing steel of 3.28%, which is treated as a lognormal distribution with 0.26 as the coefficient of variation. Additionally, one can reasonably assume that the concrete surface spalls severely, such that the concrete cover cannot prevent reinforcing steel bars from corroding in the latter period of acceleration stage.

Although the corrosion rate can be set as the corrosion rate of reinforcing steel bars unprotected by concrete, only few studies have discussed corrosion of reinforcing steel bars resulting from concrete-cover spalling [7]. To consider the effects of environmental conditions on the corrosion rate of reinforcing steel bars, this work uses data for the corrosion rate of carbon steel exposed to air at all test points along measurement lines on the basis of the reference [10].

3.2 Corrosion rate of carbon steel exposed to air in Taiwan's coastal regions

Based on the research conducted by [10], four important factors are sensitive to the corrosion rate of reinforcing steel embedded in concrete, V_{crack}: temperature, T (^{o}C), humidity, RH (%), concrete-cover thickness, c (mm), and time, t (year), as Eq. (9).

$$V_{crack} = \alpha \times exp(\beta \times T)(RH/100 - 0.45)^{\kappa} c^{-\lambda} t^{\eta} \quad (9)$$

where α、β、κ、λ and η are five coefficients to be determined.

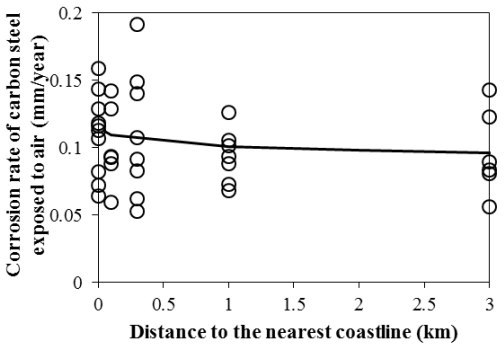

Fig. 4 Relationship between distance to the nearest coastline and corrosion rate of carbon steel exposed to air (northern zone)

Table 2 Regression equations for the corrosion rate of carbon steel for the coastal regions in Taiwan

Division Zone	Measurement Line	V_{crack} (mm/year)	Mean value of model error	COV of model error
Northern	Suao	$V_{crack} = e^{-0.0809T} \times (RH - 0.45)^{0.2288} \times d^{-0.0374}$	1.130	0.582
Middle	Taichung	$V_{crack} = e^{-0.0513T} \times (RH - 0.45)^{0.938} \times d^{-0.0522}$	1.307	0.731
Southern	Kaohsiung	$V_{crack} = e^{-0.0169T} \times (RH - 0.45)^{1.765} \times d^{-0.0601}$	1.032	0.498
Eastern	Hualien	$V_{crack} = e^{-0.0934T} \times (RH - 0.45)^{0.28} \times d^{-0.0875}$	0.923	0.30

T：mean value of temperature (^{o}C)，RH：mean value of humidity (%)，d：distance to the coastline (km)

Because this work referred to Eq. (9) to build the estimation equation for the corrosion rate of reinforcing steel exposed to air, we excluded concrete-cover thickness from the factors. Additionally, we found the longer the distance to the nearest coastline, the slower the corrosion rate of carbon steel exposed to air presents. Therefore, this work included the distance to the nearest coastline as a factor in Eq. (9). Based on the corrosion rate of carbon steel exposed to air at test points along measurement lines [2][3] and data for temperature and humidity from Taiwan's Central Weather Bureau, the equations for estimating corrosion rate in Taiwan's coastal regions were regressed (Table 2). Figure 5 shows the relationship between the distance to the nearest coastline and corrosion rate.

Referring to the above deterioration model for chloride-induced corrosion, corrosion curves of reinforcing steel bars, which show the relationship between mean weight loss and time, can be plotted to estimate degradation of the material properties of reinforcing steel bars (e.g., yielding strength, elasticity modulus, and ultimate strength).

4. HAZARD CURVE OF CORROSION OF REINFORCING STEEL BARS

4.1 Method for evaluating the corrosion degree of reinforcing steel bars

Recommendations for durability investigation /diagnosis and repair of RC buildings by the Architectural Institute of Japan [8] indicated that the appropriate repair method for RC members can be identified based on the degree of degradation and environmental factors associated with structural deterioration. Additionally, the degree of degradation can be determined based on cracking of concrete surfaces and the degree of corrosion of reinforcing steel bars. However, when cracking of concrete surfaces is caused by an external force instead of corrosion of reinforcing steel bars, the evaluation criteria of AIJ [8] are not applicable for evaluating the degradation degree. Furthermore, the degree of corrosion of reinforcing steel bars can be determined in terms of surface rust, and depends on weight loss. Taiwan has no relevant specifications or recommendations for investigation/diagnosis of the durability of RC structures or members. Thus, this work refers to the evaluation criteria of AIJ [8] to calculate the degree of degradation of corroded reinforcing steel bars.

4.2 Uncertainties considered when assessing the hazard of corrosion of reinforcing steel

When assessing the hazard of corrosion of reinforcing steel, this work considered several uncertainties, which were divided into three types. One type of uncertainty is related to environmental conditions, including mean wind speed; another type of uncertainty is related to concrete quality, which includes concrete-cover thickness, the threshold of chloride concentration for corrosion initiation, and threshold of weight loss for concrete-cover spalling; the third type of uncertainty is related to model error of estimation equations (e.g., Eqs. (4) – (7)). Statistical characteristics of uncertainties in terms of mean wind speed, airborne chloride concentration, concrete-cover thickness, and the corrosion rate for carbon steel exposed to air were determined using measurement data, while other uncertainties were values suggested by previous studies.

4.3 Procedure for computing the hazard curve of corrosion of reinforcing steel

In order to consider the certainties stated in Section 4.2, this work applies MCS to simulate the hazard curve of corrosion of reinforcing steel. Figure 5 shows the procedure for computing the chloride-induced corrosion of reinforcing steel; then, using the evaluation criteria for the corrosion degree, the occurrence probability for each corrosion degree can be simulated (Fig. 6). Based on the evaluation method for deteriorating RC members suggested by AIJ [8], cracking of concrete surfaces caused by corrosion can be seen with the naked eye when the corrosion degree of reinforcing steel bars is IV. Additionally, the width of cracks exceeds 0.5 mm

when the corrosion degree is V. Generally, when the width of cracks is <0.5 mm, concrete-cover spalling will not exist; that is, the rate of corrosion of reinforcing steel bars will not accelerate. Therefore, this work uses the corrosion degree IV of reinforcing steel bars as the threshold for the corrosion hazard curve. In this work, the horizontal axis, the x-axis, of the hazard curve of corrosion is time, and the vertical axis, the y-axis, is the probability of exceeding the corrosion degree IV. Engineers can also set the allowable degree of corrosion of reinforcing steel to get the hazard curve of corrosion using the same procedure.

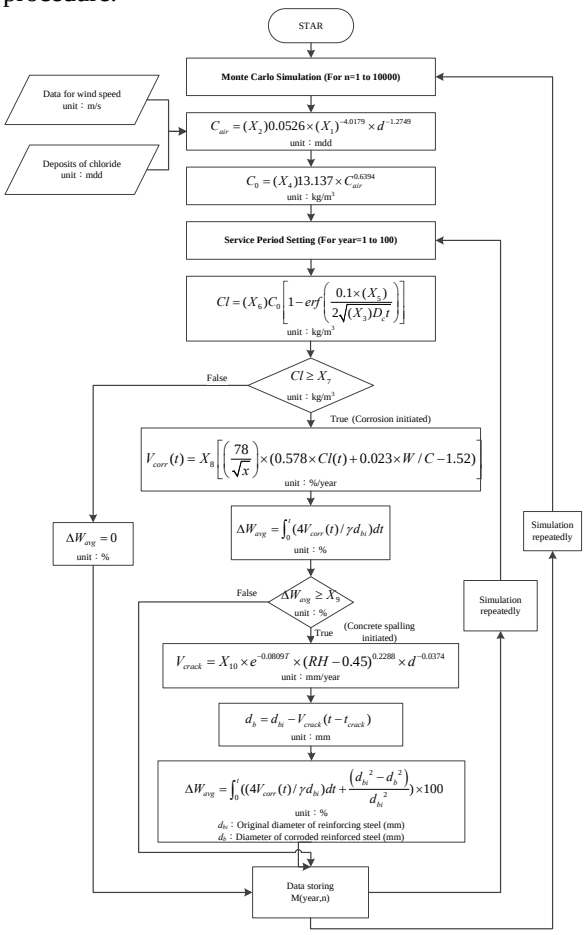

Fig. 5 Calculation process of corrosion of reinforcing steel bars (Suao)

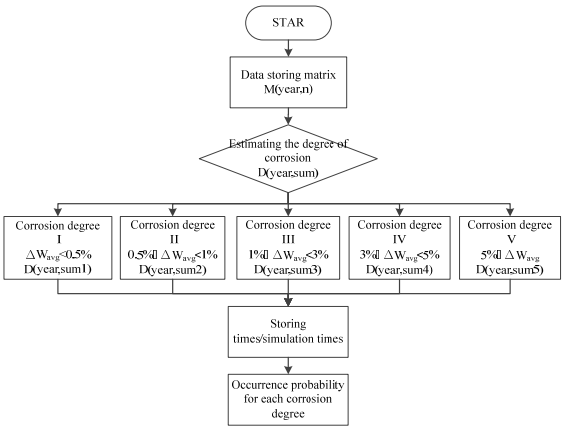

Fig. 6 Computing procedure for the hazard curve of corrosion (Suao)

5. DETERMINING THE MINIMAL CONCRETE-COVER THICKNESS FOR TAIWAN'S COASTAL REGIONS

This work investigates the thicknesses of concrete covers in Taiwan's coastal regions, including the cities of Suao, Taichung, Kaohsiung, and Hualien. These cities locate in the northern, middle, southern and eastern zones of Taiwan, respectively. The procedure for computing the corrosion hazard of reinforcing steel bars is applied to calculate the hazard curves under different concrete-cover thicknesses and distances to the nearest coastline, *i.e.*, 1 km, 2 km and 3 km (Figs. 7 – 10). In this case study, the service lives of RC structures was set at 50 and 100 years. Additionally, because the corrosion degree IV does not damage the structural damage immediately and can be detected using the naked eye of users, the limiting value of exceedance probability was set at 0.50 (its corresponding reliability is 0.50) to determine the minimum needed thickness of concrete covers. Restated, the durability reliability of an RC building is defined as the non-exceedance probability for the degree of corrosion IV in this work.

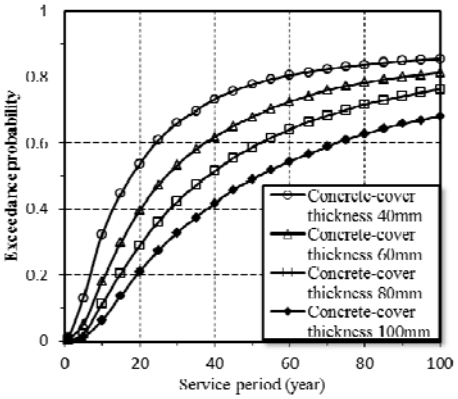

Fig. 7 Hazard curve of corrosion in Suao (distance to the nearest coastline is 0.05 km)

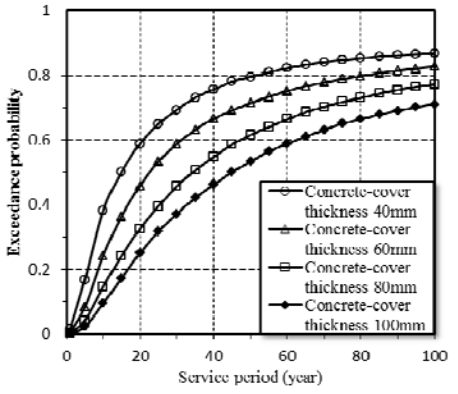

Fig. 8 Hazard curve of corrosion in Taichung (distance to the nearest coastline is 0.05 km)

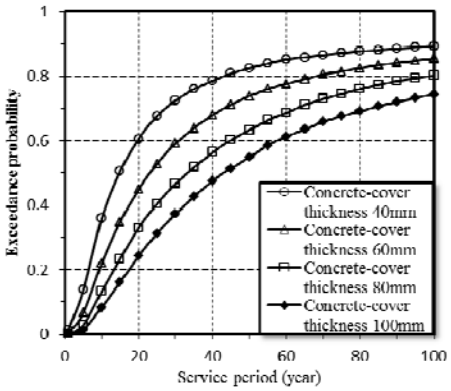

Fig. 9 Hazard curve of corrosion in Kaohsiung (distance to the nearest coastline is 0.05 km)

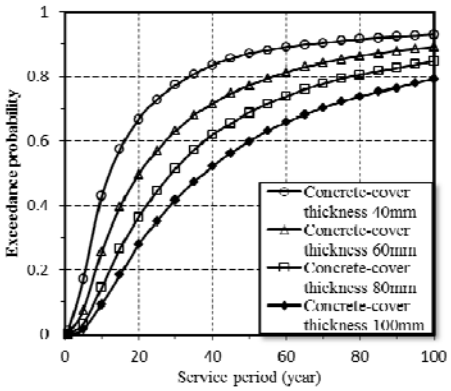

Fig. 10 Hazard curve of corrosion in Hualien (distance to the nearest coastline is 0.05 km)

When the distance between an RC structure with a specified service life of 50 years and the coastline is 0.05 km, we infer that the minimal needed thickness of a concrete cover should be 10 cm (Fig. 7). Therefore, the minimal needed thickness of a concrete cover based on the distance to the nearest coastline can be derived using the proposed procedure. Moreover, the simulated thicknesses of concrete covers can let the durable reliability of RC members equal or over a specified level regardless of building location.

MOTC [11] divided an area near a coastline into the following regions: the EZ region, which is characterized by extreme chloride-induced corrosion; the SZ region, which is characterized by serious chloride-induced corrosion; the MZ region, which is characterized by moderate chloride-induced corrosion; and the GZ region, which is characterized by little chloride-induced corrosion. These regions are based on distance to the nearest coastline. A minimal needed thickness of concrete covers is suggested for each region. Generally, for RC buildings located within 0.05 km from the coastline, when the concrete cover is only used to resist chloride ingress, this will increase construction costs and adversely affect the serviceability of the internal space of a building. In addition to the concrete cover, the concrete mix and surface coatings can function as barriers that reduce corrosion hazard for reinforcing steel bars, as suggested in previous studies. Furthermore, for RC buildings located farther than 3 km from the nearest coastline (*i.e.*, the GZ region), the thickness of a concrete cover can be the recommended value in building specifications [12]. This case study focused on RC buildings with specified service lives of 50 and 100 years that are located 0.05 – 3.0 km from the nearest coastline. Based on simulation results, Table 3 summarizes the minimal needed thicknesses of concrete covers when the limiting value of exceedance probability in the hazard curve of corrosion is set at 0.50. For an RC building with a specified service life of 50 years, when the recommended design thickness in design specifications for highways [11] of 7.5 cm is adopted, the occurrence probabilities for corrosion degree IV of reinforcing steel bars exceed 0.50 in the location, whose distance to the nearest coastline is about 0.05 km regardless of division zones according to the simulated results (Table 3(a)); that is, the durable reliability of RC members with the specified concrete-cover thickness does not meet the specified reliability of 0.50. However, for an RC building with a specified service life of 50 years located in the MZ region, the recommended design of 7.5 cm thickness in design specifications for highways [11] can let RC members' durable reliability exceed the specified value of 0.5. Therefore, on the basis of Table 7, this work suggests the ranges of the distance to the nearest coastline for the MZ and GZ regions are modified to 0.3 – 1.0 km and >3 km, respectively; the minimal needed thicknesses of concrete covers for RC buildings with a specified service life of 50 years located in the SZ and MZ regions are set at 10.0 cm and 6.0 cm, respectively. Additionally, for the GZ region, the minimal needed thickness of concrete covers of 4.0 cm is recommended.

When the specified service life of an RC building is set at 100 years, the minimal needed thicknesses of concrete covers are 10.0 cm MZ regions and 4.0 cm for the GZ region according to Table 3(b). For the SZ region, because it is not easy to use the concrete cover to reduce the corrosion hazard for reinforcing steel bars, the concrete mix or surface coatings that can function as barriers for chloride ingress should be considered in the design stage. Although this work uses the corrosion degree IV to calculate the durable reliability of RC members with a specified concrete-cover thickness, the computational procedure for deriving the corrosion hazard of reinforcing steel bars can be applied to assess the effectiveness of concrete-cover thicknesses. Additionally, building designers can set an allowable reliability of durability to determine the needed thickness of a concrete cover for RC members.

Table 3(a) Recommended concrete-cover thickness for a specified service period of 50 years in coastal regions of Taiwan (cm)

Division Zone	Distance to the nearest coastline (km)			Code-suggested value*
	0.05	0.30	1.0	
Northern (Suao)	10.0	4.0	4.0	7.5
Middle (Taichung)	>10.0	6.0	4.0	7.5
Southern (Kaohsiung)	>10.0	6.0	4.0	7.5
Eastern (Hualien)	>10.0	6.0	4.0	7.5

* Design Specifications for Highway [11]

Table 3(b) Recommended concrete-cover thickness for a specified service period of 100 years in coastal regions of Taiwan (cm)

Division Zone	Distance to the nearest coastline (km)			Code-suggested value*
	0.05	0.30	1.0	
Northern (Suao)	>10.0	6.0	4.0	7.5
Middle (Taichung)	>10.0	10.0	4.0	7.5
Southern (Kaohsiung)	>10.0	10.0	4.0	7.5
Eastern (Hualien)	>10.0	10.0	4.0	7.5

* Design Specifications for Highway [11]

6. CONCLUSIONS

This work developed equations for estimating airborne chloride concentrations in Taiwan's coastal regions, and incorporated these equations into the model for chloride-induced deterioration to construct an evaluation model that can estimate corrosion of reinforcing steel bars. This work also presented a novel computational procedure for calculating corrosion hazard of reinforcing steel, while considering uncertainties in environmental conditions, material properties, and model error. Based on the hazard curve of corrosion of reinforcing steel, building designers can set an appropriate durable reliability to determine the minimal needed thickness of a concrete cover for RC members. This work also suggested the minimal needed thicknesses of concrete covers for RC buildings with a specified service life of 50 years in the cities of Suao, Taichung, Kaohsiung, and Hualien in Taiwan. Moreover, a comparison of these values with values recommended in design specifications indicates that the durable reliability of RC members with the recommended concrete-cover thickness can be determined. Although this work used the corrosion degree IV to calculate the durable reliability of RC members with a specified concrete-cover thickness, the computational procedure for deriving the corrosion hazard of reinforcing steel bars can be applied to assess the effectiveness of concrete-cover thicknesses. The procedure can also be applied to establish design criteria or specifications for concrete covers that can let RC members be with the same durable reliability.

ACKNOWLEDGMENT

The authors would like to thank the National Science Council of the Republic of China, Taiwan, for financially supporting this research under Contract NSC 100-2628-E-011-006.

REFERENCES

[1] Lim, C. C. (2004), "Concrete durability provisions in design codes: Are they really adequate ?" (Cover feature), Buletin Ingenieur, 21, 9-12.

[2] MOTC (2010). Environmental Corrosivity Classification for Structures (1/2), Taipei: Ministry of Transportation and Communications of Taiwan.

[3] MOTC (2011). Environmental Corrosivity Classification for Structures (2/2), Taipei: Ministry of Transportation and Communications of Taiwan.

[4] JSCE (2008). Reliability-based design for concrete structures (336 committee report), Tokyo: Japan Society of Civil Engineers.

[5] Chen, Y. S. and Chan, Y. W. (2010), "On the correlation between air-borne chloride and durability of concrete in coastal region of north Taiwan", Master Thesis, National Taiwan University.

[6] Kato, Y. and Uomoto, T. (2005), "Proposal for quantitative evaluation methodology of inspection value in maintenance of concrete

structures based on repair-risk", Journal of Advanced Concrete Technology, 3(3), 363–370.
[7] Tottori, S. and Miyagawa, T. (2004), "Deterioration prediction of concrete structures concerning rebar corrosion due to carbonation", Journal of the Japan Society of Civil Engineers, 767(V-64), 35-46. (In Japanese)
[8] AIJ (1997). Recommendations for Practice of Survey, Diagnosis and Repair for Deterioration of Reinforced Concrete Structures, Tokyo: Architectural Institute of Japan. (in Japanese)
[9] Izawa, J. and Matusima, M. (2004), "The corrosion quantity of concrete crack induced by corrosion expansion" , Master Thesis, Kagawa University.
[10] Niu, D. T. (2003). Durability and Life Forecast of Reinforced Concrete Structure. Beijing: Science press (in Chinese)
[11] MOTC (2009). Design Specifications for Highway, Taipei: Ministry of Transportation and Communications of Taiwan.
[12] CICHE (2006). Specifications and Explanations for Concrete Grouting in Construction, Taipei: Chinese Institute of Civil and Hydraulic Engineering.
[13] Takahashi, T., Sakai, M., Seki, H. and Matsushima, M. (2005), "Calculation of LCC and selection system of repairing method for reinforced concrete members exposed to sea environments", Concrete Research and Technology (JCI), 16(3), 21–29. (in Japanese)

Proceedings of the 3rd JCI-KCI-TCI Symposium on Recent Advancement of Technologies in Concrete Engineering
Japan Concrete Institute, July 2012

THE ABRASION OF CONCRETE MADE OF INDUSTRY BY-PRODUCTS

Wen-Chen Jau
Department of Civil Engineering, National Chiao-Tung University, Taiwan

ABSTRACT

Concrete is widely used in hydraulic structures, such as levees, dams, spillways, etc. All these structures are subjected to abrasion and maintenance becomes a major problem. In addition, the slopes of rivers in Taiwan are generally steep, which make the abrasion even more critical due to higher velocity and debris flow. In the past, it is confirmed that high strength concrete has a better resistance of abrasion. However, it still suffers abrasion from time to time. A new concrete is thus developed.

As sustainability becoming more and more important in nowadays, how to recycle and reuse industrial waste is gaining popularity recently. This study used industrial waste to manufacture abrasion resistance concrete. It is demonstrated that the concrete made with these material shows higher abrasion resistance by tests according to ASTM C1138. The volume loss, depth of abrasion, compressive strength, and tensile splitting strength are better for the new concrete compared to conventional concrete.

Keywords: *abrasion resistance, industry by-products, hydraulic structures, hydraulic concrete*

1 INTRODUCTION

Due to the geographical characteristics of Taiwan, the rivers are short and steep. Muds, stones and debris flow downstream with water at very high speed. This phenomenon causes abrasion on hydraulic structures and piers. The concrete may be damages and the steel exposed. The durability is often reduced and may need a great deal of resources to repair it. The past studies focus mainly on increasing the strength of concrete by using slag, fly ash, silica fume and fibers. This study uses industry by-products to replace aggregates to increase the abrasion resistance. The strengths, loss of volume and abrasion depth were evaluated and compared to those of concretes made of natural aggregates.

2 TEST PROGRAMS

2.1 Materials

(1) cement: Portland cement Type I made by Taiwan cement company
(2) coarse aggregate: natural coarse aggregates from Tou-Chian river
(3) fine aggregates: natural fine aggregates from Tou-Chian river
(4) industry by-products: A and B with specific weight of 3.2 from metal company
(5) Superplasticizer: BASF GLENIUM 51TH
(6) Water reducing agent：BASF POZZOLITH 390T
(7) Water: tap water
(8) Silica fume：Elkem Microsilica® Grade 940U，

2.2 Test design

Concretes made of various aggregates were designed and tested with various w/c, strength, and abrasion resistance.

The variables of the test are:

(1) aggregates: natural aggregates and industry by-products
(2) w/c: 0.4, 0.35 and 0.3
(3) age: 7, 14, and 28 days
(4) silica fume: 10%
(5) symbol designation:

a. OPC-S0-0.4-7
   OPC: concrete with natural aggregates
   S0: 0% silica fume
   0.4: w/c=0.4
   7: tested at 7 days
b. FOPC-S10-0.3-28
   FOPC: concrete made with industry by-product
   S10: 10% silica fume in terms of cement weight
   0.3:w/c=0.3
   28: tested at 28 days

2.3 Test methods

All the specimens were made, cured, and tested according relevant Chinese National Standards. Though there are four different test methods in ASTM about abrasion, such as C418, C779, and C944. The abrasion test was performed according to ASTM C1138 “Abrasion resistance of concrete (underwater method)” to better simulate the hydraulic structures in a river.

3. TEST RESULTS AND DISCUSSION

A. The effects of aggregates

(1) The effect of aggregate on compressive strength

The compressive strengths are listed in Table 1 and Figures 1, 2 and 3. It can be observed that the concrete made of industry by-products showed a higher compressive strength than the concrete made of natural aggregates regardless of w/c and ages. The strength ratio (FOPC/OPC) is in the range of 1.03 – 1.10. This is because of the higher strength of the by-products than natural aggregates. It is well known that at the same w/c, the higher the strength of coarse aggregates, the higher the strength of the concrete. Nonetheless, as the ages increases, the ratio decreases. A possible explanation is that the by-products had a rougher surface and can develop a better bond at early age. However, as the age increases, the natural aggregates also can have a good bond with mortar and thus the difference is decreased.

(2) The effect of aggregate on splitting tensile strength

The splitting tensile strengths of specimens are listed in Table 2. Again, it can be observed that the concrete made of industry by-products showed a higher tensile splitting strength than the concrete made of natural aggregates at the same w/c and ages. This is because of the higher strength of the by-products. The splitting tensile strength ratios (FOPC/OPC) are in the range of 1.08 – 1.23 for all ages and w/c. However, the age effect in tensile strength was not clearly observed in splitting tensile strength. More study is needed to understand this observation.

Table 1 The compressive strengths of specimens

Specimens	Compressive Atrength	
	MPa	psi
OPC-S0-0.4-7	30.38	4405.44
OPC-S0-0.4-14	41.13	5963.37
OPC-S0-0.4-28	49.93	7239.23
OPC-S0-0.35-7	31.21	4525.27
OPC-S0-0.35-14	42.22	6121.77
OPC-S0-0.35-28	51.17	7420.19
OPC-S0-0.3-7	33.47	4852.48
OPC-S0-0.3-14	44.45	6445.84
OPC-S0-0.3-28	55.86	8099.32
FOPC-S0-0.4-7	33.63	4876.19
FOPC-S0-0.4-14	44.83	6500.97
FOPC-S0-0.4-28	52.58	7624.71
FOPC-S0-0.35-7	35.01	5076.43
FOPC-S0-0.35-14	45.46	6592.23
FOPC-S0-0.35-28	54.38	7885.80
FOPC-S0-0.3-7	36.73	5326.23
FOPC-S0-0.3-14	47.59	6901.02
FOPC-S0-0.3-28	57.40	8322.56

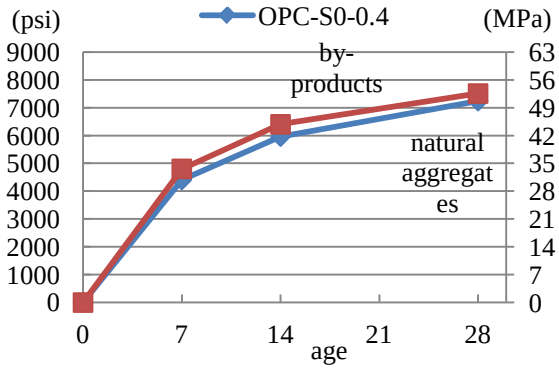

Figure 1 w/c=0.4 The compressive strength concrete with various aggregates

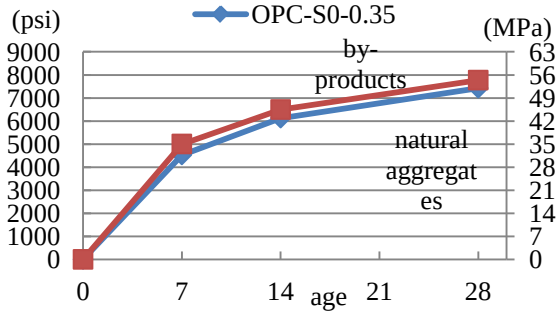

Figure 2 w/c=0.35 The compressive strength concrete with various aggregates

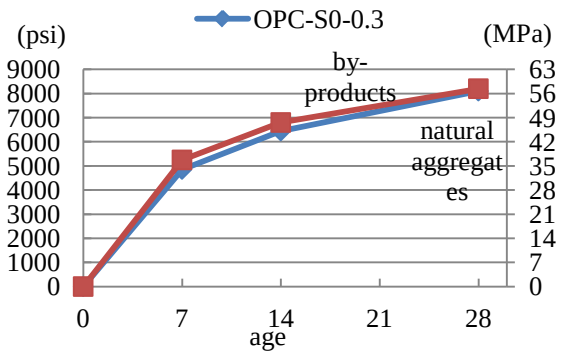

Figure 3 w/c=0.3 The compressive strength concrete with various aggregates

(3) The effect of aggregate on abrasion resistance

The test results of abrasion resistance expressed as the volume loss of the specimens are listed in Table 3 and representative Figures 4, 5 and 6. From the Table, it is clear that the concrete made of industry by-products showed a much better abrasion resistance than concrete made of natural aggregates at the same age and w/c. The loss of volume of concrete is higher at the beginning and decreases afterward. This is because the strength and hardness of surface is mainly from mortar and the abrasion of mortar is not as good as coarse aggregates. After mortar was removed by abrasion, the coarse aggregates were exposed and the strength and hardness were higher for coarse aggregates than mortar. Therefore, the abrasion rate was lower at this stage. Please note that the abrasion rate is less for concrete made of industry by-products. This is because the by-products are stronger and stiffer, and thus higher resistance to the impact and abrasion from steel balls. After 48 hours of test, the increase of volume loss starts to increase again. The reason for this phenomenon is because the first layer of coarse aggregate was lost due to the impact and abrasion of the steel balls. The bond between mortar and coarse aggregates was lost and so did the coarse aggregates. The loss of mortar contributes more in this stage, just as the beginning. It is obvious that the higher strength and stiffness of aggregates are very important factors on the strength and abrasion resistance. The ratio of loss (FOPC/OPC) varies more at the beginning in the range of 1.0 – 0.33. The range of the ratios then narrows down with the test time. At the end of 72 hours test, the ratio is in the range of 0.39 – 0.48. This is because of the higher strength and hardness of the by-products which can better endure the impact of the steel balls during the test. The variation of the ratio with time is because at beginning, the mortar is on the surface and the quality of mortar is the most important factor for abrasion resistance. The thickness and quality of surface mortar could not be easily controlled. As the testing time increases, the abrasion resistance was mainly controlled by coarse aggregates and thus a more similar ratio is realized. The use of by-products as coarse aggregates is very beneficial to concrete abrasion resistance.

Table 3 The volume loss of various concretes after

Volume loss of concrete specimens after test (cm^3)							
Specimens	0 hr	12 hr	24 hr	36 hr	48 hr	60 hr	72 hr
OPC-S0-0.4-7	0	45	70	90	112	127	150
OPC-S0-0.4-28	0	27	36	55	85	95	102
OPC-S0-0.3-7	0	33	54	73	95	109	118
OPC-S0-0.3-28	0	10	31	50	75	85	90
FOPC-S0-0.4-7	0	15	22	32	37	47	58
FOPC-S0-0.4-28	0	12	21	30	34	42	49
FOPC-S0-0.3-7	0	10	20	31	35	43	50
FOPC-S0-0.3-28	0	10	15	23	31	38	43

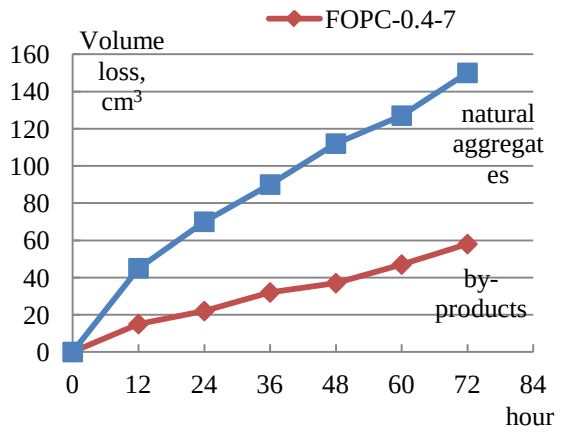

Figure 4 w/c=0.4 Volume loss of various concrete at age 7 days

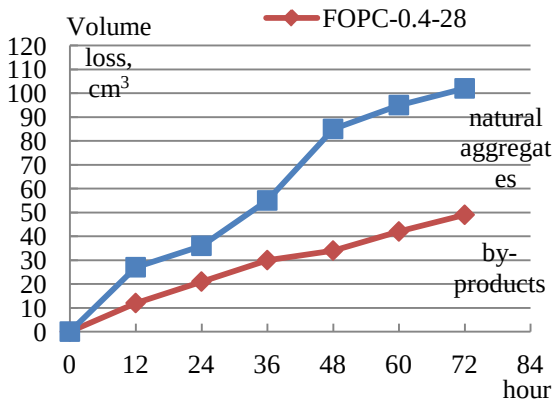

Figure 5 w/c=0.4 Volume loss of various concrete at age 28 days

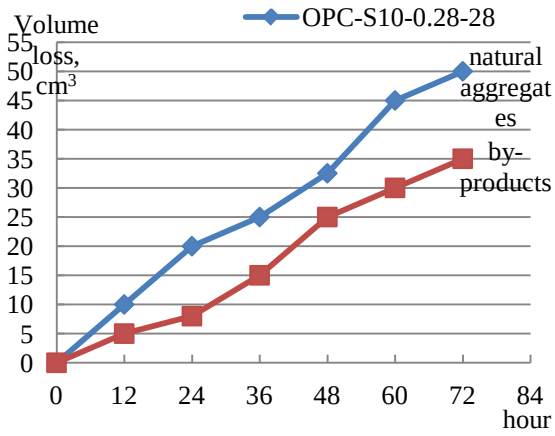

Figure 6 w/c=0.28 Volume loss of various concrete with 10% silica fume at age 28 days

B. The effect of w/c

(1) The effect of w/c on compressive strength

The effect of w/c is the same for all concretes, i.e., the lower the w/c, the higher the strength. This is true for all the types of aggregates and ages. As the w/c decreases from 0.4 to 0.3, the compressive strength increases at 28 days is 1.12 for natural aggregates and 1.09 for using by-products. The compressive strength increase at 7 days is 1.10 and 1.09 respectively for natural and by-products aggregates. The effect of by-products is not significant.

(2) The effect of w/c on splitting tensile strength

Again, the effect of w/c is the same for all concrete, regardless of the type of aggregates. That is, the lower the w/c, the higher the splitting tensile strength. As the w/c decreases from 0.4 to 0.3, the tensile strength increases at 28 days is 1.10 for natural aggregates and 1.24 for using by-products. The tensile strength increase at 7 days is 1.12 and 1.14 respectively for natural and by-products aggregates. The by-products have a role in tensile strength.

(3) The effect of w/c on abrasion resistance

Again, the effect of w/c is the same for all concrete, regardless of the type of aggregates. The lower the w/c, the higher the abrasion resistance. At the age of 7 days, the increase on abrasion resistance measured by volume loss for w/c 0.4 concrete made of natural aggregates compared to same concrete with w/c 0.3 is 1.36(150/102) and 1.16(58/50) for concrete made of by-product aggregates and tested for 72 hours. Similarly, at the age of 28 days, the increase in abrasion resistance is 1.13(102/90) and 1.14(49/43) for various aggregates also tested for 72 hours. The comparisons for different test durations show similar results. That is, the lower w/c helps to mitigate the abrasion resistance compared to that of concrete with higher w/c. However, the effect of w/c for by-products are not significant.

C. The effect of age

The longer the time, the higher the compressive strength, the tensile splitting strength, and the abrasion resistance. This is true for all concrete of various w/c, though the changes are a dependent of times and varies for different properties as reported in previous sections.

D. Comparison with previous study

It is found from literatures [5] [6] [7] that silica fume has been used to increase the abrasion resistance worldwide. A 10% of silica fume is added for this purpose. The best mix design from literature was chosen for comparison. With the same mix design, the only variable is the type of coarse aggregate. The test results are shown in Table 4. From the table, it is found that with the same mix design, the concrete which used industry by-products outperforms the concrete with natural aggregated at all testing conditions. At the end of 72 hours test, the concrete with by-products showed a loss of 30% (50 vs 35 cm^3) less loss if the concrete is tested at 28 days. If the concrete is tested at 7 days of age, the loss of concrete made of by-products is only 45% for the concrete made of natural aggregates, or a 55% reduction (88 vs 40 cm^3). This ratio is in compatible with the concretes without silica fume as discussed in section 3-(3). The superiority of by-products is justified. In addition, the surfaces of the concrete after test are shown in Figures 7 and 8. The surface of OPC-S10-0.28-28 after 72 hours test is not as smooth as the counterpart of FOPC-S10-0.28-28. This is an obvious demonstration of the advantage of using by-products as coarse aggregates. The holes of the specimens are due to the loss of coarse aggregates. The concrete used natural aggregates shows more holes and this observation proves that the natural aggregates are not as strong as by-products and were lost due to impacts of steel balls. In addition, a

possible reason is that the bond between mortar and natural aggregates is not as strong as by-products. Due to the fact that the w/c for this series is 0.28, which is not the same as previous study, no attempt is made to compare the results from this series with the previous test results.

Figure 7 the picture of specimen OPC-S10-0.28-28 after 72 hour abrasion test

Figure 8 the picture of specimen FOPC-S10-0.28-28 after 72 hour abrasion test

CONCLUSIONS

1. ASTM C1138 method is used to evaluate the abrasion resistance of underwater concrete and this method is able to tell the difference of various concrete, such as the w/c and coarse aggregates.
2. The higher the concrete strength, the higher the abrasion resistance for the w/c range from 0.3-0.4.
3. The industry by-products can produce a higher compressive and splitting tensile strength concrete, though the difference is not very significant for compressive strength.
4. The industry by-products can be used to produce a more abrasion resistant concrete. The difference is very obvious based on the lost volume and observation on the surface of specimens after test.
5. Silica fume up to 10% weight replacement of cement increases the compressive strength and abrasion resistance. However, the concrete with by-products is still stronger than the concrete made with natural aggregates.

REFERENCES

[1] ASTM C418 Abrasion resistance of concrete by sandblasting.

[2] ASTM C779 Abrasion resistance of horizontal concrete surfaces.

[3] ASTM C944 Abrasion resistance of concrete and mortar surface by the rotating cutter method.

[4] ASTM C1138 Abrasion resistance of concrete (underwater method).

[5] C. H. Chan, "The abrasion resistance of hydraulic concrete and fiber concrete," MS Thesis, National Chia-Yi university, 2005

[6] H. H. Lin, "The abrasion properties of slag concrete," MS Thesis, National Taiwan University, 2004

[7] C. H. Hsu, "The abrasion resistance and crack prevention of high strength concrete with fly ash," Ph.D. Thesis, National Chong Hsin University, 2006